Transmission grid extensions in renewable electricity systems

Dissertation
zur Erlangung des Doktorgrades
der Naturwissenschaften

vorgelegt beim Fachbereich Physik
der Johann Wolfgang Goethe-Universität
in Frankfurt am Main

von
Sarah Becker
aus Herford

Frankfurt 2014
D 30

vom Fachbereich Physik der
Johann Wolfgang Goethe-Universität
als Dissertation angenommen.

Dekan: Joachim Stroth
Gutachter: Stefan Schramm, Martin Greiner, Joachim Maruhn
Datum der Disputation: 15.10.2014

Contents

Chapter 1

Introduction

Renewable energy sources become more and more important throughout the world. During the past years, their world share in total primary energy supply (TPES) has stayed constant at about 11 % (including waste) between 1973 and 2011, while TPES itself has more than doubled, from 260 EJ (6100 Mtoe) to 550 EJ (13100 Mtoe). In the electricity sector, the world-wide share of renewables, including hydro power, has remained at around 20 % over the same period, and excluding hydro power has risen from 0.6 % to 4.5 %, while electric load almost quadrupled from 6100 TWh to 22100 TWh [1].

Even faster than that, renewable electricity shares have grown in the Organization for Economic Cooperation and Development (OECD) member countries and particularly in Europe. There, the average share rose from about 14 % (almost exclusively hydro power) in 1990 up to 23.5 % in 2012, with Denmark in the lead with a share of 38.7 % [2], mainly consisting of wind energy.

1.1 Motivations for the shift towards renewables

The main arguments for a shift of current energy acquisition to renewable technologies are (a) a necessary reduction in green house gases (GHG), mainly CO_2, to mitigate climate change, (b) energy security concerns, and (c) energy affordability and economic stability. We take a look at each of them:

1.1.1 Climate change mitigation

One main driver, at least in the OECD countries, is climate change mitigation. As Fig. 1.1 shows, there is a clear correlation between CO_2 levels and Antarctic temperature, with a Pearson r correlation coefficient of $r^2 = 0.82$ [3]. Over the period of the last 800 000 yrs, CO_2 levels are found to vary between 180 ppmv (parts per million volume) and 280 ppmv, while the temperature anomaly ranges over 12 °C.

For these measurements, ice cores from different drill holes in the Antarctic are examined. CO_2 concentration is obtained by extracting air from small bubbles in the ice. The CO_2 concentration is then determined by laser absorption spectroscopy and gas chromatography. Temperature is deduced from isotope measurements, looking at the levels of deuterium ^2D and heavy oxygen ^{18}O in the water making up the ice. Water molecules containing these heavy isotopes have a lower vapor pressure, and thus a slightly higher probability of raining out from clouds early than “normal” water when temperature drops. Cloud formation is a complex process, but on average, it can be said that they form predominantly over warm, equatorial oceans and then drift towards the poles. The colder the average temperature, the earlier the water molecules containing heavy isotopes rain out. In the early stages of its life, the cloud is likely still far away from the poles, so only few heavy isotopes reach the poles. Conversely, when temperatures rise, clouds tend to reach the Antarctic with higher concentrations of heavy isotopes. In conclusion, Antarctic snow from cold periods contains fewer heavy isotopes than snow from warmer periods. Traces of the change in heavy isotope transport with temperature can also be observed in ocean sediments, confirming the ice core observations [4].

From Fig. 1.1, the high correlation between atmospheric CO_2 levels and Antarctic temperature is evident. Current CO_2 levels are scraping at the 400 ppm mark, see Fig. 1.2. The International Panel on Climate Change (IPCC) estimates that global warming due to anthropogenic CO_2 emissions can be limited to about 2 °C, corresponding to a mean sea level rise of about 0.5 m, if the atmospheric CO_2 concentration remains below 550 ppmv [5, RCP4.5 scenario] – an ambitious goal, considering the growth by almost 100 ppmv over the last 50 yrs (Fig. 1.2), showing an almost exponential trend.

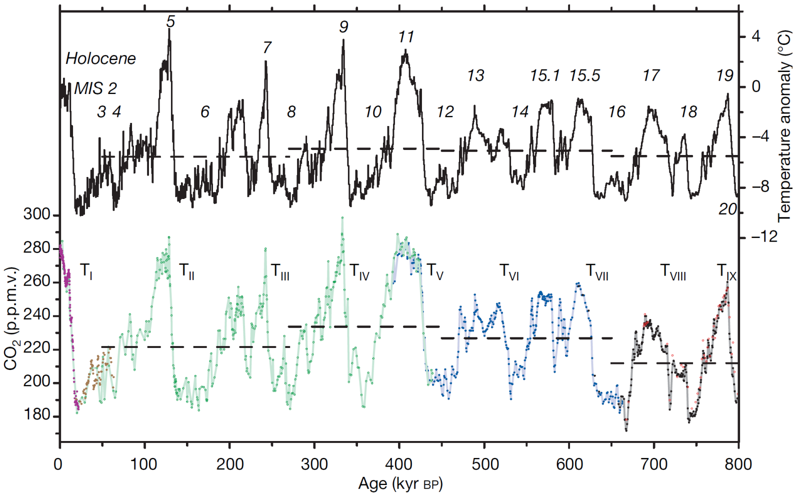

Figure 1.1: Correlation between temperature (above) and atmospheric CO_2 levels (below) during the last 800 000 years. CO_2 levels were obtained from direct measurements on extracted air in Antarctic ice cores, while temperature was inferred from Deuterium concentration. Reprinted by permission from Macmillan Publishers Ltd: NATURE [3], copyright 2008.

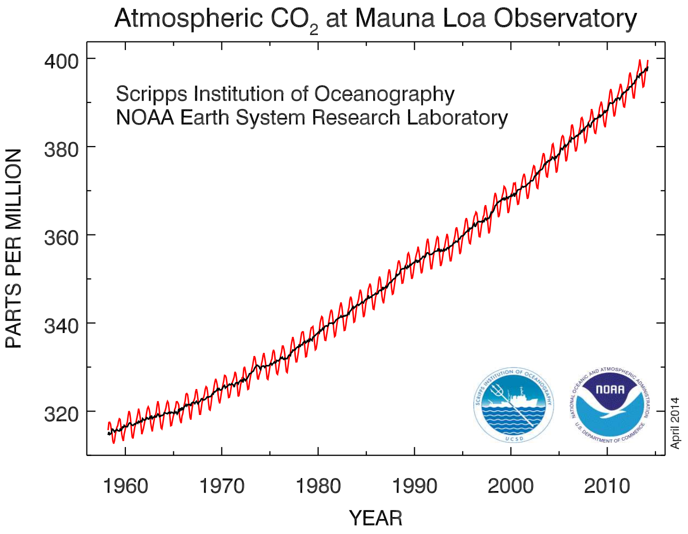

Figure 1.2: Atmospheric CO_2 concentration over the past 50 years, measured at Mauna Loa Observatory, Hawaii [6].

In the long run, it might seem to be an option that CO_2 could again be removed from the atmosphere by the formation of new coal and oil on geological timescales (and thus fossil fuels might be replenished). But coal formation is observed to have decreased substantially after the carbon period. This is generally attributed to changes in the climate and, subsequently, in the vegetation and landscape (less swamps which prevent aerobic digestion). New studies (e.g. Ref. [7] and references therein) indicate, however, that it could also be due to the evolution of microorganisms, known as white rot, that can digest the lignin, the main constituent of wood, which is the basis of fossil coal and oil. Their formation could therefore be severely inhibited.

1.1.2 Energy security and affordability

Many authors have discussed the impact of renewables on energy security and affordability, e.g. Refs. [8, 9]. Energy security concerns were first broadly discussed during the oil crisis in the early 1970s, which – among other results – lead to the foundation of the International Energy Agency (IEA) in 1973/74 [10]. Since then, fossil fuel prices have risen by factors of more than five, and price volatility has considerably increased as well [1].

As described in Ref. [11], easily accessible fossil fuel sources are more and more exploited. Therefore, prices are expected to rise in the long run, owing to more complex and thus expensive drilling and mining techniques that become necessary to tap more remote resources. A further consequence of this development is that the energy payback of fossil fuels will drop as more and more energy is needed to acquire them. Similar arguments, albeit on longer timescales, apply to the uranium needed to power nuclear plants.

Apart from these concerns about the security of supply with fossil and nuclear fuels, there is also the price of energy that a society pays, or the energy affordability. When calculating the total societal price of different energy supply technologies, there are also externalities to be considered. As mentioned above, CO_2 emissions driving climate change entail substantial costs for adaptation measures such as building dikes, resettling, or irrigation of crops. While renewables are not completely CO_2 emission free, their total life cycle emissions are orders of magnitude below fossil powered plants, and still factors of about five to 20 below fossil fuel plants with CCS or nuclear plants [8].

Air pollution is a serious environmental and medical concern: The World Health Organization (WHO) estimates that in 2012, around seven million people died prematurely due to low air quality [12]. Indoors, the main source of air pollution is cooking on coal- or wood-fired stoves. Outdoors, various sources contribute, such as industry, slash and burn land clearance, or wildland fires. In one way or another, they are mostly linked to combustion processes [13] – not least from fossil fuels.

When all these factors are internalized – non-CO_2 emissions, impact on human health arising from air pollution, water usage, the risk of nuclear proliferation, nuclear waste treatment and storage, and environmental degradation and damage –, the estimation becomes more and more complex, making accurate calculations hard. Ref. [14] estimates additional external costs of about 75 % of the internal generation costs for fossil fuels, and assuming no external costs of renewables.

Externalities also include area usage, which is typically much larger for the renewable technologies, relying on dispersed resources. As an illustration, consider some estimates for Germany: Solar PV is assumed to have an area usage of 8-30 m^2/kW [15]. With an average capacity factor of about 10 %, solar PV panels on 70-260 km^2 would produce the same yearly amount of energy as a conventional 1000 MW power plant (assumed capacity factor of 80 %). Similarly, with an assumed area usage of 90 m^2/kW (assuming 5 MW wind turbines and including spacing) and an assumed capacity factor of 40 % [8], the equivalent wind energy would require a wind park on 180 km^2. It should be noted here that the assumed wind data are relatively optimistic, especially the capacity factor will only be achieved under favorable wind conditions. On the other hand, most of the area of wind parks and a considerable share of solar parks would not be lost for other usage, e.g. crop fields between wind turbines or grazing pasture under solar panels. For comparison, lignite (brown coal) mining in Germany currently consumes an area of about 7.7 km^2/yr, which is hard to recover for agriculture and almost impossible to use for housing afterwards [16].

1.2 Low CO_2 power generation options

We will not attempt true societal cost estimates, but instead focus on climate change mitigation. We discuss the most important renewable and non-renewable low CO_2 generation techniques.

1.2.1 Wind and solar potentials

We first turn to wind and solar power. Since they are both intermittent, we term them variable renewable energy sources (VRES). The world potential for wind and solar energy can be estimated in various ways, see Tab. 1.1. First, there is the theoretical potential, consisting of the entire energy contained in wind kinetic energy and solar irradiation. These two are, of course, not to be viewed separately since the insolation is the main driver of wind. But just naively calculating their averages over time can provide us with an upper bound on the available energy. It ranges well above current human energy consumption of about 370 EJ/yr in 2013. However, technological constraints have to be taken into account. Wind turbines and solar panel cannot convert the entire energy they receive into electric energy. Some more hints can be taken from the distribution of resources across the earth's surface, reprinted from Ref. [17] in Fig. 1.3: 70 % of the earth's surface is covered in oceans, which are mostly to deep for permanent installations. Geography and climate impose further limitations, e.g. high slopes or regular flooding. Taking these into account, one arrives at the technical potential. This is further reduced by practical considerations, excluding for example very remote areas or low-yield sites. What remains afterwards is called the realistic potential, and it is actually on the same order of magnitude as human energy consumption. What Tab. 1.1 also shows is that there is a lot of uncertainty in estimating realistic potentials, resulting in a considerable spread between the two sources.

As pointed out above, although wind and solar resources are abundant, they are dispersed and therefore generating electricity from them requires a substantial amount of area. Even under the rather optimistic assumptions of Ref. [17], this still amounts to 1 % of the entire land area.

Table 1.1: World wind and solar potential estimates in EJ/yr, from Ref. [17], by Mark Jacobson and Mark Delucchi (here abbreviated as JD), and from the International Panel on Climate Change (IPCC) special report on renewables [18] (here abbreviated as IPCC).

	theoretical	technical	realistic
solar PV (JD)	$2.1 \cdot 10^5$	$4.1 \cdot 10^4$	$1.1 \cdot 10^4$
solar PV (IPCC)	$3.9 \cdot 10^6$	$1.6 \cdot 10^3 - 2.5 \cdot 10^4$	$1.6 \cdot 10^3 - 5.0 \cdot 10^4$
wind power (JD)	$5.4 \cdot 10^4$	$2.2 \cdot 10^3 - 5.4 \cdot 10^3$	$1.3 \cdot 10^3 - 2.7 \cdot 10^3$
wind power (IPCC)	$6.0 \cdot 10^3$	$1.4 \cdot 10^3 - 3.1 \cdot 10^3$	$7.0 \cdot 10^1 - 4.4 \cdot 10^2$

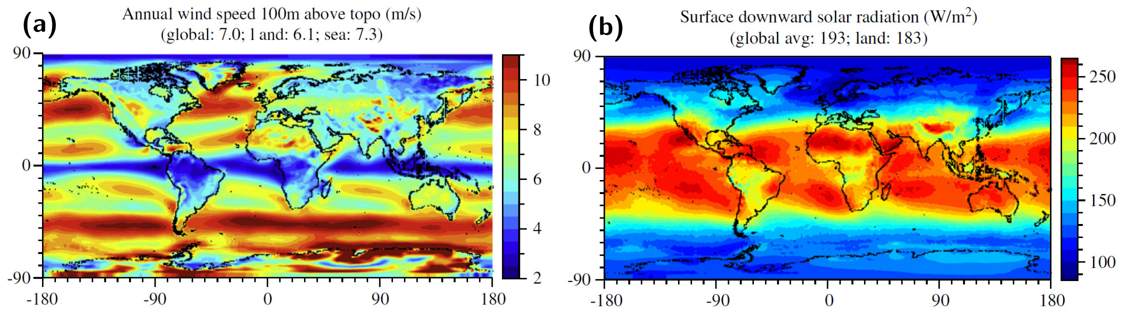

Fig. 1. Map of the yearly averaged world wind speed (m/s) at 100 m above sea level at 1.5 × 1.5° resolution, generated with the GATOR-GCMOM 3-D global model (Jacobson, 2010).

Fig. 2. Map of the yearly averaged downward surface solar radiation reaching the surface (W/m^2) at 1.5 × 1.5° resolution, generated with the GATOR-GCMOM 3-D global model (Jacobson, 2010).

Figure 1.3: Renewable resource distribution across the world: (a) mean wind speed at 100 m height, (b) annual solar surface irradiation. Reprinted by permission from Elsevier [17], copyright 2011.

1.2.2 Biomass

Biomass is a potentially CO_2-neutral energy source. Estimated theoretical potentials by the IEA are around 250-600 EJ/yr, see Tab. 1.2 for details. This amount might be able to cover the world's energy consumption of recently 370 EJ/yr. However, a central question in this field is how sustainable the supply really is, and if competition to food production occurs, or in other words, what the realistic and sustainable biomass potential is.

Biomass potentials in Europe

At the moment, biomass and waste cover 62 % of the European renewable energy generation, providing 3.6 EJ/yr in 2010 [2]. This share is projected to fall to 57 %, while absolute production is expected to rise to 5.9 EJ/yr in 2020 [20], compare also Tab. 1.3 which shows the aggregated targets of the EU member countries as documented in the National Renewable Energy Action Plans (NREAP). Production areas are then expected to cover 17-21 mio. ha, or a little less than 2 % of the entire European land area.

Limitations to biomass growth are reflected in Tab. 1.3: Its contribution to total electricity generation is only expected to double during the period 2010-2020, until it covers about 7 % of the total (2007) load. In contrast, growth by factors of four to five for the VRES technologies wind and solar PV power are anticipated.

Potentially favorable biomass regions, where arable land is available and production costs are relatively low is examined in Ref. [23]. They performed a detailed study of biomass potential in Europe under a food first policy, which only considers farm land not used for food production as potential biomass fields. They also exclude other areas due to e.g. nature conservation. Their results are reproduced in Tab. 1.4 and Fig. 1.4. Their estimate for area potentially available to biomass is up to 90 mio. ha, well above the NREAP targets. However, their study region includes the Ukraine, which contributes substantially, but is not part of the European Union. For comparison, currently (2013), biomass production takes place on roughly 5.8 % [24] of the land area in Germany.

In summary, growth in the electricity sector is constrained for biomass, firstly because agricultural areas not needed for food production are limited. Secondly, while biomass potentials on "surplus land" are still substantial, it should be kept in mind that they probably will be used to a large extent in the heating and cooling sector as well as fuels for aviation and land transport, and not in the electricity sector.

CO_2 impacts of biomass

At first glance, it is clear that biomass burning in itself is CO_2 neutral – the amount of CO_2 emitted in burning biomass is the same that has been assimilated into plant material during photosynthesis earlier. However, a more thorough life cycle analysis (LCA) can reveal further changes in the overall system that may counteract the CO_2 reduction from biomass usage, and

Table 1.2: World biomass potentials as estimated by the IEA [19]. For comparison, the World energy consumption is estimated to be 370 EJ in 2013 [1].

Kind of biomass	Energy potential in EJ/yr
Energy crops on current farm land	100-300
Energy crops on marginal land	60-110
Farming residue	15-70
Forestry residue	30-150
Manure	5-55
Organic waste	5-50

Table 1.3: Planned development of different RES technologies in the EU-27: Historical and projected gross electricity generation. Data taken from the National Renewable Energy Action Plans [20], as compiled by the Energy Research Centre of the Netherlands [21].

Electricity generation	Year	
(TWh/yr)	2010	2020
Wind (on- and offshore)	165	495
Solar (PV and CSP)	21	103
Hydro	343	369
Biomass	114	232
Geothermal	6	11
Ocean (heat, wave, and tidal)	1	7

Table 1.4: European biomass potentials as estimated in Refs. [22] (Manure and organic waste) and [23] (all others), assuming a food and feed-first policy as well as taking natural preserves into account. Final land use for dedicated biomass production is estimated to be up to 90 mio. ha. For comparison, European energy consumption was 70 EJ in 2012, with about 10 EJ electricity share [2].

Kind of biomass	Energy potential in EJ/yr
Energy crops on surplus farm land	2-14
Farming residue	3-4
Forestry residue	0-1.4
Manure and organic waste	0-0.14

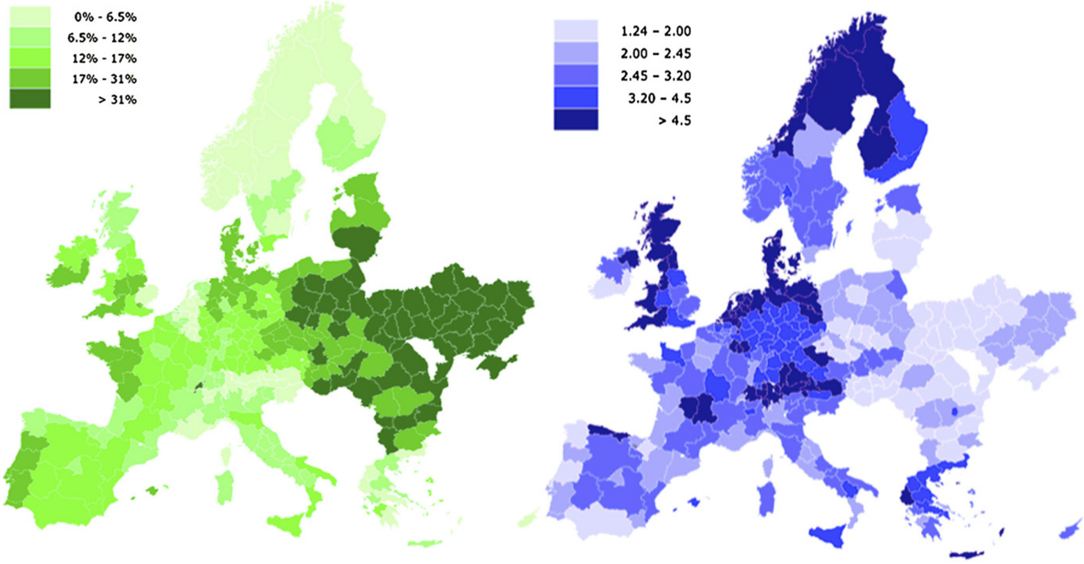

Fig. 8 – The 'surplus' land potentially available for the production of biomass by 2030 (left, green shades indicate the amount of surplus land as a percentage of the total land) and the production costs for woody crops in 2005 (right, blue shades indicate the production costs of woody crops in € GJ^{-1}) together indicate favourable locations for the production of biomass.

Figure 1.4: Distribution of Europe-wide biomass potential in terms of arable land not used for agriculture (left, in green) and land price projection (right, in blue). Reprinted by permission from Elsevier [23], copyright 2010.

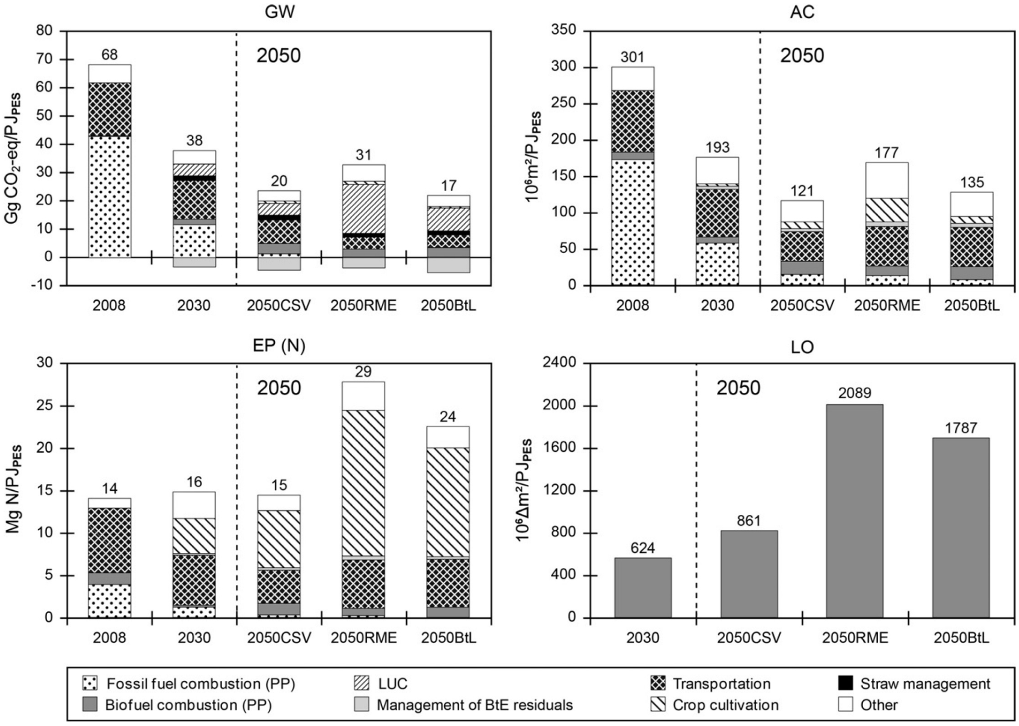

Figure 1.5: Impact of usage of diesel from fossils (2050CSV), rape methyl ester from rape seed (2050RME), and diesel produced by Fischer-Tropsch synthesis from willow wood (2050BtL) on CO_2 intensity (GW), soil acidification (AC), aquatic eutrophication with nitrogen (EP (N)), and land occupation (LO). The attribution of the different environmental indicators to different origins is indicated by the different patterns of the bars as shown in the legend below. It may come as a surprise that crop cultivation plays a part in fossil diesel scenarios. That is due to the applied methodology, which includes effects of land use changes when crops like barley are displaced with biomass production. The crop cultivation part in fossil diesel assessment represents the business-as-usual agriculture (without biomass production and its consequences). Abbreviations mean: PP – power plant, and LUC – land use change. For comparison, the 2008 status as well as an intermediate 2030 scenario is shown as well. Reprinted by permission from Elsevier [25], copyright 2012.

other undesirable side effects. As an example, look at the LCA of biodiesel in Denmark presented in Ref. [25]. They consider three scenarios for a low-carbon Denmark in 2050, which only differ by the way in which a (residual) need for transportation fuel is satisfied, and ask the question which has the least environmental impact. The three considered cases are fossil-based diesel, biodiesel from rape seed, and biodiesel from willow wood. The environmental impacts they find are shown in Fig. 1.5 (reprinted).

It is apparent that while the direct CO_2 emissions from fuel burning emissions drop, the overall CO_2 emissions from rape diesel are actually higher than from fossil diesel. This is mainly due to the land use changes caused by rape production. It is assumed that rape displaces the marginal crop on Danish farm land, spring barley, which in turn is moved to pastures. This shift causes a change in the amount of organic carbon bound in the soil, which is generally larger for perennial plants like grass or willow than for seasonal plants like barley or rape. Consequently, the overall CO_2 emissions for willow-based diesel are much lower than for rape-based diesel, but not significantly lower than for fossil fuel.

Soil acidification as well as soil eutrophication with the nutrients (molecular) phosphor and (molecular) nitrogen are both strongly linked to fertilizer usage, and it is therefore no surprise that the technology consuming most fertilizer – rape diesel again – comes out worst, while wood diesel performs better and fossil diesel best in these two categories. In terms of land occupation, both biomass technologies requires more than twice the area as fossil diesel.

1.2.3 Hydro power

Once it is built, hydro power is a very flexible and efficient technology, producing virtually no emissions while operating at low costs. It is able to balance fluctuating wind and solar PV power input as well as follow rapidly changing load curves. The conversion of the water's potential energy to electricity is very efficient, and plant lifetimes are long. The drawbacks are that it depends on favorable geography and sufficient annual precipitation, and that it dramatically changes entire landscapes when storage lakes are flooded [26]. Additionally, it may have negative impacts on fish, in particular migrating species.

Most feasible hydro power sites are already in use today in Western Europe. There are moderate further potentials in Eastern Europe. All in all, further substantial growth in Europe is not to be expected, cf. Ref. [27]. The expected hydro installation in 2020 in the EU is able to cover 11 % of the 2007 load (see Tab. 1.3); note that the significant resources of Norway are not included here, which would yield another 4 %.

1.2.4 Nuclear power, fusion, and CCS

Nuclear power and some other conventional sources of electricity, e.g. fossil fuel plants with carbon capture and sequestration (CCS) technologies, could also provide low CO_2 backup power or replace some or all VRES. However, the ever-growing acceptance problems of nuclear power makes the future role of this technology uncertain. Such concerns have already led to accomplished or planned phase-outs or bans in several countries, such as Ireland, Italy, Austria, Denmark, Belgium, Germany, and Switzerland. As CO_2 storage poses difficult siting problems, similar to nuclear waste, we also rule out CCS. Fusion power could become an option in the far future, but according to the ITER fusion reactor project, it will not provide grid electricity before 2040 [28], and consequently it cannot play a role in the transition to a decarbonized electricity system Europe is likely facing before 2050 [29].

1.3 General approach in this work

In the long run, complete avoidance of net green house gas emissions appears to be necessary to stall climate change. This entails the decarbonization of the entire energy sector – electricity, heating and cooling, and transportation. Long-term projections suggest that the decarbonization of the electricity sector and the electrification of the other sectors will play a key role in the transformation [29, 30]. We therefore focus on the electricity system. As described above, we consider nuclear and CCS options with some skepticism and therefore focus on a system based completely on renewables. Furthermore, some less evolved renewable candidate sources such as tidal power or wave power are not considered because their large-scale feasibility is not established. Geothermal energy is another option not included here, because at the moment, it seems only viable in a few regions such as Iceland. Since biomass and hydro power potentials are limited, main contributions are needed from wind and solar power in such a scenario. The fundamental difference to traditional electricity generation, which is designed to follow the load pattern as closely as possible, is that weather-driven generation is determined by forces largely out of human control, such that the rest of the electricity supply and possibly parts of the demand has to react to it.

There are a multitude of new effects in the electricity system to be expected when a high share of these variable renewable energy sources (VRES) is introduced. While there is solid engineering knowledge for the operation of dispatchable power plants, both theoretically and from practical experience, new collective phenomena emerge here. It is therefore well worthwhile to examine them with methods from theoretical physics, in particular statistical physics and the theory of complex networks, in order to gain deeper insight into the underlying mechanisms.

On very short timescales, the grid frequency and synchronization can be affected, which can lead to major outages similar to the famous blackout on Nov 4 2006, when a line in Northern Germany underwent planned and controlled disconnection, and the whole European electricity system desynchronized, leading to power outages all across the continent [31]. Desynchronization is so hazardous to grid stability because the difference in phase angle between two adjacent network nodes acts as a potential for the power flow (see Sec. 4.3 for details). In the following years, progress has been made to understand the synchronization of the electricity grid within the larger framework of synchronization on complex networks: The electricity grid can be interpreted as an inhomogeneous version of the well-known Kuramoto model [32], including additional inertia [33]. Within this framework, implications of features of renewable energies like decentralization and variable, hard-to-predict input on grid stability has been examined in Refs. [34, 35].

On longer timescales, such as those considered in the present work, there are other new effects which can be understood from a physics perspective. There have been various applications within the renewable energy group at Aarhus: The size of a hypothetical storage system that makes use of as much renewable generation as possible is found to diverge at a VRES share of 100 %, indicating a phase transition between a "mostly empty" and a "mostly full" phase. The effect could successfully be reproduced in numerical phase transition models [36].

The VRES generation data themselves can be analyzed for unusual statistics and extreme events, as e.g. in Ref. [37]. These will predominantly determine the requirements on a future electricity system.

The weather-dependent generation can be decomposed into principal components, entailing principal components of power flow. This technique has been introduced originally to predict wind power output with surprising accuracy [38] and has been applied derive characteristic spatio-temporal patterns of VRES generation as well as power flow patterns in Ref. [39].

The total flow on the network can be examined in other ways as well: While weather patterns determine the general directions, the grid topology becomes more important on smaller scales. It is a great simplification to calculate the flow on an effective network, where multiple real nodes and lines are combined into aggregated nodes and lines. There is evidence that the flow scales with aggregation length, discussed in Ref. [40], making renormalization methods applicable.

As a foundation for such investigations, wind and solar generation is modeled in detail: Long-term historical weather data time series are obtained and converted into potential generation, which is then further processed to obtain regional output. For the last step, it is necessary to define a capacity layout, that is, decide on a distribution of generation units across the study area. While the smoothing effect of large-scale aggregation of wind and solar power output is well documented in the scientific literature [41–48], long time and large range correlations in the generation persist and can be captured by our generation modeling. These provide hard boundary conditions of a wind-and-solar based system, whatever it will look like in detail.

The second main ingredient to our studies are the load data, which are available from transmission system operators. The mismatch between these two – weather based renewable generations and load – is the starting point for our considerations. The general idea is to work with relatively simple abstract and computationally lightweight formulations to scan different scenarios, rather than introducing a detailed model framework that requires a lot of assumptions about future technology and long computation times. In this way, build-up pathways of wind and solar power leading to least needs for backup power (which is assumed to come from limited resources) have been identified for Europe in Ref. [49] and the benefits of producing more renewable energy than is consumed have been investigated [50] as part of the PhD thesis of Dominik Heide at FIAS [51]. Moreover, the synergies between a fleet of backup power plants (e.g. hydro or biomass power plants), a long-term storage system (e.g. hydrogen storage), and a short-term storage system (e.g. batteries of electric cars) have been examined [52]. Building on this work, the European and the US transmission grid and extensions to facilitate renewable integration have been constructed in Refs. [53–55] and form a part of the present work.

Grid extension studies have been performed before, often with a simplified power flow model, usually with the objective of minimizing total system costs, for example in Refs. [56–59]. By contrast, we have developed a generalization of the DC approximation to full AC power flow, which focuses on optimal sharing of renewables with the least flow possible. In this way, we arrive at cost-independent results and avoid the uncertainties connected with long-term price projections.

The spread of cost assumptions in the literature is substantial: Factors of three to four between lowest and highest estimates are not uncommon, see Ref. [60] and references therein.

For the mix between wind and solar power during the renewable build-up, we have investigated the effect of renewable excess generation (assuming that it has to be curtailed) on levelized costs of electricity. It turns out that the higher the share of variable renewables, the more important it becomes to pick the mix not with respect to installation costs, but with respect to technical considerations, such as minimizing curtailment or storage needs, in order to reduce final system costs.

1.4 Organization of this work

This work starts out with a short introduction (Ch. 1), motivating the investigation of a highly renewable energy system, and presenting the general approach and some previous work. It is followed by a description of the underlying data sets for individual countries or regions (Ch. 2), which contain electrical load, wind and solar PV generation, and in some cases targets for renewable shares in the future. Some economic background to be used in the following chapters is provided in Ch. 3. It describes logistic growth curves to be used as an interpolation between today's status of renewable installations and ambitious long-term targets. Furthermore, it explains how to calculate levelized costs of electricity (LCOE) as well as annualized investment costs.

Ch. 4 then proceeds to include transmission between single nodes into the model. The DC power flow approximation to the full AC equations is derived, and the DC formulation is generalized to situations with global excess or deficit of power in the electric network. Motivated by potential balancing effects of renewable supply in large interconnected regions, upgrades of the inter-regional transmission grid are considered and constructed in Ch. 5.

The optimal mix between wind and solar energy with respect to different objectives – least storage energy capacity, least backup energy, least LCOE – are investigated in the next chapter, Ch. 6. Here, optimal build-up pathways for the US subregions are constructed. Furthermore, the effect of international transmission on the optimal mix is explored.

Up to this point, the electricity system has been assumed to consist of wind and solar PV generation, which are modeled in detail, and some kind of complementary backup or storage system that is highly idealized. The backup system is examined in much more detail in Ch. 7, where three different flexibility classes for backup power plants are introduced, with characteristic timescales of hours, days, and weeks. The load before substantial renewable installation is decomposed into these classes to find out lower bounds on already present flexibility in the backup system. Subsequently, the dispatch of backup to cover residual load in the presence of large-scale renewable installations is determined. International cooperation again proves beneficial, and transmission grids to enable it are calculated.

Finally, Ch. 8 summarizes the main findings and concludes this work. Appendices on convex optimization, the main mathematical tool used for power flow and transmission grid extensions, further input data in detail, and a side project on almost bipartite synchronization in more abstract networks are included in the appendix.

The chapters of this work are arranged in their logical order. Fig. 1.6 shows the chapters and main sections, together with their interdependencies. If one is, for example, only interested in the optimal build-up pathways (Ch. 6.3), then, as a prerequisite, the optimal mix methods are needed (Ch. 6.1-6.2), which in turn require reading about regional datasets (Ch. 2) and some economic background from Ch. 3.2.

Parts of the presented texts and figures have been published already in Refs. [54, 55, 61, 62]. Specifically, parts of Secs. 1.2.2 and 1.2.3, Sec. 1.2.4, parts of Secs. 2.5 and 3.1, a small fraction of Sec. 4.4.1, Sec. 5.1.1, most of Sec. 5.2, Sec. 6.4, and App. C are published in Ref. [54] and only slightly adapted for this work. The part of Sec. 5.2.4 discussing mismatch histograms and correlations is published in the proceedings [62].

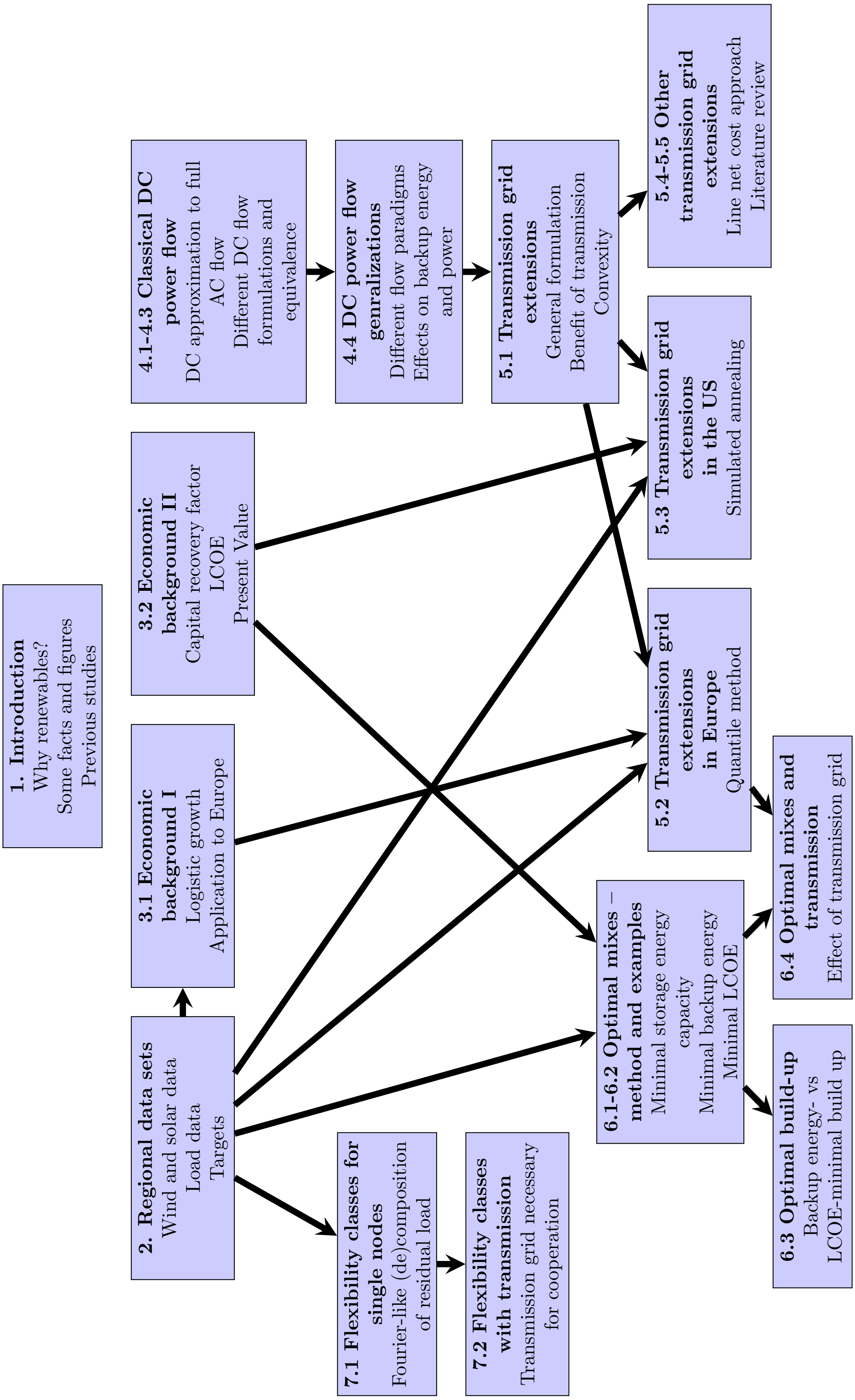

Figure 1.6: Organization and interdependencies of this work.

Part of Sec. 2.3, the parts of Secs. 2.3.1 and 2.3.2 concerning the US, the paragraph explaining the renewable gross share from Sec. 2.6, Sec. 5.3 with the exception of most of 5.3.4, Sec. 6.1.2, the last subsection of Sec. 6.1.3, Sec. 6.2, and App. B are published with only small modifications as presented here as Ref. [55]. Furthermore, Sec. 5.2.3 contains a few sentences from Ref. [55].

Additionally, Sec. 6.3 together with a few of the methodological paragraphs from Sec. 6.1 have been published (with slight modifications and extensions as suggested in the review process) as [61].

Parts from the published articles [54, 55, 61] are reprinted here by permission from Elsevier.

Chapter 2

Regional data sets

Several input data form the basis of our calculations, and shall be described in this chapter. Most important are the generation time series, which are calculated based on weather data as detailed below. Load data time series have been obtained from transmission system operators (TSOs), who are often legally required to publish them. For Europe, it was also possible to find renewable target shares for 2020, and, in some cases, later times. In the following sections, we will go through the different data.

2.1 Regions

The regional scope of the studies presented here comprises Europe and the contiguous US (that is, not including Alaska and Hawaii). Maps can be found in Figs. 2.1 and 2.2. In the European case, the single subregions shown in Fig. 2.1 are further aggregated to countries, which later form the nodes of the international transmission network. Furthermore, data from Finland and Poland are used to form synthetic load and generation data for the Baltic states, which will be described in Sec. 2.4.1. The contiguous US are split into 10 regions that are mainly divided according to their independent system operator (comparable to a transmission system operator in Europe). These subregions are called FERC (Federal Electricity Regulatory Commission) regions. The respective inter-regional transmission networks appear later in this work. Fig. 5.1 shows the European network topology, and Fig. 5.15 the North American grid, as far as we are concerned here.

2.2 Weather data

World-wide, freely available Climate Forecast Reanalysis System (CFSR) data are provided by the American National Centers for Environmental Prediction (NCEP) of the National Oceanic and Atmospheric Administration (NOAA) [65]. These weather data form the basis of the Aarhus renewable energy atlas, which converts weather time series to wind and solar PV generation [37, 66]. These production time series are used for the contiguous US. Weather data are generated by starting a weather forecast model in a certain measured configuration, and assimilating it every six hours to the observational data. Six hourly observational data are thus extrapolated to hourly resolution. The observations are largely based on satellite data, which are available back to 1979, and the reanalysis is consistently done with one model for all years since, as described in [65]. The dataset is calculated in the so-called T382 grid, which means that it contains 576×1152 grid cells (latitude$\times$longitude), corresponding to a resolution of 38 km or 0.313° at the equator. In the older version of the NCEP reanalysis (known as "R2"), they used the T62 grid with a resolution of 210 km or 1.875° at the equator. The time series span the 32 year-interval 1979-2010.

For Europe, we use the Fraunhofer Institute for Solar Energy Technology (ISET, now part of the Fraunhofer Institute for Wind energy and Energy System technology, IWES) generation

Figure 2.1: Regions used in the European data set. Figure taken from [63].

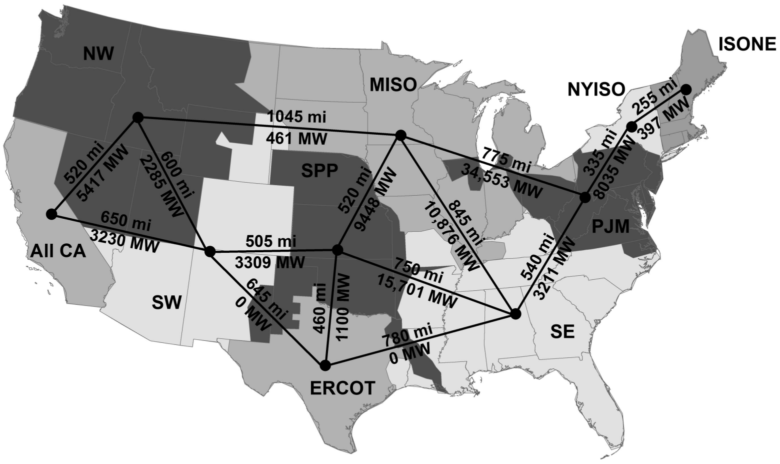

Figure 2.2: FERC (Federal Electricity Regulatory Commission) regions of the contiguous US, based on Ref. [64]. Apart from the regions, the current transmission grid is also shown, annotated with line capacities.

and load dataset, covering the years 2000-2007 [63]. The dataset has been assembled in 2008 as described in Ref. [63], as well as in the work of Dominik Heide [49–51]. The underlying weather data comes from the commercial provider WEPROG (Weather & Wind Energy Prognosis). The data were obtained by using the older, coarser version of the NCEP CFSR data discussed above as boundary conditions to calculate European level weather on a (back then) higher resolution of $48 \times 48\,\mathrm{km}^2$. It is again a reanalysis model, with six hours measurement interval and hourly forecasts assimilated to observations. In this case, the forecast is done in ensembles, that is, 75 different runs are started with very similar initial conditions, and the mean of their outcomes is returned as the best guess weather forecast.

2.3 From weather to generation data

The weather data are converted to potential wind and solar PV generation on a grid cell level, that is, with a spatial resolution of about 40 km respectively 50 km, and a temporal resolution of one hour. The actual production is then determined by applying a capacity layout to the grid cells, i.e. deciding how much capacity is installed in each grid cell. The capacity layout is used as weights with which the potential generation in each grid cell is multiplied. To calculate the total regional output, all production in a region is summed up. Note that this procedure implicitly assumes that no region-internal transmission bottlenecks are present.

We find that for solar PV, the generation time series do not depend significantly on the choice of capacity layout, as long as it is picked in some realizable way. For wind, the sensitivity to siting is considerably higher.

2.3.1 Solar generation

Solar power production is determined on grid cell level, by first calculating the total irradiation that hits a panel in a specific orientation as well as panel temperature, and then applying the technical specifications of the panel to calculate the resulting potential power output of each grid cell. Then, a capacity layout has to be constructed, assuming a certain distribution of solar panels of potentially different types across the study region.

Solar PV power in Europe

Panel temperature is calculated from ambient temperature and irradiation in the ISET dataset [63], including cooling factors in some cases. The capacity layout was derived from resource quality, and detailed assumptions on panel type (tracking or non-tracking) and orientation (tilt and east-west) were made, for each study region separately.

Solar PV power in the contiguous US

Solar power production is calculated from weather data using the Aarhus renewable energy atlas as detailed in [37, 66], assuming non-tracking, south-oriented solar panels of the type Scheuten 215 I [69] with a tilt equal to latitude. The irradiation geometry is calculated in detail, and diffusive and ground irradiation are considered in addition to beam irradiation directly from the sun. The corresponding resource map is shown in Fig. 2.3. It agrees very well with the respective solar PV resource map from the National Renewable Energy Laboratory (NREL) [70].

The actual production within a FERC region is then determined by applying a capacity layout to the grid cells. The validation plot Fig. 2.4 shows the resulting generation time series' production statistics for eight different capacity layouts: Uniform distribution of PV capacity and distribution proportional to the potential solar energy output both with or without exclusion of areas that are declared unsuitable and/or prohibited according to Refs. [67, 68], and four layouts in which the PV capacity is assigned randomly to 10 % of the grid cells. The night hours amount to a peak at zero production. The plot reveals that the choice of capacity layout does not have a large effect on the (normalized) solar generation time series. The spread in capacity factor, i.e. average power output divided by nameplate power capacity, is only 0.2 % for the example region of California shown in the plot. For FERC regions in which the resource is less homogeneously distributed, such as ERCOT or NW, a slightly larger spread of about 0.5 % is observed. To make a realistic guess for the layout, we assume a capacity distribution proportional to the potential of the grid cell under consideration with exclusion of unsuitable and/or prohibited areas according to Refs. [67, 68]. The solar capacity layout therefore looks very similar to the solar potential map Fig. 2.3.

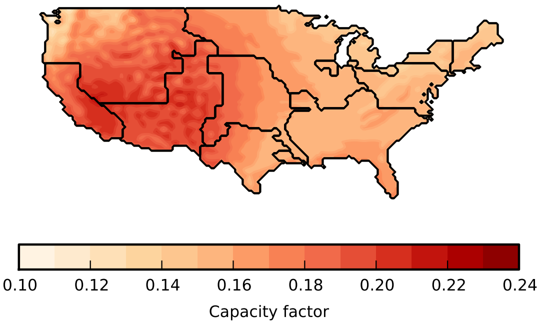

Figure 2.3: Solar resource map for the contiguous US as calculated from the Aarhus renewable energy atlas [37, 66].

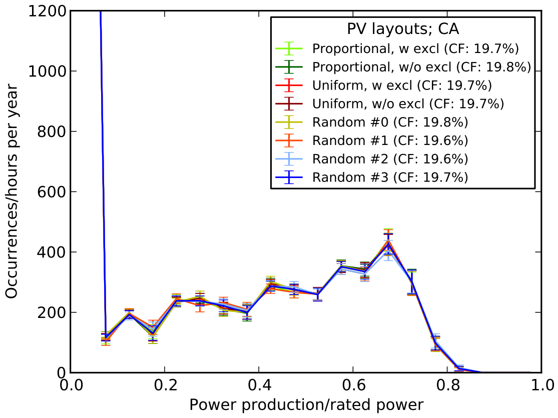

Figure 2.4: Solar power output histogram for California, for eight capacity layouts: Proportional to potential generation, not taking any excluded areas into account, proportional to potential generation, taking excluded areas from [67, 68] into account, uniform distribution with and without excluded areas, and four random layouts, in which solar power capacity is distributed randomly to 10 % of all grid cells. In the legend, the capacity factor (CF), i.e. the average power output divided by the rated capacity, that is achieved throughout the years for each layout is shown along with the layout name.

2.3.2 Wind generation

Wind generation is calculated by extrapolating wind speed to hub height, which is then fed into the power curve of the turbine under consideration. The power curve is the relationship between wind speed and wind power output. Again, the potential generation time series is calculated on grid cell level, and then further aggregated by assuming a capacity layout.

Wind power in Europe

The power curve used for the ISET dataset [63] onshore is a combination of the data of an Enercon E82 turbine and a Vestas V90 turbine, with a cut-in wind speed of 3 m/s, maximum power production between speeds of 16-21 m/s, and a smooth cut-out around 25 m/s.[1] A hub height of 100 m is assumed. Cut-out is modeled with a parametrized stochastic model, such that higher surface roughness[2] leads to a broader cut-out range. As an additional modification, general losses of 7 % are estimated and applied to the time series.

For the offshore time series, slightly different parameters have been assumed. Losses are again taken to be 7 %. Since surface roughness is assumed homogeneously small, there are no stochastic

---

[1] The cut-in wind speed is the minimal speed at which the turbine starts moving, and the cut-out wind speed is the speed above which the turbine is stopped to prevent damage.

[2] Surface roughness is a length that parametrizes the roughness of the landscape. High buildings or forests lead to large surface roughness values, while fields or the sea have very low surface roughness. Values can be found in Tab. B.1 in Appendix B.

cut-out effects. As a special feature here, leading to smoothing of the power curve in a different way, wind turbines are considered to be assembled in parks, leading to wake effects that moderate cut-in and cut-out. Data of a 7 × 7 array of unspecified 5 MW turbines are used, with cut-in around 3 m/s, peak plateau at 18-21 m/s, and cut-out around 25 m/s.

Their capacity layout is mainly based on projections from the European TradeWind study [71]. They follow then-current (2008) installations as well as resource quality, smoothed out to include less favorable sites, which was considered more realistic.

Wind power in the US

Wind speed interpolation from 10 m wind data to hub height is used:

$$u(H) = u(10\mathrm{m}) \frac{\ln\left(\frac{H}{z_0}\right)}{\ln\left(\frac{10\mathrm{m}}{z_0}\right)}\,, \tag{2.1}$$

where H is the hub height, z_0 is the surface roughness, and u is the wind speed as a function of height. This vertical extrapolation tends to underestimate hub wind speeds slightly, as discussed by Archer and Jacobson in [72]. Their research indicates that it would be better to use measurement data from soundings. However, since such data are not available for the entire US, the simple conversion method of Eq. 2.1 is employed. A hub height of 80 m onshore and 100 m offshore is chosen. To convert the wind speed at hub height to power output, the power curve of the Vestas V90 3 MW turbine is used onshore, and the Vestas V164 7 MW turbine offshore, as provided by the manufacturer [73]. These relatively new and large models were chosen since the main aim of this study is the investigation of a far future, highly renewable energy system. The wind resource map thus obtained is shown in Fig 2.5, which aligns reasonably well with the resource maps from NREL [70]. The conversion from wind speed data to wind power generation was modified with the methods of [74, 75] to take effects of orography, surface roughness, and siting into account, which will be described in detail in the next section.

For wind, the sensitivity to siting is substantially higher than for PV, as is observed from the spread in the production distribution for different capacity layouts for wind (Fig. 2.6), which is large compared to the corresponding Fig. 2.4. We therefore rely on the wind capacity layouts given by the Eastern and Western wind studies of NREL [67, 68], which include extensive siting analysis. Their layouts do not cover the FERC regions ERCOT and SE very well. For these two regions, we use a randomized layout. The wind power output distribution from eight different candidate layouts for SE is shown in Fig. 2.6, which compares power output statistics. All of them are randomly generated by distributing a number of capacity units across all available grid cells, proportional to their potential wind power output squared or cubed (cf. the legend of Fig. 2.6). The higher the exponent on the potential wind output, the more high-yield sites are preferred. The amount of capacity units is a handle on how smooth the layout becomes: The fewer units, the more grained the final layout. It is chosen between 40 % and 100 % of the number of available grid cells. Grid cells are allowed to hold more than one unit of capacity, so even in a layout using 100 % of all grid cells as the number of capacity units, not all grid cells are covered. Since the power output is normalized, only the relative capacity fraction assigned to each grid cell is important. The layout picked for SE and ERCOT in this analysis uses 40 % of all grid cells in capacity units, distributed proportional to the cube of potential wind power output. Fig. 2.7 reveals that it matches the distribution of wind sites in the rest of the US well.

The mix between on- and offshore wind is chosen such that the relative capacity between the two is the same as in the NREL wind studies [67, 68], see Tab. 2.1 for the values used. Wind installations in the Great Lakes have been treated as offshore, i.e. the offshore 7 MW turbine model is assumed to be installed there.

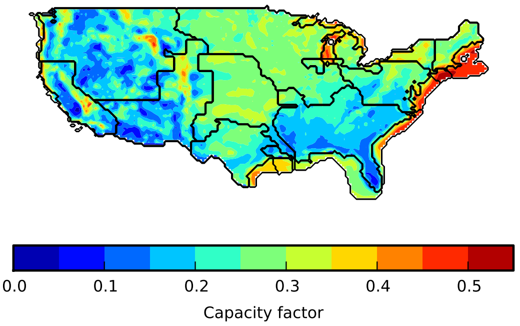

Figure 2.5: Wind resource map for the contiguous US as calculated from the Aarhus renewable energy atlas [37, 66], modified as described in the main text to take effects of orography, surface roughness, and siting into account.

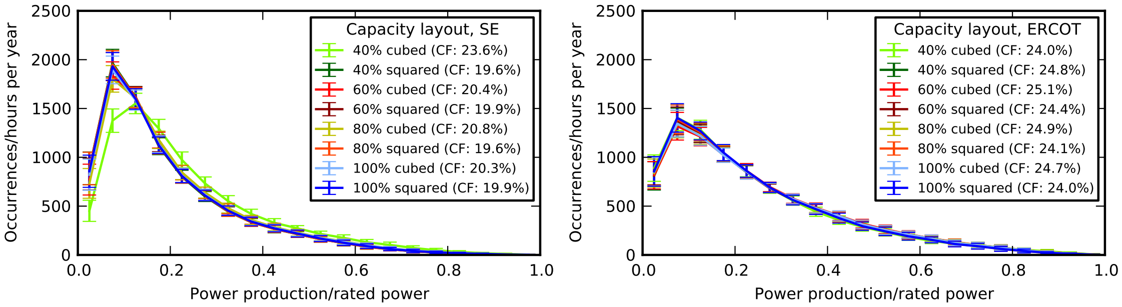

Figure 2.6: Wind power output distribution and capacity factors for different capacity layouts for the SE FERC region (left) and the ERCOT FERC region (right). The layouts are chosen randomly, with probability of picking a grid cell proportional to its wind potential squared or cubed as stated in the legend, and the total capacity was split into more or fewer units to be randomly distributed (percentage value in the legend), see main text for a detailed explanation. In the legend, the capacity factor (CF), i.e. the average power output divided by the nameplate capacity, of the layout that is achieved throughout the years is shown along with the layout name.

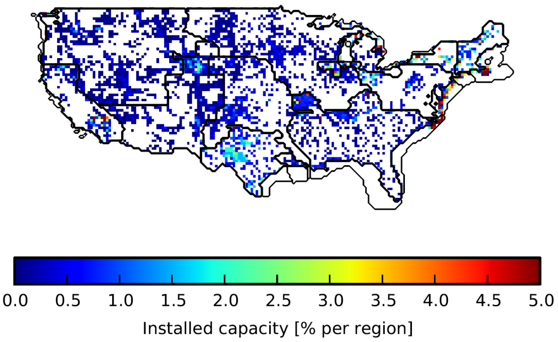

Figure 2.7: Wind capacity layout for the contiguous US used in this study. White cells do not contain any capacity. For the colored cells, color encodes the amount of capacity in percent of the installed capacity per FERC region. The 200 m bathymetry line is shown offshore. For most FERC regions, a merger of the wind capacity layouts of [67, 68] is used. For SE and ERCOT, this is not possible due to a very low number of sites in these two FERC regions in both NREL datasets. We therefore use a synthetic random layout in SE and ERCOT, distributing a number of 40 % of the number of grid cells in the region of capacity units over all grid cells. The probability of picking a specific cell is chosen proportional to its potential power output cubed, and putting more than one capacity unit into a grid cell is allowed. See main text for a detailed explanation. This layout is seen to match the distribution of capacity across the rest of the US well.

Table 2.1: Relative fraction of on- and offshore wind power installations for the layouts used in this study, for each FERC region separately.

Region	onshore fraction	offshore fraction
AllCA	98.2 %	1.8 %
ERCOT	100.0 %	0.0 %
ISONE	45.8 %	54.2 %
MISO	97.6 %	2.4 %
NW	99.9 %	0.1 %
NYISO	60.8 %	39.2 %
PJM	42.3 %	57.7 %
SE	100.0 %	0.0 %
SPP	100.0 %	0.0 %
SW	100.0 %	0.0 %

Refined US conversion

Original approach The wind conversion was initially done with the Aarhus RE atlas as described in [37, 66]. In short, the wind speed at hub height was extrapolated from measurements at 10 m height via Eq. (2.1) and then fed into the power curve to obtain wind power output.

When evaluating these data, it became apparent that this approach significantly underestimates the wind power potential, see the left panels of Fig. 2.10.

Modified approach In order to fix this issue, we turn to the literature and find a description and fix of the problem in Refs. [74, 75]. The reason that wind power potential is underestimated onshore is that the spatial fluctuations in wind speed due to surface roughness and orography (hills and valleys) are neglected when working with area mean wind speeds. But these fluctuations do contribute to the mean wind power density $e = \frac{1}{2}\rho u^2 \cdot u$, as the following calculation shows:

$$\frac{2\langle e\rangle}{\rho} = \langle u^3\rangle = \langle(\overline{u} + u')^3\rangle \approx \overline{u}^3 + 3\overline{u}\langle u'^2\rangle = \overline{u}^3 + 3\overline{u}\sigma^2 \tag{2.2}$$

Here, ρ is the mass per volume air density (assumed constant), $\overline{u}$ is the mean wind speed, u' are the fluctuations around $\overline{u}$ such that $u = \overline{u} + u'$, and σ is the standard deviation of u'.[3]

The interesting thing is now that the spatial wind speed fluctuations due to inhomogeneous terrain can be characterized in terms of its surface roughness and orography, such that we get

$$\sigma = \sqrt{\sigma_{\mathrm{oro}}^2 + \sigma_{\mathrm{rough}}^2}. \tag{2.3}$$

The details of this connection are described below. The resulting σ can then be added to the wind energy density, which leads to an increased power output.

With the additional assumption that the distribution of u' is Gaussian, we can even model the effect of siting in a simple way: Wind turbines would primarily be placed in good spots, that is,

---

[3] The wind power density is simply the wind's kinetic energy per area dA perpendicular to wind speed, passing through in a given time dt. In formulae:

$$e = \frac{\mathrm{d}E_{\mathrm{kin}}}{\mathrm{d}A\mathrm{d}t}$$

$\mathrm{d}E_{\mathrm{kin}}$ can be expressed as $\frac{1}{2}\mathrm{d}mu^2 = \frac{1}{2}\rho\mathrm{d}Vu^2 = \frac{1}{2}\rho\mathrm{d}A\mathrm{d}lu^2 = \frac{1}{2}\rho\mathrm{d}Au\mathrm{d}tu^2$, arriving at

$$e = \frac{1}{2}\rho u^3\,.$$

where u' is larger than some threshold value p. This leads to mean energy densities of

$$\frac{2\langle e\rangle}{\rho} = \langle u^3\rangle = \langle(\overline{u} + u' \cdot \theta(u' > p))^3\rangle\,, \tag{2.4}$$

where θ is a cutoff function (1 if the condition is true, 0 otherwise).

In order to include the corrections into the wind conversions, the standard deviations first have to be "de-normalized" by multiplication with the corresponding grid cell's mean wind speed (the same that was used in the normalization). Since the mean wind speeds used for roughness and orography differ slightly, we use these two different speeds before adding them together, see Eq. (2.7). Next, the corrections have to be fed into the wind conversion. This was done in the form of an effective increase in wind speed at hub height H, by setting:

$$\frac{2\Delta e(H)}{\rho} = (\overline{u}(H) + \Delta u)^3 - \overline{u}(H)^3 \overset{!}{=} 3\overline{u}(H)\sigma^2 \tag{2.5}$$

$$\Rightarrow \Delta u = \overline{u}(H)\left(\sqrt[3]{1 + 3\sigma^2_{\text{norm}}} - 1\right) \tag{2.6}$$

$$\text{with } \sigma^2_{\text{norm}} = \frac{\sigma^2_{\text{oro,norm}}(H) \cdot \overline{u}^2_{\text{oro}}(H) + \sigma^2_{\text{rough,norm}}(H) \cdot \overline{u}^2_{\text{rough}}(H)}{\overline{u}^2(H)} \tag{2.7}$$

If only the best spots in each grid cell are considered as potential wind sites (i.e. we work with Eq. (2.4) instead of (2.2)), the corresponding wind speed correction takes the following form

$$\begin{aligned}\Delta u = \frac{\overline{u}}{N}\Bigg\{ & 3 \cdot \frac{1}{\sqrt{2\pi}}\sigma_{\text{norm}}\,\mathrm{e}^{-p^2/(2\sigma^2_{\text{norm}})} \\ & + 3 \cdot \frac{1}{2}\sigma^2_{\text{norm}}\left[1 - \mathrm{erf}\left(\frac{p}{\sqrt{2\sigma^2_{\text{norm}}}}\right)\frac{2p}{\sqrt{2\pi\sigma^2_{\text{norm}}}}\,\mathrm{e}^{-p^2/(2\sigma^2_{\text{norm}})}\right] \\ & + \sqrt{\frac{2}{\pi}}\sigma^3_{\text{norm}}\left(1 + \frac{p^2}{2\sigma^2_{\text{norm}}}\right)\mathrm{e}^{-p^2/(2\sigma^2_{\text{norm}})}\Bigg\}\,,\end{aligned} \tag{2.8}$$

$$\text{with normalization } N = \frac{1}{2}\left(1 - \mathrm{erf}\left(\frac{p}{\sqrt{2\sigma^2_{\text{norm}}}}\right)\right)\,, \tag{2.9}$$

where erf is the error function. It is important to realize that the wind is upscaled before the correction is added, so the final formula reads

$$u_{\text{corrected}}(H) = u(H) + \Delta u\,. \tag{2.10}$$

Surface roughness We closely follow Ref. [74]. To obtain a roughness dataset, we use the land cover atlas from the national land cover database (NLCD) of the multi resolution land characteristics consortium (MRLC) of the US [76]. It has a resolution of 30 m. From these data, we calculate a contribution to wind speed fluctuations for each grid cell. Specifically, we first translate the land use classes to surface roughness lengths using Tab. B.1. Then, we calculate the surface layer friction velocity, $u_\star$, by numerically inverting the geostrophic drag law:

$$G = \frac{u_\star}{\kappa}\sqrt{\left(\ln\frac{u_\star}{f z_0} - A\right)^2 + B^2} \tag{2.11}$$

We assume the geostrophic wind G to be 10 m/s, $\kappa \approx 0.4$ is the Karman constant, $f \approx 10^{-4}\,\frac{\text{rad}}{\text{s}}$ is the Coriolis frequency (for the latitudes of the contiguous US), and A and B are parameters which for stable atmospheric conditions take the values 1.8 and 4.5 respectively, (see e.g. [77]). z_0 is again the surface roughness length.

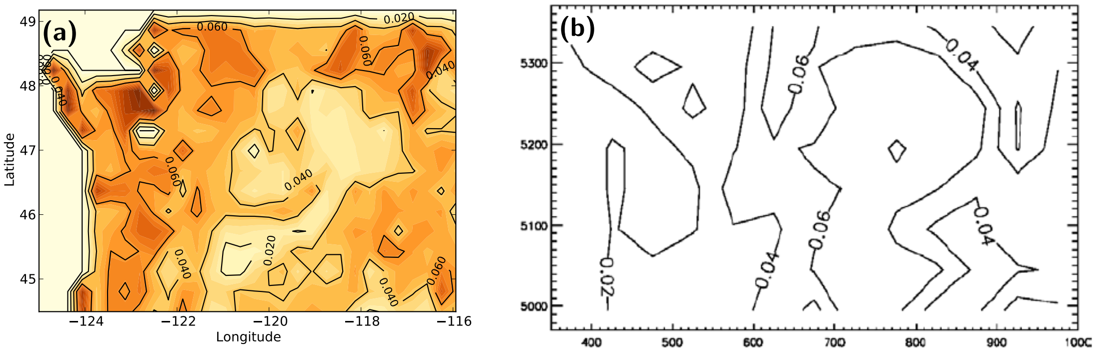

Figure 2.8: Corrections (σ_{oro}, normalized by mean wind speed $\overline{u}$) from surface roughness effects from (a) our conversion and (b) Ref. [75] for the Columbia Gorge region. Note that the two cutouts are not perfectly aligned.

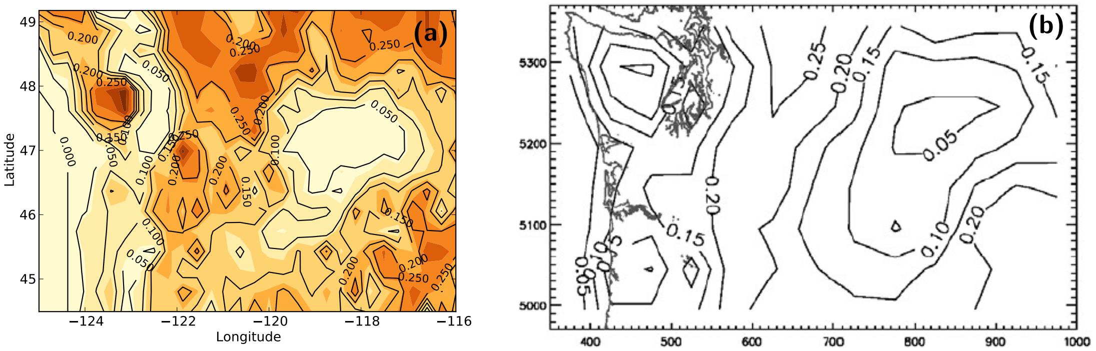

Figure 2.9: Corrections (σ_{rough}, normalized by mean wind speed $\overline{u}$) from orography effects from (a) our conversion and (b) Ref. [75] for the Columbia Gorge region. Note that the two cutouts are not perfectly aligned.

From $u_\star$, we get to the wind speed at height H by again using logarithmic scaling:[4]

$$u(H) = \frac{u_\star}{\kappa} \ln \frac{H}{z_0} \tag{2.12}$$

According to Ref. [74], the contribution to the wind speed standard deviation from this can be calculated as the standard deviation of $u(H)$ (for all points within one grid cell). Normalized by the mean wind speed of the grid cell, Ref. [75] shows the picture reproduced in Fig. 2.8 for the Columbia Gorge region. Our corresponding data are shown in the same figure, scaled by a factor of 0.6. The agreement seems reasonable. We believe that the need for scaling our results down to match theirs arises from the higher spatial resolution of our data; they use surface roughness input data with a resolution of 500 m.

Orography For orography, we follow the ideas of Ref. [74] only loosely, since the details of their implementation are not fully known to us. The basic idea is that wind speed-up due to the topography of a landscape should be proportional to its unevenness. As a measure of that, we use the standard deviation of the elevation, as reported in Ref. [78]. The data has a resolution of 1000 m. When scaled by $\frac{1}{3} \cdot \frac{1}{8\pi^2}$ (first factor from by-eye fit, second from Ref. [74]) and normalized by the mean wind speed, the agreement with Ref. [75] is reasonable.

---

[4] There are other possible interpolation techniques, e.g. proportional to $(H/z_0)^\alpha$ with $\alpha \approx 0.14$ [77].

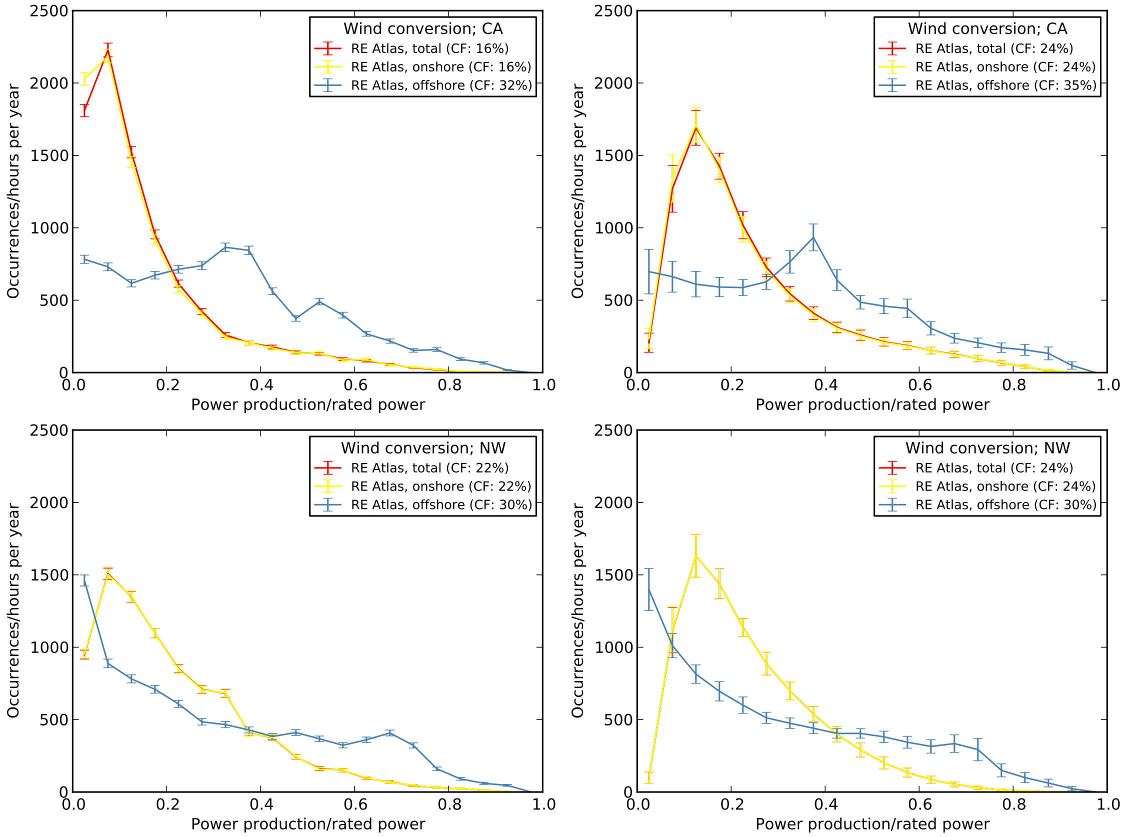

Figure 2.10: Wind power output histograms without the correction (left), and with the correction (right), including the best 20 % of the area within each grid cell, for the California region (top), and the NW FERC region (bottom). It is obvious that especially onshore, wind power output is systematically underestimated without the correction.

Table 2.2: Capacity factors from the wind time series with and without the corrections, as well as values from the NREL wind studies data.

Region	no corr.	with corr.	NREL
AllCA (all)	16 %	24 %	31 %
AllCA (onshore)	16 %	24 %	31 %
AllCA (offshore)	32 %	35 %	28 %
NW (all)	22 %	24 %	33 %
NW (onshore)	22 %	24 %	33 %
NW (offshore)	30 %	30 %	21 %

Effect of the corrections For the procedure described above with a choice of $p = 0.84\sigma$ (corresponding to picking the best 20 % of the area in each grid cell as eligible for wind farms), the power output distributions without corrections and modified is shown in Fig. 2.10.

Another way to illustrate the effects of the wind speed correction is by looking at plots analogous to Fig. 7-10 from Ref. [75], showing mean wind energy density calculated from (a) mean wind speed cubed, (b) mean of the cubed wind speed, (c) like (b) plus surface roughness and orography corrections, and (d) like (c), including only the best 10 % of all sites. These are shown in Fig. 2.11.

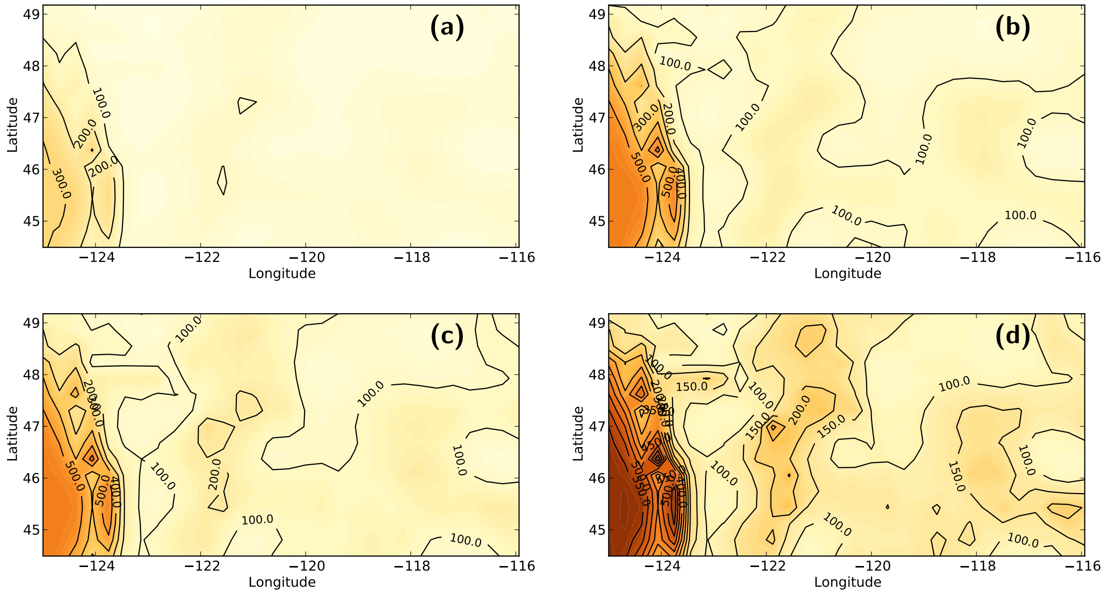

Figure 2.11: Plots analogous to Figs. 7-10 in Ref. [75], showing normalized mean energy density, calculated by various methods. From top left to bottom right: Mean wind energy density in 50 m height based on (a) mean wind speed cubed, (b) mean of the cube of the wind speeds, (c) as (b) plus the corrections, including all sites within a grid cell, (d) as (b), but including only the windiest 20 % of the wind speed distribution. Color coding is the same in all plots. White regions are out of the color code range, chosen in this way for the sake of better resolution in most parts.

2.4 Load data

Electricity consumption is published by the transmission system operators (TSOs). It comes in various formats and has to be assembled into usable time series.

2.4.1 Demand time series for Europe

European load data have been obtained for the ISET dataset [63] from UTCE (now ENTSO-E), the European association of transmission grid operators [79], as well as several other institutions. It covers the eight years 2000-2007 with hourly resolution for 50 European onshore regions, in some cases after extrapolation because not all eight years were directly available, see Sec. 4.2 in Ref. [63] for a detailed table and individual data sources. Regions are smaller countries or parts of larger countries. We use the regional data aggregated to 27 countries, plus synthetic data for the three Baltic states Estonia, Latvia, and Lithuania, generated from Poland's and Finland's load time series: Normalized load and generation time series are mixed in the ratio 25/75 Finland/Poland for Estonia, a 50/50 ratio for Latvia, and a 75/25 ratio for Lithuania. The load time series are then scaled to the corresponding mean load. Load time series have been de-trended from an average annual growth of 2 %.

2.4.2 Demand time series for the US

For the contiguous US, we use load data for the years 2006-2007, assembled by Bethany Frew (then Bethany Corcoran) for her study [64]. They are aggregated on FERC region level, see Fig. 2.2. The two-year demand time series are repeated to cover the entire 32 yr period for which wind and solar generation data have been obtained. In the case of the SW FERC region, load had to be de-trended from a net linear growth to make the end of 2007 match the beginning of 2006. For all the other FERC regions, this was not necessary.

2.5 Renewable target shares for Europe

2.5.1 Historical data and 2020 targets

The historical wind and solar penetrations originate from Eurostat [2] for EU member states as well as Switzerland, Norway, and Croatia, and from the International Energy Agency (IEA) [80] for the other Balkan countries.

The 2020 targets for EU member states are taken from their official National Renewable Energy Action Plans [20]. In the case of Denmark, this target has already been revised because of the strong growth in wind installations, and we consequently use the new target [81]. For Switzerland, the Energy Strategy 2050 of the Swiss government and the corresponding scenario from a consulting firm is employed [82, 83]. For Croatia, we use the Croatian energy strategy as officially communicated in [84]. These figures are also applied to the other Balkan states, since no other data source has been found. For Norway, the 2020 targets are estimates from the independent research organization SINTEF [85].

2.5.2 2050 targets

For the reference year 2050, we assume a very ambitious end-point scenario by setting the target penetration of VRES to 100 % of the average electricity demand for all countries ($\gamma_n = 1$). However, even at this penetration, a backup system of dispatchable power plants is needed to ensure security of supply when the production from VRES does not meet the demand. The minimum backup energy that must be provided by the backup system was investigated in [50, 52, 53], and for a penetration of 100 %, it amounts on average to between 15 % and 24 % of the demand, depending on the strength of the transmission grid. In a fully renewable power system, this energy must be provided by dispatchable renewable technologies such as hydro power and biomass, or from re-dispatch of earlier stored VRES-surplus. In general, conventional fossil and nuclear plants can also be used.

The official goal of the European Union is to reduce CO_2 emissions by 80 % before 2050 [86]. It is argued in Refs. [29, 30] that to reach this goal it will be necessary to decarbonize the electricity sector almost completely. The ambitious target of a VRES penetration of 100 % ($\gamma_n = 1$) by 2050 is consistent with this goal as the required backup energy could be provided by a combination of dispatchable renewable resources, possibly in combination with storage as investigated in Ref. [52]. More conservative end-point scenarios with a lower VRES penetration, e.g. those of Refs. [29, 58], can easily be encompassed implicitly by shifting the 100 % VRES targets to later times, e.g. 2075 or 2100.

As pointed out in Secs. 1.2.2 and 1.2.3, estimated potentials for biomass and hydropower are limited. As a conservative estimate, they are not included explicitly here. They may, however, form part of the backup system that is dispatched whenever wind and solar generation is insufficient. Nuclear power, fusion, and/or CCS technologies are viewed with some concern in a growing number of European studies, see also Sec. 1.2.4, and have therefore been excluded from this study. In summary, this means that most of the growth of CO_2-free electricity generation until 2050 has to come from wind and solar power.

The mix between wind and solar power in 2050 is chosen such that the backup energy becomes minimal for each single country for the base scenario. A detailed description of the backup-minimal mix is given in Sec. 6.1.1. As an example, Fig. 3.2c shows the backup energy as a function of the mix for Germany, for a penetration $\gamma_{\mathrm{DE}} = 1.0$, with a clear minimum at 0.72. For all other countries a similar behavior can be observed, and the average mix of the base scenario becomes 0.71, with individual countries ranging from 0.64 for Croatia to 0.85 for Norway [53].

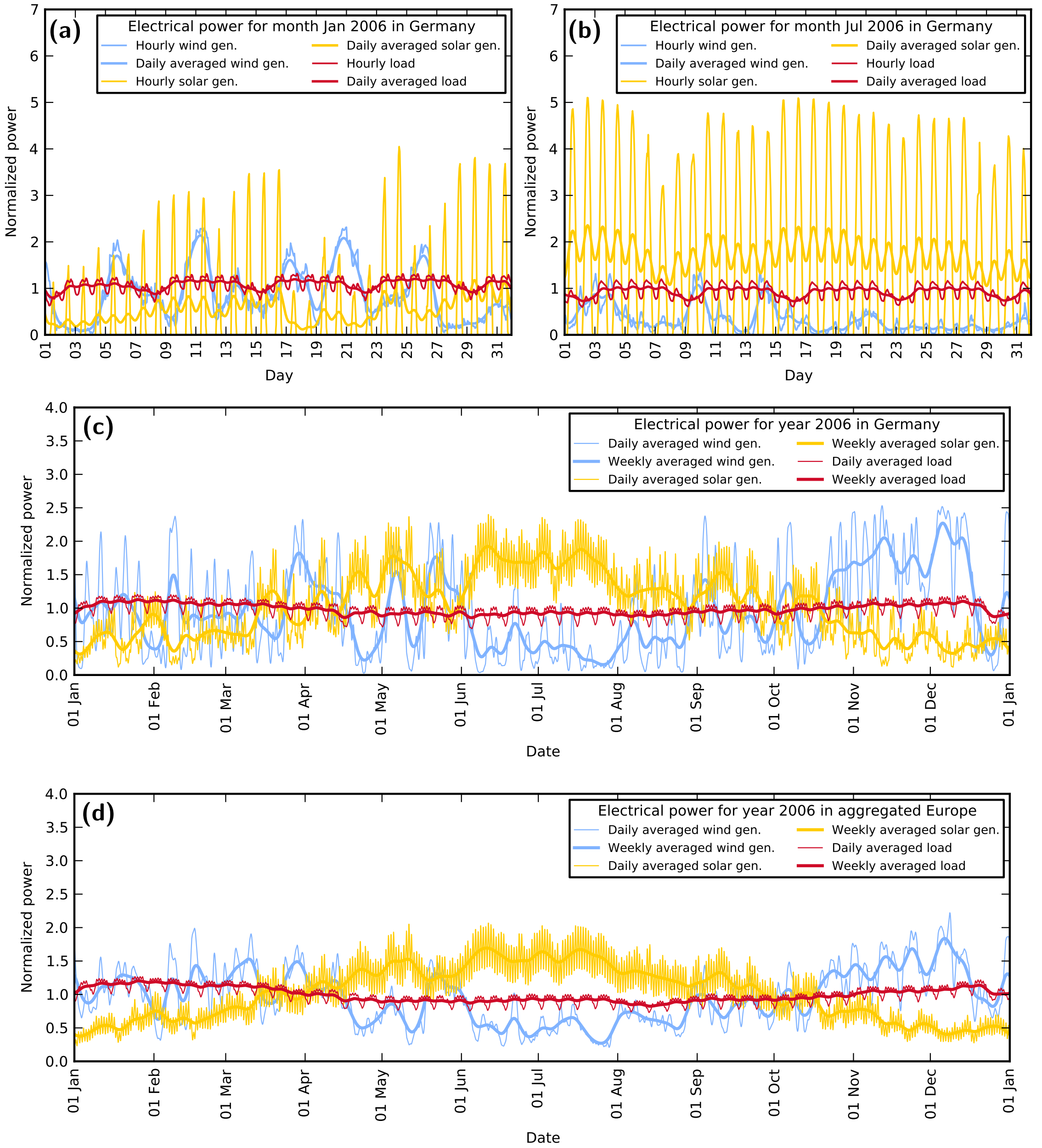

Figure 2.12: Wind and solar generation time series for Germany as well as for aggregated Europe, for the year 2006. The upper two plots show hourly time series as well as daily averages (convolution with a Gaussian with the width of a day) for the months (a) January and (b) July in Germany, while the lower plots show the daily as well as weekly averaged time series throughout the entire year 2006, for (c) Germany and (d) an aggregation of all of Europe. All time series are normalized to a mean of one.

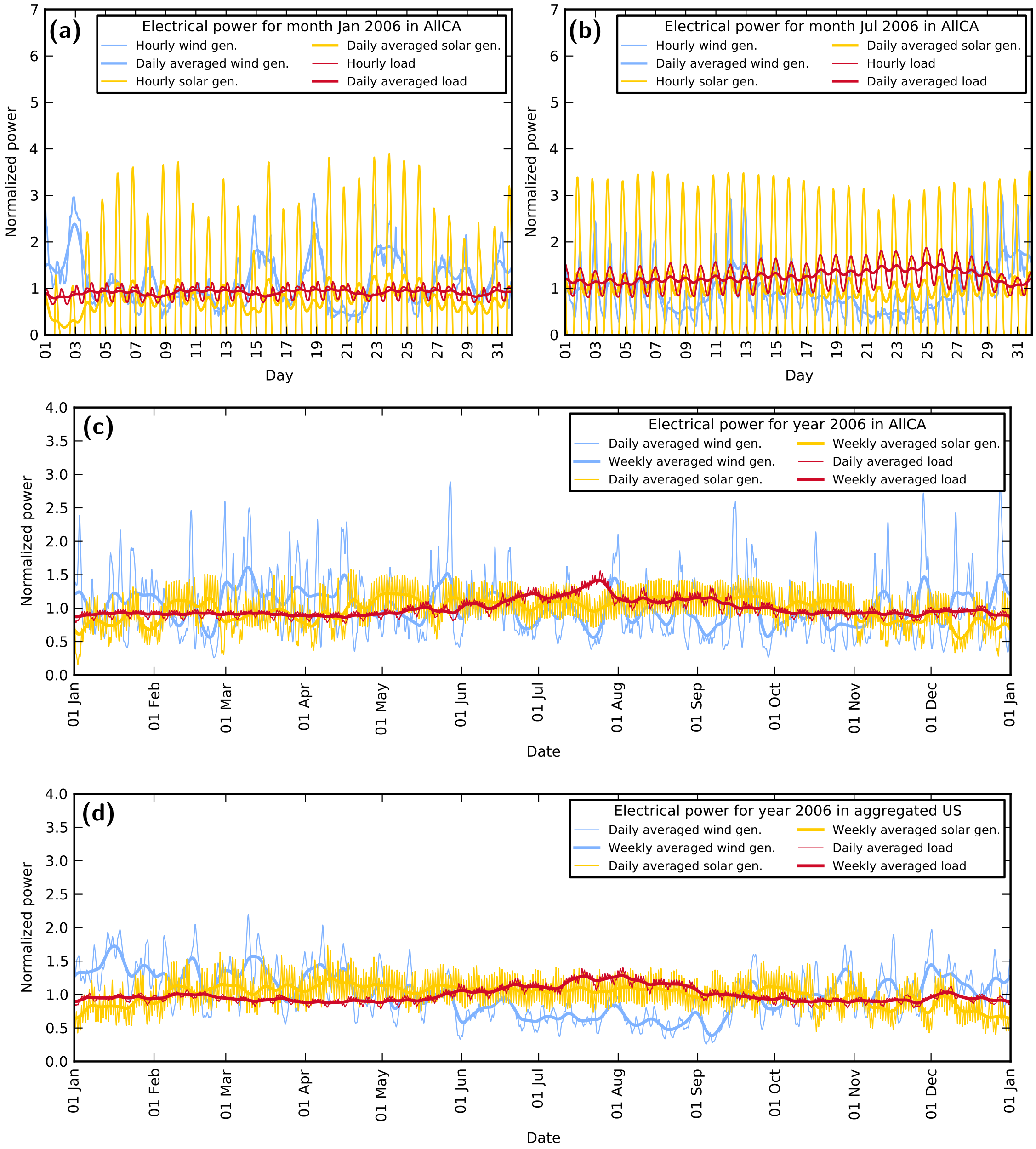

Figure 2.13: Wind and solar generation time series for the AllCA region as well as for the aggregated US, for the year 2006. The upper two plots show hourly time series as well as daily averages (convolution with a Gaussian with the width of a day) for the months (a) January and (b) July in the AllCA region, while the lower plots show the daily as well as weekly averaged time series throughout the entire year 2006, for (c) the AllCA region and (d) an aggregation of all of the US. All time series are normalized to a mean of one.

2.6 Mismatch between load and generation

Load and generation data are assembled into sets for the single sub-regions, countries in Europe and FERC regions in the US. Generation data are normalized to an average of one. Normalized wind generation is denoted $G_n^{\mathrm{W}}(t)$, and solar generation by $G_n^{\mathrm{S}}(t)$. On top of that, we introduce two factors characterizing the renewable generation in region n: The renewable gross share γ_n, which equals the total VRES generation divided by the total load, and the relative share α_n^{W} of wind in VRES. With these quantities, we can express the mismatch between renewable generation and load $L_n(t)$ as:

$$\Delta_n(t) = \gamma_n \left(\alpha_n^{\mathrm{W}} G_n^{\mathrm{W}}(t) + (1 - \alpha_n^{\mathrm{W}}) G_n^{\mathrm{S}}(t)\right) \cdot \langle L_n \rangle - L_n(t) \tag{2.13}$$

This mismatch time series will form the starting point for all of the analysis presented in this work.

Note that the VRES gross share γ_n is the ratio between the average VRES production and the average load, not to be confused with the share of VRES electricity in the total consumption, the VRES net share. This is due to the fluctuating nature of VRES generation, which especially for $\gamma_n > 50\%$ leads to surplus VRES production that does not contribute to covering the electric load. γ_n will in general be higher than the percentage of VRES in the electricity mix.

As an example, snippets from normalized generation and load time series for Germany as well as aggregated Europe is shown in Fig. 2.12, and for California, together with the aggregated US, in Fig. 2.13. In the monthly plots, the daily solar generation pattern is clearly visible. For Germany, it is significantly smaller for January as compared to June, while the difference is much less pronounced for California, which is located much closer to the equator. This seasonal solar pattern also shows in the yearly plots. Wind generation shows synoptic patterns on a timescale on the order of weeks, and is generally stronger in winter as compared to summer, both in Europe and the US, as can be seen from the aggregated year plots. Again, for Europe, the seasonal difference in generation is higher than for the US.

These plots also show the load patterns, which are similar on a daily and weekly scale for the US as well as Europe: There is a daily double-peaked high demand period around midday, and a nightly low-demand time. Weekends are also clearly visible as low-demand times. Conversely, opposite trends can be observed between Europe and the US on the seasonal timescale: While European loads peak in winter, due to the increased illumination needs and electric heating in some regions, US load generally peak in summer, when air-condition is required.

Chapter 3

Economic background

This chapter first introduces logistic growth, a theoretical approach to model technology transitions, and in particular its application to the ongoing changes in the electricity sector. It will be helpful in Sec. 5.2 to model transmission needs across Europe as renewable shares grow, and to construct a suitable transmission grid. The second section deals with basic notions from the economy of assets in the electricity sector, such as power plants or transmission lines. These will be used in Secs. 5 and 6 to formulate cost-minimal optimizations of the electricity system.

3.1 Logistic growth

3.1.1 Applicability in the energy sector

Logistic curves have proven to be able to successfully model the diffusion of new technologies across various fields such as infrastructures, e.g. canals, railroads, roads [87], electrification, and household appliances such as refrigerators and dishwashers [88].

The case of energy transitions is discussed in Ref. [89], and the current switch to CO_2-neutral generation is further analyzed in Refs. [90, 91]. They show that past energy transitions – for example the switch from oat to coal to oil in transportation (from horses to steam-powered trains to cars and trucks) or from candles to gas to electricity in lightning – roughly followed logistic growth curves. Ref. [90] traces the characteristics of these developments back to common boundary conditions: First, a new technology evolves in a niche market, where the newcomer offers new or significantly improved services, albeit at a (much) higher price. Initial markets are dominated by performance and relatively cost-indifferent demand. In this phase, the technology matures and considerably improves, in the example of steam engines gaining efficiency from 1 % up to about 20 %. Notably, the evolution often follows the path of “many before big”, that is, once the technology is sufficiently mature to become affordable for many, initial growth is in numbers before upscaling takes place. Another important factor is what the authors call “clustering and spillover”: Several technologies combined open up new ways of production, transportation, or services. Connected to this, they observe that it is generally end-use that drives technology transitions: The increasing use of oil instead of coal for transportation is due to the invention of cars, which do not run on steam engines burning coal (like trains), but on oil-fueled motors. Another example is the widespread use of electricity, driven by the demand for electric illumination, which would not have been possible without the light bulb. Even with strong drivers from new demand, observed time constants range between about 80 and 130 years from inventions to significant market shares. This is mainly due to considerable required investments in technology as well as infrastructure like roads, railroads, or electricity grids.

Based on these observations, the readers are cautioned that the current energy transition to low carbon technologies is non-generic in several ways: Growth and upscaling take place relatively early due to government incentives, without long-standing niche markets that would have allowed for optimization and experimentation (although one could argue that early adopters such as Denmark for wind energy or Germany for solar photovoltaics have formed such niche markets). Furthermore, the transition is not end-use driven by demand for a new product or service, but is "just" a replacement of old ways of providing energy with new ones. Recognizing the need to mitigate climate change, the concluding suggestion of the authors of Ref. [90] is, however, not to slow down the process, but to allow for improvements by experimenting with a broad portfolio of technologies, to protect market niches, to focus on end-use (for example efficiency measures), and to provide a stable policy environment.

3.1.2 Fit function

In spite of the outlined concerns with the applicability of logistic growth predictions to renewables, we still use it as a best guess to extrapolate between historical data and the future development in Europe by assuming that the gross share of wind and solar PV electricity production will follow a logistic growth curve for each individual country.

A general logistic function is given by

$$f(y; y_0, a, b, m) = \frac{a \cdot b \cdot \mathrm{e}^{m(y-y_0)}}{a(\mathrm{e}^{m(y-y_0)} - 1) + b} \,. \tag{3.1}$$

In our application, f denotes either the wind ($\gamma_n \cdot \alpha_n^{\mathrm{W}}$) or the solar ($\gamma_n \cdot (1 - \alpha_n^{\mathrm{W}})$) penetration. The reference year is denoted y, with y_0 and $a, b, m \geq 0$ being the fit parameters. a is the value of f in year y_0, b is the limiting value for late years, and m determines the maximal slope, which is given by $\frac{ma}{4}$. This function is least-square fitted to historical and projected wind or solar penetration data as described in Sec. 2.5.

The logistic function is symmetrical to its inflection point. Since we target relatively high end-point shares for 2050, this may lead to almost step-like growth for countries which do not have a significant share of VRES yet. To remove this artifact, we limit the growth rate to the rate necessary to replace old production capacity for wind turbines and solar panels at the end of their lifetime in the end scenario, i.e. we modify the fit function (3.1) by imposing a maximal slope. As a rough estimate, the lifetime is set to 20 yrs for both wind and solar installations for this purpose [92]. That corresponds to a maximal slope for each node n of $m_{\max}^{(n)} = \max_t(\gamma_n(t) \cdot \alpha_n^{\mathrm{W}}(t))/20$ (for wind) and $m_{\max}^{(n)} = \max_t(\gamma_n(t) \cdot (1 - \alpha_n^{\mathrm{W}}(t)))/20$ (for solar). The part of the logistic function where this maximal slope is exceeded is replaced with linear growth with the maximum slope in the following way:

- Calculate the points y_{low} and y_{high} where the slope starts respectively stops exceeding $m_{\max}$ from

  $$\frac{\partial}{\partial y} f(y; y_0, a, b, m) \overset{!}{=} m_{\max} \,.$$

  If f never exceeds the maximal slope, this equation has no solutions and we are done.

- Denote

  $$f_{\mathrm{low}} = f(y_{\mathrm{low}}; y_0, a, b, m) \qquad \text{and} \qquad f_{\mathrm{high}} = f(y_{\mathrm{high}}; y_0, a, b, m) \,.$$

- Modify f: Below y_{low}, nothing changes. Above y_{low}, f is replaced with a straight line of slope $m_{\max}$, until it reaches f_{high}. From that point on, the shifted original f is used again, cf. also Fig. 3.1.

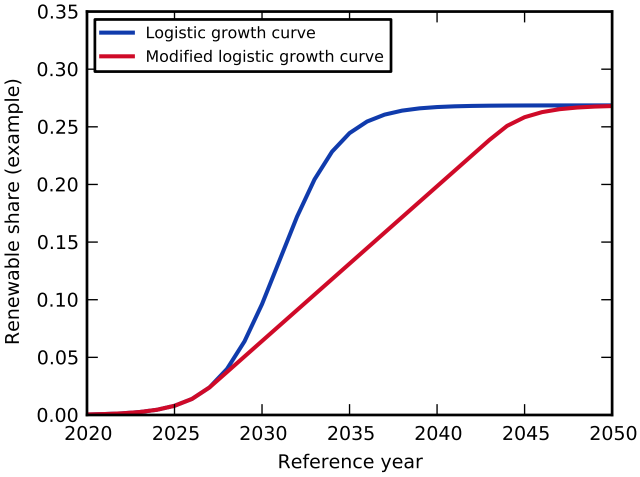

Figure 3.1: Logistic fit function that exceeds the maximal slope compared to the modified fit function given by Eq. (3.3), in which the part of the growth where the maximal slope is exceeded is replaced with a straight line of maximal slope, and further growth is shifted to the right.

Explicitly, we arrive at the following modified fit function f_{mod}:

$$f_{\mathrm{mod}}(y;y_0,a,b,m,m_{\mathrm{max}}) \tag{3.2}$$

$$= \begin{cases} f(y;y_0,a,b,m) & \text{if } \frac{ma}{4} \leq m_{\mathrm{max}} \\ f(y;y_0,a,b,m) & \text{if } \frac{ma}{4} > m_{\mathrm{max}} \text{ and } y < y_{\mathrm{low}} \\ m_{\mathrm{max}} \cdot (y - y_{\mathrm{low}}) + f(y_{\mathrm{low}};y_0,a,b,m) & \text{if } \frac{ma}{4} > m_{\mathrm{max}} \text{ and } y_{\mathrm{low}} \geq y \geq y_{\mathrm{high}} \\ f(y-\delta_y;y_0,a,b,m) & \text{if } \frac{ma}{4} > m_{\mathrm{max}} \text{ and } y > y_{\mathrm{high}} \end{cases} \tag{3.3}$$

with

$$y_{\mathrm{low}} = -\frac{\ln(1/(a-b))}{m} \cdot \frac{ab}{f_{\mathrm{low}} - b}$$

$$y_{\mathrm{high}} = -\frac{\ln(1/(a-b))}{m} \cdot \frac{ab}{f_{\mathrm{high}} - b}$$

$$\delta_y = \frac{f_{\mathrm{high}} - f_{\mathrm{low}}}{m_{\mathrm{max}}} - (y_{\mathrm{high}} - y_{\mathrm{low}})$$

and f_{low}, f_{high} obtained from

$$f_{\mathrm{low}} = a/2 - \sqrt{\frac{a^2}{4} - \frac{am_{\mathrm{max}}}{m}}$$

$$f_{\mathrm{high}} = a/2 - \sqrt{\frac{a^2}{4} + \frac{am_{\mathrm{max}}}{m}}$$

The calculations leading to this result are a little tedious, but only involve nontrivial analysis techniques well known from school-level curve tracing, and some geometric considerations. The effect of the modifications is illustrated in Fig. 3.1.

3.1.3 Application to renewables in Europe

The historical and targeted wind and solar penetrations in Europe are fitted with logistic growth curves. In order to model the growth of VRES installation from today's values up to a fully VRES-supplied energy system, we let α_n^{W} and γ_n from Eq. (2.13) depend smoothly on a reference year. The reference years correspond to real years in the sense that historical penetrations of wind and solar power are made to follow historical values. In a similar fashion, future penetrations are based on official 2020 targets and 2050 assumptions. γ_n and α_n^{W} are obtained by fitting growth curves

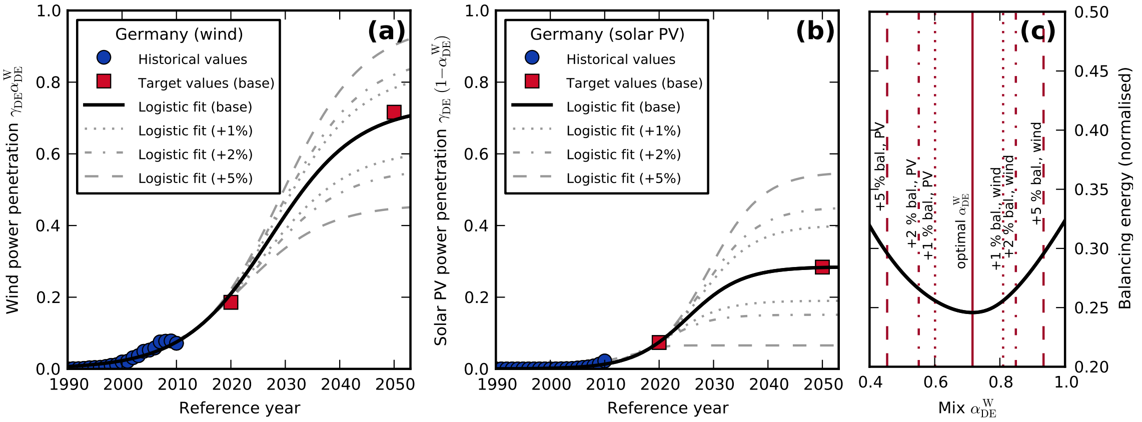

Figure 3.2: Logistic fits to historical and targeted wind (a) and solar PV (b) penetration in Germany 1990 - 2050. In panel (c), backup energy as a function of the wind/solar mix for Germany is shown, for a renewable penetration of $\gamma_{\mathrm{DE}} = 1.0$. The solid vertical line in this panel points out the backup optimal mix, and the dotted, dashed-dotted and dashed lines indicate the mixes that lead to backup needs increased by 1 %, 2 %, and 5 % of the load, respectively. These mixes are used for seven different 2050 targets in panels (a) and (b): the optimal mix corresponds to the base scenario (solid black lines), and the other mixes lead to the three wind heavy and three solar heavy logistic growth scenarios (gray broken lines). In calculating the backup needs of single countries as in (c), imports and exports are not considered. Backup is normalized by the average load.

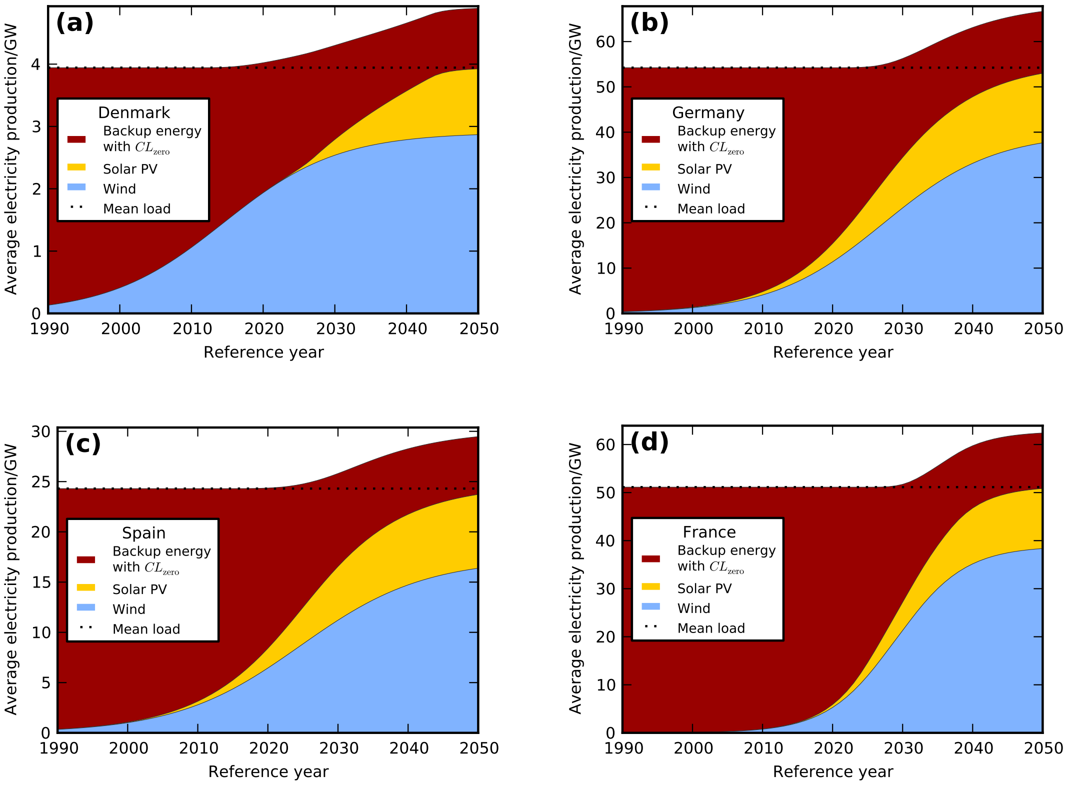

Figure 3.3: Logistic growth of wind (blue) and solar PV (yellow) power production, replacing conventional backup, for (a) Denmark, (b) Germany, (c) Spain, and (d) France. Shown is the base scenario, where the single country backup optimal mix is reached in 2050. The backup energy (red) has been determined with the no-transmission layout. The conversion from the shares $\gamma_n \cdot \alpha_n^{\mathrm{W}}$ (wind) resp. $\gamma_n \cdot (1 - \alpha_n^{\mathrm{W}})$ (solar PV) to average generation in GW is done using the 2007 load.

to historical and targeted penetrations. The year variable of the fit is termed reference year to emphasize that the fit does not exactly pass through neither the historical nor the targeted values. Example fits can be seen in Fig. 3.2, see also Fig. 3.3. Detailed numerical values are found in Tabs. C.1 and C.2.

3.1.4 Alternative end-point mixes

To investigate whether the optimal mix changes as soon as transmission comes into play, we calculate logistic growth curves for a further range of end-point mixes α_{W} of wind and solar energy apart from the single country backup-minimal mix (base scenario, introduced in Sec. 6.1.1). The final mix is varied over a range from roughly $\alpha^{\mathrm{W}} = 0.40$ to $\alpha^{\mathrm{W}} = 0.90$ wind share in six additional scenarios apart from the optimal mix base scenario: three solar heavy and three wind heavy scenarios, see Fig. 3.2c. In the base scenario, the end-point mix of each country is chosen as the mix that minimizes the average backup energy of the country on its own, i.e. without transmission. The wind heavy scenarios are defined by identifying the mixes to the right of the minimum that lead to increases in backup by 1 %, 2 %, and 5 % of the average load. The three solar heavy scenarios are defined in analogy to the left of the minimum. All seven scenarios are indicated in Fig. 3.2c for Germany. Similar pictures emerge for the other countries; the different end-point mixes are given in Tab. C.1 In the following, we examine the interplay between backup and transmission in all seven scenarios with a focus on the base scenario, and then investigate the effect of transmission on the optimal mix comparing all scenarios.

3.2 LCOE and annualized cost derivation

The presentation here closely follows [93]. I will stick with the official English terms and give their German translation in brackets to aid the reader when comparing to German sources. The goal is to derive (a) how to annualize an investment and (b) the levelized costs of electricity (LCOE, Stromgestehungskosten). These will be used further on to investigate cost-optimized developments in the US in Secs. 5.3, 6.2.3, and 6.3.2.

3.2.1 Interest/discount rate

We will be using the *nominal* interest rate (nominaler Zinssatz) aka discount rate i, which includes inflation plus expected rate of return (what is gained from the investment) plus a possible risk surcharge factor (which is added because it is not clear whether the project will succeed). It is always calculated as the effective rate for a year.

$$i = \text{inflation rate} + \text{investment return rate} + \text{risk surcharge rate}$$

Note that it is possible to justify different rates for different projects, due to different risks in different sectors. $(1 + i)$ is also know as the discount factor (Auf-/Abzinsungsfaktor).

3.2.2 Present value

The interest rate is used to convert every future payment to today's values by dividing ("discounting") by $(1 + i)^t$, and past payments by multiplying by $(1 + i)^t$ for each year t in the future/past. A subtlety here is whether interest is paid at the beginning or end of each year, here we assume (as is most common) that it is at the year's end.

The Present value (PV, Barwert) of future investments or income is obtained discounting all incoming or outgoing payments with the appropriate discount factor to today's value, and then summing up the result:

$$\mathrm{PV} = \sum_{t=1}^{N} \frac{I_t}{(1 + i)^t}$$

where I_t is the payment in year t, and N is the number of years considered.

3.2.3 Annualized investment

Here, the question is how to convert a one-time investment I_0 in an asset into annual rates or annuities (Annuitäten/Rente) k over the asset's lifetime of N years. It applies to the case where there are investment costs in the first year of an asset, but no further cost during the lifetime. It will be used later for transmission lines. The problem can be pictured as taking out all the money for the initial investment as a loan with a run time equal to the expected lifetime of the asset. The annualized costs then equal the annual payback amount k necessary to pay off the loan by the end of the project's lifetime, given an interest rate i. The PV of the payback at the project's start time, that is, the sum of the discounted payments, has to equal the original investment sum I_0:

$$\begin{aligned} I_0 &= \sum_{t=1}^{N} \frac{k}{(1+i)^t} = \frac{(1+i)^N - 1}{i(1+i)^N} k \\ \Leftrightarrow k &= \frac{i(1+i)^N}{(1+i)^N - 1} I_0 \end{aligned} \tag{3.4}$$

In the first line, the sum can be evaluated easily because it is a geometric series. The factor linking the total investment sum and the annual payments is also know as the capital recovery factor (CRP, Annuitätenfaktor), named from the point of view of the party granting the loan.

3.2.4 Levelized costs of electricity (LCOE)

The PV of an asset in the electricity sector can be expressed as

$$\sum_{t=1}^{N} \frac{I_t + M_t + F_t}{(1+i)^t}$$

where N is the project's expected lifetime, I_t is the investment in year t, M_t is the maintenance cost in year t, and F_t is the fuel cost in year t. Of course, some of the costs may be zero in some years, e.g. most infrastructure assets have non-zero investment costs only during construction in the first year, or renewable assets do not have fuel costs. These costs have to be balanced by an equal income from the sale of electricity, that is

$$\begin{aligned} \sum_{t=1}^{N} \frac{I_t + M_t + F_t}{(1+i)^t} &\overset{!}{=} \sum_{t=1}^{N} \frac{LCOE}{(1+i)^t} E_t \\ \Leftrightarrow LCOE &= \frac{\sum_{t=1}^{N} \frac{I_t+M_t+F_t}{(1+i)^t}}{\sum_{t=1}^{N} \frac{E_t}{(1+i)^t}}, \end{aligned} \tag{3.5}$$

where E_t is the energy produced in year t. LCOE are thus the average nominal value of the electricity cost over the asset's lifetime, since the discount factor (that would normally go with the costs) is kept together with the electricity production. LCOE are in this way effectively lifetime interval-dependent (instead of year-dependent).

Chapter 4

Transmission

In this chapter, I will discuss how power dispatch and transmission is implemented in our code. The main method used is convex optimization, which is described in short in the first section 4.1, and in more detail in Appendix A. Then, based on convexity of the problem, two dual formulations of DC power flow are given in Sec. 4.2. Subsequently, the derivation of DC power flow as an approximation of AC power flow is given in Sec. 4.3. Finally, our adaptations of the DC power flow to situations with finite link capacities and global mismatches between load and generation is discussed, and two proposed algorithms are compared in Sec. 4.4.

4.1 Convex optimization

Convex optimization is the central technique to be used in this chapter and the following Ch. 5. It is discussed in detail in App. A, where the main definitions are given and the major theorems are proven. Here, I will give only a short sketch of how it works.

Convexity: A convex function "smiles" $\smile$ at you: A straight line connecting any two points on the graph will always lie above the graph. If the function is twice differentiable, its second derivative will be positive.

Regions in $\mathbb{R}^n$ can also be convex, and the graphic inspiration for the definition is very similar as for functions: A straight line connecting any two points in the region has to be completely contained in the region. An example for a convex region is the area above a convex function.

Convex optimization problem: A minimization of a convex function f_0 over a convex domain. In standard form, the domain is given as the intersection of areas above convex functions (inequality constraints with convex functions f_i) plus additional affine (linear plus constant) equality constraints h_i:

$$\begin{aligned} &\text{minimize}_x f_0(x) \\ &\qquad \text{given } f_i(x) \leq 0, \quad i = 1..N\text{and} \qquad\qquad h_j(x) = 0, \quad j = 1..M\,. \end{aligned}$$

Convex optimizations are "well behaved" in the sense that if any minimum exists, it is always global. There is no "getting stuck" in local minima. If the objective function is strictly convex (see Appendix A for the exact definition), the minimum is unique.

Lagrange duality: Most (but not all!) convex problems fulfill Lagrange duality, that is, the original problem is equivalent to maximizing a concave function:

$$\begin{aligned} &\text{maximize}_{\lambda,\nu} g(\lambda,\nu) = \inf_x L(x,\lambda,\nu) = \inf_x f_0(x) + \sum_{i=1}^{N} \lambda_i f_i(x) + \sum_{j=1}^{M} \nu_i h_i(x) \\ &\qquad \text{given } \lambda_i \geq 0 \end{aligned}$$

The function $L(x,\lambda,\nu)$ is called the "Lagrangian" of the problem, which is not to be confused with the usual physicist's Lagrangian (although of course not unrelated).

4.1.1 Whitelist of convex expressions

Apart from the definition of convexity of a function, it will be useful for our purposes, especially for numerical implementation, to have a whitelist of convex expressions. It is, of course, not exhaustive. Most proofs can simply be done by checking the definition directly, see [94, Ch. 3] for more details.

A function $f : \mathbb{R}^N \to \mathbb{R}$ is convex if it is

- affine $f(x) = a^T x + b\,,\ a \in \mathbb{R}^N, b \in \mathbb{R}$.
- a weighted sum $f(x) = \sum_{i=1}^M a_i f_i(x)$ of M convex functions f_i with non-negative weights $a_i \geq 0$.
- a pointwise supremum $f(x) = \sup_i f_i(x)$ of a finite set of convex functions f_i.
- the composition $f(x) = h \circ g(x) = h(g(x))$ of a convex function h with an affine function g.
- the composition $f = h \circ g$ of a convex, non-decreasing function h with a convex function g.
- the Legendre transform
$$f^*(y) = \sup_x \{\langle y|x\rangle - f(x)\}$$
of any function $f : \mathbb{R}^n \to \mathbb{R}$, a property which is exploited e.g. in the study of first-order phase transitions in classical thermodynamics.

4.2 DC power flow in two formulations

Solving the DC power flow problem means calculating how the electric current will flow in a direct current network, given the in- and outflow at the node points. It can be expressed in two standard ways, and the proof of their equivalence is the most important application of Lagrange duality in our context. Before we come to the equivalence, we first have to introduce some network terminology.

4.2.1 Network terminology

We consider a network of N nodes, connected by L lines. The network topology is encoded in its $N \times L$ *incidence matrix* K:

$$K_{nl} = \begin{cases} 1 & \text{if link } l \text{ starts at node } n \\ -1 & \text{if link } l \text{ ends at node } n \\ 0 & \text{else} \end{cases}$$

The link orientation does not make a physical difference in our context; we say that the network is *undirected.* Link direction can be picked randomly, and just has to be kept consistent throughout the calculation. We only allow for one link between any two nodes. The $N \times N$ matrix $\Lambda = KK^T$, the *network Laplacian*, is an alternative way of encoding the network structure. Explicitly,

$$\Lambda_{nm} = \begin{cases} -1 & \text{if } n \neq m \text{ and } n \text{ linked to } m \\ 0 & \text{if } n \neq m \text{ and } n \text{ not linked to } m \\ d_n & \text{if } n = m \end{cases}$$

The diagonal entries Λ_{nn} contain the *degree* d_n of node n, that is, the number of links connected to node n. The degree can also be written as the sum of off-diagonal entries in the row: $d_n = \Lambda_{nn} = -\sum_{m\neq n} \Lambda_{nm}$. This implies that each row sums up to zero, that is, the Laplacian has one eigenvalue zero and is thus not invertible. Since the network is undirected, the Laplacian is symmetric. Of more practical importance here is the network's *admittance matrix* E, which consists of the admittances (the inverse of the resistances) of the lines. Using the diagonal $L \times L$ matrix R which contains the resistance of line l in entry R_{ll}, we can write the admittance matrix as

$$E_{nm} = (KR^{-1}K^T)_{nm} = \begin{cases} -\frac{1}{R_{ll}} & \text{if } n \neq m \text{ and link } l \text{ links nodes } n \text{ and } m \\ 0 & \text{if } n \neq m \text{ and } n \text{ not linked to } m \\ \sum\limits_{l \text{ connected to } n} \frac{1}{R_{ll}} & \text{if } n = m \end{cases}$$

For convenience, we will also use the notation R_{nm} for the resistance of the link between nodes n and m, with $R_{nm} = \infty$ if n and m are not linked.

4.2.2 Two formulations and their equivalence

Ohm's law

With the admittance matrix, it is possible to write down the network generalization of Ohm's law ($1/R \cdot U = I$).

$$EU = I\,, \tag{4.1}$$

where $I \in \mathbb{R}^N$ is the given net outflow vector, and $U \in \mathbb{R}^N$ is the vector of electric potentials at each node, which is to be calculated. The parallel to Ohm's law becomes clearer in components:

$$I_n = \sum_m E_{nm}U_m = \sum_{m \neq n} -\frac{1}{R_{nm}}U_m + \sum_{m \neq n} \frac{1}{R_{nm}}U_n = \sum_{m \neq n} \frac{U_n - U_m}{R_{nm}}$$

Just as for the Laplacian, the admittance matrix has row sum zero and is therefore not directly invertible. Mathematically speaking, the matrix equation Eq. (4.1) is underconstrained, it does not fully determine U. However, there exist standard techniques to make the problem solvable. The physical interpretation of the "missing constraint" is the arbitrariness of the choice of the zero level of the electric potential. It is thus possible to solve Eq. (4.1) by fixing the value of one entry of U. Another commonly used approach is calculating the Moore-Penrose pseudoinverse E^+ of E [95, 96], for which efficient algorithms exist.

One consequence of E being non-invertible is that the image of E $\{Ex | x \in \mathbb{R}^N\}$ does not span the entire $\mathbb{R}^N$, but only those vectors I that fulfill

$$\sum_{n=1}^{N} I_n = 0$$

(as is easily checked by direct calculation). Physically, this means that the total inflow is required to equal the total outflow, or in other words, that the total charge is conserved.

Once the electric potentials and thus voltage differences of the network are known, it is easy to calculate the corresponding flows from

$$F = R^{-1}K^TU\,. \tag{4.2}$$

Written in components, if link l starts at node n and ends at node m:

$$F_l = \frac{1}{R_{nm}}(U_n - U_m) = \frac{\Delta U_{nm}}{R_{nm}}$$

As the flow can be derived from the potentials, it is often called a *potential flow.* In such a situation, Kirchhoff's laws are fulfilled: the total inflow at each node equals its total outflow, and the potential difference along closed loops is zero. The flow is correspondingly also called a *Kirchhoff flow.*

Minimum dissipation principle

In this formulation, the variables to be calculated are the flows directly, without the intermediate step of determining the potential. Here, the task is to minimize the total dissipation which is proportional to RF^2, while guaranteeing that the flows redistribute the net in- and outflows from sources to sinks.

$$\begin{cases} \min_F F^T RF \\ \text{given } \; KF = I \end{cases} \tag{4.3}$$

The constraint in problem (4.3) is the direct equivalent of Eq. (4.1). In fact, if potentials U are known and the flows are calculated from them by (4.2), it reduces to (4.1).

The requirement $KF = I$ does not, however, fully determine the flows, because there is still the possibility of circular flows that do not contribute to any net transport between different nodes. These are eliminated only in the dissipation minimization $\min_F F^T RF$.

Equivalence

We will show that these two problems are Lagrangian dual convex problems with unique optimizers. As problem (4.3) has a strictly convex objective function – a convex parabola – and only linear equality constraints, it is evidently a convex optimization problem with unique solution. We form its dual problem:

$$g(\nu) = \inf_F L(F, \nu) = \inf_F F^T RF + \nu^T (KF - I)$$

This expression is still a strictly convex parabola in F, and therefore, its minimum can be found by finding the (only) critical point where its gradient in F vanishes. Since R is diagonal, this is easy:

$$\begin{aligned} \frac{\partial}{\partial F} L(F^*, \nu) &= 2RF^* + K^T \nu \overset{!}{=} 0 \\ \Leftrightarrow F^* &= -\frac{1}{2} R^{-1} K^T \nu \end{aligned}$$

Inserting F^* into the Lagrangian yields

$$\begin{aligned} g(\nu) &= \frac{1}{4} (R^{-1} K^T \nu)^T R (R^{-1} K^T \nu) - \frac{1}{2} \nu^T (K(R^{-1} K^T \nu)) - \nu^T I \\ &= -\frac{1}{4} \nu^T E \nu - \nu^T I \,. \end{aligned}$$

The Lagrange dual of (4.3) is thus the unconstrained problem

$$\max_\nu g(\nu) = \max_\nu -\frac{1}{4} \nu^T E \nu - \nu^T I \,.$$

g is a concave parabola in ν, with a sole maximum, which can be found simply by forming the derivative:

$$\begin{aligned} \frac{\partial}{\partial \nu} g(\nu) &= -\frac{1}{2} E \nu - I \overset{!}{=} 0 \\ \Leftrightarrow E \left(-\frac{1}{2} \nu \right) &= I \end{aligned}$$

which is the formulation of DC power flow in (4.1) under variable renaming $\left(-\frac{1}{2}\nu\right) \equiv U$. The dual of the second formulation is thus equivalent to the first. From the KKT condition (A.10) (the gradient of L with respect to F must vanish), we furthermore obtain the relation between flow and voltage:

$$\begin{aligned}\partial_F L(F,\nu) &= 2RF + K^T\nu \overset{!}{=} 0\\ \Rightarrow F &= -\frac{1}{2}R^{-1}K^T\nu = R^{-1}K^TU\,.\end{aligned}$$

An interesting side remark: This equivalence has been exploited for the construction of fast algorithms to calculate the inverse of symmetric matrices with largest absolute entry on the diagonal, also called SDD (symmetric diagonal dominant) matrices: These can be transformed into matrices that can be interpreted as network admittance matrices, and then solved via a variant of the minimum dissipation principle. For details, see the presentation in Ref. [97].

4.3 From AC to DC power flow

We will mainly be dealing with alternating current (AC) networks, provoking the question why we spend so much time on DC power flow. As it turns out, it is possible to derive an approximation of AC power flow that is mathematically equivalent to DC power flow. It has become a standard in the engineering literature, see e.g. Ref. [98].

The starting point for the derivation are the full AC flow equations, which are usually expressed in terms of complex numbers. Split into real and imaginary part, they read:

$$\Delta_{\text{real},n} = \sum_{m=1}^{N} |U_n||U_m|(H_{nm}\cos\delta_{nm} + C_{nm}\sin\delta_{nm}) \tag{4.4a}$$

$$\Delta_{\text{imag},n} = \sum_{m=1}^{N} |U_n||U_m|(H_{nm}\sin\delta_{nm} - C_{nm}\cos\delta_{nm}) \tag{4.4b}$$

where $\Delta_{\text{real},n}$ is the active power (real part of the power) net outflow at node n, $\Delta_{\text{imag},n}$ is the reactive power (imaginary part) net outflow, $|U_n|$ is the absolute of the (complex) voltage, $\delta_{nm} = \delta_n - \delta_m$ is the difference in phase angle between nodes n and m, H_{nm} is the real part of the admittance between node n and m, and C_{nm} is the imaginary part of the admittance. C_{nm} and H_{nm} are zero if nodes n and m are not linked.

The AC equations (4.4) can be read as power balance equations with net outflows (consumption or generation at the nodes) on the left hand side compensated by net inflows from the network on the right hand side. Since they are nonlinear, they are generally solved numerically.

There are, however, a couple of assumptions that are justified in a stable network without significant active power losses, that is, small resistances $H_{nm} \approx 0$. In this case, reactive power (Eq. 4.4b) can be neglected, and voltage levels are constant throughout the network ($|U_n| \approx |U|$). Network stability also entails small phase angle differences δ_{nm}, such that $\sin\delta_{nm} \approx \delta_{nm}$. This reduces Eqs. (4.4) to

$$\Delta_n = \sum_{m=1}^{N} E_{nm}\delta_m\,. \tag{4.5}$$

Here, the power has been rescaled such that $|U| \equiv 1$, notation has been simplified by setting $\Delta_n \equiv \Delta_{\text{real},n}$, and E is constructed from the imaginary part C of the impedances via

$$\sum_m C_{nm}\delta_{nm} = \sum_m C_{nm}(\delta_n - \delta_m) = \sum_{m\neq n} C_{nm}\delta_n - \sum_{m\neq n} C_{nm}\delta_m \equiv E_{nm}\delta_m\,.$$

Comparing the DC power flow (Eq. 4.1) to this simplification (Eq. 4.5), we see that they are structurally equivalent. The current I from (4.1) corresponds to the nodal power Δ in Eq. (4.5), the admittance matrix consisting of the inverse resistances E is replaced by the (suggestively named) E matrix consisting of the inverse reactances, and the part of the electric potential U is played by the phase angles δ. Note that the two E matrices also both have the property that their rows sum up to zero, such that the problem can be solved with the same techniques.

For the rest of this work, we conveniently assume all reactances to be unity, such that the admittance matrix coincides with the Laplace matrix.

4.4 Generalizations of DC power flow

Our starting point is the minimum dissipation principle as formulated in Eqs. (4.3). With the simplifications from Sec. 4.3, it reads

$$\min F^T F \tag{4.6a}$$

$$\text{given } (\Delta - KF) = 0 \tag{4.6b}$$

We now want to include constraints on the flows that model the finite transmission capacity of a power line, i.e. inequalities of the form

$$h_- \leq F = K^T \delta \leq h_+ \tag{4.7}$$

The transmission capacity limits $h_\pm$ can be direction dependent, since we are dealing with effective networks in which nodes represent larger regions and one link stands for several power lines, such that region-internal bottlenecks are neglected, which can lead to asymmetric effective line capacities. Compare for example the net transfer capacities between European countries as reported by ENTSO-E [99], which are also reproduced in Tab. C.3.

In the formulation (4.6), flow constraints cannot be included, since solutions are unique and do not allow for further constraints on the flows.

Furthermore, we want to treat cases in which there is a global power mismatch between load and generation, i.e.

$$\sum_i \Delta_i \neq 0\,. \tag{4.8}$$

This is obviously not possible in our setting so far, since there are no solutions at all if $\sum_i \Delta_i \neq 0$ (that would violate the conservation of energy).

In order to deal with global power mismatches, we introduce *backup*, i.e. extra power generation from non-VRES sources when there is less renewable generation than load, and *curtailment*, i.e. the shedding of overproduction of VRES. The net export P_n of each of the nodes can be expressed in terms of the flows F_l via

$$P_n = \sum_{l=1}^{L} K_{nl} F_l. \tag{4.9}$$

Total backup can now be expressed as:[1]

$$B_{\text{tot}} = \sum_{n=1}^{N} (\Delta_n - P_n)_- = \sum_{n=1}^{N} B_n\,. \tag{4.10}$$

and curtailment likewise as

$$C_{\text{tot}} = \sum_{n=1}^{N} (\Delta_n - P_n)_+ = \sum_{n=1}^{N} C_n\,. \tag{4.11}$$

The need for backup B_n at node n is what is potentially left of a negative mismatch Δ_n after it has been reduced by the net imports P_n, and the curtailment C_n equals the positive part of this residual mismatch.

---

[1] $(x)_- = \max\{-x, 0\}$ denotes the negative part of a quantity x, $(x)_+ = \max\{x, 0\}$ the positive part.

4.4.1 Base case: Maximize VRES usage

This algorithm has been employed in Refs. [53–55]. The idea is to make the system use as much of the renewable generation as possible, while reducing flow dissipation $F^T F$.

Priorities:

1. Minimize total backup ⇔ maximize VRES usage
2. Minimize transmission dissipation

As a first step, we minimize backup linearly. In this way, we ensure that it will be optimally little, but we do not care about the distribution among the nodes, i.e. the necessary backup power capacities. Since minimizing the backup leaves some degrees of freedom unfixed, we minimize flow dissipation in a second step. This method can be thought of as a straightforward generalization of the DC power flow to situations with global mismatches: The requirement that zero mismatch remains after transmission, Eq. (4.6b) is relaxed to minimizing the total negative mismatch after transmission, and the flow dissipation minimization Eq. (4.6a) is retained.

Algorithm: We loop over time once. For each time t:

1. Minimize total backup:

$$\min_{F(t)} B_{\text{tot}}(t) = \min_{F(t)} \sum_{n=1}^{N} (\Delta_n(t) - (KF(t))_n)_- = B_{\min}(t)\,.$$

2. Minimize transmission dissipation, subject to the constraint that total backup must stay at the minimal value found in the first step:

$$\min_{\substack{F(t) \\ \sum_{i=1}^{N}(\Delta_n(t)-(KF(t))_n)_- = B_{\min}(t)}} \sum_{l=1}^{L} F_l^2(t)$$

If the line capacities are constrained by (possibly direction dependent) net transfer capacities (NTCs), $h_{-l} \leq F_l \leq h_l$, these constraints have to be included. We end up with two minimization steps, the first representing maximal sharing of renewables, and the second minimizes transmission dissipation:

$$\text{Step 1:} \quad \min_{h_{-l} \leq F_l \leq h_l} \sum_{n=1}^{N} (\Delta_n - (KF)_n)_- = B_{\min} \tag{4.12a}$$

$$\text{Step 2:} \quad \min_{\substack{h_{-l} \leq F_l \leq h_l \\ \sum_{n=1}^{N}(\Delta_n-(KF)_n)_- = B_{\min}}} \sum_{l=1}^{L} F_l^2 \tag{4.12b}$$

The two minimizations are both convex optimization problems. In order to see this, we need to show that all constraint and objective functions are convex. For the flow constraints, this is clear because they can easily be restated as two affine constraints

$$h_{-l} \leq F_l \leq h_l \quad \Leftrightarrow \quad \begin{cases} F_l - h_l & \leq 0 \\ -F_l + h_{-l} & \leq 0 \end{cases}.$$

For the objective function in the first minimization, we make use of our whitelist of convex functions: Affine functions are convex, and therefore, $\Delta_n - (KF)_n$ is convex. $f(x) = (x)_-$ is obviously a convex function, and since the composition of an affine function with a convex function is convex, so is $(\Delta_n - (KF)_n)_-$. Finally, the sum of convex functions is convex, and so $\sum_{n=1}^{N}(\Delta_n - (KF)_n)_-$ is convex. The first minimization is therefore a convex optimization problem.

In the second minimization, the objective function is clearly convex, since it is a parabola. But, strictly speaking, using $\sum_{n=1}^{N}(\Delta_n - (KF)_n)_- - B_{\mathrm{min}} = 0$ as an equality constraint violates the convexity of the problem, since only linear equality constraints are allowed. There is, however, an easy workaround: Instead of requiring equality, we can just as well demand that

$$\sum_{n=1}^{N}(\Delta_n - (KF)_n)_- - B_{\mathrm{min}} \leq 0\,. \tag{4.13}$$

In this way, it is sufficient that the left hand side of (4.13) is convex (which holds – it is a convex function minus a constant), while actually, equality is guaranteed since B_{min} is the minimal possible value of $\sum_{n=1}^{N}(\Delta_n - (KF)_n)_-$.

4.4.2 Finite backup power capacities

We know that if backup is minimized linearly in each time step, it will not be shared between the different nodes. VRES are shared between the nodes, but the distribution of them is chosen solely such that flows are minimized, leading to high backup power quantiles. On the other hand, the even distribution of backup is able to reduce backup power quantiles significantly, but it requires a lot of transmission, even at times when the single node's backup power capacities would be completely sufficient to cover their needs without significant power flow. As a possible compromise, we propose the linear minimization of backup duties, but with backup power capacities capped to some value that is sufficient to cover the deficits on the network as a whole. In this way, unusually high backup events are covered by the nodes together, like in the evenly shared backup case, but for "normal" times, the nodes cover their own deficits themselves.

Priorities:

1. Minimize total backup ⇔ maximize VRES usage
2. Minimize maximal values for backup ⇔ reduce backup power capacities
3. Minimize transmission dissipation

Algorithm: In order to determine sufficient backup power capacities that stay constant in time, we need two loops over time. In the first loop, we determine the minimum necessary backup energy as well as the maximal necessary power capacities for each hour.

1. Minimize total backup:

$$\min_{F(t)} B_{\mathrm{tot}}(t) = \min_{F(t)} \sum_{n=1}^{N}(\Delta_n(t) - (KF(t))_n)_- = B_{\mathrm{min}}(t)\,. \tag{4.14}$$

2. Minimize maximal backup energies:

$$\min_{\substack{F(t)\\ \sum_{i=1}^{N}(\Delta_n(t)-(KF(t))_n)_-=B_{\mathrm{min}}(t)}} \left\{\max_n \frac{B_n(t)}{\langle L_n\rangle}\right\} = A_{\mathrm{min}}(t) \tag{4.15}$$

   Note that this does not mean that we only look at the node that *initially* shows the largest backup value, minimize this and then we are satisfied. Rather, the node n at which the maximal backup value occurs changes with varying flow. Generically, first the backup of the node with the highest backup will be distributed to other, less strained nodes, until it reaches a backup level equal to that of the next largest node. Then both their backup gets reassigned to others and so on. If there are no constraints on the line capacities, all nodes will end up doing the same amount of backup, only scaled by their mean load $\langle L_n\rangle$, compare also Fig. 4.1.

Between the loops, we calculate the minimal backup power capacities that are sufficient for all times and introduce a corresponding backup capacity constraint:

$$\begin{aligned} A &= \max_t A_{\min}(t) \\ B_n(t) &\leq \langle L_n \rangle \cdot A \end{aligned} \tag{4.16}$$

In the second loop over time, we finally fix the distribution of backup duties by flow dissipation minimization:

3. Minimize transmission dissipation:

$$\min_{\substack{F(t) \\ \sum_{i=1}^{N} (\Delta_n(t) - (KF(t))_n)_- = B_{\min}(t) \\ B_n(t) \leq \langle L_n \rangle \cdot A}} \sum_{l=1}^{L} F_l^2(t) \tag{4.17}$$

In case of constraints on the transmission line capacities, all optimizations are subject to

$$h_{-l} \leq F_l(t) \leq h_l \,. \tag{4.18}$$

4.4.3 Comparison of different flow schemes

The two flow schemes show pronounced differences in backup dispatch. As an illustrative example, we look at the following model case: VRES gross share is chosen to be $\gamma_n = 1$ and relative wind share in VRES $\alpha_n^{\mathrm{W}} = 0.7$ for all nodes in the European network. These are combined with a strong transmission grid to see the effects of transmission more clearly. The transmission capacities are chosen such that on each link, the flow is unimpeded by transmission limits for 99% of the time. The construction of such quantile layouts, as we choose to call them, is described in more detail in Ch. 5.

The backup distribution across the nodes is illustrated for one hour of high backup demand in December 2002 in Fig. 4.1. It is clearly seen how the backup is redistributed from nodes that produce a lot of backup energy in the linear minimization case, like Bulgaria or France, to less active neighbors like Spain, Germany or Greece when going to the capped capacities (blue).

In order to compare the different flow paradigms, we look at the mismatch distributions before and after flow takes place. The two flow paradigms are compared by looking at their mismatch distribution and the dissipation they cause. The mismatch distribution approximates the probability density of the mismatch between generation and load. It is calculated before transmission

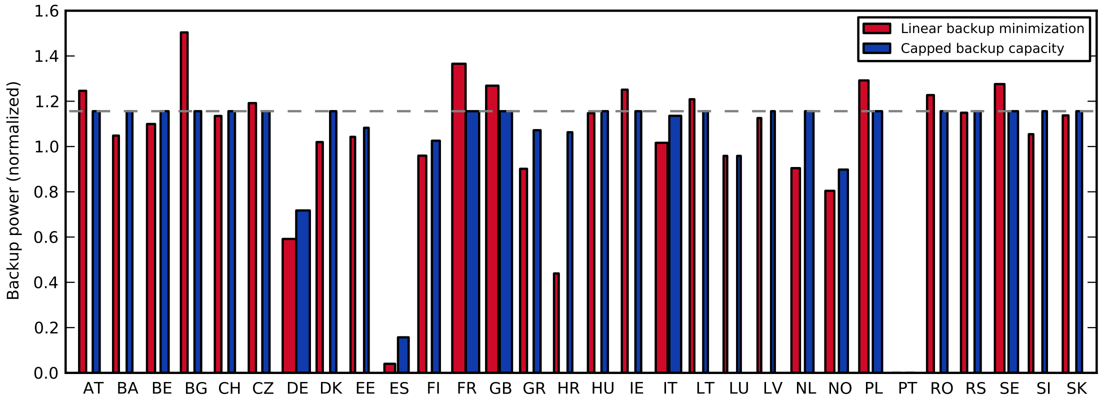

Figure 4.1: Backup distribution (dispatch) across the European countries with the linear backup minimization (red) and the capped backup capacities (blue), for one example hour in Dec 2002. Backup power is normalized with respect to mean load for each node separately. The dashed line indicates the capacity cap. Bar width grows with mean load (but is not to scale).

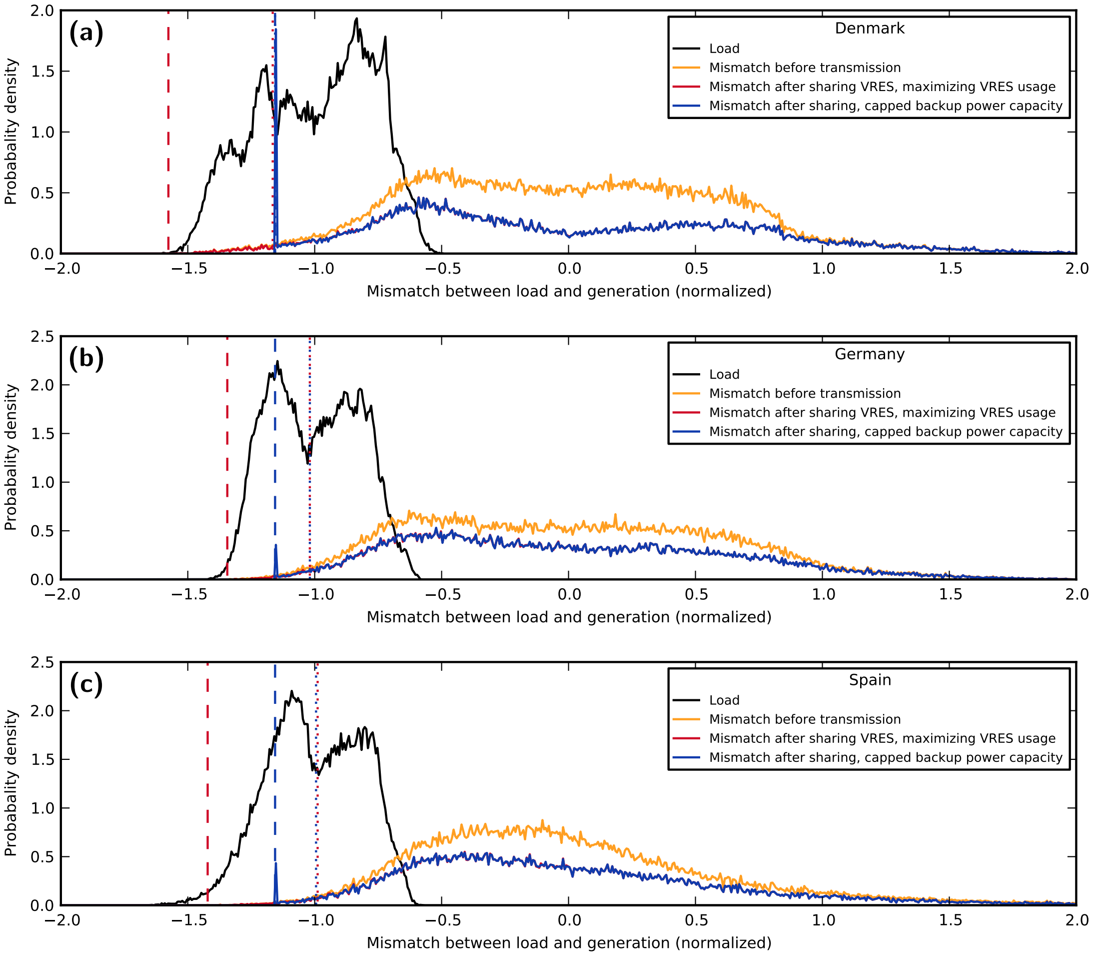

Figure 4.2: Distribution of load (black) and non-zero mismatches between load and renewable generation in (a) Denmark, (b) Germany, and (c) Spain before transmission (yellow), after transmission with the linear backup minimization (red), and after transmission with the capped backup capacities (blue). The dotted lines show the 99% quantiles of the deficits after transmission (which have to be covered by backup), and the dashed lines show the maximal deficit. Note that the vertical lines sometimes overlap, for instance in the case of Denmark where the blue dashed line coincides with the blue dotted line. The transmission grid is assumed to be strongly reinforced, with total capacity roughly sixfold of present (2011) total capacity, see main text for details.

takes place, and after transmission takes place with either the linear backup minimization or the capped backup capacities flow paradigm. The positive part of the mismatch after transmission is curtailed, and the negative part is what has to be covered by the backup system. The "loss of probability" (reduction of area under the probability density) going from the distributions before to those after transmission is actually shifted to a peak at zero which is left out in the plot because it would not fit in. The results are shown for the example cases of Denmark, Germany, and Spain in Fig. 4.2. It is apparent that the capped backup capacities (blue line) do not change much in most of the mismatch distribution with respect to linear backup minimization (red line). The lines overlap almost everywhere. The only difference is at large deficit events, when the backup system is strained. In these cases, the backup power cap makes itself felt, and backup events get cut down to the cap, leading to the peak in the mismatch distribution at around -1.2 times the average load and the lack of events below that. By contrast, the linear backup minimization does lead to a much longer tail in the backup needs, down to more than -1.5 times the average load in some cases.

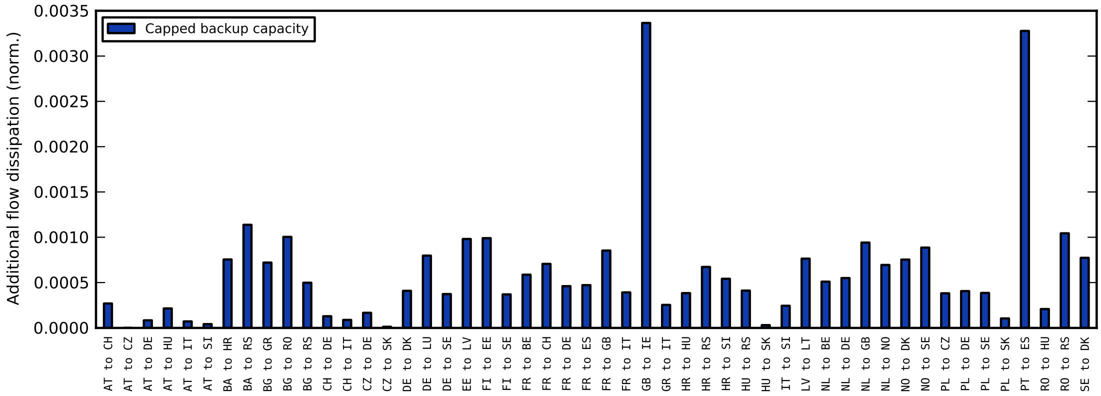

Figure 4.3: Additional flow dissipation as measured from F^2 values summed over the entire data period, for each link separately, for the capped backup capacities case, where finite backup capacities are assigned to each node. Flow dissipation is normalized, for each link separately, by the respective base case dissipation values, where only VRES usage is maximized. Shown is the normalized difference between the capped capacities and the base case. The strong 99% quantile transmission grid is assumed again, as in Fig. 4.2.

While capped backup capacities are able to reduce the maximal residual load after renewables and transmission considerably (compare the blue and the red dashed line in Fig. 4.2), it does not diminish quantiles of the backup distributions (dotted lines). To the contrary, the requirement to help neighbors in times of severe deficits may lead to more hours of running at the capacity limit, especially for small countries. In an energy system which is designed to serve demand under all circumstances, the backup caps would therefore be able to reduce installed backup capacity by about 25%, while in a system designed to meet a (high) quantile of the demand, they would not make a difference in required installed capacity.

Having now discussed the “benefits” of capped capacities in terms of reduced need for backup power, we turn to the “costs” of more transmission, namely the flow dissipation, which is proportional to the square of the flow. It is illustrated in Fig. 4.3. For each link, the total flow dissipation $\sum_t F_l(t)^2$ is calculated. It is normalized by the dissipation of the respective link in the base case. It turns out that the flow dissipation increases only minimally, even for the extreme cases of Portugal-Spain and Great Britain-Ireland by less than 3.5‰.

4.4.4 Generalized flow paradigms vs potential flow

In the case where transmission constraints are present, the generalizations of the DC power flow may lead to violations of Kirchhoff’s voltage law: It is in general not possible to find a set of phase angles at each node such that they act as a potential for the power flow along the links. Put differently, there is no set of phase angles that induce the flows that fulfill $\sum_{(i,j)\in\mathcal{P}} \delta_{ij} = 0 \mod 2\pi$ along all closed loops $\mathcal{P}$.

To see the discrepancy, consider this example in a very simple two-node network: Imagine a line between the two nodes with a thermal transmission limit of 5 units. If we were to build a second link alongside the other, with a transmission capacity of 1 unit, then the total transmission capacity would suddenly drop to 2 units: Since the two lines are assumed to be the same except for their total capacity, the power flow will always be the same on both lines, $F = B_{12}\delta_{12}$. There is only one phase difference to control the power flow. In this setting, the additional line counterintuitively diminishes the total power capacity. This is not, however, what would happen in our network model: We would minimize $F^T F = F^2_{\text{line }1} + F^2_{\text{line }2}$ under the constraints $|F_{\text{line }1}| \leq 5$, $|F_{\text{line }2}| \leq 1$, and can thus arrive at values larger than 2 for the total transmission between node 1 and 2.

This violation of the voltage law (which holds in a real AC power network) is, however, not as severe as it may seem at first sight. Firstly, our network model neglects control mechanisms of real world networks: For links between asynchronous regions or for sea cables, high voltage DC lines (HVDC) are used. It is proposed to use HVDC also for long-distance land lines to build a super grid overlay of the European power grid [100–102], because they do not suffer from the skin effect in AC lines and therefore can be thinner, and have fewer losses over long distances. HVDC lines are tunable according to external requirements, and could thus be used to realize flows as calculated here. Secondly, the networks to be considered here are "effective": Large regions are aggregated into single nodes, and likewise, a multitude of links between two countries are replaced by one effective link. The resulting additional degrees of freedom make it appear more plausible that power flow as calculated in this work is realizable.

4.4.5 Alternative: PTDF approach

As an alternative to the above quadratic minimization, it is also possible to include line constraints via the so-called PTDF (power transfer distribution factor) approach, see e.g. Refs. [103, 104]. In this case, the DC power flow is expressed directly in terms of the nodal power mismatches (rather than regarding the flows as the free variables). The constraints on transmission line flows are translated into constraints on nodal power dispatch: Combining Eqs. (4.2) ($F = K^T\delta$) and (4.5) ($\delta = E^+P$) with the usual substitutions when going from DC to AC[2], we see that the flow on a link can be expressed as

$$F = K^T E^+ P \equiv \mathrm{PTDF} \cdot P$$

The power flow can thus be expressed as a linear function of the nodal power mismatch after backup dispatch, P. The above constraint says that backup power dispatch must not happen in a way that would violate the transmission capacity constraints. Note, however, that if line impedances are considered, they appear in K and E, such that the PTDF depend on the impedances in a nonlinear fashion, thus transmission line upgrades have a nonlinear effect on the power flow distribution.

In this way, it is possible to include flow constraints into the combined backup dispatch and flow problem that we treated above. There is, however, more input necessary to determine the distribution of backup energy to the nodes, given the flow constraints, for instance a market model as used in Refs. [103, 104].

---

[2] voltage $U \leftrightarrow$ phase angle δ, nodal in/outflow $I \leftrightarrow$ nodal power in/outflow P, resistances $\leftrightarrow$ reactances

Chapter 5

Extensions of the electric transmission grid

In this chapter, extensions of the power transmission network are treated. First, the problem as it is understood here is stated in Sec. 5.1, and its general convexity is proven. Afterwards, two different transmission grid extensions are constructed: For the example case of Europe, a ramp-up of the transmission grid in parallel to the logistic growth of renewables introduced in Sec. 3.1.3 is considered in Sec. 5.2. For the contiguous US, a transmission grid for a fully renewable scenario is calculated by extensive optimization in Sec. 5.3. Finally, further ideas that did not turn out to be as fruitful are discussed in Sec. 5.4, and some alternative approaches in the literature are described in Sec. 5.5.

5.1 General problem

Transmission grids can be viewed from different perspectives: They enable energy exchange between different electricity markets for competition and cost-efficient dispatch, they combine renewable output from different regions to smooth it out and match it better to demand, and they reliably connect to backup power to provide security of supply [56, 57, 103, 105–120]. In the spirit of Ch. 4, we will focus on the reduction of backup energy here. As pointed out in Sec. 4.4.1, this simultaneously leads to maximal VRES usage.

In an indirect way, total backup B_{tot} is a function of the line capacity layout CL:[1]

$$B_{\text{tot}}(CL = \{h_{\pm l}\}_{l=1..L}) = \sum_{n,t} B_n(t) = \sum_{n,t} \left(\Delta_n(t) - \sum_l K_{nl} F_l(t) \right)_- \tag{5.1}$$

In this equation, the flows $F_l(t)$ are those calculated under the line capacity constraints of CL by the generalized DC power flow, see Eq. (4.12) in Sec. 4.4.1. Via this link, CL has an influence on B_{tot}. Line capacity additions can be constrained by already present capacity:

$$h_l \geq h_l^{(\text{today})} \tag{5.2}$$

Eq. (5.2) requires that the new capacity h_l of line l must be larger than its present capacity, $h_l^{(\text{today})}$. Considering the long lifetime of transmission lines of typically 50-70 yrs [14, 121], this is a reasonable approximation for medium-future scenarios. Grid extensions also come with investment costs, for which we use a simple approach:

$$C_{\text{tot}} = \sum_l C_l(h_l - h_l^{(\text{today})}) \tag{5.3}$$

---

[1] This sum is usually normalized in some way, either to an annual value or to a fraction of total load. Since both denominators are constant, this is irrelevant for the considerations in this section.

Eq. (5.3) is the total new investment C_{tot}, consisting of the sum of single line investments, expressed as individual line costs per unit of line transfer capacity C_l times new capacity $h_l - h_l^{(\text{today})}$. Depending on the chosen degree of modeling detail, C_l can be assumed the same for all lines, proportional to line length, or include further factors that mirror regional line differences (e.g. the difference between synchronous and asynchronous AC grid interconnections).

5.1.1 Benefit of transmission

The benefit of transmission for backup reduction can be quantified like this: Let CL be some arbitrary capacity layout. The two extreme cases are a zero capacity layout CL_{zero}, where all transmission capacities are set to zero, and an unconstrained layout $CL_{\text{unconstrained}}$, where the transmission capacities are determined from what is necessary for unimpeded flow. The relative benefit of transmission $\beta(CL)$ of a generic layout CL can then be expressed as the reduction of backup achieved by installing CL, divided by the maximum possible benefit of transmission, which is obtained when switching from CL_{zero} to $CL_{\text{unconstrained}}$:

$$\beta(CL) = \frac{B_{\text{tot}}(CL_{\text{zero}}) - B_{\text{tot}}(CL)}{B_{\text{tot}}(CL_{\text{zero}}) - B_{\text{tot}}(CL_{\text{unconstrained}})} \,. \tag{5.4}$$

Here, B_{tot} denotes the sum of all backup energy for all nodes and all hours (Eq. 5.1). By construction, the relative benefit of transmission is zero for a zero capacity layout, and it is one for an unconstrained capacity layout.

5.1.2 Convexity of backup energy with respect to capacity layout

In the following sections, transmission grid extensions will be constructed explicitly. The questions asked are: Given a certain desired benefit of transmission, how much new line capacity is at least necessary, and where should it be placed? Or a slight variation: Given a certain total investment in new capacity (in terms of money or total additional line capacity), how should it be distributed to achieve the largest benefit of transmission? In formulas, the first question is equivalent to minimizing the costs of additional capacity from Eq. (5.3) while keeping the line benefit (5.4) constant. The second question translates into maximizing transmission benefit (5.4) while keeping investment (5.3) constant. Both optimizations may be subject to the constraint of no line capacity dismantling, Eq. (5.2). Since convex optimizations are much more easy to handle and much more likely to succeed (see Sec. 4.1 and App. A), it is very interesting whether or not these problems are convex. Eqs. (5.2) and (5.3) contain linear expressions and are therefore convex (see Sec. 4.1.1), but it is harder to decide for the benefit of transmission (5.4).

First of all, since $B_{\text{tot}}(CL)$ is the only CL-dependent term in Eq. (5.4), it is easily seen that maximizing the benefit of transmission $\beta(CL)$ is equivalent to minimizing total backup energy $B_{\text{tot}}(CL)$ (Eq. 5.1). It is therefore sufficient to prove that $B_{\text{tot}}(CL)$ is a convex function of CL. What needs to be shown is that if there are two capacity layouts, $CL^{(1)} = \{h_{\pm l}^{(1)}\}_{l=1..L}$ and $CL^{(2)} = \{h_{\pm l}^{(2)}\}_{l=1..L}$, the total backup energy fulfills

$$B_{\text{tot}}\left(\lambda CL^{(1)} + (1-\lambda)CL^{(2)}\right) \leq \lambda B_{\text{tot}}(CL^{(1)}) + (1-\lambda)B_{\text{tot}}(CL^{(2)})$$

for all $\lambda \in [0,1]$ and CL is interpreted as a vector with components $h_{\pm l}$. Now, for each hour in the time series, we get a certain flow vector from the generalized DC flow described in Sec. 4.4.1. Let $F^{(1)}$ and $F^{(2)}$ denote the flows resulting for $CL^{(1)}$ and $CL^{(2)}$, respectively. By construction, they minimize backup energy for their respective capacity layouts. Since the flows also satisfy their respective flow capacity constraints and $\lambda, (1-\lambda) \geq 0$, we have on each link l, for all hours t:

$$\begin{aligned} \lambda h_{-l}^{(1)} &\leq \lambda F_l^{(1)}(t) && \leq \lambda h_{+l}^{(1)} \\ (1-\lambda) h_{-l}^{(2)} &\leq (1-\lambda) F_l^{(2)}(t) && \leq (1-\lambda) h_{+l}^{(2)} \\ \Rightarrow \lambda h_{-l}^{(1)} + (1-\lambda) h_{-l}^{(2)} &\leq \lambda F_l^{(1)}(t) + (1-\lambda) F_l^{(2)}(t) && \leq \lambda h_{+l}^{(1)} + (1-\lambda) h_{+l}^{(2)} \end{aligned} \tag{5.5}$$

Because of inequality (5.5), we can conclude that the convex combination of capacity layouts is at least able to accommodate the convex combination of the corresponding flows, which we denote

$$F^{(\lambda)}(t) \equiv \lambda F^{(1)}(t) + (1-\lambda) F^{(2)}(t) \,.$$

In other words, $F^{(\lambda)}(t)$ is a feasible point for the backup energy minimization with the combined capacity layout $CL^{(\lambda)} \equiv \left(\lambda CL^{(1)} + (1-\lambda) CL^{(2)}\right)$ with entries $h_{\pm l}^{(\lambda)} \equiv (\lambda h_{\pm l}^{(1)} + (1-\lambda) h_{\pm l}^{(2)})$ at time t. For the total backup energy $B_{\text{tot}}^{(\lambda)}(t)$ in hour t, this means:

$$\begin{aligned}
B_{\text{tot}}^{(\lambda)}(t) &= \min_{\{F \mid h_{-l}^{(\lambda)} \le F_l \le h_{+l}^{(\lambda)} \, \forall l\}} \sum_n \left\{ \Delta_n(t) - (KF)_n \right\}_- \\
&\le \sum_n \left\{ \Delta_n(t) - (KF^{(\lambda)}(t))_n \right\}_- \qquad (5.6) \\
&= \sum_n \left\{ \Delta_n(t) - \left[K(\lambda F^{(1)}(t) + (1-\lambda) F^{(2)}(t)) \right]_n \right\}_- \\
&= \sum_n \left\{ \lambda \left[\Delta_n(t) - (KF^{(1)}(t))_n \right] + (1-\lambda) \left[\Delta_n(t) - (KF^{(2)}(t))_n \right] \right\}_- \\
&\le \lambda \sum_n \left\{ \Delta_n(t) - (KF^{(1)}(t))_n \right\}_- + (1-\lambda) \sum_n \left\{ \Delta_n(t) - (KF^{(2)}(t))_n \right\}_- \qquad (5.7) \\
&= \lambda \sum_n B_n^{(1)}(t) + (1-\lambda) \sum_n B_n^{(2)}(t) \\
&= \lambda B_{\text{tot}}^{(1)}(t) + (1-\lambda) B_{\text{tot}}^{(2)}(t) \\
\Rightarrow B_{\text{tot}}^{(\lambda)}(t) &\le \lambda B_{\text{tot}}^{(1)}(t) + (1-\lambda) B_{\text{tot}}^{(2)}(t) \qquad (5.8)
\end{aligned}$$

The first inequality (5.6) is clear – the minimum over all feasible flows is smaller or equal to the value for any given feasible flow. Physically speaking, this reflects that the combined capacity layout may be able to accommodate a flow reducing backup energy more than $F^{(\lambda)}(t)$, because $F_l^{(1)}(t)$ and $F_l^{(2)}(t)$ may have opposite signs for some l, or because new paths through the network can open up due to some links being only present in $CL^{(1)}$ and others only in $CL^{(2)}$. This (potential) additional freedom can be used to reduce the backup energy of the combined layout further in the backup minimization step of the flow calculation. The second inequality (5.7) is justified because the negative part of a sum is potentially reduced by cancellations (one summand is positive, one negative), which are not possible when the negative parts are taken separately. This argument is valid for each n separately, and therefore also for the sum over all n.

As inequality (5.8) holds for all hours t, it also holds for the sum over all hours,

$$\begin{aligned}
B_{\text{tot}}\left(\lambda CL^{(1)} + (1-\lambda) CL^{(2)}\right) &= \sum_t B_{\text{tot}}^{(\lambda)}(t) \\
&\le \sum_t \lambda B_{\text{tot}}^{(1)}(t) + (1-\lambda) B_{\text{tot}}^{(2)}(t) = \lambda B_{\text{tot}}(CL^{(1)}) + (1-\lambda) B_{\text{tot}}(CL^{(2)}) \,, \qquad (5.9)
\end{aligned}$$

which is what we wanted to show.

If other constraints are present in the flow calculation, like the backup power capacity cap introduced in Sec. 4.4.2, one needs to ascertain that the convex sum $F^{(\lambda)}(t)$ fulfills the additional constraint (= is a feasible flow vector for the modified problem) if $F^{(1)}(t)$ and $F^{(2)}(t)$ are feasible. If that holds true, the proof works in the same way as above. In the example of backup capacity caps, this is indeed the case: The need for backup $b_n^{(\lambda)}(t)$[2] at node n if $F^{(\lambda)}(t)$ is realized does not

---

[2] b_n instead of B_n because this is the backup need for some flow and not for the flow minimizing total backup energy.

exceed the capacity cap $A\langle L_n\rangle$ from constraint (4.16).

$$\begin{aligned} b_n^{(\lambda)}(t) &= \left\{\Delta_n(t) - (KF^{(\lambda)}(t))_n\right\}_- \\ &= \left\{\lambda\left[\Delta_n(t) - (KF^{(1)}(t))_n\right] + (1-\lambda)\left[\Delta_n(t) - (KF^{(2)}(t))_n\right]\right\}_- \\ &\leq \lambda\left\{\Delta_n(t) - (KF^{(1)}(t))_n\right\}_- + (1-\lambda)\left\{\Delta_n(t) - (KF^{(2)}(t))_n\right\}_- \\ &= \lambda B_n^{(1)}(t) + (1-\lambda)B_n^{(2)}(t) \\ &\leq \lambda A\langle L_n\rangle + (1-\lambda)A\langle L_n\rangle = A\langle L_n\rangle \end{aligned}$$

The steps in this calculation work in much the same way as above in the convexity proof. The last inequality holds because the backup energies $B_n^{(1)}(t)$ and $B_n^{(2)}(t)$ result from feasible flows that comply with the backup power cap $A\langle L_n\rangle$.

5.2 Europe: Quantile method

For Europe, we are interested in the transmission grid build-up in parallel with the logistic growth of renewable installations introduced in Sec. 3.1.3. We study first how backup energy evolves for two fixed layouts, the no transmission layout CL_{zero} and today's layout CL_{today}, then compare what happens if transmission is unconstrained and construct the corresponding layout $CL_{\text{unconstrained}}$, and finally move to two smaller layouts that yield a constant benefit of 70 % and 90 %, $CL_{70\,\%}$ and $CL_{90\,\%}$. Since the demand for international transmission grows with growing share of renewables, the latter three layouts are time-dependent. The network topology employed is shown in Fig. 5.1.

5.2.1 Time dependence of backup energy for two fixed transmission layouts

We first focus on the single country backup optimal mix, i.e. the base scenario introduced in Secs. 2.5.2 and 3.1.3. The impact of different end-point mixes will be discussed in Sec. 6.4. The first two transmission layouts we investigate are constant in time:

1. CL_{zero} – Zero transmission.
2. CL_{today} – Today's transmission layout: Net transfer capacities as of winter 2010/2011 from ENTSO-E, plus the three new links BritNed, NorNed, and SwePol [99, 122–124].

The resulting normalized backup energies for the single countries Denmark, Germany, Spain, and France are shown in Figs. 5.2, in dark red for CL_{zero} and in red for CL_{today}. For each reference year, the annual backup energy has been averaged over the available 8 years of weather and load data. Backup needs rise quite steeply for the case of no power transmission, until it amounts to about 25 % of the average load in 2050. This is mitigated slightly if line capacities as of today are assumed. As discussed in more detail in Sec. 5.2.4, single countries show different intermediate behavior due to different trade opportunities. The corresponding figure for all of Europe is Fig. 5.3a, where backup for CL_{zero} and CL_{today} is shown also in dark red and red, respectively. Fig. 5.3b illustrates the relative benefit of transmission for today's capacity CL_{today}. It decreases with progressing reference years and converges from above to about $\beta(CL_{\text{today}}) = 0.34$ for the final reference years.

For comparison, Fig. 5.3a also shows the theoretical minimum value for backup as a thin, gray line. This would be obtained if the entire VRES production could be used to cover the load, i.e. if no excess production occurred. In this case, only a fraction of $(1 - \gamma_{\text{avg.}}(t)) = (1 - \sum_n \gamma_n(t)\langle L_n\rangle/\langle L_{EU}\rangle)$ of the total load needs to be covered from backup. It can be seen that the backup needs of CL_{zero} depart already before 2030 from this optimal line, while CL_{today} follows the optimum up to 2030.

5.2.2 Maximum reduction of backup energy for the time-dependent unconstrained transmission layout

The next transmission layout is chosen to be:

3. $CL_{\text{unconstrained}}$ – Unconstrained transmission.

It is possible to a posteriori associate a finite line capacity layout to unconstrained transmission, simply by setting the link capacities to the maximum value of the flow that is observed during the eight years of data, see Fig. 5.4a. Detailed numerical values can be found in Tab. C.3. Since in this layout a single hour's flow determines the capacity of a link, it sometimes happens that these capacities drop from one reference year to the next for single links. This would correspond to a downgrade of an already built link, which is unrealistic. Such artifacts have therefore been removed, making the single links' capacities monotonously increasing in reference year by keeping them at least at the levels reached in previous years.

To see the effect of this layout on backup energy, we look again at Figs. 5.3a (green line) and 5.2 (orange area). We see that in Fig. 5.3a, backup energy follows the theoretical minimum (gray line)

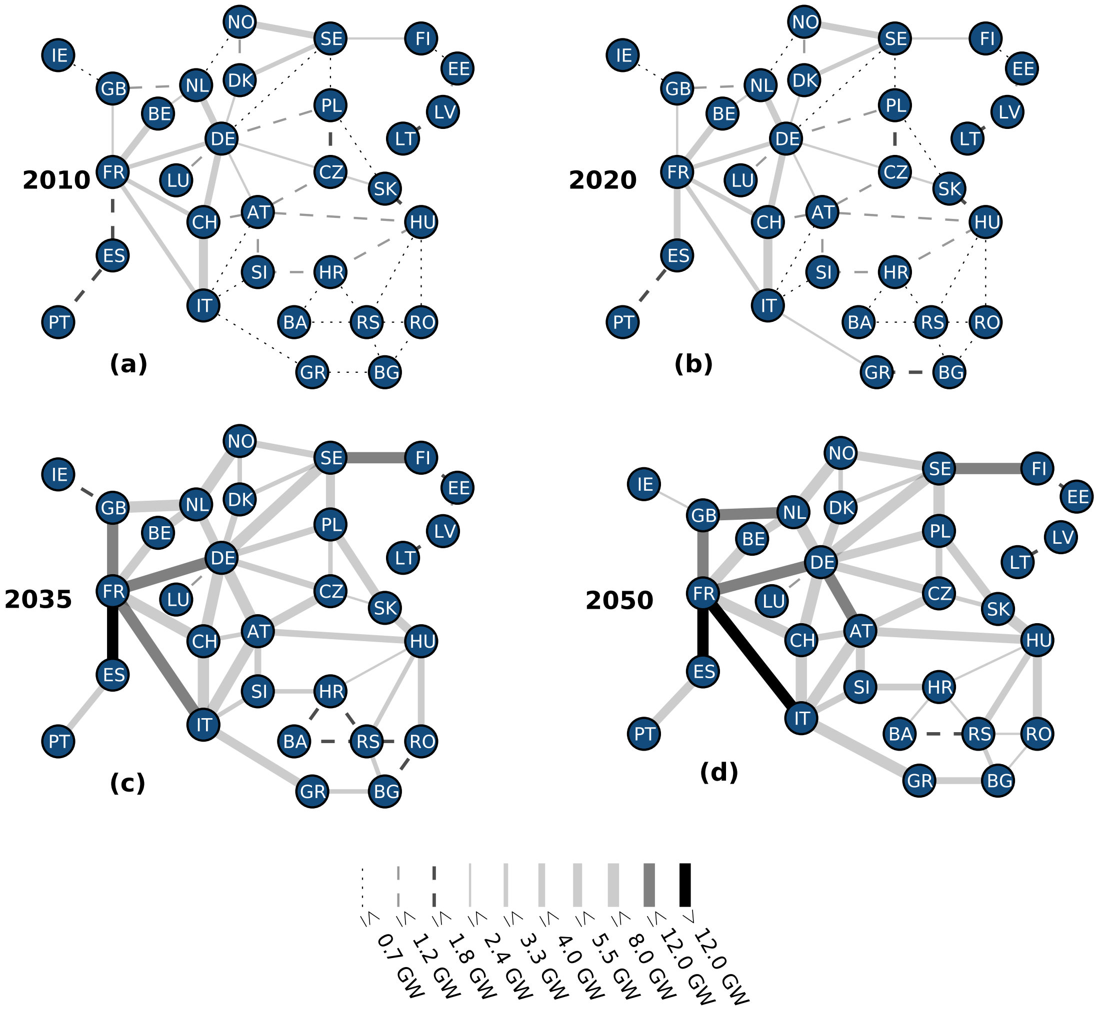

Figure 5.1: Network topology and strength as used in our model: (a) present layout (winter 2010/2011) as reported by ENTSO-E plus the three new links GB-NL, NO-NL, and SE-PL [99, 122–124], (b)-(d) development of the 90 % benefit of transmission line capacities (see Sec. 5.2.3) for the years 2020, 2035, and 2050. Line style and thickness represents the larger one of the two net transfer capacities of each link. Line lengths and node sizes are not to scale.

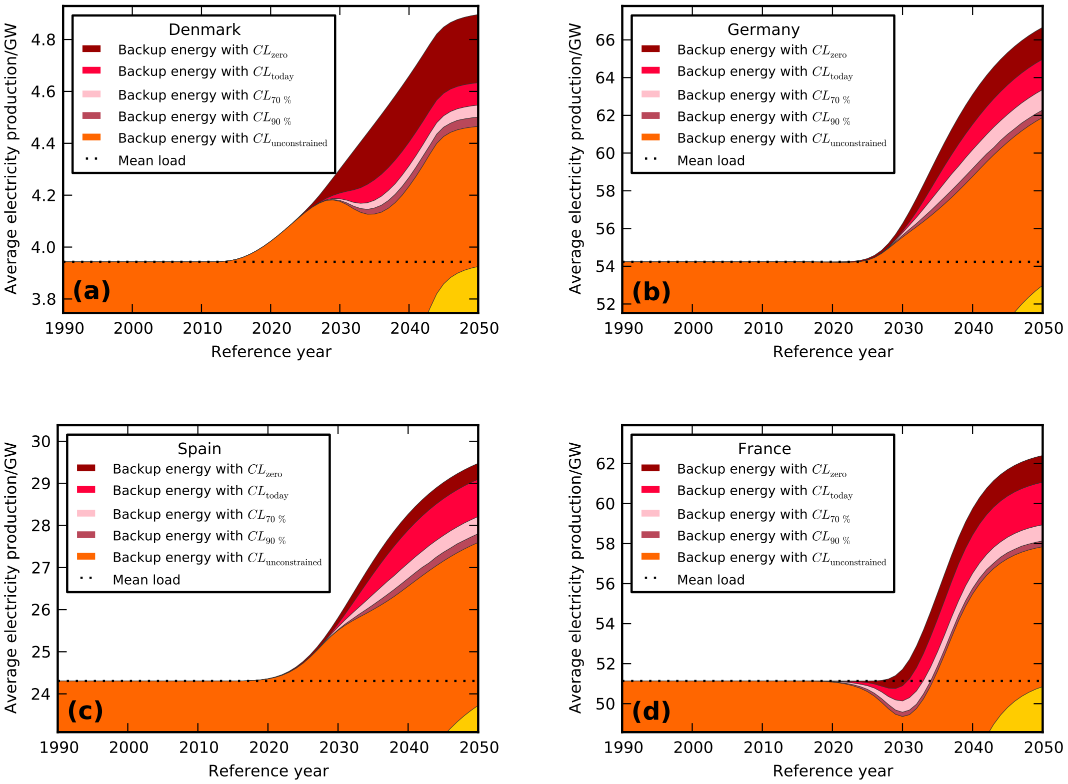

Figure 5.2: Average backup energy generation on top of wind and solar PV generation, for (a) Denmark, (b) Germany, (c) Spain, and (d) France. These plots are zooms into the upper right corner of Figs. 3.3, with backup energies shown for all transmission capacity layouts CL_{zero}, CL_{today}, $CL_{70\,\%}$, $CL_{90\,\%}$, and $CL_{\text{unconstrained}}$. The yellow bottom right corner is the top of the solar PV generation part, cf. Figs. 3.3. For details on the transmission layouts, see Secs. 5.2.1-5.2.3. Shown is the base scenario, where the single country backup optimal mix is reached in 2050. The conversion from the shares of wind, solar PV, and backup to average generation in GW is done using the 2007 load.

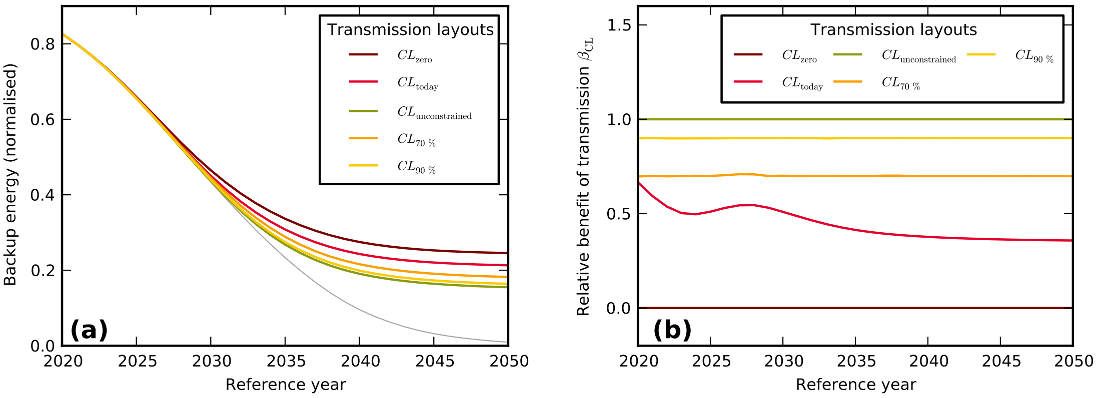

Figure 5.3: (a): Backup energy vs. reference year for the various transmission layouts in the base scenario. Note how the backup is reduced by 70 % ($CL_{70\,\%}$) or 90 % ($CL_{90\,\%}$) of what is achievable by suitable transmission grid extensions (see Sec. 5.2.3). This is also visible in panel (b), where the relative benefit of transmission is shown, cf. Eq. (5.4). In panel (a), the thin gray line shows the theoretical minimum backup energy in each reference year, i.e. the average normalized load minus the average VRES penetration γ. Backup energy is normalized by the mean load.

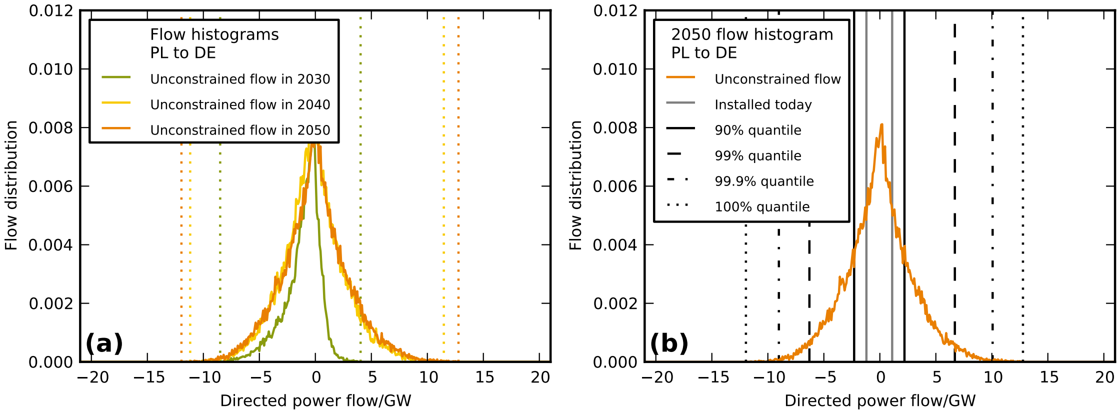

Figure 5.4: (a): Distributions of the unconstrained flow across the link between Germany and Poland for the years 2030, 2040 and 2050. Only non-zero flows are shown. The corresponding unconstrained line capacity layouts are assigned by setting the capacity of a given link to the maximum value that occurs in the unconstrained flow during the eight year data time series (dotted vertical lines). These values can be found in the last four columns of Tab. C.3. (b): 2050 unconstrained flow for the same link, with (direction specific) quantiles. The e.g. 90 % quantiles is obtained from what is necessary for unimpeded flow for 90 % percent of all hours, separately for positive flows (from Poland to Germany) and negative flows (from Germany to Poland).

about five years longer than CL_{zero}, up to about 2032. Additionally, it is able to reduce the final backup needs considerably, by about 40 % of its value at zero transmission. It cannot, however, reduce backup energy down to zero: Power transmission is only able to match surpluses at some nodes with deficits at others. If there is a global deficit across all of Europe, backup energy is needed no matter how strong the transmission grid. In Fig. 5.2d, it is seen that backup for France drops temporarily such that combined own VRES generation and own backup become lower than the average load. This is due to imports of VRES and will be discussed in more detail in Sec. 5.2.4.

Figs. 5.5 show in green the total necessary line upgrades to obtain $CL_{\text{unconstrained}}$. Fig. 5.5a depicts the total line capacities that need to be installed, and Fig. 5.5b shows the increments per five-year interval. For calculating the total transmission capacity, the larger one of the two NTC values of each link is used as a proxy to its physical capacity. These yield a sum of approximately 74 GW for the total line capacities installed today. The necessary total line capacities are plotted as multiples of this number. It is seen that line capacities for $CL_{\text{unconstrained}}$ would amount to almost twelve times of today's installation in the end, and require a top installation speed of roughly adding today's installation each year between 2025 and 2030.

5.2.3 Two compromise transmission layouts

While the absence of new line investment of the two fixed CL_{zero} and CL_{today} makes them attractive, they lead to large backup needs. Backup needs are considerably reduced by the unimpeded power exchange of the unconstrained $CL_{\text{unconstrained}}$. This, however, requires huge investments in reinforced transmission lines. The idea is now to choose a line capacity layout which yields a certain reduction of backup needs while keeping new line investments in a reasonable range.

Two new proposed compromise transmission layouts are:

4. $CL_{70\,\%}$ – 70 % benefit of transmission capacities: For all links, fix a quantile of the unconstrained 2050 flows as transmission capacity (cf. Fig. 5.4b), such that 70 % of the relative benefit of transmission is harvested (cf. yellow lines in Figs. 5.3).
5. $CL_{90\,\%}$ – 90 % benefit of transmission capacities: Analogously to 70 % benefit of transmission capacities.

There are a multitude of possible interpolations between zero transmission and unconstrained transmission that lead to the same desired backup energy reduction and benefit of transmission as

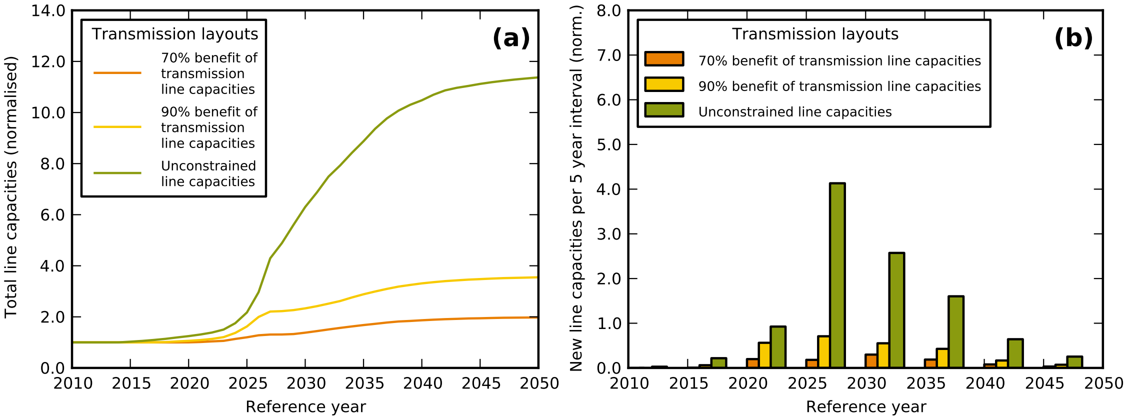

Figure 5.5: (a): Growth of total installed line capacity for the three time-dependent line capacity layouts unconstrained transmission ($CL_{\text{unconstrained}}$), 70 % benefit of transmission ($CL_{70\,\%}$), and 90 % benefit of transmission ($CL_{90\,\%}$). It is seen that $CL_{\text{unconstrained}}$ requires a final installation of almost twelve times of what we have today, $CL_{70\,\%}$ about twice as much, and $CL_{90\,\%}$ a little less than four times as much. (b): Five-year increment of line installations for the same three layouts. In both panels, the total installation is normalized by the installation of today (see Sec. 5.2.2 for details).

depicted in Fig. 5.3. We choose the quantiles of the corresponding end-point (2050) unconstrained flow distribution. These are calculated by first solving the generalized DC power flow as described in Sec. 4.4.1, without the constraint $h_{-l} \leq F_l \leq h_l$, for all hours in the time series. This yields time series for the unconstrained flows on each link, which are binned in a histogram, see Figs. 5.4 for examples. It has been observed that these unconstrained distributions generally peak around zero and have broad convex tails, such that a fraction of the line capacity that would be necessary to enable the maximal unconstrained flow is sufficient to let the flow pass through unimpededly most of the time. The Quantile capacities are obtained by taking a certain quantile of the unconstrained flow in each direction, for each of the links. In terms of backup energy reduction, these have been shown to perform much better than, for instance, global scaling of current line capacities [53].

We work with quantiles of the unconstrained end-point (2050) flows. In contrast to using quantiles of the unconstrained flow of the reference year under consideration, this approach allows us to consistently build up the capacity layout that is actually needed in the end. The so obtained quantile line capacities are further modified: They are capped by the unconstrained capacities of the corresponding years in order to avoid a premature installation of lines that are not used immediately. Furthermore, $CL_{70\,\%}$ and $CL_{90\,\%}$ start from today's NTCs, that is, no dismantling of existing lines is assumed, as expressed in Eq. (5.2).

The total transmission line capacities required to obtain the 70 % and 90 % benefit of transmission and the amount of new installations per five year intervals are shown in Figs. 5.5. In addition, the capacity of each single link in the years 2020, 2030, 2040, and 2050 in the base scenario for the year-dependent line capacity $CL_{\text{unconstrained}}$, $CL_{70\,\%}$, and $CL_{90\,\%}$ can be found in Tab. C.3. The build-up of $CL_{90\,\%}$ is also illustrated in the network plots of Figs. 5.1. About two and four times as much as what is installed today is needed to harvest 70 % and 90 % of the possible benefit of transmission, respectively. Both schemes seem within reach. For single links, the 90 % benefit layout agrees nicely with the results of [101], which finds e.g. a line capacity of 19.5 GW between Spain and France for the fully renewable stage, compared to 17.3 GW found in our base scenario. For the link between France and the UK, they report a final capacity 6 GW, while we find 11.9 GW. But this is due to the different grid topology they use, which includes an additional link from Great Britain to Norway with a capacity of 3.5 GW, and a substantial offshore grid in the North Sea with a total capacity of 16.5 GW.

Notably, the build-up in line capacities has to start no later than 2020 if the desired 70 % or 90 % benefit of transmission is to be harvested throughout the years. We have to keep in mind that the absolute reduction in backup is small in the beginning (cf. Fig. 5.3), such that the total losses from not building the lines would be small at first. But, as backup needs grow, the need for

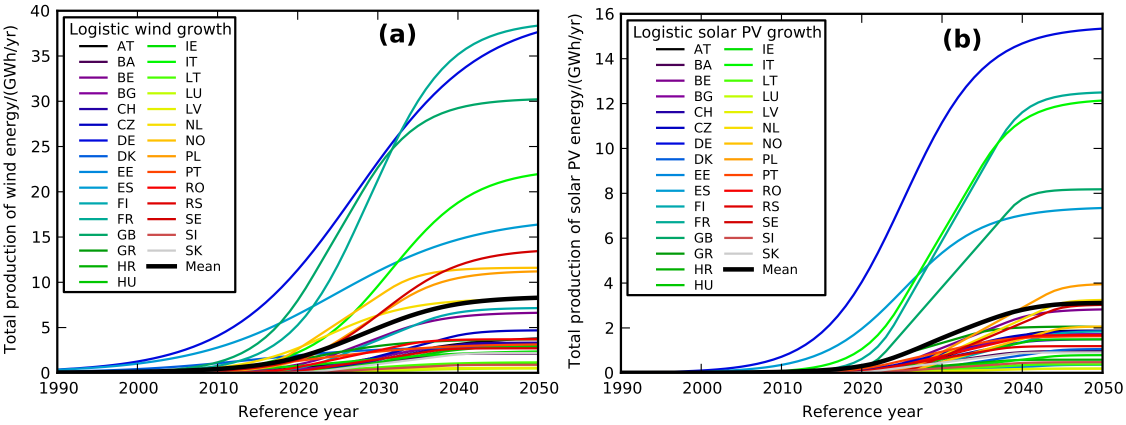

Figure 5.6: (a) Plot of all logistic fits of wind growth curves for the base scenario (single country backup-minimal mix). (b) Same for solar PV.

transmission capacity quickly increases. So it would be advisable to start the line build-up as soon as possible.

We take a combined look at Tab. C.2 and Figs. 5.3, 5.5 and 5.6. Fig. 5.6 and Tab. C.2 show that the main part of the wind installation growth takes place 2015-2035, while solar PV installations are a little later, about 2020-2040. The main transmission investments take place in parallel with the largest renewable build-up, during 2020-2035, when both of them are installed. Fig. 5.3a shows an interesting feature: The onset of additional backup energy beyond the minimum of $(1-\gamma_{\text{avg.}})$ times the average load can be postponed by five years with a strong transmission grid. In order to achieve this, the main transmission line growth has to happen from 2025 to 2030, leading to the peak in new installations seen in Fig. 5.5b at that time.

5.2.4 Import and export opportunities

It is possible to investigate the effects of a strong transmission network on the import and export opportunities of single countries. We only consider trade with VRES since other forms of electricity generation are not treated explicitly in our model. There are roughly three coordinates which determine export and import opportunities of a country, namely the size of its mean load, its position in the network (central or peripheral) and the time of transition to VRES with respect to its neighborhood. Let us take a closer look at each of them.

Load size A country's load size influences the ratio of imported or exported energy to its deficit or surplus. A country with a high absolute load will experience high deficit as well as high excess. If its neighbors have a substantially smaller load, they will in most cases neither be able to absorb a large excess nor cover a large deficit. This means that the fraction of the deficit that can be covered by imports and the fraction of the excess that can be exported is smaller the larger a country's load. There is a negative correlation between exchange opportunities, measured as the fraction of deficit that can be covered by imports, or the fraction of excess that can be exported, and country load size, see Figs. 5.7a and d, which becomes more pronounced as renewable shares grow towards late reference years.

This effect is mitigated by spatial smoothing effects both on load and on renewable generation that are experienced in large countries, reducing their deficit (excess) before transmission takes place.

Position The position of a country in the network is another factor that influences its trade opportunities. This point is a little more subtle and partly due to our power flow modeling which minimizes the overall flow in the network. Neglect for a moment restricted transmission line capacities. Imagine a situation where some countries are in deficit and some are in excess, such that there is an overall shortage. The question is now which of the countries with a deficit receives the excess from those which see a surplus production. In a specific situation, the answer depends on the details of the distribution of excess and deficit in the network, but on average, transport of energy to a remote country causes flow across more links than to a central country, such that the central country will be preferred by the dissipation minimization, Eq. (4.12b). The same goes for a situation where there is global excess, and some countries in deficit: Central countries have a higher chance of exporting than peripheral ones, because this will on average cause less flow. Taking now limited transmission capacities into account, the situation is accentuated: A lot of flow to or from peripheral countries is not only suppressed by the flow minimization, but may be altogether impossible.

As a proxy for node position in the network, the betweenness centrality of each node in the network is calculated. It is defined as the fraction of shortest paths between all possible node pairs which pass through the node under consideration. The correlation of betweenness centrality to exported (imported) fraction of excess (deficit) is shown in Figs. 5.7b and e. It is very noisy, but slightly positive for exports for all transmission layouts, while there is no clear trend for imports.

Time of transition The transition at different times in different countries has some interesting effects. Whether it occurs early or late in a country does not have an effect on the end-point import/export capabilities, but becomes important during the transition. If the transition in a country takes place early, it experiences deficit and excess situations earlier than its neighbors. For the first years, this means that in case of a deficit, neighbors are probably not able to export anything because they do not see VRES excesses yet. On the other hand, because VRES generated electricity is shared wherever possible, if the early country has a surplus production, it can almost certainly export it to later neighbors, where it replaces their backup. In short, an early transition may mean poor import opportunities, but on the other hand good export opportunities during the first years. These differences are subsequently diminished as all countries switch to VRES-based electricity supply, and then size and position become the dominant factors determining import and export opportunities.

The correlation between exported (imported) excess (deficit) fraction and transition time is shown in Figs. 5.7c and f. The transition time is measured as the year in which a country's renewable gross share exceeds $\gamma_n = 0.5$. For unconstrained transmission, $CL_{\text{unconstrained}}$, there is a clear indication of an export boom during the reference years until 2040. This effect is smaller for the three constrained layouts. The imported deficit fraction starts out with a negative correlation to transition time around 2025, but then quickly becomes positive.

In the reference year 2050, all countries reach a VRES gross share of (almost) $\gamma = 1$. As shown in [53], even unlimited transmission can reduce the total backup in Europe by only 40 % in the $\gamma = 1$ case, due to the spatio-temporal correlations in the weather. This implies that in 2050, only 40 % of the total deficit can be covered by imports and equally only 40 % of the total excess can be exported. This statement is valid for the load-weighted average over all countries. Single countries see deviations due to their position and load size as explained above.

These findings are further illustrated when looking at mismatch histograms for the three example countries Denmark, Spain, and France, Figs. 5.8, 5.9, and 5.10. They fall into different classes which arise from the large – small, central – peripheral, early – late distinctions. For the influence of load size, compare the situation in France and Denmark in 2050, Figs. 5.8b and 5.10b. The mismatch before sharing renewables (yellow curves) is comparable, since it is normalized by the mean load in both cases. After sharing with the strong 90 % benefit of transmission capacity layout (blue curves), Denmark's residual mismatch is much smaller than the German one. The correlation between load size and fraction of the surplus that can be exported/fraction of the deficit that can be imported (Fig. 5.7a and d) shows that this is not just an accident, but a general trend.

The effect of position in the network is well illustrated when comparing Spain (Fig. 5.9b) and Denmark (Fig. 5.8b), and looking again at mismatch before (yellow) and after sharing with the strong transmission layout (blue). Again, we see that Spain's reduction is smaller than Denmark's.

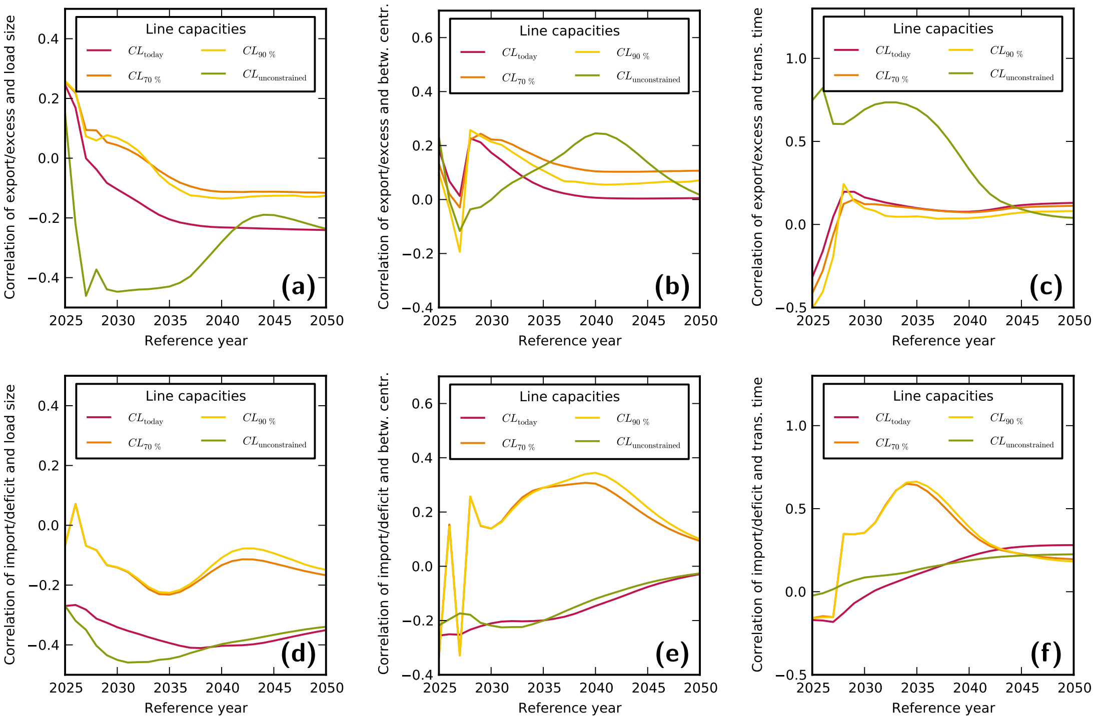

Figure 5.7: The ratio of the deficit that can be covered by imports, or the excess that can be exported, depends on several factors, as described in the main text. Here, the correlations between the fraction of the excess (deficit) that can be exported (imported) and load size, network position, and time of transition to renewables are shown. For each reference year, the exported (imported) fraction of the excess (deficit) is retrieved for each node, and the correlation between exported (imported) fraction and nodal load size, time of transition (year in which γ_n exceeds 50 %), and network betweenness centrality are calculated, yielding a yearly value of the correlation. This is done for all non-zero transmission layouts, CL_{today}, $CL_{70\,\%}$, $CL_{90\,\%}$, and $CL_{\mathrm{unconstrained}}$. (a) – correlation between exported fraction and load size, (b) – correlation between exported fraction and network betweenness centrality, (c) – correlation between exported fraction and time of transition, (d) – correlation between imported fraction and load size, (e) – correlation between imported fraction and network betweenness centrality, and (f) – correlation between imported fraction and time of transition. Correlation between two quantities X and Y is understood here as the Pearson r coefficient, calculated as $r = \frac{\sum_n (X_n - \overline{X})\cdot(Y_n - \overline{Y})}{\sigma_X \sigma_Y}$, where $\overline{x}$ denotes the mean of a quantity x and σ_x its standard deviation. The sum is over the $N = 30$ nodes of the network. X can stand for the imported fraction of deficit or the exported fraction of excess (in a given reference year) and Y stands for load size, betweenness centrality, or time of $\gamma_n = 0.5$ (reference year-independent). As the correlations are calculated with relatively few data points (only one network with 30 nodes), noisy behavior is to be expected and can be observed in these figures, especially for early years.

The early export boom in Denmark and Spain can be guessed from the almost complete elimination of the surplus production tail by exports in 2030 (Fig. 5.8a and 5.9a).

There are other general observations from the mismatch histograms, Fig. 5.8-5.10. One is that transmission is able to reduce the bulk of the mismatch, roughly the region between −1 times the average load and +1 times the average load. Here, enhanced transmission clearly leads to fewer mismatch events. However, the tails of the distributions are almost unaffected. This corresponds to a reduction of mismatch energy by transmission (which we calculated above to be at most 40 % of the total mismatch energy in a fully renewable scenario), but not so much of the "mismatch power capacity". From these plots, it seems that large surplus as well as large deficit events hit Europe more or less synchronously, thus preventing the countries from smoothing the mismatch out by distributing it geographically. This effect can be mitigated to some extend by sharing not only VRES generation, but also backup and possibly surplus energy. The capped backup capacities

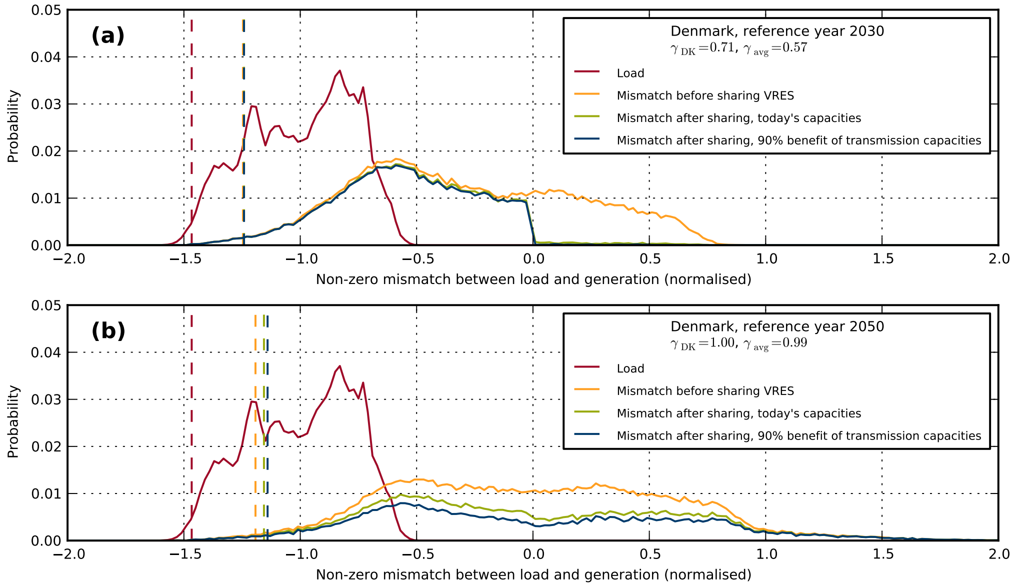

Figure 5.8: Distribution of the load (red), distribution of the mismatch between renewable generation and load before power sharing takes place (yellow), after sharing takes place with today's line capacities (green), and after sharing takes place with the 90 % benefit of transmission line capacities (blue), for the years 2030 (a) and 2050 (b), for Denmark. The dashed lines indicate the 99 % quantile of the residual deficit. For clarity, the peak at zero is not shown here. Some of the lines cover each other.

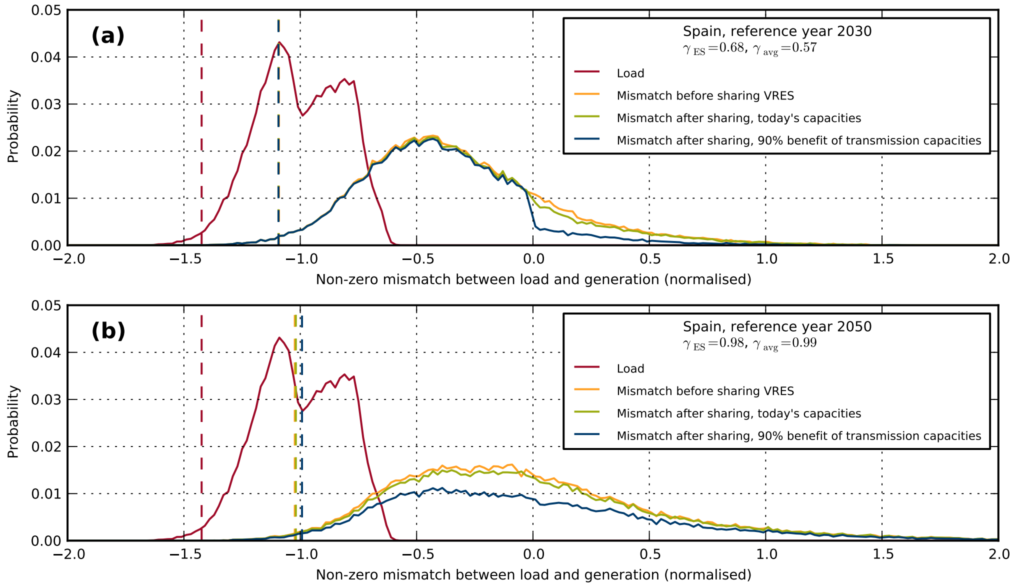

Figure 5.9: Distribution of the load (red), distribution of the mismatch between renewable generation and load before power sharing takes place (yellow), after sharing takes place with today's line capacities (green), and after sharing takes place with the 90 % benefit of transmission line capacities (blue), for the years 2030 (a) and 2050 (b), for Spain. The dashed lines indicate the 99 % quantile of the residual deficit. For clarity, the peak at zero is not shown here. Some of the lines cover each other.

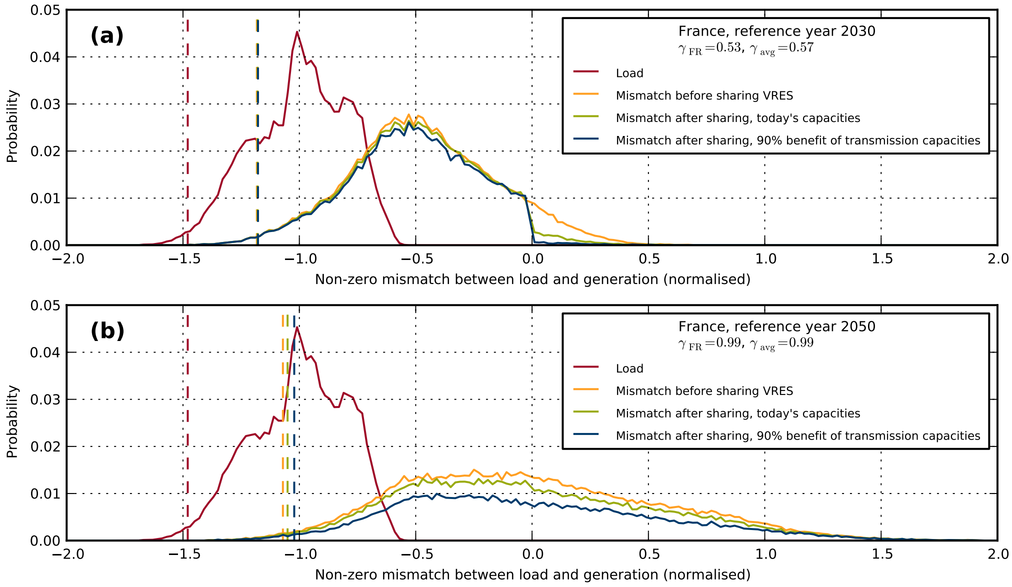

Figure 5.10: Distribution of the load (red), distribution of the mismatch between renewable generation and load before power sharing takes place (yellow), after sharing takes place with today's line capacities (green), and after sharing takes place with the 90 % benefit of transmission line capacities (blue), for the years 2030 (a) and 2050 (b), for France. The dashed lines indicate the 99 % quantile of the residual deficit. For clarity, the peak at zero is not shown here. Some of the lines cover each other.

introduced in Sec. 4.4.2 is one example of such an idea. A radical approach of "complete sharing" is able to reduce the high quantiles of backup from about 100 % of the average load to about 80 % of the average load, see Fig. 8 and the corresponding discussion in Ref. [53].

The other observation to be made is that the transmission grid as it is is highly inhomogeneous. While it does not make much of a difference for Denmark whether we have the line capacities seen today or the 90 % benefit of transmission layout, for Spain this is the crucial difference between being able to participate in European trade or not (compare the green and the blue curves in Fig. 5.8b and Fig. 5.9b).

We now take a look at the three example countries from a different perspective. We start with Denmark, which is small, central and an early adopter; see Figs. 5.11a and b as well as Fig. 5.2a. Denmark's wind power installation covers on average more than 33 % of the load already today [125]. Up to now, the excess production can easily be exported into the neighboring countries. On the import side, at first there are no neighbors willing to export any VRES generation because they can use everything domestically. This changes quickly as soon as the neighbors catch up with their VRES installation, causing them excess production. Since the neighbors have a larger total production, resulting in more excess, the import opportunities are actually very good then, even leading to a temporary reduction in backup energy between 2030 and 2040 for reinforced transmission grids, see Fig. 5.2a. Between 2045 and 2050, finally all countries reach a VRES share close to 100 %. This means that export opportunities are reduced: Since import can only replace backup, but not domestic VRES production, it becomes less probable to find a customer for excess production.

For comparison, we now look at Spain (Figs. 5.11c and d and Fig. 5.2c), which also has ambitious VRES targets for the near future, but is peripheral. There is only one strong connection to Portugal. This connection does not improve the import/export capabilities of Spain much, since Portugal's load is less than one fifth of the Spanish load, and therefore, it cannot absorb much of the Spanish fluctuations. We see that Spain starts similarly to Denmark with good potential export opportunities and no good chances to cover its deficits by import. However, there is a significant difference between the transmission capacities needed: While for Denmark today's transmission

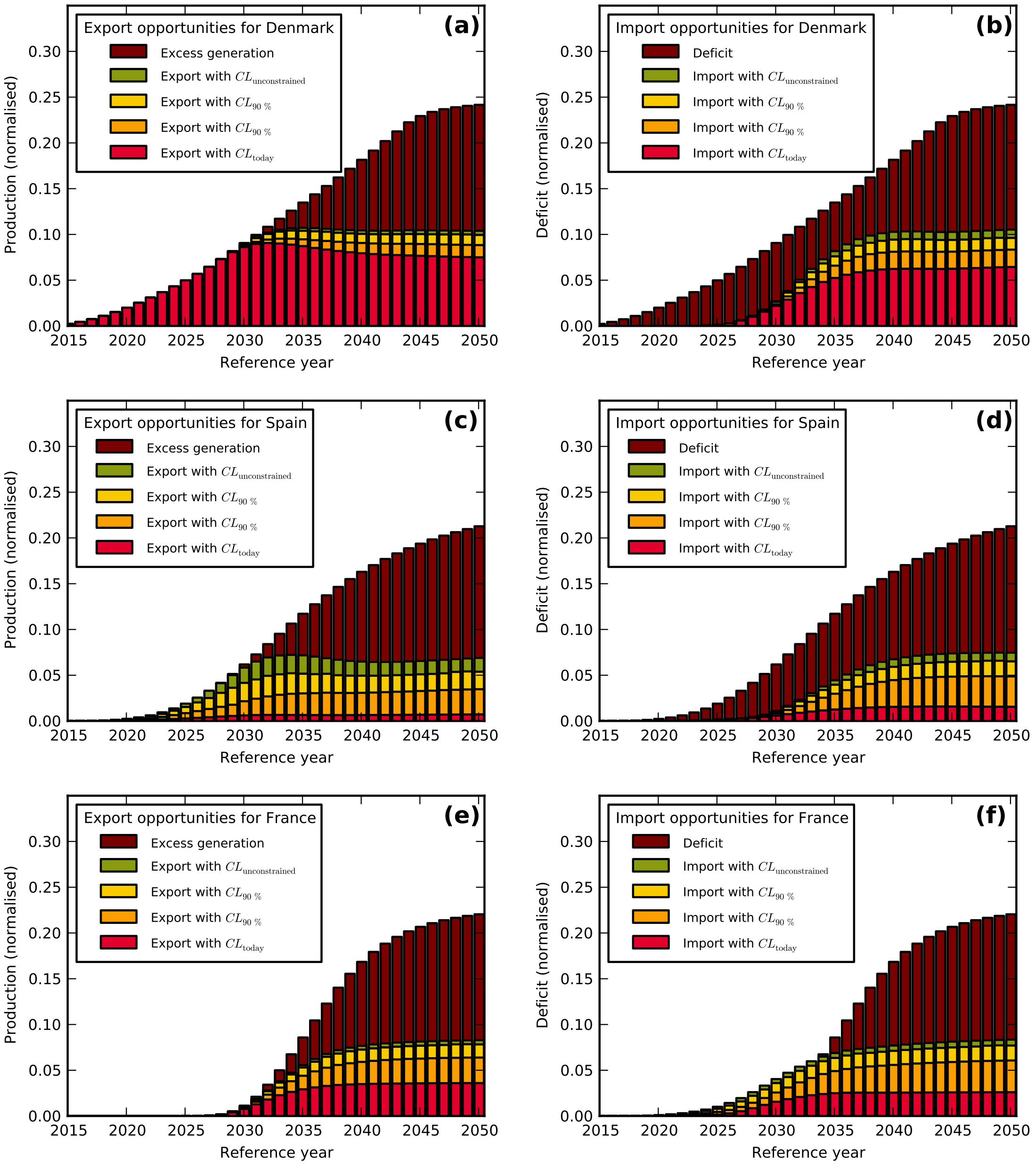

Figure 5.11: Export and import opportunities for selected countries, in the base scenario (single country backup minimal wind/solar mix). Panels (a), (c), and (e) show the export opportunities in case of a domestic overproduction for Denmark, Spain, and France, respectively. Panels (b), (d), and (f) depict the import opportunities for the same countries, which are used to cover a domestic deficit or to replace domestic backup.

capacities are already sufficient to export most of its excess, the weak link from Spain to France blocks almost all export if it is not reinforced. The same is true to a lesser degree for the import opportunities. In the further development, the import evolves appreciably different: Compared to Denmark, Spain's import opportunities are poor. This is due to two reasons: Firstly, Spain has a larger mean load. Its total deficit is therefore larger and harder to cover. Secondly, it is peripheral. In cases where there is only an insufficient supply of excess power which some countries want to export, while Spain and other countries have a deficit, the export flow will probably dry out before reaching Spain.

As a last example, we look at a central country which is large and relatively late, namely France (Figs. 5.11e and f and Fig. 5.2d). Its import opportunities are reasonably good for a country with a relatively large load, but could be significantly improved by increased transmission capacities. The same holds for the export. As the transition to VRES is expected to be rather late in France, there are no deficits that cannot be covered by imports during the first years. In fact, VRES imports can already be used to replace backup even before there is a significant domestic VRES installation, causing France to produce less than its own load from VRES and backup. The rest can be covered by VRES imports (see the dip for all non-zero transmission layouts in Fig. 5.2d). On the other hand, France does not experience an export boom in the beginning.

5.3 US: Simulated annealing

In this section, the relatively small 10 nodes 15 links US inter-FERC regional transmission grid as introduced in Fig. 2.2 is used as a test bed. A fully renewable US is envisioned: The mix between wind and solar PV power is kept at the single node backup optimal mix, gross VRES share is 100 %, and no storage system is included, such that all deficits have to be covered by the (abstract) backup system. In this setting, transmission grid extensions are calculated by thorough optimization.

We first make some general observations, and then examine three different transmission layouts. Their size is chosen such that they can all be built for an additional capital investment C_{tot} twice as large as the cost of existing installations.

$$C_{\text{tot}} = \sum_l C_l(h_l - h_l^{(\text{today})}) \overset{!}{=} 2 \cdot \sum_l C_l h_l^{(\text{today})} = 2 \cdot C_{\text{tot}}^{(\text{today})} \tag{5.10}$$

As a reminder, C_l are the costs per unit of line transmission capacity for line l, h_l is the resulting total capacity, and $h_l^{(\text{today})}$ is today's existing capacity. A technical constraint is that line capacities cannot decrease below the present layout (no line dismantling allowed), see Eq. (5.2). It is not a priori clear how the given investment should be distributed to reinforce single lines in order to achieve a maximal reduction in backup energy needs (see Eq. 5.1), so we develop different methods of assigning capacity to single links. The first layout is done based on quantiles of the distribution of unconstrained flows analogous to the studies presented in Sec. 5.2 and in Refs. [53, 54] for Europe ("Quantile layout"). The second is done by cost optimization for the hypothetical case where all lines have the same costs ("Even layout"). The last one uses cost optimization adopting Real line cost estimates from Refs. [64, 126] ("Real layout"). The latter two layouts are obtained by simulated annealing, a widely used technique for non-convex optimization problems, since it had not become clear that the optimization is actually convex at the time this investigation was performed. Our implementation of the algorithm is introduced before the optimized layouts are discussed. The numerical results provide further evidence for the analytical convexity proof from Sec. 5.1.2.

5.3.1 Maximal backup energy reduction

The first thing to observe is that the maximal possible backup energy reduction from transmission can be calculated ad hoc, just by comparing the isolated backup needs,

$$B_{\text{tot}}^{\text{isolated}} = \sum_t \sum_n \left[\Delta_n(t)\right]_- , \tag{5.11}$$

with the aggregated ones,

$$B_{\text{tot}}^{\text{aggregated}} = \sum_t \left[\sum_n \Delta_n(t)\right]_- . \tag{5.12}$$

In Eq. (5.11), all negative mismatches for the different nodes are summed up, yielding the total backup energy in the case of isolated nodes. Meanwhile, in Eq. (5.12) the mismatches are first added, thus allowing a negative mismatch at one node to be canceled by a positive mismatch at another. The negative part of this aggregated mismatch, summed over all time steps, gives the minimal possible amount of backup energy. For the contiguous US, these two numbers are $B_{\text{tot}}^{\text{isolated}} = 25.7\,\%$ of the total load covered from backup energy for the isolated case, compared to $B_{\text{tot}}^{\text{aggregated}} = 19.0\,\%$ in the aggregated case when keeping the wind/solar mixes fixed (no optimization of the mix for the aggregated US as in Sec. 6.2.2). Transmission can thus effect a backup energy reduction by roughly a quarter. Compared to the corresponding scenario for Europe, the isolated nodes (countries in the European case) have to balance around 24 % of the total load, which drops to around 15 % in the aggregated case, thus a reduction by about two fifths [53]. This indicates that although Europe covers a smaller area, low production phases of wind and solar PV are less correlated there, and hence the aggregated output is smoother than for the US.

5.3.2 Quantile capacity layouts

Neglecting different costs for different lines, the best grid build-up in terms of backup energy reduction found so far (to our knowledge) are the “Quantile line capacities” introduced in Sec. 5.2.3. The costs of this layout are calculated by taking the Real cost estimates from Refs. [64, 126] (see Tab. 5.1) and applying them to the capacity that needs to be added on top of what is installed today to reach the Quantile layout. The quantile for all links is chosen to be 98.36 %, such that in total, the additional investment is twice the cost of today’s layout. The resulting capacity layout for the US is shown in Fig. 5.14, together with the other two layouts described below.

5.3.3 Line cost estimates

The “Real line costs” estimates are composed of different contributions:

$$C_l = a_l \cdot b_l \cdot C_l^{\text{line}} + C_l^{\text{substation}} + C_l^{\text{async.}}\,, \tag{5.13}$$

where C_l^{line} are the costs of building just the line in $\$_{2006}/(\text{MW} \cdot \text{mi})$, a_l is the line length, b_l is a region-specific cost multiplier, comprising differences in overall building costs as well as different assumed prevalences of HVAC and HVDC lines with different operating voltages, $C_l^{\text{substation}}$ is the cost of substations per MW, and $C_l^{\text{async.}}$ is the cost of building interties when linking asynchronous regions (the Eastern FERC regions, Western FERC regions, and ERCOT are not synchronized with each other). Cost data come from Refs. [64, 126], and are converted to single lines, adjusted to 2006 values and annualized as described in Sec. 3, assuming a yearly interest rate of $i = 7\,\%$ and a lifetime of $A = 60\,\text{yrs}$.

$$C_l^{\text{annualized}} = C_l \cdot \frac{i(1+i)^A}{(1+i)^A - 1}$$

Costs are given in Tab. 5.1. Line lengths are approximated by the distances between the geographical center points of the FERC regions they connect. They can be found in Fig. 2.2, together with current transmission capacities.

The transmission costs used here are higher than those from Ref. [14] by an average factor of more than five. This is mainly due to the fact that this model assumes links between different FERC regions to be spread out over several lines, which are based on the prevalence of HVAC lines (see [126] for details), whereas the authors of Ref. [14] assume the entire transmission capacity to be aggregated in a few HVDC lines, which are much less expensive for long-distance lines. For a fair comparison, it has to be noted that the usage of a few HVDC lines for long distance transmission entails more distribution lines from the end-points of these HVDC lines which are not included in long-range transmission in Ref. [14], but which are partly incorporated in our approach since the lines we are considering are distributed. Whether one or the other idea is realized depends on how well the line build-up is coordinated and how concentrated load and generation are within the FERC regions linked.

Table 5.1: Table of the costs incurred for electricity lines. a_l is the line length in miles, calculated as described in [64] as the distance between midpoints of the connected FERC regions (see also Fig. 2.2), b_l is a region-specific, dimensionless line cost multiplier, C_l^{line} is the line cost in $\$_{2006}$ per MW-mi, and $C_l^{\text{async.}}$ is the cost of building AC-DC-AC interties when linking asynchronous regions, in $\$_{2006}$ per kW. Not shown is the constant substation cost of $C_l^{\text{substation}} = 16.3\,\$_{2006}$ per kW. From this input, the total annualized costs in $\$_{2006}$ per MW shown in the last column are calculated. Data are taken from [126], adjusted to refer to lines (instead of regions) and annualized as described in [64], assuming an interest rate of 7 % and a lifetime of 60 years.

Link	a_l	b_l	C_l^{line}	$C_l^{\text{async.}}$	total
AllCA-NW	520	2.28	1411	0.0	$1.20\cdot10^5$
AllCA-SW	650	2.28	1411	0.0	$1.50\cdot10^5$
ERCOT-SE	780	1.00	1411	216.4	$9.50\cdot10^4$
ERCOT-SPP	460	1.00	1411	216.4	$6.28\cdot10^4$
ERCOT-SW	645	1.00	1411	216.4	$8.14\cdot10^4$
ISONE-NYISO	255	3.56	1129	0.0	$7.42\cdot10^4$
MISO-NW	1045	1.00	1270	216.4	$1.11\cdot10^5$
MISO-PJM	775	1.78	1129	0.0	$1.12\cdot10^5$
MISO-SE	845	1.00	1270	0.0	$7.76\cdot10^4$
MISO-SPP	520	1.00	1270	0.0	$4.82\cdot10^4$
NW-SW	600	1.00	1411	0.0	$6.15\cdot10^4$
NYISO-PJM	335	3.06	1129	0.0	$8.37\cdot10^4$
PJM-SE	540	1.78	1270	0.0	$8.84\cdot10^4$
SE-SPP	750	1.00	1411	0.0	$7.66\cdot10^4$
SPP-SW	505	1.00	1411	216.4	$6.73\cdot10^4$

5.3.4 Simulated annealing

Simulated annealing is a well-known and widely used tool from statistical physics to determine the minimum of a general function by mimicking numerically the process of a physical system settling into its ground state while it is cooled [127, 128]. Since the problem of cost-optimal transmission could not be proven to be convex prior to this investigation, this approach was chosen.

Algorithm

To explain the implementation and parameters, a walk-through of the pseudo code (see Fig. 5.12) is presented, and descriptions of what the called functions do are given along the way. This explanation closely follows Ref. [129]. The main variables are the state s, which is a capacity layout in the form of single link capacities $\{h_{\pm l}\}$, and its energy E, which is in our case the total backup energy that is incurred with the capacity layout s in place, as given in Eq. (5.1). The other variables are closely related to those two and their meaning is easily guessed from their name and the context.

Initialization When starting from scratch, the initial state $s0$ is chosen by distributing the available total investment evenly over all links. It is then converted to different increments in MW line capacity, due to the different costs per MW on different lengths. These line capacity increments are then added to the line capacities already present.

When not cold starting, it is also possible to choose a (promising) initial layout with the correct total investment.

Temperature profile T is the temperature parameter, controlling how the space of potential layouts is scanned. If T is large, the transition probability is close to one for any candidate layout,

```
$s\_curr \leftarrow s\_0$; $E\_curr \leftarrow E(s)$
$s\_best \leftarrow s$; $E\_best \leftarrow E\_curr$
$k \leftarrow 0$
while $k \leq k\_max$ do
    $T\_curr \leftarrow T(k)$
    $s\_cand \leftarrow neighbor(s)$
    $E\_cand \leftarrow E(s\_cand)$
    if $P(E\_curr, E\_cand, T\_curr) > random()$ then
        $s\_curr \leftarrow s\_cand$
        $E\_curr \leftarrow E\_cand$
    end if
    if $E\_curr < E\_best$ then
        $E\_best \leftarrow E\_curr$
        $s\_best \leftarrow s\_curr$
    end if
end while
return $s\_best$
```

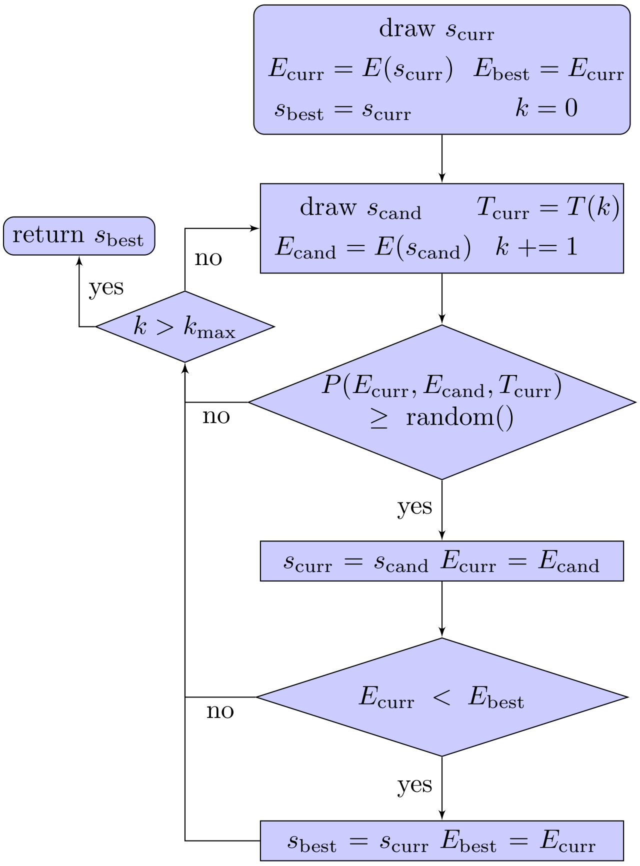

Figure 5.12: Pseudo code and flow chart of the employed simulated annealing algorithm.

even if E_{cand} is much larger than E_{curr}, and the system moves like a random walk from layout to layout. For low temperatures, the acceptance probability for shifts to layouts of higher energy goes to zero, and the system performs an almost monotonous descend toward lower backup energy layouts.

We measure temperature in units of energy, i.e. we set $k_B \equiv 1$. In the classical version of simulated annealing, the temperature is just decreased "slowly enough". Heuristics has it that a good starting temperature is such that the thermal energy is 1.2 times the largest energy gap between two random states [130]. After some experimentation, it was set to $T_{\text{start}} = 1.2 \cdot 10^{-4}$ times the average load. At this temperature, the probability to take a step towards a higher energy state is typically of the order of 90 %.

Instead of simply cooling linearly, the state space is first sampled for 6000 steps ($k\_max = 6000$) at the high temperature T_{start}. Then, 12 start states from these samples are picked, with a low E and a sufficient spread, in order to find several minima if they exist. These states are fed as initial states into the code, and the temperature is cooled linearly in 2000 steps from $0.6\,T_{\text{start}}$ to zero. For $T = 0.6\,T_{\text{start}}$, the typical probabilities to go towards higher energies are around 50 %. To refine the results, a second cooling stage of another 2000 steps from $0.06\,T_{\text{start}}$ is applied to the states resulting from the first cooling. This is almost equivalent to a random descent in backup energy landscape.

Neighboring states When choosing a neighbor, two random links are picked and an investment that is roughly equivalent to 100 MW is tentatively transferred from one to the other. While doing so, it is ensured that no link ends up with a capacity lower that today's. If such a link is thrown as a candidate to have its capacity reduced, it is rejected and a different one is chosen. The total amount of investment (Eq. (5.10)) is kept constant by not shifting a certain amount of capacity from one link to the other, but the capacity equivalent of a given cost increment.

Acceptance probability For the acceptance probability, the classical, asymmetric (thermodynamically inspired) choice is used:

$$P(E_{\text{curr}}, E_{\text{cand}}, T) = \begin{cases} 1 & \text{if } E_{\text{cand}} < E_{\text{curr}} \\ \mathrm{e}^{-(E_{\text{cand}} - E_{\text{curr}})/T} & \text{otherwise} \end{cases}$$

A random number with uniform distribution on the interval $[0; 1]$ is obtained from the evaluation of a random number generator random(). The probability of P being larger than random() equals P.

Due to computational limitations, the optimization is constrained to the first two years of data. In the algorithm as stated above, only the best state s is kept and returned. In practice, the record of all tested capacity layouts and their backup energies is saved, as a check as well as a reservoir of possible starting points.

5.3.5 Spread in annealed layouts

Line capacities for all links as well as details for the example link between AllCA and SW are shown in Fig. 5.13, for twelve optimized states found by annealing. It is visible that the capacities almost coincide. The same holds true for the other links. This finding is further corroborated by looking at the spread in backup energy among the twelve resulting layouts, shown in Tab. 5.2. Minima and maxima of backup energy almost coincide, indicating that there is a single optimal value. In retrospect, this provides further numerical evidence for the convexity of the problem.

Tab. 5.2 also shows the effect of calculating backup energy during all available years versus only relying on the first two years. While the shift this introduces is larger than the spread between the layouts for either 2 or 32 years, it does not affect their relative distances in backup energy much, and in particular has no impact on their ranking.

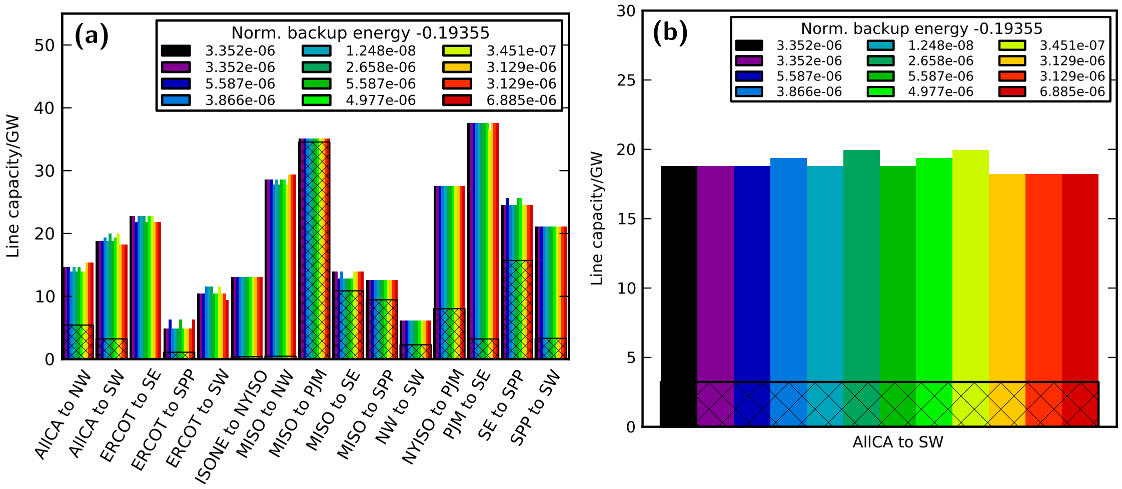

Figure 5.13: (a): Optimized link capacities for twelve annealing runs from different start points. Today's line capacity is overlayed, which serves as a lower bound (cross-hatched bars). The legend shows the resulting backup energy (minus a constant offset to compare the very similar numbers) as a fraction of the total load, which the different line capacity layouts produce during the 32 years of data. This plot shows the situation for the Real line costs, see Sec. 5.3.3 for details on the costs. For the Even line cost case, the corresponding results resemble this plot. (b): Zoom of (a), looking at the link between AllCA and SW only.

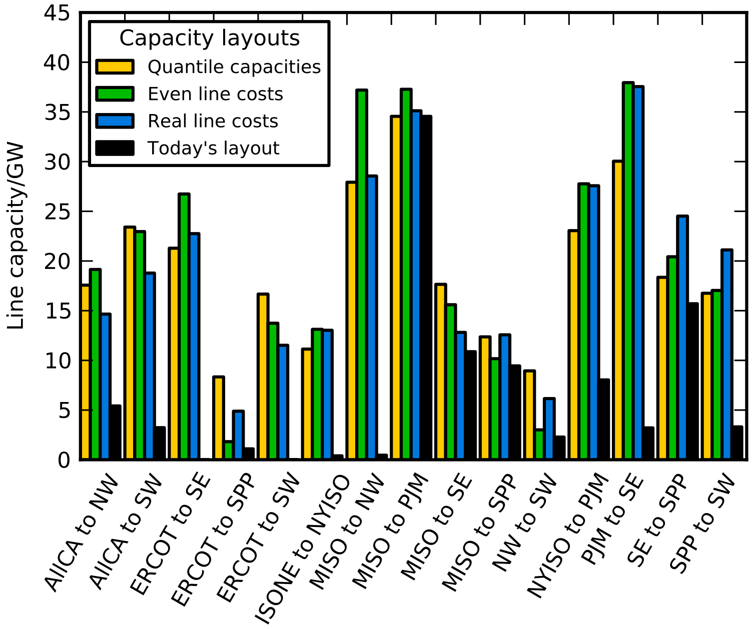

Figure 5.14: Quantile line capacity layout and two optimized transmission capacity layouts: if all line costs are assumed equal (Even line costs) and if line cost estimates as given in Tab. 5.1 are assumed (Real line costs). In all the layouts, the total investment is set to twice of what is present today, and the total additional line capacity is chosen accordingly. For comparison, today's line capacity layout is shown as well. It serves as a lower bound to the grid extensions.

Table 5.2: Percentage of total electricity consumption covered by backup energy, for the three different line capacity layouts: Quantile capacities, cost optimal line capacities if all lines cost the same (Even layout), and for line cost estimates as given in Tab. 5.1 (Real layout). For the latter two layouts, the maximal and minimal values across the twelve candidate layouts from the different annealing runs is also shown. The optimization over the first two years of data is shown and compared to the results for the whole 32 years to assess the influence of running the optimization with two years of data only.

Timespan		32 years	2 years
Layout			
Quantile		19.42754 %	19.11674 %
Even	opt.	19.29423 %	18.98273 %
	min.	19.29423 %	18.98273 %
	max.	19.29576 %	18.98289 %
Real	opt.	19.35500 %	19.03232 %
	min.	19.35500 %	19.03232 %
	max.	19.35569 %	19.03244 %

Table 5.3: Cost of different line capacity layouts when they are scaled such that they yield the same backup energy reduction as the quantile capacity layout. Cost calculations have all been done based on the line cost estimates from Tab. 5.1. The first row shows the total annual cost. The second row contains the total annual cost normalized by the yearly backup energy reduction that is achieved (compared to today's layout) by the new line investment. The last row shows the percentage difference in costs with respect to the Quantile layout.

Layout	Quantile	Even	Real
Cost in 10^9\$/yr	17.99	16.25	16.10
Cost in $\frac{\$/\text{yr}}{\text{MWh/yr}}$	141.02	127.38	126.22
Δ Cost	0.0 %	-9.7 %	-10.5 %

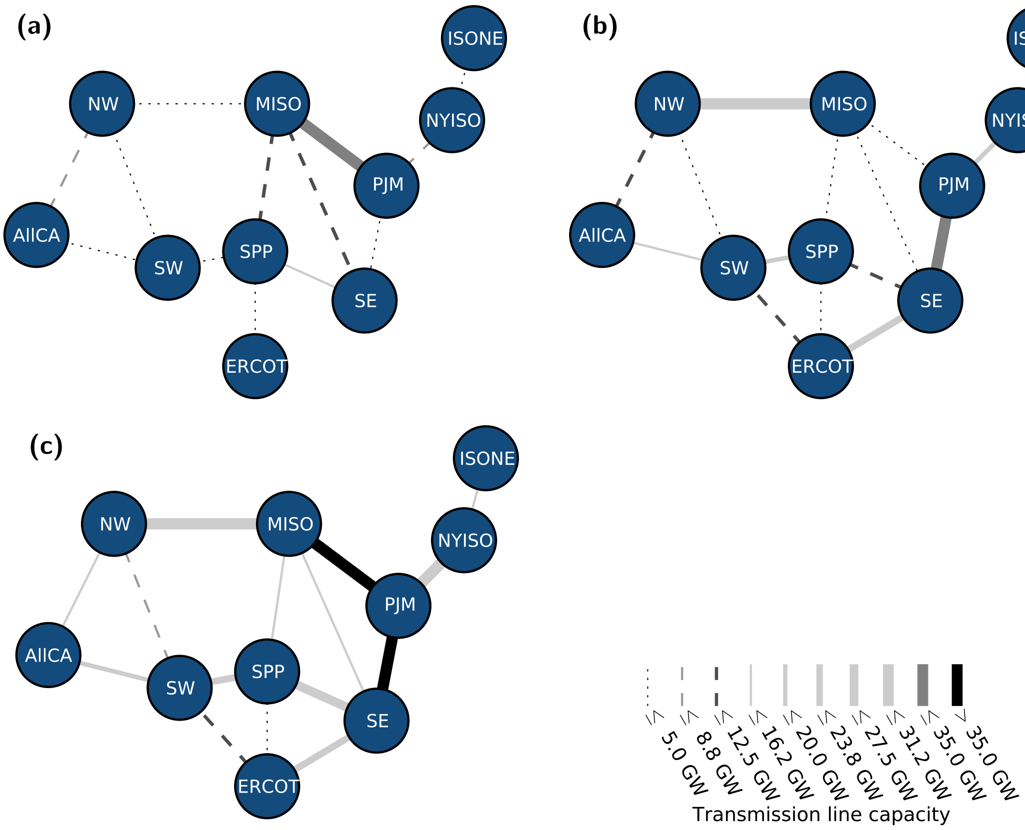

Figure 5.15: Today's layout (a) plus additional capacity to realize the Real cost capacity layout (b) gives the Real layout (c). Line thickness and style indicate transmission capacity as described in the legend. Node sizes and positions are not to scale.

5.3.6 Comparison between line capacity layouts

Cost-optimal line capacity layouts are calculated with simulated annealing for two sets of prices: First, all lines are assigned the same price (an average of the Real cost estimates from Tab. 5.1) to obtain the Even layout. It serves as a test of the Quantile line capacities, which should produce very similar results if performing well, as well as a sensitivity check for the second calculation, in which we insert the line cost estimates from Tab. 5.1 to produce the Real layout.

The Even and Real line capacity layouts resulting from simulated annealing as well as the Quantile line capacity layout are shown in Fig. 5.14. Quantile line capacities and Even line capacities are generally similar, but differ visibly (compare the yellow and the green bars in Fig. 5.14). Although they generally are within 2-5 GW of each other, deviations up to 10 GW occur. The performance of the different layouts in terms of backup energy reduction is shown in Tab. 5.2. It is seen that the backup energy minimization with Even line costs yields lower backup energies than the Quantile line capacities by more than 0.1 % of the total yearly load, or roughly 170 TWh (using 2007 load values). This means that simulated annealing outperforms the Quantile method at the task of optimally distributing a certain amount of additional MW in transmission capacity while neglecting regional differences.

When different line costs enter the game, the line capacity is redistributed to the cheaper links, and thus backup energy drops not as low as for the Even cost line capacities. It should be noted, however, that the optimization still reduces backup energy usage further than the Quantile capacities.

To make a cost comparison between the different capacity layouts without using backup energy costs which are highly complex and diverse, the Real as well as the Even layout are scaled down linearly until they lead to the same amount of total backup energy as the Quantile layout. The costs of the resulting layouts are then all calculated using the line cost estimates from Tab. 5.1, and compared in Tab. 5.3. They are reduced by about 10 % in both of the optimized layouts, as compared to the Quantile capacity guess.

The additional transmission line capacity for the three cases considered here (Quantile, Even, and Real layout) show large additions along the East Coast (ISONE, NYISO, PJM, and SE FERC regions), West Coast (CA, NW, and SW), and across the boundaries of the three interconnects (ERCOT to adjacent FERC regions; MISO-NW; and SW-SPP), cf. Fig. 5.15. The grid enhancement in the NREL Futures study (for 2050), Ref. [131], by contrast, is mainly east-west oriented and concentrated in the middle and southwestern areas of the US, with key additions to/from ERCOT, SE, SW, SPP, and MISO FERC regions. These results reflect their greater emphasis on transmitting wind and solar energy from the middle and southwestern areas of the US to large-load, adjacent regions, while in our simulation all FERC regions are assumed to be on average self-supplying, thus reducing the need for transmission.

5.4 Link costs versus link benefits

A different idea is to assign not only the construction costs to the links, but also a certain benefit to each of the transmission lines. The cost function to be minimized looks like this:

$$\begin{aligned} \textit{Net cost} &= \textit{Cost} - \textit{Benefit} \\ &= \sum_l C_l \cdot h_l - \sum_{l,t} P_l(t)|F_l(t)| \\ &= \sum_l C_l \cdot h_l - \sum_l b_l(h_l)\,, \end{aligned} \tag{5.14}$$

where C_l is the line cost of line l, and $P_l(t)$ is the revenue from link l at time t. Simple choices for $P_l(t)$ include a constant price P, or a price linear in the flow demand $F_l(t)$, such that the benefit becomes a quadratic function of the flow.

5.4.1 Convex approximations

We seek to formulate a convex optimization problem. The variables are the transmission capacities h_l. The constraints on them are only positivity (or being no smaller than currently, cf. Eq. (5.2)), that is, linear inequalities that are trivially convex, so the difficulty lies solely in checking that the target function (5.14) is actually a convex function in the transmission capacities h_l. The cost term is again linear and thus convex, so we concentrate on the benefit term. This question needs some thought. Its answer also depends on the flow paradigm employed. Here, we make use of the generalized DC power flow introduced and explored in [53, 54] and described in this work in Sec. 4.4.1. As a reminder, the algorithm has two prioritized objectives, namely to minimize the usage of backup energy, and thus maximize the usage of VRES, and, as a secondary goal, to minimize flow dissipation.

The benefit term in (5.14) is restated to decide whether it is concave (as it should be if its negative was convex). Look at the time-integrated benefit b_l for a single link l. This sum can be interpreted as a moment of the absolute flow distribution on the link:

$$b_l(h_l) = \sum_t P_l(t)|F_l(t)| = \int_0^{h_l} p_l(x) x \overline{\rho}_{h_l}(x) \mathrm{d}x \tag{5.15}$$

The probability density $\overline{\rho}_{h_l}(x)$ of the flow gives the probability for a flow of magnitude x to occur. For the two simple cases mentioned above, $p_l(x)$ is either a constant or linear in x, so $p_l(x) = p_l x^n$, with n being either 0 or 1. Inserting this yields:

$$b_l(h_l) = \int_0^{h_l} p_l x^{n+1} \overline{\rho}_{h_l}(x) \mathrm{d}x \tag{5.16}$$

For the unconstrained case, the shape of the probability density has been observed to be highly convex, with a high peak at zero and quickly decaying to 0 for large values of flow magnitude x. For example, take a look at Fig. 5.4, which shows the distribution of the directed (not absolute) flow. For capped line capacities, the free distribution is assumed to get redistributed such that all flows larger than the cap h are cut off at h, forming a peak at the link's full capacity. We call this effect "tail-to-peak shift". There may also be redirection effects, where flows from other capped links are now passed through the link under consideration, where they can come in at any magnitude ("tail-to-bulk shift"), or redirection from the given link to others, but for the moment, the problem will be treated as if link l was the only one constrained and effects other than the tail-to-peak shift are neglected. Under this assumption, $\overline{\rho}_h(x)$ can be written in terms of the unconstrained flow distribution $\rho(x)$ as

$$\overline{\rho}_h(x) \approx \rho(x)\theta(h-x) + \delta(h)\int_h^\infty \rho(x)\mathrm{d}x\,, \tag{5.17}$$

with the cutoff function θ (one if argument is larger than zero, zero else). This approximation has the decisive advantages that the distribution now depends on h in an explicit, simple manner, and that the link benefits are decoupled between the single lines. Inserting this into (5.16), we get

$$b_l(h_l) \approx \int_0^{h_l} p_l x^{n+1}\rho(x) + p_l h_l^{n+1}\int_{h_l}^\infty \rho(x)\mathrm{d}x\,. \tag{5.18}$$

To determine whether this is a concave function of h_l, it suffices to check whether the second derivative of it is non-positive for all h_l[3]. We find

$$\partial^2_{h_l} b_l(h_l) = p_l \cdot \begin{cases} -\rho(h) & \text{for } n=0 \\ 2\int_{h_l}^\infty \rho(x)\mathrm{d}x - 2h_l\rho(h_l) & \text{for } n=1 \end{cases} \tag{5.19}$$

Thus, for $n = 0$, we are sure that this function is concave, and for $n = 1$, it is also probable at least for sufficiently large h_l, but depends on the specific form of the unconstrained distribution.

This means that, at least for a constant flow revenue, the net cost function (5.14) is indeed a convex function of the line capacity constraints h_l – if the above approximations are valid.

5.4.2 Tests of the flow distribution assumptions

To get an idea how good (or bad) the above approximation to the flow distribution for constrained line capacities is, several capacity layouts are tested in the fully renewable US case (same as in Sec. 5.3). The flow distribution on the single links and the tail-to-peak ratio is shown in Figs. 5.16 and 5.17 as well as Tabs. 5.4 and 5.5. The constrained line capacity layouts are chosen in two different ways: First, as quantiles of the unconstrained flow, or, to be precise, as multiples of the 99.99 % quantiles of the unconstrained flow (b factor in the plot legends and the tables), and second as multiples of the line capacity existing today (bt factor). The results look encouraging for some links, for example MISO to SE shown in Fig. 5.16 and Tab. 5.4, while less nice for others, for example ERCOT to SPP shown in Fig. 5.17 and Tab. 5.5. The assumption that the area is shifted from the tail of the unconstrained distribution to the peak of the constrained distribution is tested by calculating the ratio of peak- to tail area. These values are calculated for the different values of the multiplier b, and are found in Tabs. 5.4 and 5.5.

From the second columns of Tabs. 5.4 and 5.5, it appears that if only the single line under consideration is constrained, the peak is indeed just the shifted tail, as expected. If all lines are constrained (columns three and five in Tabs. 5.4 and 5.5), the general tendency is that the peak-to-tail ratio decreases with decreasing total capacity, which is due to the network supporting less

---

[3] We know from higher dimensional analysis that we actually need to check that the Hessian of the total cost function (5.14) is a negative definite matrix. With the above approximations, however, the cost has been split into a sum of single link costs, making all off-diagonal entries in the Hessian 0. Thus, we really only have to look at the diagonal elements.

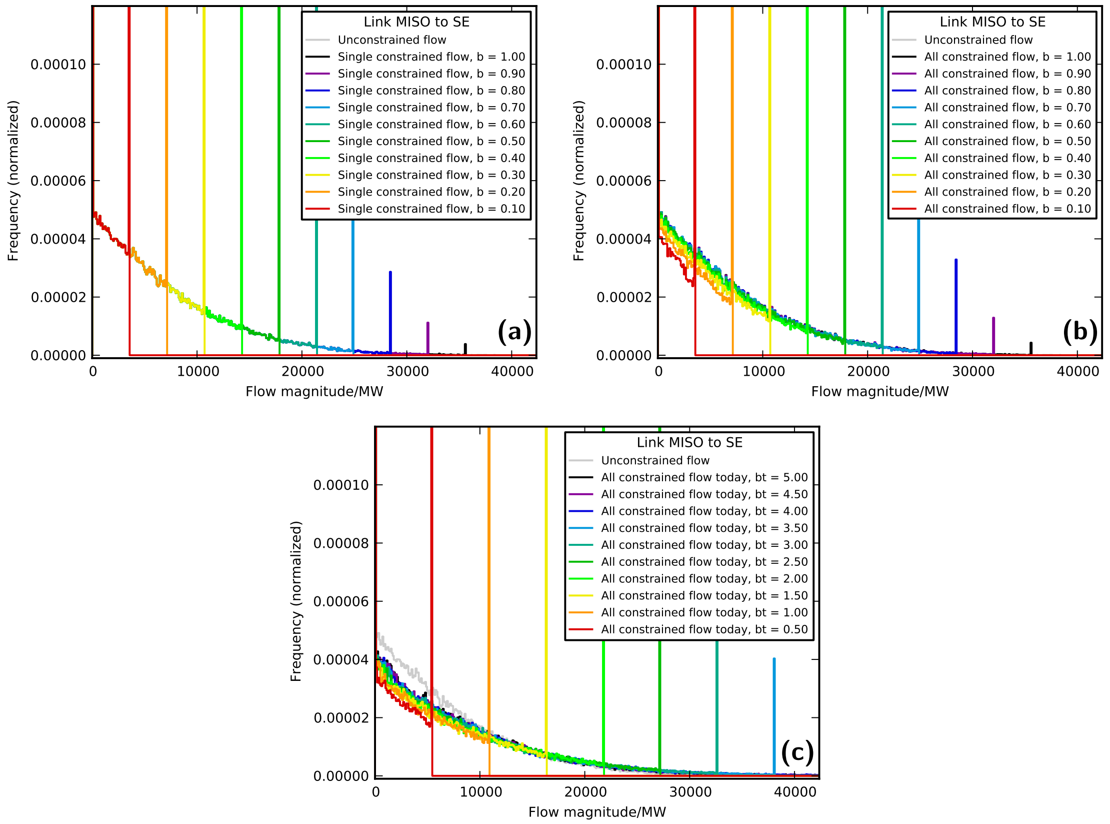

Figure 5.16: Flow distribution on the link between MISO and SE, for different capacity layouts. (a): Only the capacity on this link is constrained with a fraction b of its 99.99 % quantile capacity (see b in the legend), while the other links remain unconstrained. (b): All line capacities are constrained simultaneously with fractions b of the 99.99 % quantile of the unconstrained flow. (c): All line capacities are simultaneously constrained by multiples (factor bt) of today's capacities.

Table 5.4: Ratio of the peak area of the constrained flow distribution to the tail area of the unconstrained flow distribution (integrated from the peak position), for the link between MISO and SE, for the case where only the link under consideration is constrained with a fraction b of the 99.99 % quantile capacities (labeled "single"), and the case where all links are constrained simultaneously with a fraction b of the 99.99 % quantile capacities (labeled "all"), as well as for the case where the links are all constrained to a multiple bt of today's line capacities (labeled "today").

b	ratio "single"	ratio "all"	bt	ratio "today"
1.00	1.009	1.132	5.00	inf
0.90	1.003	1.154	4.50	inf
0.80	1.001	1.149	4.00	76.857
0.70	1.001	1.151	3.50	22.020
0.60	1.000	1.151	3.00	8.737
0.50	1.000	1.129	2.50	4.360
0.40	1.000	1.077	2.00	2.721
0.30	1.000	0.998	1.50	1.798
0.20	1.000	0.897	1.00	1.264
0.10	1.000	0.772	0.50	0.912

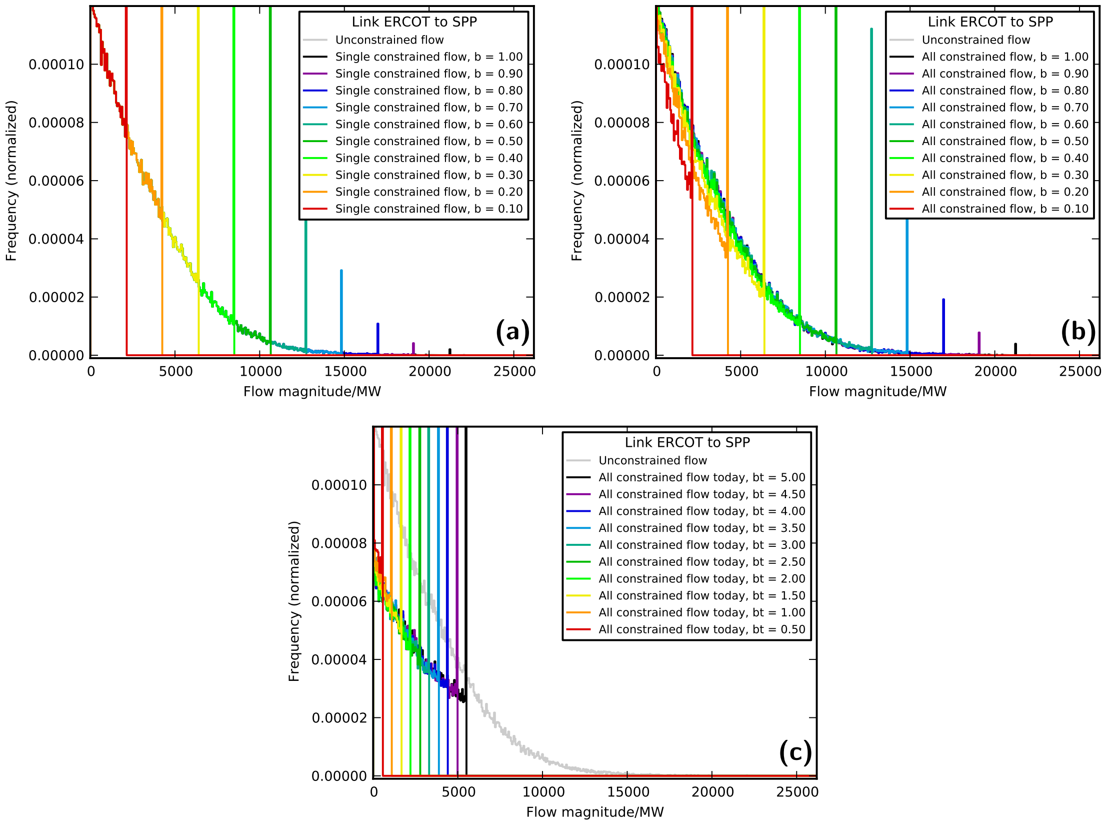

Figure 5.17: Flow distribution on the link between ERCOT and SPP, for different capacity layouts. (a): Only the capacity on this link is constrained with a fraction b of its 99.99 % quantile capacity (see b in the legend), while the other links remain unconstrained. (b): All line capacities are constrained simultaneously with fractions b of the 99.99 % quantile of the unconstrained flow. (c): All line capacities are simultaneously constrained by multiples (factor bt) of today's capacities.

Table 5.5: Ratio of the peak area of the constrained flow distribution to the tail area of the unconstrained flow distribution (integrated from the peak position), for the link between ERCOT and SPP, for the case where only the link under consideration is constrained with a fraction b of the 99.99 % quantile capacities (labeled "single"), and the case where all links are constrained simultaneously with a fraction b of the 99.99 % quantile capacities (labeled "all"), as well as for the case where the links are all constrained to a multiple bt of today's line capacities (labeled "today").

b	ratio "single"	ratio "all"	bt	ratio "today"
1.00	1.034	2.000	5.00	2.925
0.90	1.017	1.917	4.50	2.504
0.80	1.006	1.780	4.00	2.146
0.70	1.002	1.634	3.50	1.879
0.60	1.001	1.517	3.00	1.637
0.50	1.000	1.389	2.50	1.466
0.40	1.000	1.184	2.00	1.306
0.30	1.000	0.949	1.50	1.170
0.20	1.000	0.740	1.00	1.002
0.10	1.000	0.582	0.50	0.756

and less flow (feeding links become overloaded). For the quantile constraints on the links (column three in Tabs. 5.4 and 5.5), we see that for all links, the ratio goes down to between 0.4 and 0.8 for $b = 0.10$. The starting points for large b differ significantly, from 2.0 for links over which flow gets redirected to 0.8 for links which get less feed-in from the start. These tendencies have been confirmed by looking at all the links on the US network as shown in Fig. 2.2. When the links are all constrained by multiples of today's line capacities (column five in Tabs. 5.4 and 5.5), the story becomes different: Tail-to-peak ratios deviate much more from unity, and the flow distributions are significantly changed in the bulk as well.

Generally, it can be said that the approximations of the flow distribution become worse the further the line capacity layout deviates from the unconstrained case. Put differently, an algorithm based on this could be useful for finding a cost-optimal strong transmission grid layout, while one needs to be very careful when trying to apply it to a low-capacity layout.

5.5 Other approaches

Transmission grid planning is an important task for TSOs as well as governmental agencies concerned with transmission system adequacy and reliability. Apart from that, the problem has attracted interest from the scientific community, on applied, engineering as well on more theoretical, abstract levels.

For their Ten Year Network Development Plan (TYNDP) [120], ENTSO-E and its members conduct a comprehensive scenario analysis, based on long-term scenarios constructed in their Scenario Outlook Adequacy Forecast (SOAF) [119]. Demand is modeled, and the dispatch to serve it is calculated in a market model. Afterwards, resulting transmission flows are derived, and bottlenecks are identified. Each infrastructure project proposed to mitigate the situation is then subject to detailed assessment in terms of its technical impact (security of supply, flexibility, resilience etc.), its costs, environmental and social impact, compliance with EU 20-20-20 targets (20 % renewable share in energy consumption, 20 % reduction in consumption, and 20 % reduction in green house gas emissions by 2020 [132]), and its economic and social welfare impact. In contrast to our approach in Secs. 5.2 and 5.3, where backup energy needs and total transmission system costs are minimized, respectively, multi-criteria decisions are taken here.

A similar approach is pursued by the German TSOs and the Bundesnetzagentur for the German network development plan (Netzentwicklungsplan) [118]. The ENTSO-E TYNDP is used as boundary conditions for international trade, and market dispatch is calculated. Market dispatch leads to trade flows, the exchange between network nodes. From these, physical power flow is calculated. Total transmission demand is derived as the amount of transmission capacity needed to transfer all of the market-required energy flows; curtailment or redispatch are not considered as options. Additionally, $(N-1)$ grid stability is required[4]. Our coarse modeling of the European grid indicates that this approach leads to extremely high transmission demand estimates, entailing transfer capacities that will be used only for a very small fraction of the time. In a second step, concrete realizations of possible networks supplying the flow necessary to enable the market-based dispatch are calculated, and broken down into single corridors for transmission lines. These single projects are then evaluated and prioritized according to how important they are for system reliability and stability, their cost efficiency, and other criteria. In this process, the effect of the single projects on curtailment and redispatch needs is also evaluated.

Other network extension models exist in the scientific literature. Most prevalent are models minimizing total electricity system costs. Some simplified versions of such a model, where the total costs of transmission lines and power generation are minimized simultaneously, have been addressed as early as the 1970s. In these early versions, only marginal generation costs were considered, such that total generation costs became simply marginal cost times the amount of generation. In the classical formulation, projected lines are either built or not, entailing integer

---

[4] $(N-1)$ stability means that if one system element fails, e.g. a transmission line, such that only $(N-1)$ elements are left, the system is still able to operate and serve all demand.

decision variables. The first approach used the simplified transport power flow [105]. This model was subsequently refined to work with DC power flow [106], but could only be applied to small networks due to severe computational limitations (at the time). For the more realistic DC power flow, the problem has been tackled successfully for larger networks with simulated annealing [107, 108], and genetic algorithms [109] as early as the 1990s. Heuristic models that include DC power flow with transmission losses are further pursued, e.g. [133].

More recently, with the advent of mixed-integer programming, new implementations have become feasible, see e.g. Refs. [112, 113]. Other routes followed include Benders decomposition, e.g. [110, 111]. In Ref. [114], taboo search, genetic algorithms, and artificial neural networks are applied to the problem of electric network extensions in Saudi-Arabia.

In the last years, Refs. [56, 57] employ an approach of total system cost minimization to determine European power grid reinforcements. Power flow is approximated as a transport problem to keep the entire system linear, but generation is modeled much closer to reality, not only as dispatch, but also including investment costs and observing ramping constraints.

In Ref. [103], the transmission network and power generation facilities are optimized simultaneously, by iteratively solving a detailed market dispatch constrained by transmission limits (PTDF approach sketched in Sec. 4.4.5), and updating the transmission grid to avoid congestion or overcapacities. Both transmission grid and power generation are associated with costs, and total system costs are minimized. The method is applied to Europe in a detailed long-term study [58].

Gradual (step-by-step) grid upgrade schedules have been considered and optimized economically with genetic algorithms as well as differential evolution in Ref. [115].

Ref. [116] employ a multi-objective approach, calculating Pareto-optimal curves, for transmission grid extension planning. They take into account congestion surplus (that is, roughly speaking, the gain of the transmission line owner due to a split of the electricity market into two different price zones at both ends of her transmission line, which occurs whenever the line is congested), transmission line investment costs, and power outage costs. For the UK, a similar multi-objective study has been performed by [117], additionally including reinforcement of existing lines, and the further objective of CO_2 emission minimization.

Chapter 6

Optimized wind/solar mixes

Central to our research is the mismatch Δ_n between load L_n and generation G_n^{S}, G_n^{W} from solar PV and wind, respectively, in region n. As a reminder:

$$\Delta_n(t) = \gamma_n \langle L_n \rangle \big((1 - \alpha_n^{\mathrm{W}}) G_n^{\mathrm{S}}(t) + \alpha_n^{\mathrm{W}} G_n^{\mathrm{W}}(t) \big) - L_n(t) \tag{6.1}$$

Wind and solar generation are understood to be normalized to an average of one, and then scaled with the mean load $\langle L_n \rangle$ to a given gross share γ_n of the load. The relative share of wind in the VRE generation is denoted α_n^{W}, the corresponding relative share of solar PV is $(1 - \alpha_n^{\mathrm{W}})$.

The idea in this chapter is now to optimize α_n^{W} in different ways. The different objectives are explained in Sec. 6.1, while the following Secs. 6.2 and 6.3 deal with the application of these methods to the US electricity system. Throughout these sections, the optimal mix will always be calculated for a single node in the network or the aggregation of all nodes, and not in combination with transmission. The interplay with transmission is investigated in the final Sec. 6.4, this time for the European example.

There are various technologies to deal with the mismatch. One option is to use backup power, as has been introduced in Sec. 4.4. The natural quantity to minimize in this case it the total backup energy needed. Another option is to use storage, in which case total storage energy capacity is to be minimized.

The wind/solar mix also has an influence on the levelized costs of electricity (LCOE), when viewed from a system-level perspective. LCOE minimization and its implications will also be discussed below.

6.1 Methods

6.1.1 Backup energy-minimal mix

Here, the only concern is to keep the need for backup energy, which is calculated as the sum of negative mismatches throughout all time steps, as small as possible. In other words, the sum of the negative parts (denoted $(.)_-$) of the mismatch in Eq. (6.1) is minimized as a function of α_n^{W}:

$$\min_{\alpha_n^{\mathrm{W}}} \sum_t B_n(t) = \min_{\alpha_n^{\mathrm{W}}} \sum_t (\Delta_n(t))_- \tag{6.2}$$

The backup energy minimization is performed independently for different VRES gross shares γ_n. Since in our modeling, the VRE gross share γ_n and hence the total energy produced from VRES is fixed, least backup energy needs are equivalent to least surplus generation. In other words, when minimizing the need for backup energy, the surplus energy from renewable sources is minimized at the same time.

When the VRES gross share γ_n is less than 100 %, at least a fraction of $(1-\gamma_n)$ of the demand has to be covered by the backup system, even if no VRES generation comes as surplus energy. The energy provided by the backup system beyond this minimal share is termed additional backup energy, and this is the part of the backup energy that can be reduced by a suitable choice of the wind/solar mix.

6.1.2 Storage energy capacity-minimal mix

A scenario is considered where each node is isolated from the others and each of them have reached a VRES gross share of 100 %, $\gamma_n = 1 \, \forall n$ in Eq. (6.1). For comparison, the analogous results for an aggregation are calculated as well. We look at an electricity system where all the surplus generation (positive mismatch in Eq. (6.1)) is put into an idealized, 100 % efficient storage system and all deficits are covered by re-extracting the stored energy. Since VRES generation equals on average the load and storage losses are neglected, such a system provides enough power at all times.

Our objective is to minimize the storage energy capacity E_n^H. It can be calculated from the storage filling level time series $H_n(t)$ as follows:

$$\begin{aligned} H_n(t) &= H_n(t-1) + \Delta_n(t) \\ E_n^H &= \max_t(H_n(t)) - \min_t(H_n(t)) \end{aligned} \tag{6.3}$$

The storage optimal mix for region n is defined to be the α_n^{W} that minimizes this quantity.

6.1.3 LCOE-minimal mix

Regional LCOE

LCOE are expected to vary spatially due to different external conditions. The main cause of deviations is the weather-dependent capacity factor CF_n for each region (indexed n), i.e. the ratio of average generated power to the maximal generator capacity. Since the costs of VRE plants are to a large part installation and maintenance costs and thus proportional to the total installed capacity, but largely independent of the total power output, the costs per unit of energy are in good approximation anti-proportional to the total generated energy. Expressed in terms of the capacity factor, this yields a regional weight of

$$w_n = \frac{N}{\sum_m 1/CF_m} \cdot \frac{1}{CF_n}$$

The normalization (first factor) is necessary to keep the average of the weights at unity. N is the number of regions, in this case, 10.

The second reason for variations in LCOE in the different regions are different labor and material costs. For the US, they have been compiled by the US Army Corps of Engineers [134], and adapted to the problem at hand in Ref. [135]. These yield another factor c_n of the order of one, which modifies the regional LCOE. Taken together, the regional LCOE are calculated as:

$$\mathrm{LCOE}_n = w_n c_n \mathrm{LCOE}_{\mathrm{avg}} \tag{6.4}$$

They are calculated separately for wind and solar PV. The results are shown in Fig. 6.1, for an assumed equal $\mathrm{LCOE}_{\mathrm{avg}}$ of 0.08 \$/kWh for both VRES. The capacity factor weights w_n as well as the regional cost factors c_n are given in Tab. 6.1, which also shows the relative LCOE in the different FERC regions, for solar PV and wind power separately. It is observed that solar installations have lowest costs in the southern and western regions, while they are expensive on the northern East Coast, and vice versa for wind costs.

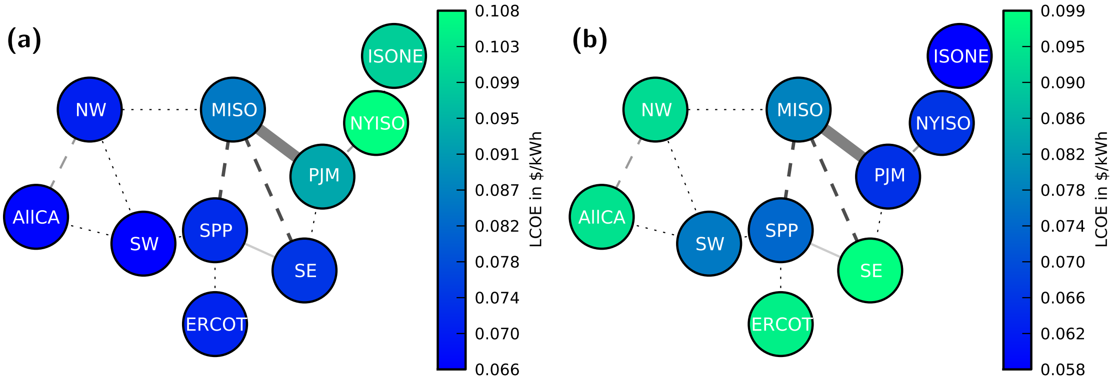

Figure 6.1: Regional LCOE of (a) solar PV and (b) wind for the case of an average LCOE of 0.08 $/kWh for both, calculated using Eq. 6.4.

Table 6.1: Relative regional LCOE for the 10 FERC regions, for solar (left) and wind (right), together with the capacity factor CF_n and regional material and labor cost weights w_n and c_n. Note that the NW FERC region also comprises Nevada and Utah (cf. Fig. 2.2), thus explaining the low solar LCOE there.

Region	CF_n	w_n	c_n	rel. LCOE$_n$	Region	CF_n	w_n	c_n	rel. LCOE$_n$
AllCA	0.20	0.87	1.04	89.8 %	AllCA	0.25	1.15	1.04	119.5 %
ERCOT	0.18	0.98	0.97	94.0 %	ERCOT	0.24	1.24	0.97	120.0 %
ISONE	0.15	1.12	1.02	113.5 %	ISONE	0.42	0.70	1.02	71.0 %
MISO	0.17	1.03	1.01	103.6 %	MISO	0.30	0.97	1.00	96.8 %
NW	0.19	0.91	1.00	90.4 %	NW	0.25	1.17	1.00	116.9 %
NYISO	0.15	1.15	1.10	125.6 %	NYISO	0.36	0.80	1.04	83.6 %
PJM	0.16	1.10	1.03	112.8 %	PJM	0.37	0.80	1.01	80.5 %
SE	0.16	1.05	0.94	98.2 %	SE	0.23	1.27	0.98	124.0 %
SPP	0.18	0.94	0.96	90.0 %	SPP	0.31	0.93	0.98	91.5 %
SW	0.20	0.84	0.98	82.1 %	SW	0.30	0.97	0.99	96.2 %
avg.	0.17	1.00	1.00	100.0 %	avg.	0.30	1.00	1.00	100.0 %

Calculation of the LCOE-optimal mix

The regional LCOE of wind and solar are then combined and modified to include the effects of curtailment by multiplying them by the ratio of generated to used energy:

$$\mathrm{LCOE}_0(\alpha_n^{\mathrm{W}}) = \alpha_n^{\mathrm{W}}\mathrm{LCOE}_n^{\mathrm{W}} + (1-\alpha_n^{\mathrm{W}})\mathrm{LCOE}_n^{\mathrm{S}} \tag{6.5}$$

$$\mathrm{LCOE}_{\mathrm{mod.}}(\alpha_n^{\mathrm{W}}) = \mathrm{LCOE}_0(\alpha_n^{\mathrm{W}}) \cdot \frac{E_{\mathrm{generated}}(\alpha_n^{\mathrm{W}})}{E_{\mathrm{generated}}(\alpha_n^{\mathrm{W}}) - E_{\mathrm{curtailed}}(\alpha_n^{\mathrm{W}})} \tag{6.6}$$

This reflects that the LCOE are incurred for all the energy generated, but only recovered by sales of the non-curtailed part (in an idealized economy where retail prices equal the LCOE). Surplus generation thus becomes undesirable in this formulation, because it leads to an effective rise in LCOE.

6.2 Optimized VRES mixes for a fully renewable US

Feasibility of a highly renewable electricity supply has been shown in various studies [131, 136–138]. Here, we take a look at the mix between wind and solar PV with the three different optimization methods explained above. They are applied to a fully renewable US energy system, with a VRES gross share of $\gamma_n = 1$ for all FERC regions n. Storage energy capacity, backup energy, and levelized costs of renewable electricity generation are minimized. The mixes are all calculated in a scenario where each FERC region operates independently (that is, no inter-FERC transmission) as well as for full aggregation across the entire US (corresponding to unlimited transmission).

6.2.1 Minimizing storage energy capacity

The mix minimizing storage energy capacity needs is heavily leaning toward solar PV power, leading to almost exclusive use of solar for the southernmost FERC regions, see Fig. 6.2a. This is due to the general trend that solar irradiation shows less seasonal variation close to the equator, and is therefore more favorable in terms of storage needs, since these are mainly determined by seasonal timescales [50]. Additionally, the load in most of the US peaks in summer due to air conditioning needs. It is thus correlated with the solar PV power output, further shifting the US storage optimal mix toward solar PV. This mix may change when the seasonal load pattern in the US changes, e.g. due to more electrical vehicles being used and needing to be charged throughout the year. In contrast to the US, wind gains a higher share in the European storage optimal mixes, which are on the order of 50 %-60 % wind power [50]. This is due to two effects: The load in Europe peaks in winter due to heating and illumination needs and is thus anti-correlated to solar PV, and because of the higher latitudes, the seasonal variation in solar PV output is more pronounced. The aggregation of the entire contiguous US favors a higher share of wind, as shown in the leftmost bar of Fig. 6.2a.

The error bars in Fig. 6.2a indicate mixes that lead to storage energy capacities larger than the optimum by one percent of the load. They spread across 10 % to 25 % relative share. It is thus apparent that the sensitivity of the storage energy capacity to the mix is relatively weak: A large change in the mix leads to a rather small change in storage energy capacity.

The optimal storage energy capacity shown in Fig. 6.2b is around two to three months of average load, which is comparable with European values [50]. This figure also shows that a wind-

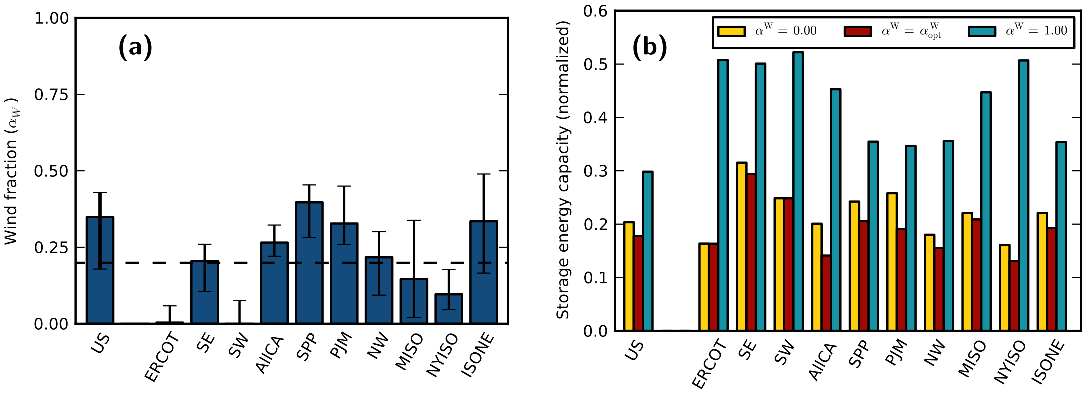

Figure 6.2: (a): Storage optimal mix between wind and solar power, given as the percentage of wind power, for the contiguous US FERC regions as well as their aggregation (marked "US"), at 100 % renewable penetration. This mix leads to minimal storage energy capacity needs (assuming that all residual loads have to be covered from a stored surplus; no storage losses). The error bars indicate mixes that lead to a storage energy capacity that is larger by one percent of the load than for the storage optimal mix. The dashed line marks the weighted average of the storage optimal mixes across all FERC regions. (b): Storage energy capacity, normalized by the average annual load, for different mixes of wind and solar PV power: Solar PV only, the storage optimal mix, and wind only.

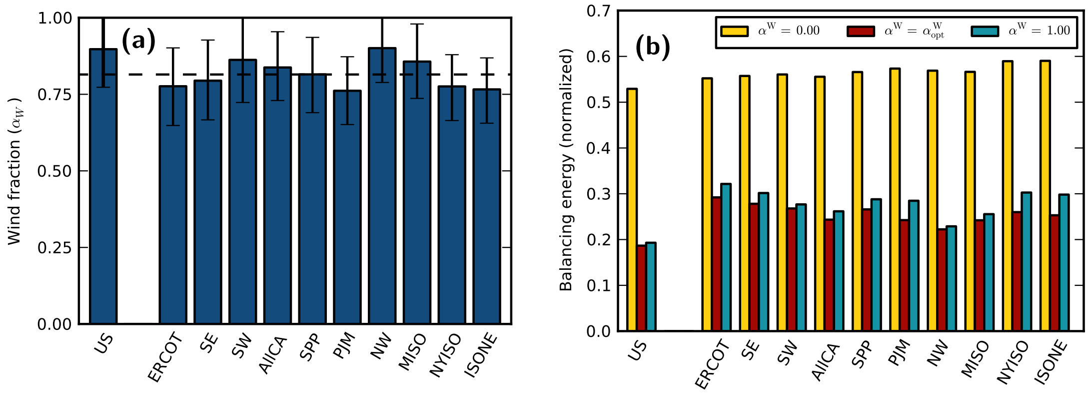

Figure 6.3: (a): Backup optimal mix between wind and solar power, given as the percentage of wind power, for the contiguous US FERC regions, at 100 % renewable penetration. This mix minimizes backup energy or, equivalently, residual load. The error bars extend to mixes that would lead to one additional percent of the total load being covered from dispatchable sources. The dashed line indicates the weighted average of the backup optimal mix across all FERC regions. (b): Backup energies for different mixes: Solar PV only, the backup optimal mix, and wind only.

only power system has a highly unfavorable effect on storage capacities needed, roughly tripling the storage needs in extreme cases such as ERCOT and, interestingly, also NYISO, which has very good wind resource quality, cf. Fig. 2.5.

6.2.2 Minimizing backup energy

In Fig. 6.3a, the backup optimal mix between wind and solar power is shown for the contiguous US FERC regions. It is seen that the mix minimizing residual load is around 80 % wind, almost homogeneously distributed throughout the country. Again, for the aggregated contiguous US, the share of wind is seen to rise, in this case to 90 %. This is due to long-range decorrelation effects in the range of 500 km to 1000 km [46, 47]. The total backup energy necessary is shown in Fig. 6.3b. For the backup-minimimal mix, single-region values range from a little more than 15 % to about 30 % of the annual load. Looking at other mixes, the solar PV-only mix is found to perform worst. This is easily explained, because PV only requires backup to cover the total demand for all hours when the sun does not shine, that is, at least half of the time. Both the backup optimal mix and the optimal backup energies are similar to what has been calculated earlier with the same method for Europe [53]. The only noticeable deviation occurs in the fully aggregated case, where for Europe optimal backup energies as low as 15 % of the annual load have been found, compared to 18 % for the contiguous US, see also Sec. 6.3.1.

6.2.3 Minimizing LCOE from VRES

We now calculate an optimized mix of wind and solar PV power based on their LCOE. Like in Sec. 6.2.2, the contiguous US with 100 % gross share of VRES are considered ($\gamma_n = 1$). It is assumed that no storage system is in place. Surplus generation (positive $\Delta_n(t)$ in Eq. (6.1)) is curtailed, while insufficient generation has to be balanced by dispatchable power.

LCOE-optimal mix

If the LCOE of wind and solar are equal in a given FERC region, the LCOE optimal mix reduces to the backup minimization discussed in Sec. 6.2.2. In this case, LCOE_0 in Eq. (6.6) becomes independent of the mix, and since the total generated VRES energy $E_{\text{generated}}$ is constant, the optimum is found when $E_{\text{curtailed}}$ is minimal. Since the average VRES generation equals the average load, the total curtailed energy is equal to the total backup energy, and therefore minimal

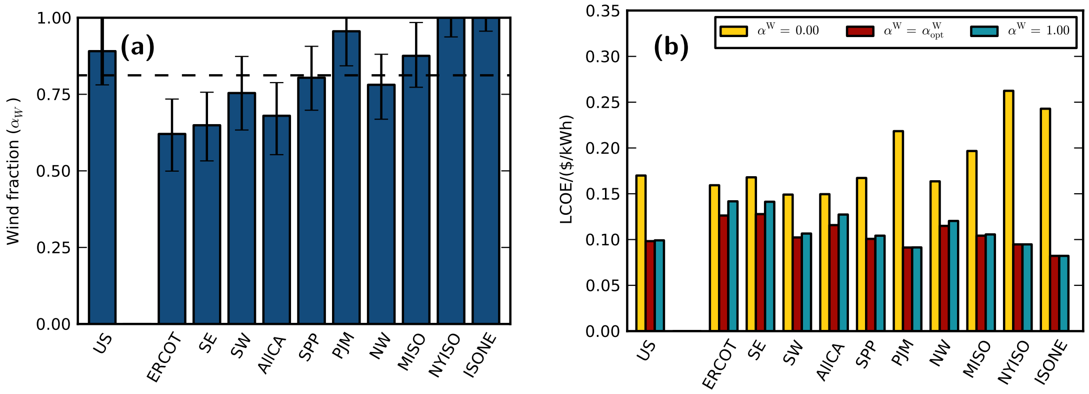

Figure 6.4: (a) LCOE-optimal mixes for the case of equal average wind and solar LCOE of 0.08 \$/kWh, calculated as described in Secs. 6.1.3. Note that (a) does not reproduce Fig. 6.3, because although the mean LCOE for wind and solar are the same here, they are not the same for all FERC regions. (b) Corresponding LCOE in the FERC regions as well as on an aggregated level (denoted ”US”), of different wind and solar mixes: Solar PV only, LCOE optimal mix, and wind only.

curtailment and minimal backup are equivalent here.

We first investigate a case where wind and solar power have the same average LCOE of 0.08 \$/kWh (before taking the regionalization from Eq. (6.4) or the curtailment corrections from Eq. (6.6) into account). Due to the regionalization of LCOE, this translates into different LCOE in the different FERC regions, and thus we do not simply reproduce the results of Sec. 6.2.2. Comparing the regional LCOE optimal mixes shown in Fig. 6.4a to the backup optimal mixes in Fig. 6.3a, we see a shift of the mix toward wind in the North East (particularly in ISONE and NYISO), where wind resources are very good and local wind LCOE are thus low, while it is shifted toward solar in the South (particularly in ERCOT, SE and AllCA) because of the good solar resources there.

The LCOE of different mixes (LCOE-optimal, solar only and wind only) is shown in Fig. 6.4b. It is apparent that picking the LCOE-optimal mix is able to reduce average LCOE significantly, especially compared to solar-only scenarios. For example, for the aggregated US (leftmost bars), solar only is 70 % more expensive than the optimal mix, and for the North East, it is more than twice as expensive. The LCOE for the aggregated US are about 0.10 \$/kWh, as could have been directly predicted from Eq. (6.6): Since wind and solar LCOE are equal in this case, the LCOE optimal mix equals the backup optimal mix. As calculated in Sec. 6.2.2, the optimal backup energy, which equals the curtailed energy, is 18 % of the load. Eq. (6.6) thus yields

$$\mathrm{LCOE}_{\mathrm{mod.}} = \mathrm{LCOE}_0 \cdot \frac{1}{1-0.18} = \frac{0.08\,\$/\mathrm{kWh}}{0.82} \approx 0.10\,\$/\mathrm{kWh}\,.$$

Sensitivity to different average LCOE ratios

Today, wind and solar PV differ significantly in their installation price, and they may continue to do so in the future. Various projections of average LCOE for wind and solar PV power across the US have been compiled by Open Energy Information (OpenEI) [139]. We use the price projections for 2020 from the most recent available reports (from 2012) to illustrate the large LCOE ranges, see Tab. 6.2.

To investigate the effect of different average wind and solar LCOE, we look at three combinations of wind and solar LCOE in addition to the equal prices discussed above. All in all, we use the following values from Tab. 6.2: 1) wind at its maximum and the lowest assumed price for solar, 2) wind at its maximum and solar at its lower quartile (which is the case of equal wind and solar LCOE shown above), 3) wind and solar both average, and 4) wind at its minimal assumed price and solar at its upper price quartile. It would have been straightforward to also include wind at its

Table 6.2: Levelized cost of electricity (LCOE) from various reports, as compiled by Open Energy Information (OpenEI [139]). For wind, only two reports were available, so the average is used instead of the median, and quartiles are not meaningful and therefore omitted. In order to calculate a mean price for wind (on- and offshore), a mix of 25 % offshore and 75 % onshore installations is assumed.

Technology	LCOE in $/kWh					# of reports
	min.	1st quartile	median	3rd quartile	max.	
Wind (onshore)	0.060	-	0.065	-	0.070	2
Wind (offshore)	0.100	-	0.105	-	0.110	2
Wind (75/25 mix)	0.070	-	0.075	-	0.080	2
Solar PV	0.040	0.080	0.120	0.190	0.240	12

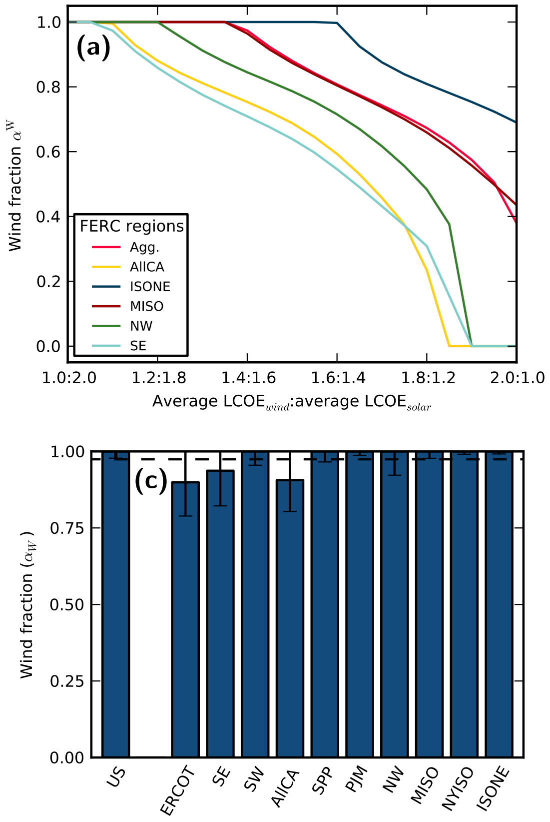

Figure 6.5: (a): Cost-optimal wind/solar mixes for five geographically representative FERC regions, for different ratios of the LCOE of wind and solar power. The regional differences in mix due to the climate differences are clearly visible: Southern FERC regions such as AllCA and SE switch to 100 % solar if this is half as expensive as wind, while other FERC regions never do. Conversely, if solar is twice as expensive as wind, all FERC regions switch to 100 % wind power, starting from the north eastern regions, here represented by ISONE. (b)-(d): Cost-optimal mixes for different average costs of wind and solar power: (b) wind 0.080 $/kWh, solar 0.040 $/kWh, (c) wind 0.075 $/kWh, solar 0.120 $/kWh, and (d) wind 0.070 $/kWh, solar 0.190 $/kWh.

lowest and solar PV at its highest as a fifth scenario, but this is skipped because 4) already leads to 100 % wind everywhere. The mean US mix of wind and solar power changes accordingly in the leftmost bars of Figs. 6.4a (equal LCOE) and 6.5b-d (other LCOE ratios). In this way, most of the available combinations of prices are sampled, since the LCOE-optimal mix (Eq. (6.6)) is sensitive to relative price differences between wind and solar only.

For the representative FERC regions of AllCA, ISONE, MISO, NW, and SE, as well as for the aggregated US, the impact of different wind and solar price ratios is also depicted in Fig. 6.5a, which shows the regional LCOE-optimal mix as a function of the ratio of average LCOE. We see that if wind LCOE are half of the solar LCOE on average, then 100 % wind will be the optimal mix for all FERC regions. Conversely, if average solar LCOE are half of the wind LCOE, this does *not* lead to a 100 % solar cost optimal mix in all FERC regions, cf. Fig. 6.5a. This is due to the large curtailment and backup such a mix entails. As seen in Sec. 6.2.2, the mix minimizing backup energy lies around 80 % wind. Solar only is very unfavorable because it would lead to large backup and curtailment needs, even if solar LCOE were much lower than wind LCOE.

Comparing the different LCOE combinations from Figs. 6.4a and 6.5b-d, we observe that the results when solar and wind have the same cost most closely match those from the NREL Renewable Electricity Futures study [131], which uses a cost-based optimization tool to determine the least-cost portfolio of generators, storage, and transmission for various scenarios of an 80 % renewable US electric system. In the NREL study, for the 2050 LCOE values for comparable installed capacity values, wind is more heavily installed in the Great Plains, Great Lakes, Central, Northwest, and Mid-Atlantic areas (roughly corresponding to the MISO, SPP, NW and PJM FERC regions) and solar is more heavily installed in CA, the Southwest, Texas, and the South (roughly corresponding to AllCA, SW, ERCOT, and SE FERC regions).

The high sensitivity of solar PV to prices, relative to that of wind, is corroborated by the significant price impact on solar PV build-out observed in Ref. [138]. The NREL Renewable Electricity Futures Study also recognized a high sensitivity of the solar energy (PV and CSP) build-out to varying cost estimates [131]. Furthermore, they found that the relative contributions of wind and solar generation were on average 75 % wind to 25 % solar across the contiguous US in their optimized scenario. This agrees well with the cost-optimal α^{W} value for equal wind and solar LCOE found here of slightly less than 80 %.

6.3 Optimal VRES build-up in the US

6.3.1 Minimal backup energy pathways

Backup energy minimizing build-up pathways have been calculated by optimizing the wind/solar mix for VRE gross shares between 0 % and 100 %, see Eq. (6.2) in Sec. 6.1. A detailed example is shown in Fig. 6.6a for California. The minimizing pathways for all other FERC regions are included in Fig. 6.6b. The figure presents the optimal pathway (white line), along which backup energy is minimal for each given VRES share. Additionally, parameter combinations that lead to increasingly more backup energy than the optimal path are indicated: In the green region, average backup energy requirement is less than 1 percentage point (pp) of the average load more than optimal, in the yellow region, 5 pp, in the red region, 25 pp, and in the dark red region, more than 25 pp. The green region is seen to successively shrink during the build-up, showing that the minimum in backup energy becomes more and more pronounced with growing VRE share. This observation is corroborated by Fig. 6.10a, where the backup energy needs are shown as a function of the wind/solar mix for several renewable gross shares. Only additional backup energy is included, which is required due to VRE fluctuations rather than insufficient VRE energy production. It is equal to the excess of backup energy over the expected "missing energy" of total electricity demand minus total VRES generation; see Sec. 6.1 for details.

In the early stage of VRE installations, until wind and solar PV cover about 30 % of the load, the sensitivity of backup energy need with respect to the mix of wind and solar is relatively low, because both wind and solar PV generation hardly ever exceed the demand, so all energy they produce can be used in the electricity system and no additional backup energy is required. Toward a fully renewable system, the mismatch between load and generation grows. Once VRE gross shares reach 30 % to 50 %, substantial VRE surplus generation and hence need for backup energy at other times occurs, which can be minimized using the mix of wind and solar PV as a handle. Backup minimal mixes are observed around 80 % wind and 20 % solar PV, with a spread of about 10 % across the FERC regions.

6.3.2 Minimal LCOE pathways

Country-average LCOE of wind and solar PV are first regionalized, mainly according to resource quality, as described in Sec. 6.1.3. For each region n, the resulting wind and solar PV regional LCOE are then combined into an average regional LCOE of VRES, depending on the relative wind share in VRES, α_n^{W}. These are then modified to account for the effects of surplus production: It is initially assumed that the surplus production has no value and thus effectively raises LCOE by reducing the amount of usable electric energy produced, as stated in Eq. 6.6. Notice that the amount of surplus energy here equals the amount of additional backup energy requirements due to VRES fluctuations, discussed in Sec. 6.3.1.

An LCOE-optimized VRES build-up path is shown in Fig. 6.7a for the example of California in detail, and similar pathways in Fig. 6.7b for all FERC regions. All pathways are calculated under the assumption of equal country-average VRES LCOE for wind and solar PV. In contrast to the backup optimal pathways of Figs. 6.6a and b, the LCOE optimal mix strongly favors the lower cost technology – solar PV for the California example under our cost assumptions – for low renewable penetrations, because in the early stages of the deployment, both can be integrated equally well into the system. Only when surplus production and additional backup requirements become an issue, around VRES gross shares of 30 % to 50 %, the mix shifts toward minimal backup energy requirements. This effect is further illustrated in Fig. 6.10b, where the shift of the LCOE minimum from least generation cost for low VRE gross shares toward least surplus/additional backup for higher shares is clearly visible. It can be interpreted as an indication that although in the short run it appears cheaper to settle for the lower generation cost resource, in the long run it pays to sustain a mixed portfolio, which is able to reduce backup energy needs and surplus production.

It is interesting to compare the build-up pathway for California obtained here to the results of the more detailed SWITCH model [138]. In contrast to our modeling, they assume a solar PV installation cost about twice as high as for wind, which results in early VRES growth almost exclusively in wind. Subsequently, solar PV costs are assumed to decrease in a steep learning curve, dropping almost down to the cost of onshore wind at the end of their simulation period in 2029. This leads to significant solar installations in later years. Similar to our modeling, VRES installations start with the lowest cost technology, which is complemented by others in the following

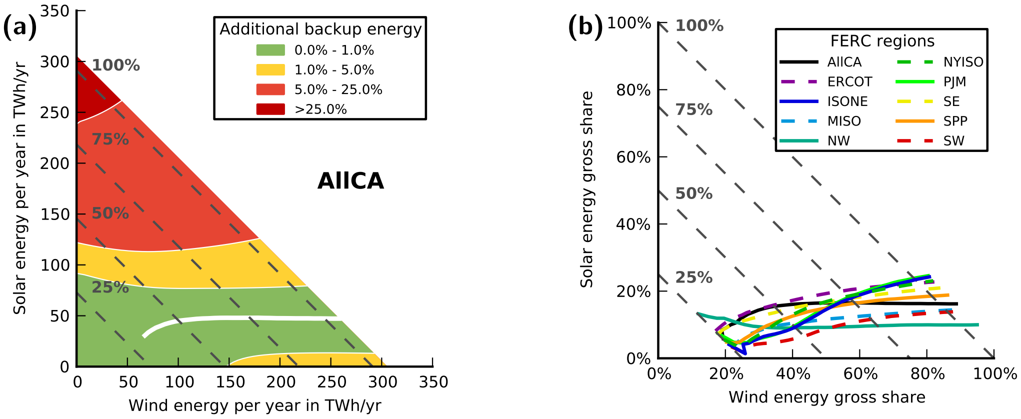

Figure 6.6: (a): Build-up pathway from a renewable gross share of 0 % to 100 % for California that minimizes backup energy needs (Eq. (6.2) in Sec. 6.1) during the entire renewable build-up. The white line indicates the build-up pathway minimizing backup energy requirements at the later stages of the installation process. In the green region, backup energy is up to 1 percentage point (pp) of the load larger than optimal. In the yellow region, it is up to 5 pp larger than optimal. In the light red region, it is up to 25 pp larger, and in the dark red region, more than 25 pp larger. The dark gray dashed lines indicate the renewable gross share γ_n of 25 %, 50 %, 75 %, and 100 %. (b): Build-up pathways minimizing backup energy for all FERC regions, analogous to the white line in (a), starting from 25 % VRE gross share. For lower shares, the minimum in backup energy is very shallow and not indicative.

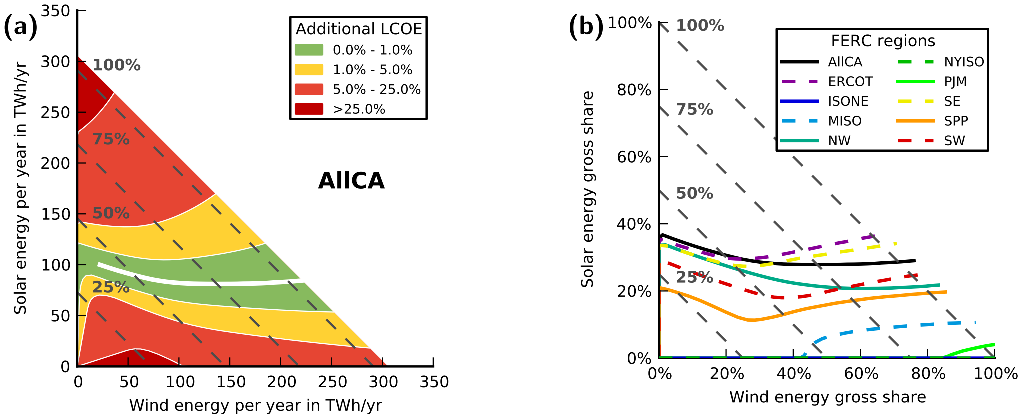

Figure 6.7: (a): Build-up pathway from a renewable gross share of 0 % to 100 % for California that minimizes combined renewable LCOE (Eq. (6.6)) during the entire renewable build-up. The white line indicates the build-up pathway minimizing LCOE at the later stages of the installation process. In the green region, LCOE are up to 1 percentage point (pp) larger than optimal (for the given renewable share $gamma_n$). In the yellow region, they are up to 5 pp larger than optimal. In the light red region they are up to 25 pp larger, and in the dark red region, more than 25 pp larger. The dark gray dashed lines indicate the renewable gross share γ_n of 25 %, 50 %, 75 %, and 100 %. LCOE are assumed to be equally 0.04 \$/kWh for both wind and solar PV on average across the contiguous US, which translates into 0.048 \$/kWh for wind and 0.036 \$/kWh for solar PV in California when LCOE are regionally adjusted (see Sec. 6.1). (b): LCOE-minimal build-up pathways for all FERC regions, analogous to the white line in (a). Note that since the LCOE-minimal mix for ISONE and NYISO is 100 % wind during the entire build-up, their pathways coincide with the x-axis.

years, as renewable shares grow. Due to the complexity of the SWITCH model, this analogous development cannot, however, be traced back to the same mechanism of avoiding backup energy needs and surplus production by shifting the mix that we observed in our model.

Note that, since LCOE are minimized for all renewable shares independently, the optimal build-up pathway (white line in Fig. 6.7a and paths in Fig. 6.7b) sometimes traces an uninstallation or under-usage of previously existing renewable capacity. However, the green region, where LCOE are less than one percent larger than optimal, is broad enough to accommodate a modified pathway that does not include uninstallation. An analogous statement holds for the minimal backup energy pathways, Figs. 6.6a and b.

6.3.3 Usage of surplus energy

It may be argued that no value of all occurring surplus energy is an unrealistic assumption. A future electricity system will likely include sources of flexibility to capture some value from surplus generation. For example, demand-side management measures or storage systems may be used, reducing surplus energy. Additionally, inter-FERC region transmission leads to surplus being exported to other parts of the country, where it can be used to replace backup energy. As shown in Sec. 5.3.1 that in a 100 % renewable scenario, unlimited transmission reduces the residual surplus by roughly one fifth.

To address such effects, modified LCOE-minimal pathways are investigated, where only a fraction of the surplus is treated as not giving any gain, thus subtracting only a fraction of the surplus energy from the total generated energy in the denominator of Eq. (6.6). For example, 20 % gain on the surplus could be achieved by recovering the full LCOE of 20 % of the surplus by selling it to some alternative consumer (e.g. storage, transmission, synthetic fuel production), or by recovering part of the LCOE on a corresponding larger fraction of the over-generation. The results are illustrated in Fig. 6.8a, again for the AllCA region. Shown are three cases where 20 %, 40 %, and 60 % of the incurred LCOE are gained from surplus energy. It is seen that while for the 20 % case, not much changes with respect to the no-value-surplus case depicted in Fig. 6.7, already 40 % of

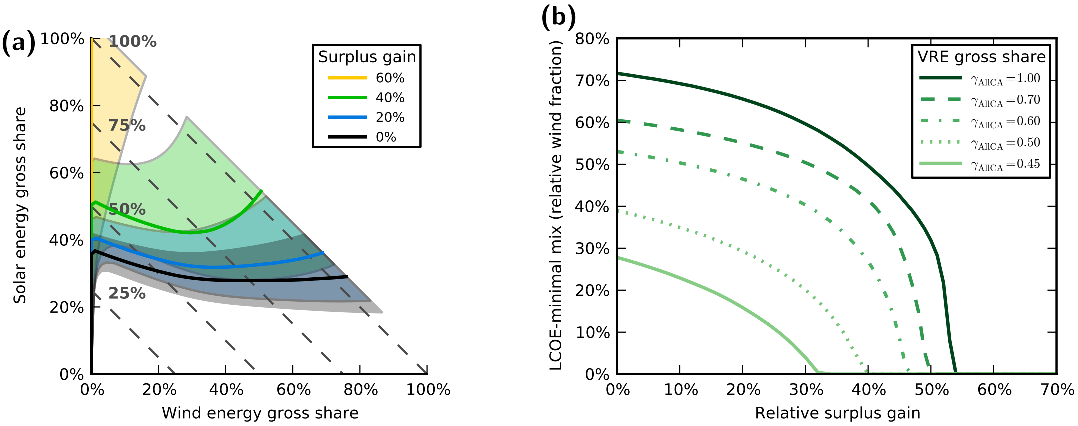

Figure 6.8: (a): LCOE-minimizing build-up pathways if it is possible to gain 0 %, 20 %, 40 %, and 60 % of the average LCOE for the surplus energy, for the example region AllCA, for wind and solar LCOE of 0.048 $/kWh and 0.036 $/kWh (before accounting for lower-value surplus), respectively. The shadowed regions indicate the 1 pp higher LCOE wind-solar combinations for each surplus gain percentage. (b) shows the LCOE-minimal mix for different VRE gross shares as a function of the surplus gain. The surplus gain can be realized by selling part of the surplus for the normal price, or all of it for a lower than normal price, or something in between.

the surplus energy's generation costs gained means a significant shift in the LCOE-minimal path toward the cheaper technology, in this example, solar. However, there is still a significant share of wind power in the 100 % LCOE-minimal mix. This changes beyond about 50 % of the gains on surplus energy, compare Fig. 6.8b, when the LCOE-minimal mix shifts to solar PV all the way to 100 % VRES gross share. In conclusion, a high share of the surplus energy has to be used for other goals than satisfying the electricity demand to shift the LCOE-minimal mix back to where it was on a pure generation-cost basis.

6.3.4 Sensitivity to different generation costs

Fig. 6.9a shows what happens to Fig. 6.7 when cost assumptions change. It depicts the LCOE-minimal build-up of wind and solar PV if the initial LCOE are changed such that one is 0.005 $/kWh more expensive and the other 0.005 $/$kWh$ less expensive. While this shifts the least-cost path toward the now cheaper technology, it does not change the qualitative characteristics of the picture.

These can be broken only if larger perturbations are applied, as shown in Fig. 6.9b. If LCOE of wind and solar PV are equal, the backup energy minimizing mix is picked. For lower wind LCOE, wind quickly becomes the only generation technology, while solar PV LCOE have to drop down to less than half of wind LCOE to make a solar PV only mix the cheapest option. This is due to the large mismatch between solar generation alone and the load. For all curves, the sensitivity to initial LCOE becomes lower and lower (curves are less steep) with increasing VRES gross share, because this leads to more surplus/additional backup energy that needs to be minimized besides generation costs.

6.3.5 Comparison and Conclusions

Fig. 6.10a shows that for low VRES gross shares, surplus production entailing additional backup energy needs hardly ever occurs, and thus the choice of the wind/solar mix is largely irrelevant for the backup energy minimization. Starting from a gross share of about 30 %, this changes: Surplus production sets in, and hence backup minimization becomes more important, leading to successively narrower minima in backup energy. The wind/solar mix becomes more important with growing installations. In contrast, for the LCOE (Fig. 6.10b), there is a clear minimum for small VRES gross shares on the side of the cheaper technology, in this example figure, solar PV.

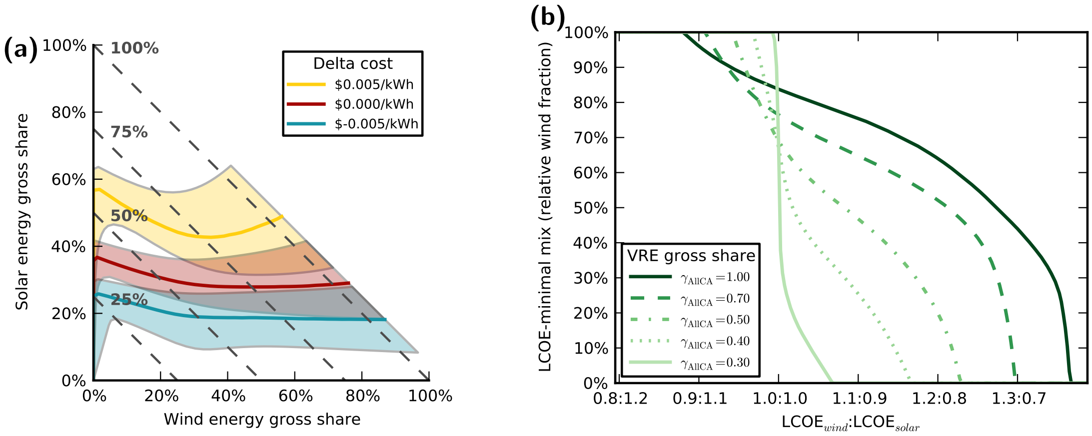

Figure 6.9: Cost sensitivity of the least cost build-up pathway. (a) shows the effect of cost changes on the optimal pathways, comparing three cases: (1) LCOE (before accounting for no-value surplus) remain unchanged at 0.036 $/kWh for solar and 0.048 $/kWh for wind (Delta cost = 0.000 $/kWh in the legend), (2) wind LCOE are reduced by 0.005 $/kWh and solar PV LCOE increased by 0.005 $/kWh (Delta cost = −0.005 $/kWh), and (3) wind LCOE increased by 0.005 $/kWh and solar PV LCOE reduced by 0.005 $/kWh (Delta cost = 0.005 $/kWh). The shaded areas indicate the regions where LCOE are less than 1 % larger than optimal. (b) shows the LCOE-minimal mix as a function of the LCOE ratio, for five different VRE gross shares.

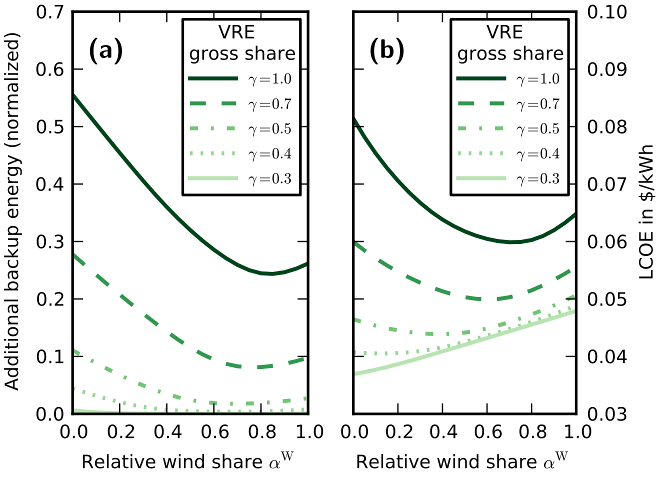

Figure 6.10: (a) Additional backup energy, normalized by the average load, and (b) LCOE as a function of the wind/solar mix, for different VRES gross shares γ, in the example FERC region AllCA.

Once surplus production begins, leading to economically disadvantageous loss of value, the minimal LCOE region starts to shift from lower installation and maintenance costs towards lower surplus production. The effect is mitigated if alternative usages of the surplus energy are found, however, unless more than half of the generation costs of the surplus energy can be recovered in some way, at 100 % VRES gross share, the LCOE-minimal mix still includes a significant share of the more expensive technology.

These observations can be interpreted in two ways: First, they can be taken as an indication that while in the beginning of the renewable build-up, least generation costs pathways can be pursued without incurring additional backup energy and subsequently additional costs, the picture changes drastically as soon as renewable penetrations reach beyond 30 %-50 %. Then, surplus production becomes an issue, technically as well as economically. One way of tackling this challenge is to examine the backup energy-minimal wind/solar mix and create a mixed renewable portfolio, even if generation costs alone clearly favor only one technology.

Second, the situation can be viewed as a high incentive to make use of (and thus gain from) VRES electricity over-generation. In the example of California with a VRES gross share of 100 % and LCOE-minimizing mixes, the minimal LCOE if surplus has no value is almost twice as high as in the case where all surplus earns the same value as grid electricity. Surplus usage can be achieved using inter-FERC-regional transmission, storage and demand-side management, and coupling of the electricity system to heating and transportation. A strong transmission grid that effectively allows for long-range aggregation of wind generation is able to smooth it considerably [41–43, 46, 47], thus providing a better match to the load. As is shown in Secs. 6.2.2 and 6.4 that aggregation of load and generation shifts the backup-minimal mix toward a higher wind share, and results in a reduction of backup energy needs by about 20 % in the contiguous US. Solar PV integration benefits much from short-term storage, which shifts the backup-minimal mix towards solar PV [52]. An alternative to solar PV combined with storage is concentrated solar power with inherent heat storage. Going beyond that, remaining over-generation in electricity can be used for heating or to produce CO_2-neutral synthetic fuels for aviation and road transport. This would lead to a strong coupling of future energy infrastructures across the three big energy sectors electricity, heating and cooling, and transportation.

6.4 Shift of optimal mix with transmission in Europe

In Sec. 3.1.4, six mix scenarios in addition to the base backup-minimal optimial mix have been defined. Three of them have an increasingly larger share of wind power generation and the other three have an increasingly larger share of solar power generation, leading to backup energy higher by 1 %, 2 %, and 5 % higher backup energy needs, respectively. We will now use these six additional scenarios and investigate the impact of different relative mixes between wind and solar power generation on the combined backup as well as transmission needs.

Fig. 6.11 shows the dependence of the annual European backup energy on the different mix scenarios and on the different transmission layouts for the final reference year 2050, in which all countries are assumed to have reached 100 % renewable gross share. Once transmission is introduced, a higher wind share performs better in terms of backup reduction. Compared to the base scenario, the two wind-heavy +1 % and +2 % scenarios result in a lower European-wide backup energy once the strong transmission layouts with 70 %, 90 %, and 100 % benefit of transmission (see Sec. 5.2) are considered. The result is consistent with [53], where an optimal end-point mix $\alpha^{W}_{\text{agg.}} = 0.822$ was found for aggregated Europe with unconstrained transmission capacity layout. The underlying reason for the shift towards more wind when large regions are interconnected is that the spatial correlation of wind power generation drops significantly over distances of 500 to 1000 km, while solar PV remains more correlated. The effect is well illustrated for the case of Sweden in [46]. When comparing the total backup energy required in the base scenario and the +1 % and +2 % wind heavy scenarios, it becomes clear that the absolute difference between the three is relatively small for the strong transmission capacity layouts. This is again demonstrated in Fig. 6.12a, which shows the backup energy as a function of the reference year, based on the 90 % benefit of transmission line capacities.

Fig. 6.12b illustrates the development of the total line capacities and reveals that a high wind share leads to higher transmission needs. This is due to the fact that for a high wind share, there is a high chance of covering a shortage in one country with excess from another. Solar PV power output, on the other hand, is much more correlated, being bound to the day-night pattern. Therefore, in case of a high share of solar PV, it is less probable that deficit and surplus production can cancel each other, implying less transmission needs.

The impact of the different scenarios for the relative mixes between wind and solar power generation on the combined backup and transmission needs is summarised in Tab. 6.3. An opposing trend is observed: whereas the backup energy decreases with an increasing, not-too-large share of wind power generation, it is the opposite for the total transmission capacity needs. This finding shows that when determining the complex features of a fully renewable energy system for Europe, it is not sufficient to look at isolated regions only, but also at the interplay between regions.

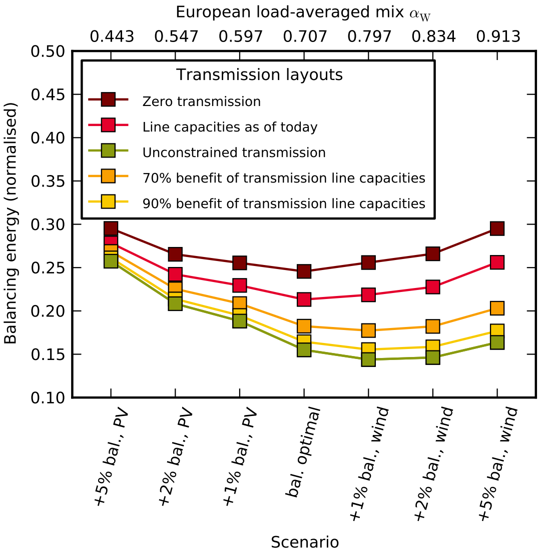

Figure 6.11: Annual European backup energy for different average end-point mix scenarios for the year 2050. Note that the average mix can be read off the nonlinear top axis. Backup is normalized by the average load.

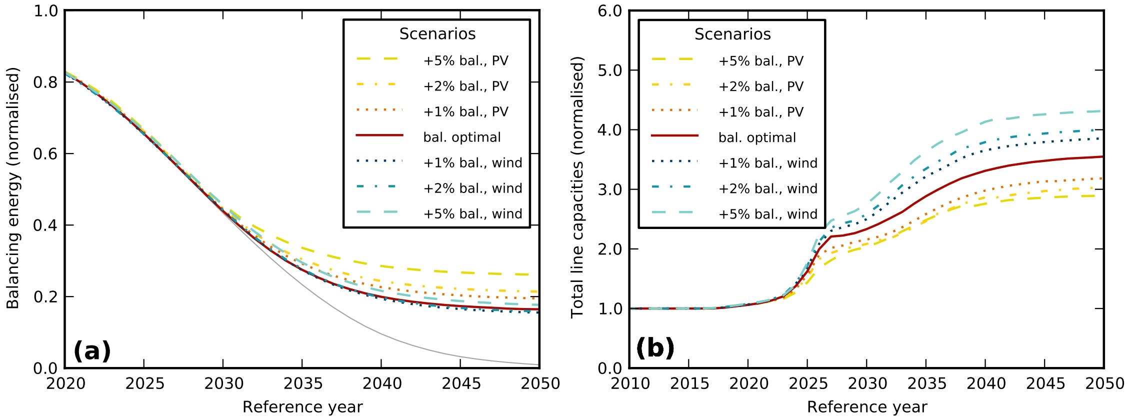

Figure 6.12: (a) Backup energy and (b) total net transfer capacities vs. reference year for the base scenario, the three wind heavy and the three solar heavy scenarios, based on the 90 % benefit of transmission line capacities (layout 5). Total net transfer capacities have been normalized by the total installation of today. The dark red curves for the base scenario in panels (a) and (b) are identical to the yellow curves in Figs. 5.3a and 5.5a, respectively.

Table 6.3: Backup energy needs and total transmission investment in 2050 resulting for different end-point mix scenarios, based on the 90 % benefit of transmission line capacities. All quantities are given as the relative deviation from the base scenario.

Scenario	Change in backup energy	Change in transmission investment
+5 % backup, PV	58.8 %	−18.9 %
+2 % backup, PV	30.0 %	−14.8 %
+1 % backup, PV	18.5 %	−10.6 %
base	0.0 %	0.0 %
+1 % backup, wind	−5.3 %	9.1 %
+2 % backup, wind	−3.5 %	13.1 %
+5 % backup, wind	7.9 %	22.0 %

Chapter 7

Backup flexibility classes

Up to now, we have treated the entire backup system as one black box, which is always able to produce what is required when it is required. This is a very coarse model, and this section deals with a refined version.

There are three "natural" timescales both in renewable production and in demand, also visible in Figs. 2.12 and 2.13. The first is the daily timescale. Demand varies according to human activity, which takes mainly place during the day. Supply changes mainly due to solar production varing with the sun's position, but wind can show daily patterns as well, consider for example sea and land breezes due to differential heating over land and ocean, that occur quite predictably along some coastal areas.

The second timescale is the synoptic timescale of one or two weeks. This is the typical time it takes a weather front to cross Europe. On the other side, weekly demand changes due to weekends are clearly recognizable.

Finally, the third timescale we want to consider is the seasonal timescale, where demand changes due to different heating and lightning needs, and production due to different solar position and general weather trends. In Europe, for example, significantly higher wind power production is observed during the winter [49].

In order to capture what happens on these timescales, we split the load into a weekly average, following the seasonal changes, a daily average, following the weekly changes, and the remaining hourly load, which depicts the daily pattern.

In the following sections, the split of load into different flexibility classes and the use of these to cover the mismatch between load and renewables is introduced first for single regions (7.1), before we come to the problem how to combine flexible dispatch with transmission (7.2). The work presented in Sec. 7.1 is a reworked version of previous work by Gorm Bruun Andresen and Morten Grud Rasmussen, which has been presented at the "10th International Workshop on Large-Scale Integration of Wind Power into Power Systems as well as on Transmission Networks for Offshore Wind Power Plants" in 2011, at the 2012 "European Energy Conference" in Maastricht, see the proceedings (Refs. [140, 141]), and in unpublished lectures.

7.1 Flexibility of single nodes

7.1.1 Guiding principles

The idea of this analysis is to determine the flexibility present in the system not in a bottom-up approach (i.e. obtaining data of presently installed dispatchable power generation), but rather in a top-down approach, just by examining the load pattern which it is able to follow. Flexibility in the power plant portfolio is present to avoid overgeneration, so the first principle we introduce is the minimization of (dispatchable) excess generation:

$$\min E(t) = \left(\sum_i B_i(t) - L(t)\right)_+ \tag{7.1}$$

where $L(t)$ is the (potentially residual) load in hour t, and $\sum_i B_i(t)$ is the sum over all backup flexibility classes. Since it is only a minimization rather than a strictly enforced condition, we think of it as a "soft constraint".

The second guiding principle is a "hard constraint", namely the security of supply. Instead of requiring that the load be met during all hours, which would lead to capacities determined by the extreme situation of a single hour, we demand that generation must be sufficient to cover the load during 99 % of all hours. This rather low security bound can be justified by considering that a future system is likely to include more flexible demand. Sufficient generation during 99 % can be formulated as

$$Q_{99\,\%}(\sum_i B_i - L) \overset{!}{\geq} 0\,, \tag{7.2}$$

where $Q_{99\,\%}$ denotes the 99 % quantile of the distribution of total generation minus total load. Whenever this is positive, generation is sufficient, and it is required to be positive during 99 % of all hours.

7.1.2 Method

The load on different timescales is calculated as moving averages, which are obtained by convolution of the load with Gaussian kernels of the width of the respective timescale. Our timescales are hours (no convolution, or if you like, a convolution with a "delta function", which would be an array with a 1 in one hour and zeros elsewhere in terms of our finite-resolution timeseries), days (24 hours) and weeks (168 hours). Properly normalized, the Gaussian kernel reads:

$$\mathrm{Ker}_\tau(t) = \sqrt{\frac{\pi}{2\tau^2}}e^{-\pi^2 t^2/(2\tau^2)}$$

7.1.3 Capacity determination

Before we consider dispatch of backup on the residual load, we first have to determine the present capacities from the load timeseries. We denote the capacities as K_slow, K_medium, and K_fast, and likewise the three backup timeseries as B_slow, B_medium, and B_fast. It is assumed that as much of the load as possible is covered by the slower systems, and that the faster systems only get as much capacity as is absolutely necessary. This is inspired by the idea that fast systems are generically more expensive and will not be built unless they are inexpendable. Furthermore, we assume that the present system provides enough flexibility to avoid all excess generation. For a visual aid to understand the decomposition, take a look at Fig. 7.3. The capacity calculation is done in the following way:

- Split load into slow moving average (convolution of load with Gaussian kernel of width 168 h) plus rest:
$$L(t) = L_\text{slow}(t) + L_\text{rest}(t)$$
- Shift L_slow downward by $\delta_\text{slow} = -\min_t L_\text{rest}(t)$ such that $L_\text{rest}(t) + \delta_\text{slow}$ becomes nonnegative at all times t.
- Assign the backup
$$B_\text{slow}(t) = (L_\text{slow}(t) - \delta_\text{slow})_+$$
to the slow backup system. The slow capacity becomes:
$$K_\text{slow} = \max_t B_\text{slow}(t)$$

- Split remaining uncovered load into medium and fast component:
$$L_{\text{rest}}(t) + \delta_{\text{slow}} = L_{\text{medium}}(t) + L_{\text{fast}}(t)$$
- Assign medium backup:
$$B_{\text{medium}}(t) = (L_{\text{medium}}(t) - \delta_{\text{medium}})_+$$
with $\delta_{\text{medium}} = -\min_t L_{\text{fast}}(t)$ such that $L_{\text{fast}}(t) + \delta_{\text{medium}}$ is nonnegative, and medium capacity:
$$K_{\text{medium}} = \max B_{\text{medium}}(t)$$
- Assign fast backup:
$$B_{\text{fast}}(t) = (L_{\text{fast}}(t) + \delta_{\text{medium}})_+$$
and fast capacity
$$K_{\text{fast}} = Q_{99\,\%}(B_{\text{fast}})$$

At this point, there is still some fine-tuning required. Taking the positive parts $(.)_+$ looks innocent, but ultimately leads to excess backup generation because negative summands are reduced to zero. Parts of that can be avoided by subtracting as much as possible of the excess from the fast dispatch. On top of that, the fast dispatch has to be modified to take into account that its capacity limit is below its maximal value:

$$\begin{aligned}
E(t) &= (B_{\text{slow}}(t) + B_{\text{medium}}(t) + B_{\text{fast}}(t) - L(t))_+ \\
B_{\text{fast}}(t) &= (B_{\text{fast}}(t) - E(t))_+ \\
B_{\text{fast}}(t) &= \min\{B_{\text{fast}}(t), K_{\text{fast}}\}
\end{aligned} \tag{7.3}$$

For the sake of readability, we will drop the explicit time dependence from now on. As a reminder, backup B and load L as well as excess E are time-dependent, while the shifts δ are not. Furthermore, it is still possible to reduce the total installed capacity by forcing the fast and medium system to cover the slow system's load peaks whenever it does not excess their combined capacity. This leads to reduced capacities and modified dispatch timeseries:

$$\begin{aligned}
K_{\text{slow,red}} &= \max\{(B_{\text{slow}} + B_{\text{medium}} + B_{\text{fast}}) - (K_{\text{medium}} + K_{\text{fast}})\} \\
K_{\text{medium,red}} &= \max\{(B_{\text{slow}} - K_{\text{slow,red}})_+ + B_{\text{medium}} + B_{\text{fast}} - K_{\text{fast}}\} \\
K_{\text{fast,red}} &= Q_{99\,\%}(L - \min\{B_{\text{slow}}, K_{\text{slow,red}}\} - \min\{B_{\text{medium}}, K_{\text{medium,red}}\})
\end{aligned} \tag{7.4}$$

$$\begin{aligned}
B_{\text{slow,red}} &= \max\{B_{\text{slow}}, K_{\text{slow,red}}\} \\
B_{\text{medium,red}} &= \max\{B_{\text{medium}} + (B_{\text{slow}} - K_{\text{slow,red}})_+, K_{\text{medium,red}}\} \\
B_{\text{fast,red}} &= \max\{B_{\text{fast}} + (B_{\text{medium}} + (B_{\text{slow}} - K_{\text{slow,red}})_+ - K_{\text{medium,red}})_+, K_{\text{fast,red}}\}
\end{aligned} \tag{7.5}$$

Notice that the sum of the three modified timeseries is still the same as before, only the distribution among the systems has changed. In the following, we will ommit the "red" index again.

7.1.4 Dispatch of flexible capacity

Here, the finite capacities and the objective of minimizing the excess is what drives the dispatch choices. Excess minimization is constrained by the condition that security of supply must be fulfilled. We dispatch from slow to fast in order to be able to accomodate the slow system (which causes most overgeneration) best, or, put differently, such that the faster systems can react to accomodate the slow system best. Since $K's$ are given, $\delta's$ determine dispatch uniquely. To calculate dispatch, we go from slowest to fastest. Dispatch of the ith system:

- Remaining residual load:
$$L_i = \left(L - \sum_{j\in\text{slower systems}} B_j\right)_+$$

- L_i is split into a moving average with width τ_i and the rest:

  $$L_i = L_{i,\tau_i} + L_{i,\text{rest}}$$

- Dispatch of ith system, taking into account capacity limits and removing negative generation:

  $$B_i(\delta_i) = \min\{K_i, (L_{i,\tau_i} - \delta_i)_+\}$$

At the end of this procedure, excess is subtracted from fast backup as much as possible like in Eq. (7.3) above, and capacities are reduced as in Eqs. (7.4) if possible.

The downward shifts of the single components, the $\delta's$, are now optimized numerically. Some heuristics can be applied to obtain a reasonable starting point for the optimization:

- δ_{slow}: The slow component should probably be shifted downwards as much as possible to avoid excess generation, therefore we guess that δ_{slow} should fulfill approximately

  $$\max(L - B_{\text{slow}}) \approx \max(L - L_{\text{slow}}) + \delta_{\text{slow}} \overset{!}{=} K_{\text{medium}} + K_{\text{fast}}\,.$$

- For δ_{medium}, we apply the same argument and require

  $$\max(L - B_{\text{slow}} - B_{\text{medium}}) \approx \max(L - L_{\text{slow}} - L_{\text{medium}}) + \delta_{\text{slow}} + \delta_{\text{medium}} \overset{!}{=} K_{\text{fast}}\,.$$

  For this calculation, we assume the δ_{slow} guessed above.

- δ_{fast} is the downward shift of the last remaining load component. The fast component is assigned the remaining load minus δ_{fast}. It is thus reasonable to assume $\delta_{\text{fast}} = 0$, because if it is positive, there will be excess generation during all hours, and if it is negative, generation will be insufficient during all hours.

7.1.5 Preliminary results

Scenarios compared

We will compare data from three different implementations:

1. A new implementation, which works as described above. It will be abbreviated MI.
2. A revised implementation by Gorm Bruun Andresen and Morten Grud Rasmussen, which will be abbreviated as GM in the following. In their method, power capacities are obtained in a nested fashion. K_{fast} is determined just like in my algorithm. K_{medium} and K_{slow} are, however, calculated using the dispatch algorithm: K_{medium} is obtained by setting K_{slow} to a large value, and successively reducing K_{medium} until the power dispatch algorithm returns surplus generation exceeding 10^{-3}, varying the medium capacity in steps of percents of the average load. Subsequently, K_{slow} is calculated as the smallest possible capacity such that the load is covered 99 % of the time, such that security of supply is guranteed. Furthermore, their dispatch algorithm itself also slightly differs from the MI implementation in the numerical optimization of δ_{slow} and the order in which positive parts are taken, capacities are reduced, and moving averages are calculated.
3. The original implementation by Andresen and Rasmussen, which will be abbreviated as GMO. The main difference to the revised version is the determination of K_{medium}, which is not as small as possible, as it turned out. Nonetheless, for this version, published results to compare against are available [140, 141], which is why it is used here.

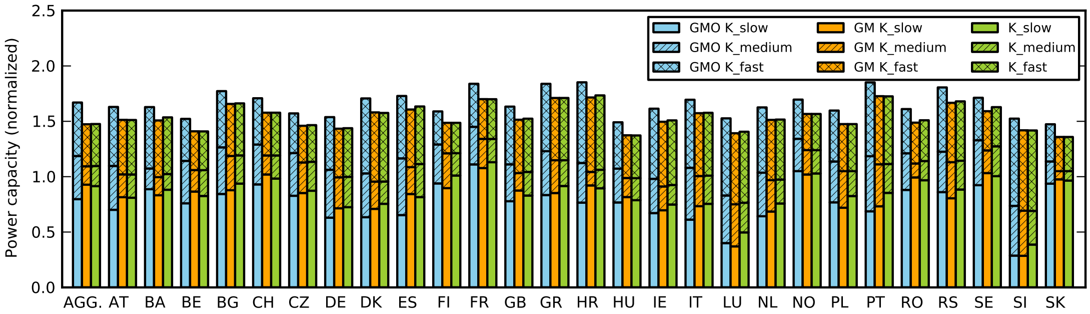

Figure 7.1: Power capacities obtained with the GMO implementation (blue bars), the GM implementation (yellow bars), and the MI implementation (green bars). Power capacities, normalized by mean load, are shown stacked from slow (not hatched) through medium (hatched) to fast (cross-hatched) capacity.

Power capacities

First, we compare the capacities obtained by the reimplementation MI with the results of the prior implementations GM and GMO. Fig. 7.1 shows all three sets of backup power capacities as stacked bars. Total capacity as well as fast capacity agrees very well between the GM and the MI codes. Since MI avoids excess altogether, while the GM algorithm allows for a certain extend, the MI fast capacities are slightly larger in some cases. The split between slow and medium capacity is more uneven between the two, compare the yellow and green bars. In most cases, the MI algorithm arrives at slighly higher K_{slow}, which is desirable since it is our intention to cover as much load as possible from low flexible capacity. In some cases, however, the opposite is true. For the GMO implementation, it is clearly visible that the medium power capacities are substantially larger than for the other two, resulting often in smaller slow capacities, but also in higher total power capacities.

Power dispatch: excess per node

Next, we take a look at the excess that results from the GM and the MI dispatch algorithm, for the GMO as well as for the MI power capacities shown above (blue respectively green bars in Fig. 7.1). The residual load to be covered by the backup system stems from a scenario in which renewable gross share is picked to be homogeneously $\gamma_n = 1$, and the wind/solar ratio is the backup energy-minimal mix for the individual countries as described in Sec. 6.2.2 (the weighted average of these is used for the European aggregation). The higher GMO medium power capacities (and their lower slow capacities) lead to significantly smaller excess values, as is to be expected. The agreement in total excess energy between the GM and the MI implementation is very close, which is an indication that the numerical optimization (Sec. 7.1.4) arrives at the desired results.

Power dispatch in detail

We compare the power dispatch from GM and MI for a couple of regions in detail. The MI power capacities, $\gamma_n = 1$ for all nodes, and backup energy-minimal wind/solar mixes are used. As seen above, relative excess is highest for Slovakia (SK), and lowest for the aggregation of all of Europe. Additionally, we look at the dispatch in a country with moderate excess, and pick Denmark. These three are shown in Fig. 7.3a-c. The dispatch is seen to agree very well between the two models. The three examples mainly differ in the level of slow dispatch, which is also the main cause of excess. Where fast and medium capacity are insufficient, such as in Slovakia, the slow dispatch is required to cover a large fraction of the residual load, and leads to high excess levels. On the other hand, in Denmark and more so in the European aggregation, when fast and medium capacities are sufficient, slow capacities will be dispatched only sparingly. In the case of aggregated Europe, the

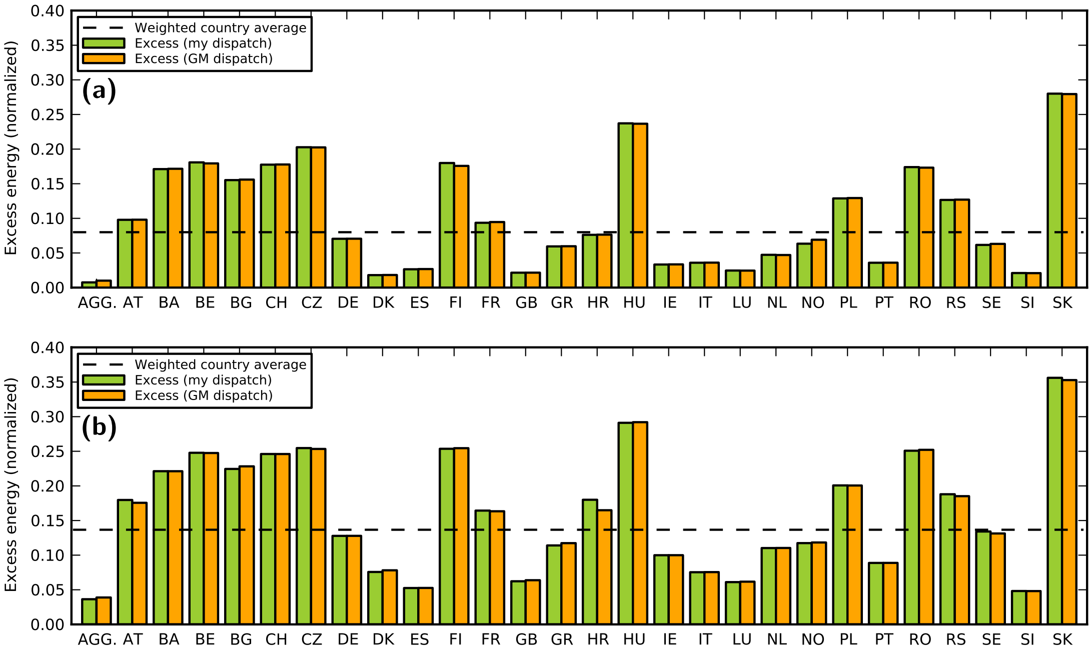

Figure 7.2: Excess energy, normalized by total load, for $\gamma_n = 1$ and backup-minimal α_n, for (a) old GMO power capacities, and (b) new MI power capacities (which agree quite well with the revised GM capacities, see Fig. 7.1).

additional benefit of a smoothed mismatch, leading to smaller fluctuations in residual load, also facilitates low-excess backup dispatch.

Excess as a function of renewable gross share

GM and MI codes with GMO power capacities The two codes are compared in detail, using the example of aggregated Europe. Plots of power capacities, backup excess, and total energy produced as a function of renewable gross share γ_n are shown in Fig. 7.4. Generally, results agree very well between the two implementations for the same set of start capacities.

For the power capacities (Fig. 7.4a and b), the development is quite parallel for $\gamma_n \leq 1$. After that, the MI implementation shows bumps which are likely due to numerical instabilities. They can occur because for each γ_n value, dispatch is calculated assuming the initial power capacities as a starting point. They are only reduced to the values reported in the figure after the dispatch. In this way, there is nothing to enforce that they are monotonously decreasing. Apart from that, the match is still quite close. Beyond $\gamma_n = 1.7$, the reduction in power capacities stalls for the GM implementation, for reasons that are not clear to me. It continues for the MI implementation, more or less as expected.

Excess is attributed to the single flexibility classes as follows:

- Slow excess:
$$E_{\text{slow}} = [B_{\text{slow}} - L]_+$$
- Medium excess:
$$E_{\text{medium}} = [(B_{\text{slow}} + B_{\text{medium}}) - E_{\text{slow}} - L]_+$$
- Fast excess: If our algorithms work correctly, fast excess should be avoided altogether because it is always possible to ramp down fast capacity when required. As a check, it is calculated as:
$$E_{\text{fast}} = [(B_{\text{slow}} + B_{\text{medium}} + B_{\text{fast}}) - (E_{\text{slow}} + E_{\text{medium}}) - L]_+$$

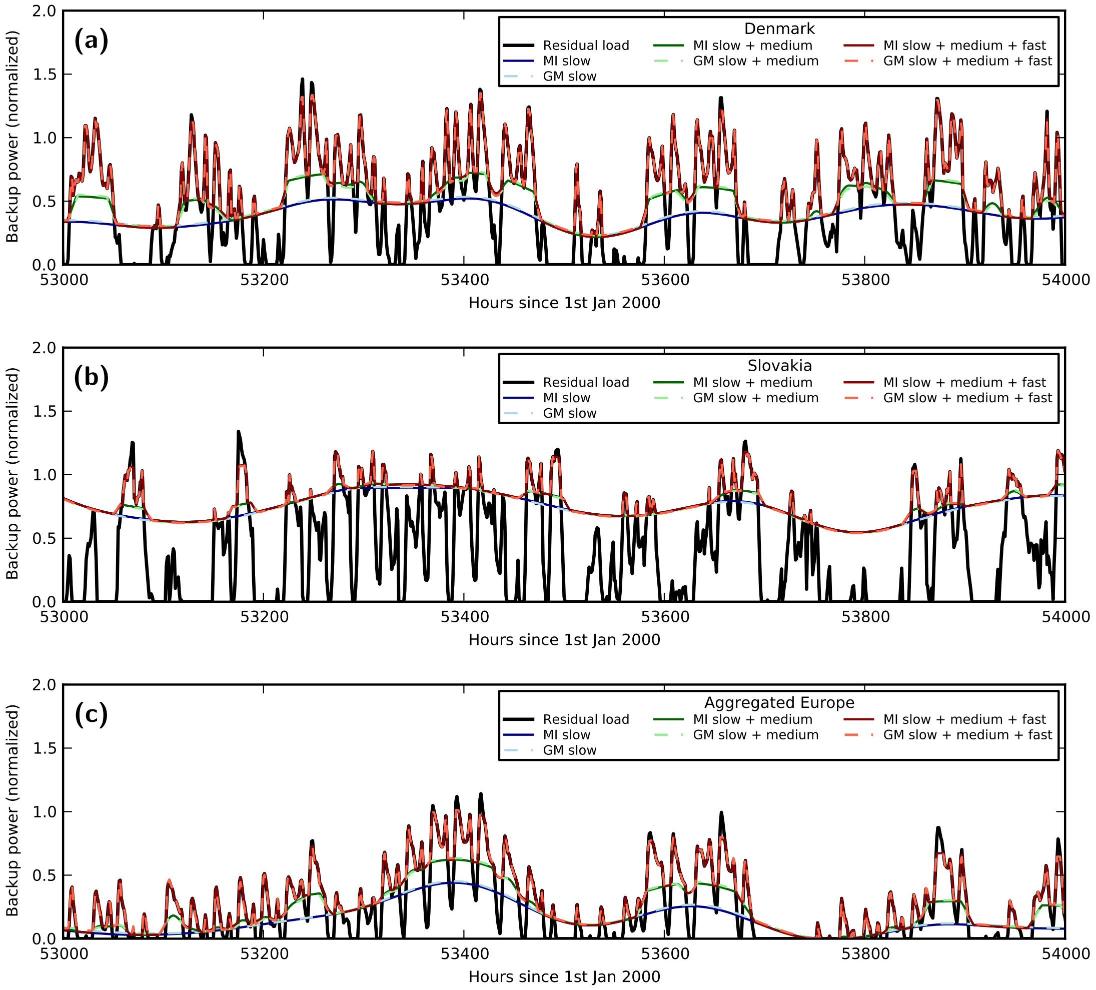

Figure 7.3: Backup power dispatch for $\gamma_n = 1$ and backup-minimal α_n, during the hours of largest residual load (summed over Europe), which occurs in January 2006 (in hour 53417) in our timeseries. Shown are the examples (a) Denmark, (b) Slovakia, and (c) aggregated Europe. The dispatch of the GM code is shown dashed, while the new MI implementation is shown as solid lines. The three flexibility classes' dispatch is shown stacked: The lowest line shows the slow dispatch alone, the next, slow plus medium dispatch, and the uppermost slow plus medium plus fast dispatch. In this way, it becomes visible how the dispatch subsequently covers the residual load. For reference, the residual load to be covered is shown as a black line in the background. All power output is normalized to mean load. The examples of Denmark and Slovakia are chosen because of their moderate respectively extremely high relative excess, whereas aggregated Europe covers the case of lowest excess, cf. Fig. 7.2.

Calculated excess (Fig. 7.4c and d) is below 1 % of the load all the time, with a peak at $\gamma_n = 1$, in agreement with the results of the GMO implementation for the aggregated case. For the European weighted average, when no international cooperation is assumed (not shown here), excess rises to about 7-8 % for all implementations.

The total energy production (Fig. 7.4e and f) is again very similar between the two implementations. If there were no excess generation, the total energy production would follow the dashed white horizontal line below $\gamma_n = 1$, and the diagonal dashed line above $\gamma_n = 1$. The backup system is seen to be gradually replaced by renewable generation, albeit only at renewable shares around $\gamma_n = 1.5$-2.

Aggregated vs averaged European countries Here, we compare the European weighted averaged country to a European aggregation. The former case corresponds to isolated countries,

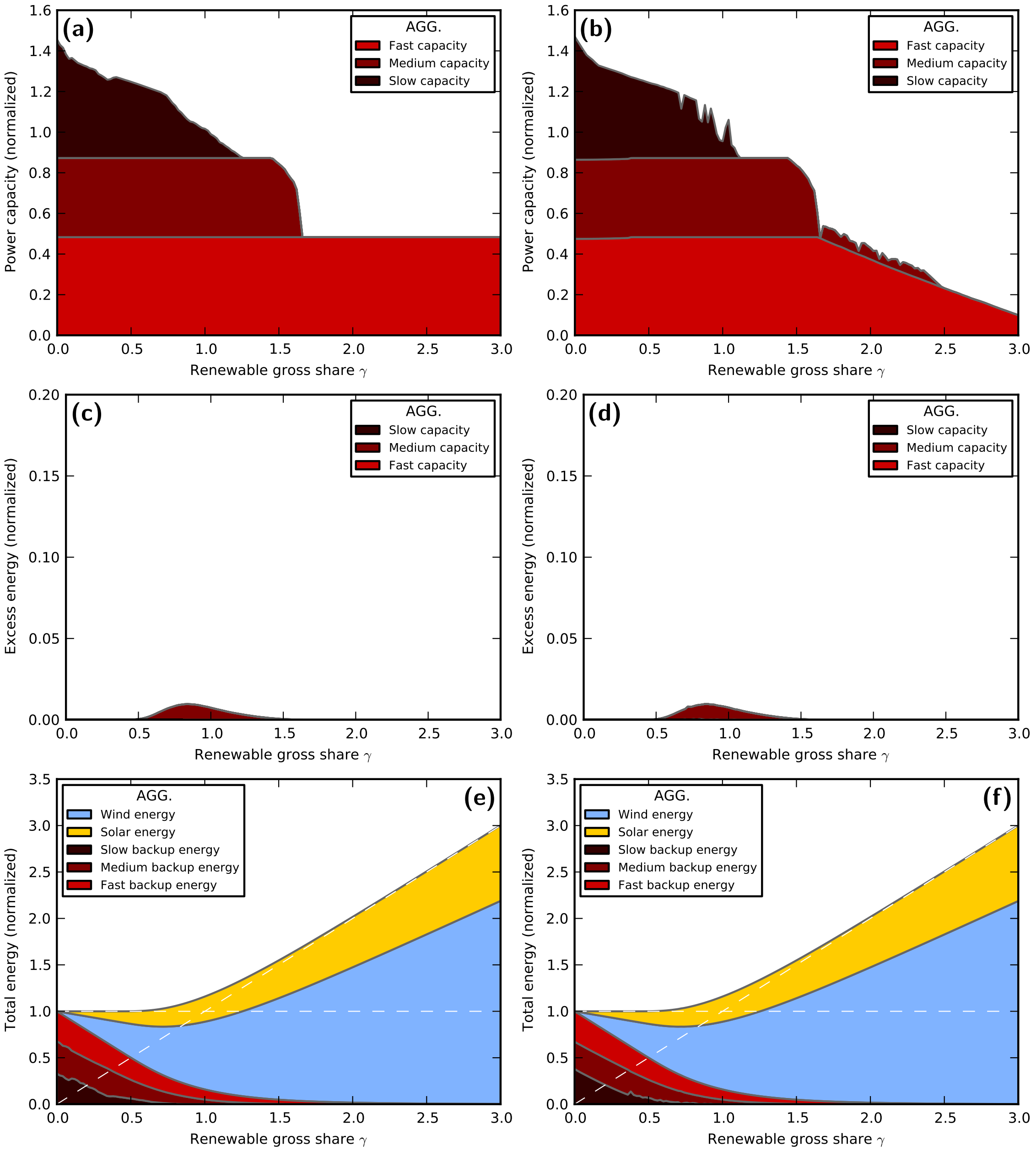

Figure 7.4: Comparison of GM (left) and MI (right) implementation, for the example of the European aggregation, starting out from the GMO backup power capacities. Panels (a) and (b) (upper row) show power capacities, divided into flexibility classes, as a function of renewable gross share γ_n. Capacities are normalized by mean load. Note that in both calculations, capacities are "reset" to their start values and reduced after the dispatch in each calculation for each renewable share γ_n. That explains why capacities (panels (a) and (b)) are not always monotonously decreasing. Panels (c) and (d) (middle row) show excess energy, attributed to the different flexiblity classes as described in the main text and normalized by total load. Finally, panels (e) and (f) (bottom row) depict the total energy generation by source (the renewables wind and PV, and the fast, medium, and slow backup), normalized by mean load. The white dashed lines indicate mean load (horizontal line) and γ_n, the largest possible share of renewables in the electricity mix.

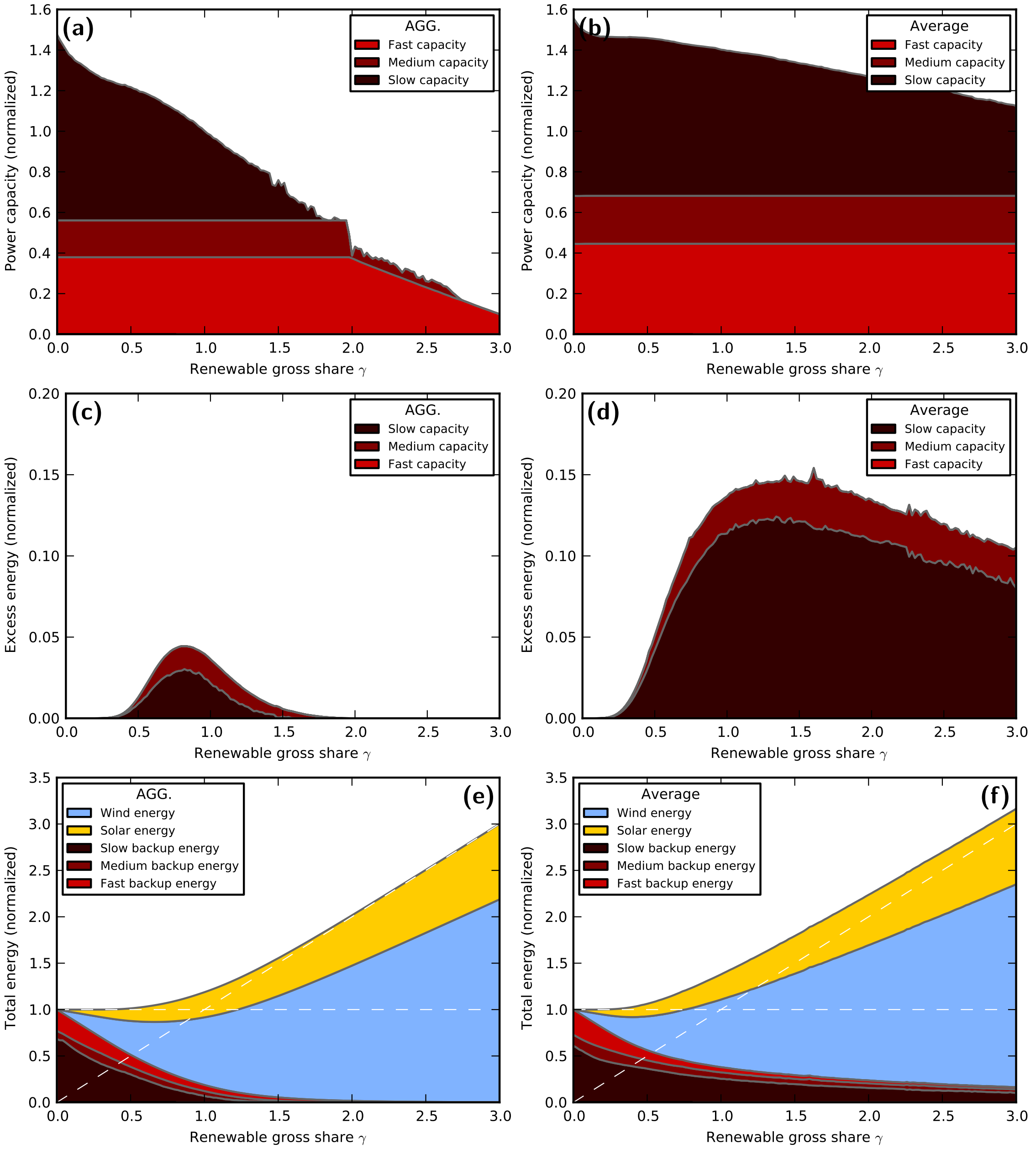

Figure 7.5: Comparison of European aggregation (now calculated with the MI implementation), corresponding to the most extreme form of cooperation (left) to the weighted average of the isolated countries (right). Panels (a) and (b) (upper row) show power capacities, divided into flexibility classes, as a function of renewable gross share γ_n. Capacities are normalized by mean load. Note that in both calculations, capacities are "reset" to their start values and reduced after the dispatch in each calculation for each renewable share γ_n. That explains why capacities (panels (a) and (b)) are not always monotonously decreasing. Moreover, the aggregated capacities in (a) are seen to be smaller than the load-weighted average of single node capacities in (b) right from the start at $\gamma = 0$, reflecting capacity reductions possible by aggregation even before renewables enter the electricity mix. Panels (c) and (d) (middle row) show excess energy, attributed to the different flexiblity classes as described in the main text and normalized by total load. Finally, panels (e) and (f) (bottom row) depict the total energy generation by source (the renewables wind and PV, and the fast, medium, and slow backup), normalized by mean load. The white dashed lines indicate mean load (horizontal line) and γ_n, the largest possible share of renewables in the electricity mix.

each serving their own needs, while the latter is the case of full Europe-wide cooperation, which means sharing of renewables as well as backup energy and backup power capacities completely. Results are shown in Fig. 7.5.

This time, we start out from the new set of capacities determined with the MI implementation. Since these include significantly less medium flexible power capacities, the overall excess generation rises, compare Fig. 7.4c and Fig. 7.5c.

European aggregation is seen to be highly favorable (Fig. 7.5) since it reduces both necessary power capacities and excess backup generation. Power capacities can be ramped down to close to zero at $\gamma_n = 3$ in the aggregated case, while even with this extremely high renewable gross share, only a reduction in slow capacity by about 50 % is possible. Excess generation is reduced significantly as well, its maximum dropping from 16 % of the total load down to 4-5 %. This also means a higher European renewable share in the electricity mix.

As discussed in the introduction, the main reason for flexiblity in the generation system is avoidance of excess generation. The driving question behind this investigation is whether or not already present flexibility is sufficient (at least at hourly timescales) to integrate a high share of renewables. Whether or not excess energy generation of 4-5 % is sufficiently low to answer this question with yes is up to the reader's judgement.

What we have definitely shown above is that European cooperation has the potential to facilitate the integration considerably. None of the two extreme cases compared here – full cooperation, with the need for a "sufficiently large" transmission grid, or no cooperation at all – is realistic. Therefore, we next investigate the effects of a transmission grid of limited strength, which provides an interpolation between the cases of no and full cooperation.

7.2 Flexibility on networks

The decomposition of backup power generation into three classes is assumed to be a given input in this chapter. It can be based on a Fourier-like decomposition as described above, but it could also come from some other source, like e.g. a ramp rate decomposition, where the slope of single components is predefined rather than its characteristic timescales, see e.g. Ref. [142] for a discussion of some other ways to measure flexibility. In this section, the question how to combine the decomposition with different amounts of transmission is addressed. The idea is to calculate the flexible backup dispatch for single nodes (no international transmission) as well as for aggregated ones (unlimited international transmission), and then interpolate between the cases of no transmission and full sharing in a suitable manner. In this way, transmission capacities become derived quantities; they are picked in such a way that they become sufficient for the desired amount of sharing of renewables as well as all three classes of backup generation.

To avoid confusion, we summarize the variable names used in this section in Tab. 7.1.

7.2.1 Flexibility and transmission

The calculation of the three flexibility classes' dispatch for the single nodes yields

$$K^0_{n,\text{slow}}, K^0_{n,\text{medium}}, K^0_{n,\text{fast}}, B^0_{n,\text{slow}}, B^0_{n,\text{medium}}, \text{ and } B^0_{n,\text{fast}}$$

For the aggregated nodes, we get

$$K^1_{\text{agg.,slow}}, K^1_{\text{agg.,medium}}, K^1_{\text{agg.,fast}}, B^1_{\text{agg.,slow}}, B^1_{\text{agg.,medium}}, \text{ and } B^1_{\text{agg.,fast}}$$

The first question is how to distribute the aggregated backup generation across the nodes in the full transmission case. We formulate two requirements:

$$\sum K^1_{n,\text{slow/medium/fast}} = K^1_{\text{agg.,slow/medium/fast}} \tag{7.6}$$

$$\sum B^1_{n,\text{slow/medium/fast}} = B^1_{\text{agg.,slow/medium/fast}} \tag{7.7}$$

Table 7.1: Variable names and their meaning

Variable name	Denoted quantity
n	index of a node
agg.	index of "all nodes", i.e. of the aggregated time series
L_n	load of node n
κ	transmission strength parameter: $\kappa = 0$ means no transmission lines, $\kappa = 1$ means as much transmission as desired (in any given situation)
$K^{\kappa}_{n,\text{slow}}$	capacity for the slow component of balancing at node n with a transmission strength κ
$K^{\kappa}_{n,\text{medium}}$	analogous to $K^{\kappa}_{n,\text{slow}}$ for the medium component of balancing
$K^{\kappa}_{n,\text{fast}}$	analogous to $K^{\kappa}_{n,\text{slow}}$ for the fast component of balancing
$B^{\kappa}_{n,\text{slow}}$	slow component of balancing at node n with a transmission strength κ
$B^{\kappa}_{n,\text{medium}}$	analogous to $B^{\kappa}_{n,\text{slow}}$ for the medium component of balancing
$B^{\kappa}_{n,\text{fast}}$	analogous to $B^{\kappa}_{n,\text{slow}}$ for the fast component of balancing
$\langle . \rangle$	time average of a quantity

Eq (7.6) states that we do not allow for overcapacities: In the worst hours, the nodes will have to cooperate to serve everybody's needs (up to the required security of supply). Eq (7.7) expresses that transmission losses are included. There is another, slightly more subtle requirement to be made: When splitting the backup up, care has to be taken not to distribute slower backup in such a way that it becomes faster backup by shifting it from one node to another from one hour to the next. That is, $B^1_{n,\text{slow/medium}}$ has to remain "smooth enough".

The simplest way to fulfil all of these conditions is to split backup up such that every node does the same, possibly scaled by a factor parametrizing its size. An obvious choice for such a factor is the fraction of the mean load of this node in the mean load of all nodes, yielding:

$$K^1_{n,\text{slow/medium/fast}} = \frac{\langle L_n \rangle}{\sum_m \langle L_m \rangle} K^1_{\text{agg.,slow/medium/fast}} \tag{7.8}$$

$$B^1_{n,\text{slow/medium/fast}} = \frac{\langle L_n \rangle}{\sum_m \langle L_m \rangle} B^1_{\text{agg.,slow/medium/fast}} \tag{7.9}$$

This will be the test bed case. There are other possible choices of this distribution. One main shortcoming of (7.8) and (7.9) is that it causes unnecessary transmission in hours where the renewable generation is slightly deficient. In these hours, having the nodes supply themselves would probably not exceed their capacities and save transmission, which in reality always comes with losses.

In an attempt to keep transmission capacities small, capped backup power capacities have successfully been implemented for the case of only one kind of backup (no splitting of backup in fast, medium, and slow, thus assuming perfect flexibility of all dispatchable power plants), as described in Sec. 4.4.2. This leads to nodes working to serve their own needs as long as they can, and sharing backup power only during the worst-case hours. A similar distribution of backup may be achievable here by looking at the backup distribution as it is found for self-sustaining nodes. In this case, every deficit remaining after sharing of renewables is covered by the node where it occurs. If we now want to assimilate the distribution of the three classes of flexibility to this, a possible direction to look into is taking the slow, medium and fast component of the residual load at each of the self-sustaining nodes and use these as some sort of weight. Such attempts are, however, beyond the scope of this work.

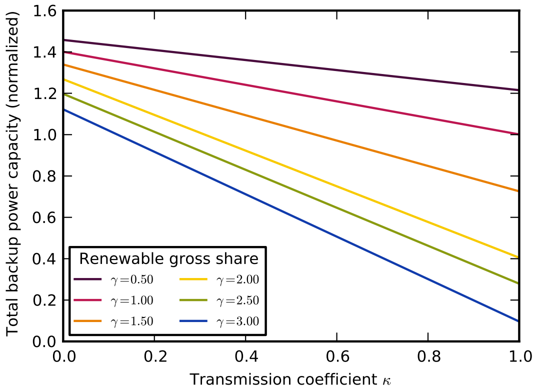

Figure 7.6: Total power capacity as a function of transmission parameter κ, for various renewable gross shares γ_n. Since backup generation is interpolated linearly between the single country case and the split of the aggregated case (cf. Eq. (7.9)), total power capacities are simply linear functions of the transmission parameter κ.

Different degrees of transmission availability are modelled by shifting the backup distribution gradually from the no transmission to the full transmission case. We set

$$B^{\kappa}_{n,\text{slow/medium/fast}} = (1-\kappa)B^{0}_{n,\text{slow/medium/fast}} + \kappa B^{1}_{n,\text{slow/medium/fast}}\,,$$

so a linear interpolation between the single node and the aggregated case is assumed. $\kappa \in [0,1]$ will be called the "transmission parameter". $\kappa = 0$ means no transmission, $\kappa = 1$ means full sharing of backup with however much transmission this entails. Once the backup distribution is fixed in this way, the flows F can be calculated from

$$\min F^2 \quad \text{such that} \quad \Delta_n + \sum_{x=\text{slow,medium,fast}} B^{\kappa}_{n,x} - (KF)_n \geq 0 \tag{7.10}$$

The required transmission capacities are then obtained as high quantiles or the minima and maxima of this flow.

A sticking point remaining with this way of obtaining the flows is that there are cases where load must be shed because generation is insufficient (the three flexibility class decomposition only goes to 99 % security of supply). This load is shed uniformly at all nodes that experience a deficit; a suitable percentage of their load remains uncovered. Without this modification, the flow problem (7.10) would become infeasible.

Since the solution of the transmission problem does get the chance to redistribute renewables among the nodes such that security of supply is fulfilled even better than the 99 % required in the definition of security of supply for the single nodes, the nodal security of supply increases in most cases. For small κ values, it goes up to as much as 100 %; for higher κ values, it stays a little lower.

7.2.2 Results

First, take a look at the total power capacity as a function of the transmission parameter κ, Fig. 7.6. As backup is interpolated in a linear fashion between the single country dispatch and (fractions of the) aggregated dispatch, backup power capacities simply depend linearly on κ. It is interesting to note how the effect of transmission increases from a maximal capacity reduction of less than 20 % for $\gamma = 0.5$ up to reductions by more than 90 % in the case of $\gamma = 3.0$. The higher the renewable share, the more benefit is to be reaped from European (or generally, inter-regional) cooperation.

The derived total transmission capacities are shown in Fig. 7.7, for different combinations of γ's and sufficiency quantiles (as a proxy to the fraction of all hours for which the link capacity is sufficient). They are calculated in the same way as in Sec. 5.2.2, as quantiles or maxima and minima

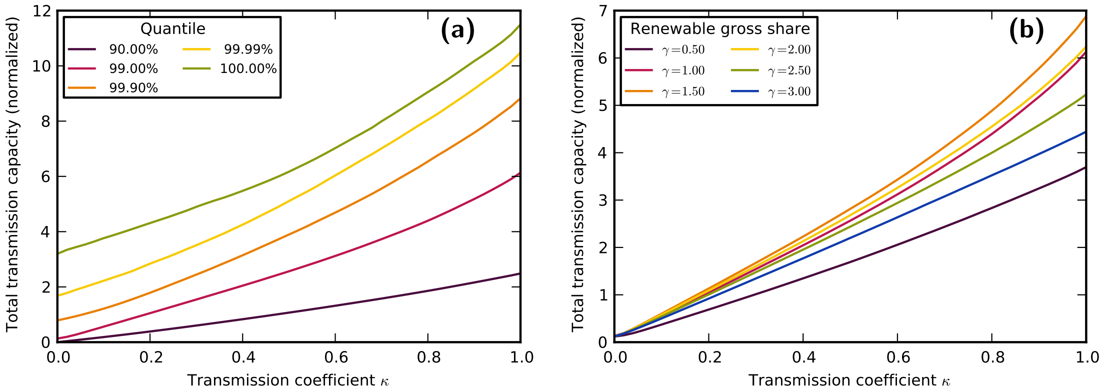

Figure 7.7: Necessary line capacities, normalized by the total line capacity available in winter 2010/2011 as reported by ENTSO-E [99] plus the BritNed, NorNed, and SwePol links [122–124], for the interpolation between single nodes and aggregated nodes, with an even splitting of backup among the nodes as described in Eq. (7.9). (a) shows the total line capacity as a function of transmission parameter κ for a renewable gross share of $\gamma = 1.$ for various quantiles for which the capacity should be sufficient: 90 % of all hours, 99 %, 99.9 %, 99.99 %, and 100 %. (b) shows the 99 % quantile for different γ values, covering the range between $\gamma = 0.5$ and $\gamma = 3.0$ in steps of 0.5.

of the flow distribution resulting from Eq. (7.10). Panel (a) shows how increasing security demands increase required transmission capacity for $\gamma = 1$, going from 90 % of all hours to 99 %, 99.9 %, 99.99 %, and 100 %. Roughly speaking, each additional "9" translates into additional transmission capacity of the order of 1-2 times the total capacity installed today.

It is salient how the transmission capacities for higher than 99 % sufficiency do not decrease to zero in the no-transmission limit $\kappa \to 0$ (see the green, yellow, and orange curves in Fig. 7.7), indicating rare, large flow events. These can be explained in the following way: Recall that the single-node dispatch only covers the load for 99 % of the time at each node. On the other hand, load shedding in the flow calculation employed here is only activated when there is a global deficit in the network. For some hours, it can therefore happen that there is no global deficit (and thus no load shedding), but local deficits at some nodes. These cancel with (renewable or dispatchable) surplus from other nodes. But this matching requires flows, including rare, large flow events that show up in the capacities for a sufficiency higher than 99 %. Since deficit hours are not time-aligned between the nodes, the network, in fact, experiences deficits in single nodes during more than 1 % of all hours, leading to non-zero capacities at $\kappa = 0$ even at 99 % sufficiency. These are, however, small enough to be neglected. All in all, it is considered appropriate to work with 99 % sufficient line capacities here.

Fig. 7.7b again depicts total line capacity as a function of transmission parameter κ, this time for a range of different γ values, all for a sufficiency quantile of 99 %. Here, an interesting observation can be made: While transmission capacity requirements first rise with rising renewable share, up to $\gamma = 1.5$, they decrease afterwards. While the $\gamma = 1.5$ transmission network needs about seven times the present capacity for full cooperation, the $\gamma = 3.0$ can make do with 4-5-fold of today's total capacity.

The transmission capacity layouts for a few example cases at $\gamma = 1$ are shown in Fig. 7.8. For $\kappa = 0$, no transmission network is present, so this case is omitted. Shown are $\kappa = 0.24$ in (a), $\kappa = 0.50$ in (b), $\kappa = 0.74$ in (c), and $\kappa = 1.00$ in (d). The total network capacity is comparable between these plots and Fig. 5.1, but the capacity distribution across the links is slightly different.

As derived quantities, the capacities discussed here can be smaller than presently installed capacities. But, already for $\kappa = 0.24$, there are only a few links of the same size, compare Figs. 7.8a and b to Fig. 5.1a, which shows present-time capacities. Strong reinforcements are seen for all of the sea cables (GB-FR, GB-NL, NO-NL, SE-DE, SE-PL, IT-GR) as well as the link across the Pyrenees between France and Spain. This means that for most links, already present capacities are not sufficient for sharing of backup with a transmission factor as low as of $\kappa = 0.24$.

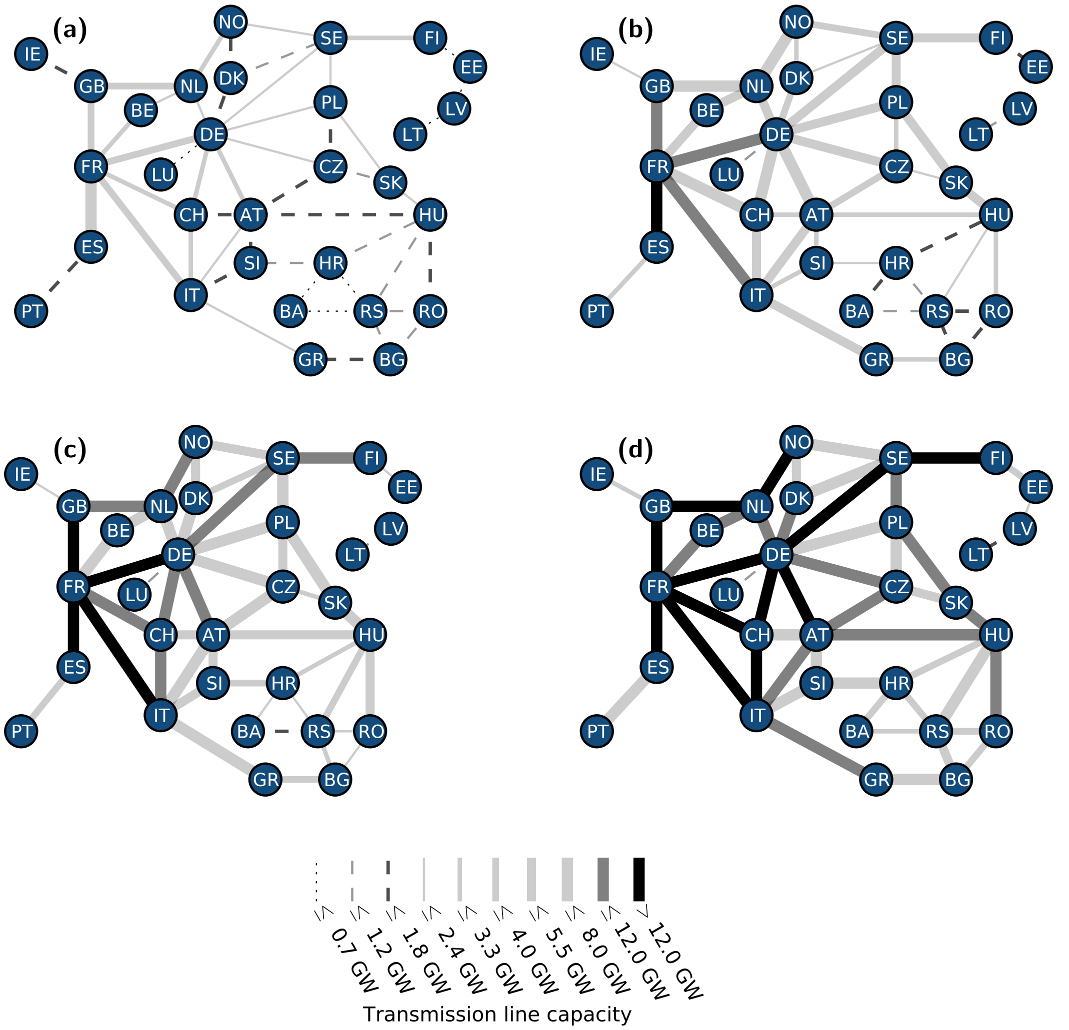

Figure 7.8: Different network capacity layouts, all for $\gamma = 1$ and a sufficiency of 99 %, with increasing transmission parameter: $\kappa = 0.24$ in (a), $\kappa = 0.50$ in (b), $\kappa = 0.74$ in (c), and $\kappa = 1.00$ in (d). The κ values were chosen according to the numerical resolution of (already performed) example calculations.

When comparing the network capacities depicted above for higher transmission factors (Figs. 7.8b, c and d) with the proposed transmission grid extensions shown in Figs. 5.1c and d, it is noticed that $\kappa = 0.5$ becomes feasible (for 99 % of the time) with the proposed 2035 transmission grid (Fig. 5.1c). For higher transmission parameters, a reinforcement stronger than the proposed 2050 line capacities is necessary. This is in accordance with the observation that total line capacities increase by a factor of roughly four in the scenario discussed in Sec. 5.2 for the 90 % benefit of transmission capacities depicted in Fig. 5.1, while here, we observe total capacities of about six times what is present today for $\kappa = 1$ at $\gamma = 1$, cf. Fig. 7.7.

Chapter 8

Conclusions

8.1 Main results

This work spans a broad scope of features of renewable electricity systems: On the basis of weather-driven generation data, partly calculated in this work and combined with other sources previously collected in the group, a future electricity system, based to a large extend on variable renewable wind and solar PV (variable renewable energy sources, VRES) generation, has been investigated. Central to all considerations is the mismatch between the weather-dependent renewable generation and the load. If it were not for this mismatch, every energy unit of electricity produced from renewables could directly be used to replace conventional, dispatchable generation. As it is, even in scenarios where VRES produce on average as much energy as is consumed, about a quarter of the consumption has to be met from other sources than directly from VRES, because generation is not sufficient during all hours. Different measures can be taken to cover this amount: A storage system can be introduced, shifting overgeneration during some hours to deficits at other times. A backup system of dispatchable power plants (renewable or non-renewable) can be used. An international transmission network, distributing the mismatch over the scale of continents – distances of about 1000 km –, can significantly smooth the mismatch and mitigate residual deficits. Additionally, it is very important to pick the right mix of wind and solar PV power to reduce the strain on the complementary systems.

Here, different parts and properties of electricity grids with a high share of wind and solar PV power have been explored. The effect of the transmission grid on the integration of renewables is analyzed for the example cases of Europe and the US. Dispatch and flow algorithms are developed, to maximize VRES usage and minimize the need for backup energy (∼ fuel needs in dispatchable plants) while keeping flow dissipation small. Apart from backup energy, backup power capacity (∼ number of dispatchable power plants to be kept online) is addressed as well and reduced significantly in a variant of the original dispatch and flow algorithm. On the basis of the flow and dispatch algorithms, transmission grid extensions are constructed with the objective of reducing backup energy even more, while keeping new line investments in a reasonable range. Further expanding this investigation of the interplay between backup system and transmission grid, backup energy and capacity needs in a future system have been examined more closely by decomposing the residual load into components with different time constants. These are assumed to be covered from dispatchable plants of different flexibility. In this way, the requirements on backup and transmission in a far-future, predominantly VRES based system have been identified, indicating the possibility of partly phasing out conventionals. Moreover, effects of the mix between wind and solar PV power on storage needs, backup needs, and levelized costs of electricity have been investigated, revealing substantial potential for reduction in the requirements on non-VRES system components by picking the right relative amount of wind and sun in the system. We will now go through the results in detail.

In Ch. 2, we have introduced a novel, long-term and high-resolution dataset of generation data for wind and solar PV for the contiguous US. To obtain the wind dataset, the conversion algorithm has been refined considerably. Introducing the methods of Refs. [74, 75] to the conversion framework provided in Refs. [37, 66], we were able to construct credible wind time series. Included are now the effects of surface roughness, that is, the land surface structure (e.g. buildings, forests, grassland; see Tab. B.1 for details) and orography (hills and valleys) on spatial wind power variability. Specifically, the variance in wind speed has been calculated from the variance in land cover and elevation. Furthermore, siting was accounted for by an effective model. It assumes a Gaussian distribution of deviations in wind speed and only considers the windiest 20 % of the area to be eligible for wind turbines.

A large part of the present work deals with the interaction between the renewable mismatch, the backup system, and the transmission grid. As we want to treat situations with line capacity constraints and global mismatches, the common DC power flow approach cannot be used. Instead, the DC power flow is examined thoroughly and generalized in different ways in Ch. 4. Working with global mismatches means that in addition to a pure power flow, dispatch or curtailment decisions need to be taken: Where should backup power be produced? And where should excess power be shed? Two slightly different ideas are presented. Both first use power flow to reduce the total need for backup energy as much as possible. The first algorithm then dispatches backup (or distributes curtailment) such that total flow dissipation is minimized. The flow minimization entails that backup energy is always produced locally, at those nodes that cannot import enough energy to cover their deficits. Likewise, curtailment is always local. Only VRES generation is shifted between the nodes.

As this approach leads to relatively high backup power capacities, a modification is developed: In addition to the steps described above, backup power capacities are capped at a low, sufficient level. This leads to a redistribution of backup generation during the hours of largest deficits such that nodes share backup, but does not alter the dispatch during “normal” hours.

After making use of a given transmission grid to reduce backup energy, the next step is to construct transmission grid extensions to decrease backup energy requirements even further (Ch. 5). Fortunately, it could be proved in this work that this task is a convex problem, making it well-behaved both mathematically and numerically.

Since the problem is still computationally expensive, a heuristic approach is chosen for a detailed study performed for Europe: Quantiles of the unconstrained flow are employed as a guess for an effective transmission capacity layout. For this study, VRES installations are extrapolated between historical values and fully renewable ($\gamma = 100\,\%$) 2050 targets, using logistic growth curves as introduced in Ch. 3. The main growth in renewable installations is observed between 2015 and 2035 for wind and between 2020 and 2040 for solar PV. Lines are modeled to be built in parallel, such that backup energy is reduced by a constant fraction throughout the years. Corresponding to the renewable installation growth, new transmission capacity is mainly installed between 2020 and 2035. It is found that to achieve a decrease of backup energy by 90 % of what is possible by transmission, about four times the total grid capacity of today is necessary. As this would have to be built over the course of more than thirty years, the proposal seems realizable. If only a reduction by 70 % is demanded, then twice today’s amount is sufficient.

There is a lower limit to backup energy reduction while renewable gross shares are below $\gamma = 100\,\%$. In this case, total VRES generation falls short of total load by a fraction of $(1 - \gamma)$. This insufficient VRES generation has to be covered by complementary backup. Backup energy needs beyond this minimum, which are due to the mismatch between load and generation, become an issue at a VRES gross share around 35 % (corresponding to the year 2025 in our model) without a transmission grid. With an unconstrained grid, this effect can be postponed to $\gamma = 50\,\%$, corresponding to the year 2035.

Along with the transmission grid, the export and import opportunities of single countries are seen to change. Generally, VRES exchange is aided by a strong transmission grid. This is especially important for peripheral countries which reach high renewable shares early, like Ireland or Spain. With a strong transmission grid, they see good export opportunities, especially during the early years of the renewable transition. Import and export is, however, limited not only by line capacities but also by the correlations in the renewable generation. This becomes more and more important towards later years, when all countries reach substantial renewable shares. In the fully renewable (2050) endpoint scenario, backup energy can only be reduced by about 40 % (from 24 % to 15 % of the average European load) via transmission. For the average country, this means that they can import only 40 % of their deficit or export about 40 % of their surplus generation in the end-point (2050) scenario. Single countries fare better or worse, depending on their load size and network position.

Another observation regarding different transmission layouts is the shift of the optimal mix: For the average European country, it is around 70 % wind when it is considered isolated from the rest. Aggregated Europe – corresponding to a strong international transmission grid – sees an optimal mix above 80 % wind. This is due to the better wind integration that comes with spatial aggregation over scales longer than the typical correlation length of 500-1000 km [46]. For solar PV, decorrelation effects are much less pronounced as it is bound to the day-night-cycle.

As a second example of transmission grid extensions, an explicit optimization of the transmission grid has been accomplished for the US. Compared to a quantile layout of equal size, the optimized layout is found to reduce backup energy slightly more. More importantly, when the layouts are scaled such that they lead to the same amount of backup energy, the optimized layout is 10 % more cost-effective.

In the last chapter (Ch. 7), the backup system is modeled in more detail, and the interaction of the extended model with the transmission grid is examined. Backup is split into three different flexibility classes, corresponding to different timescales, namely the seasonal, synoptic, and daily scale. This is not done using the bottom-up approach of counting present power plants and tracking their flexibility, but by decomposing the load time series – which the conventional plants are able to follow – in a Fourier-like manner. In this way, lower bounds on present flexible capacity are derived directly. It is then investigated whether these capacities are sufficient during the transition to VRES, and when they can be phased out. It turns out that if one accepts a conventional overproduction of 4 % of the average load, the present capacities are sufficient to guarantee 99 % security of supply. Calculating with some less stringent capacity constraints can even reduce the excess production below 1 %.

In addition to avoiding excess, renewable generation turns out to be able to replace some or all of the dispatchable capacity: Beginning with the slowest plants, conventional capacity can be decreased considerably. Starting at 1.5 times the average load when no renewable generation is present, they arrive at a little more than 1.0 times the average load at a VRES gross share of 100 %. Aggressive overinstallation could bring conventional power capacity down below 10 % of the average load, albeit only at $\gamma = 300\,\%$.

However, as a prerequisite to both little excess and capacity replacement, European cooperation is required. Otherwise, excess generation rises up to about 15 %, while capacity reductions become almost impossible. This means that backup as well as VRES have to be shared. A possible grid for this purpose is constructed explicitly. It turns out to be a little larger than the network constructed above for the fully renewable case ($\gamma = 100\,\%$), with about 6-7 times the total capacity of today's grid. Notably, overinstallation could reduce grid requirements somewhat, down to 4-5 times today's capacity.

Apart from the detailed investigation of the interaction of backup system and transmission, the effects of the mix between wind and solar PV power on single system components have been explored in Ch. 6. In the Federal Electricity Regulatory Council (FERC) regions comprising the contiguous US, several scenarios have been examined: VRES plus storage and VRES plus backup power plants, with the objectives of either reducing storage energy capacity, backup energy, or levelized costs of electricity from VRES. It turns out that backup energy needs are minimal for a wind share of 70 %-80 %. Comparable values have been observed previously for Europe [53]. These mixes reduce backup energy from more than 50 % for a hypothetical solar PV only system down to about 25 % for the single FERC regions and about 20 % for an aggregated contiguous US (corresponding to unlimited transmission capacities). Again, similar values are seen for Europe, with the notable exception that the backup energy drops as low as 15 % of the total consumption for a European aggregation.

The storage optimal mix for the FERC regions is close to 100 % solar PV for the Southern FERC regions, and never falling below 50 % solar share. This is in marked difference to Europe, where storage optimal mixes also contain more solar PV than backup energy minimal mixes, too, but generally remain above 30 % wind share. This can be attributed to the observation that storage optimal mixes are determined by the mismatch on different timescales than backup optimal mixes [50]: While backup energy is sensitive to the daily scale, storage energy capacity is more sensitive on a seasonal scale. Put differently, the backup energy minimal mix is driven by matching load and generation on a daily scale, while the storage energy minimal mix tries to match seasonal averages of load and generation to each other. Thus, in the backup minimal mix, a high solar PV share, which would lead to deficits every night, is suppressed. Conversely, daily mismatches do not have a large influence on the storage energy of a seasonal storage system – it will in general be large enough to accommodate them. Instead, the storage energy capacity is sensitive to the mismatch on seasonal scales, and therefore optimized mixes are found such that the seasonal average of the generation follows the seasonal average of the load. This explains the more solar-heavy storage optimal mixes in the US: As opposed to Europe, their load generally peaks in summer and not in winter. Therefore, it coincides with the seasonal peak in solar generation, favoring a higher share of solar PV in the system.

Apart from these technical optimizations, the generation costs from VRES have also been considered for the US, in a VRES plus backup plants scenario. As only US-average levelized costs of electricity (LCOE) values were found in the literature, the LCOE are first regionalized, mainly according to resource quality. This leads to some regions where wind is less costly than solar, and others where solar PV is less expensive. Furthermore, LCOE are modified by considering surplus generation as not marketable, and therefore increasing the LCOE of VRES generation so as to make up for these losses on surplus. Some interesting insights have been derived from the comparison of LCOE-minimal mixes to backup energy-minimal mixes during the renewable build-up: At the beginning, backup energy in addition to what is to be expected because of insufficient VRES production rarely reaches noticeable values, no matter what the mix. Total backup energy is therefore very insensitive to the mix and has only a very shallow minimum. Conversely, LCOE have a clear minimum at the lower generation cost technology. That has the same reason: Generation from both technologies can be integrated equally well into the electricity system as surplus production hardly ever occurs, and so the optimal mix clearly favors the technology with the lower generation costs.

This picture changes as soon as renewable surplus becomes a factor, at gross shares around $\gamma = 40\,\%$. Then, the backup energy becomes more sensitive to the mix, and therefore the backup minimal mix lies in a deeper and deeper valley. Opposed to that, the LCOE-minimal mix gets drawn towards less surplus generation (which is equivalent to less backup energy needs). The minimum widens and eventually approaches the backup-minimal mix. This can be interpreted in two ways: Firstly, it can be read as a caution that it pays to keep a mixed portfolio of technologies that can adapt to different needs which arise during the renewable build-up. Secondly, it can be understood as a strong incentive to find alternative and profitable end-uses for the renewable surplus, because in this way, LCOE can be significantly reduced, even halved in some cases such as California.

8.2 Outlook and future work

A straightforward extension of this work is the application of similar methodology to other continents and/or extended grids. New lines can be added to already studied grids (an example is the planned link between Great Britain and Norway), or already studied regions can be expanded to adjacent countries, or entirely new regions can be examined. As generation data can be calculated for the entire World using the Aarhus renewable energy atlas, the only remaining hurdle is obtaining or synthesizing load data.

For sunnier regions, such as the Southern US, Northern Africa, Spain, or Greece, it is also important to consider concentrated solar power (CSP) plants as a further renewable option. In such plants, solar energy is collected with mirrors and used to heat some working fluid, e.g. molten salt, which is further processed like in a thermal power plant. They are likely to shift the picture significantly, because the reservoir of heated work fluid forms an inherent storage system, giving them more freedom to adapt to the load and a different temporal generation pattern than solar PV. They are a hybrid technology between weather-dependent and dispatchable power generation, in the sense that they have some ability to shift their output in time, but are not completely dispatchable. For instance, their output will be highly correlated with solar PV.

Moreover, the modeling of highly renewable energy systems can be refined and combined in various ways: The distribution of renewable assets can be optimized to significantly improve total power output per capacity unit and reduce output variance. Advances in this direction have been made, using optimal portfolio theory, in the Aarhus renewable systems group. To further validate the generation time series, it is important to know how stable they are under climate change, which may entail shifts in the predominant weather patterns. This concern can be addressed by obtaining a range of different climate-changed weather scenarios and comparing the resulting generation time series as well as the findings based on them, like optimal mixes or transmission grid extensions.

With regard to the backup system, the flexibility analysis can be performed with ramp rates instead of relying on a Fourier-like decomposition. This makes the work more accessible to power engineering and other fields. Such an approach also helps to include the technical constraints directly. Further along this road of a refined model of the backup system, fully renewable systems with renewable, dispatchable backup can be investigated. This requires the inclusion of the dispatchable renewable technologies, mainly biomass and hydro power. Detailed regional potentials have been studied (e.g. in Refs. [23, 27] for Europe) and can be converted into certain amounts of backup energy and backup capacity that are available to a fully renewable system at each node. As hydro power is relatively concentrated in mountainous regions – in Europe mainly in Norway and the Alps – this would lead to more transmission. Likewise, biomass distribution is not even, leading to additional “backup centers”. Not unlike CSP, hydro power and in particular run-of-river plants is not completely dispatchable, being dependent on enough precipitation. Similarly, biomass production is weather-dependent on long time scales while dispatchable on short time scales. Including these dependencies into the weather-dependent modeling could help to capture important correlations between all different renewable technologies.

The favorable effects of combining a backup system with storage have been shown in Ref. [52], and storage is therefore to be included in parallel with backup generation. Storage systems can be implemented in geographical detail. Small, localized storage, representing e.g. batteries, can be combined with central storage, e.g. as hydrogen in salt caverns such as those currently used for natural gas storage in Northern Germany. Like central backup systems, central storage systems will lead to additional transmission.

Reducing the mismatch by shifting load in time is also effected by demand-side management. Until now, such ideas work on smaller time scales (see e.g. [143]), but with growing mismatches and opportunities for arbitrage, they may grow in the future. Understanding demand-side management in a broader sense, further shifts of the mismatch can be reached by coupling to different infrastructures: The heating/cooling and transportation sectors can be electrified to some degree, using heat pumps and electric vehicles. Conversely, surplus electricity production can be used to produce synfuel for land transport and aviation. Connections to heating could also be provided by power-to-gas options, and electric cars could be used as battery storage.

Eventually, the combination of all these technologies has to be optimized simultaneously, taking the constraints on all components into account, to construct an effective, reliable, and highly renewable energy system.

Acknowledgements

First of all, I would like to thank my external supervisor, Martin Greiner, for the opportunity to work with him, for his guidance and advice during the thesis, and his hospitality in Aarhus. Furthermore, I am also grateful to my supervisor Stefan Schramm, who did not hesitate to accept me as a PhD student even though my topic was a little out of the scope of his previous work. His support and encouragement is greatly appreciated.

Especially during the first months of my studies at FIAS, Mirko Schäfer has been of great help, introducing me to the topic of complex networks and supervising the side project presented in App. D. This provided me with a good overview of complex networks science that proved helpful during the further steps of the thesis. In the final stages of this work, he patiently proofread the entire thesis. Besides Mirko, the entire FIAS community and in particular the administration deserve credit for a friendly atmosphere and a very reliable and supportive infrastructure.

Gorm B. Andresen helped me find my way on many different levels: geographically around in Aarhus, scientifically at my first conference, and management-wise – after all, a three-year thesis is a pretty large project. He has been very open to discussions, and put in a lot of time for our common publications. Moreover, he also supported my visits to Aarhus financially. I am also indebted to Rolando Rodríguez, who did his PhD alongside mine, albeit in Aarhus. We spent many fruitful hours developing algorithms, and shared quite a lot of useful code. Apart from that, he manages to balance the mood at almost all times with his cheerfulness.

Other people in Aarhus have contributed insights and ideas to this work: The power flow algorithm presented in Sec. 4.4.1 was developed in repeated discussions with Rolando, Gorm, and Uffe V. Poulsen, and Tue V. Jensen originally came up with the idea of using logistic growth curves for renewable shares in Europe. Anders A. Søndergaard and Timo Zeyer helped a lot getting to grips with the Aarhus renewable energy atlas that Anders developed in his master thesis. Anders also never hesitated to help with any computer problem that arose, and in general, he was successful.

The Aarhus group also received me well outside of the office walls, and I remember many an evening of cooking, eating, and laughing together at somebody's place.

Apart from regular visits to Aarhus, I was lucky to successfully apply for the HGS-HIRe abroad stipend to work with another foreign group. I used it to go to Stanford University, where I worked with the group of Mark Z. Jacobson, and especially with his PhD student Bethany A. Frew. Mark and Bethany and all her colleagues welcomed me very warmly, and it was a productive and adventurous stay. I very much appreciate Bethany's hospitality and care, but also her dedication and persistence. She greatly supported me in my work on the US.

I would also like to thank my friends and family, in particular my parents, who supported me through my undergraduate studies and encouraged me to continue further. And I would like to thank Bjørn for all his support and the good times. He also helped with the proofreading of the present work.

Last but not least, credit is due to the people who made my PhD studies possible with their financial support: Oda and Horst Stöcker as well as Margarete and Herbert Puschmann. Without them, this work could not have been conducted.

Appendix A

Convex optimization

Convex optimization is a mature branch of mathematics, and I will not attempt to cover it exhaustively here. Instead, I will introduce the main concepts and the derivations of properties that will be used later on. This section closely follows the presentation in Ref. [94].

Definition. *A function f is said to be* convex *if it fulfills*

$$f(\vartheta x + (1-\vartheta)y) \leq \vartheta f(x) + (1-\vartheta) f(y) \quad \forall \vartheta \in [0;1],\ \forall x, y \in \mathcal{D} \subseteq \mathbb{R}^n$$

where $\mathcal{D}$ is the domain of f_k. If the strict inequality holds ("$<$" instead of "$\leq$"), the function is called strictly convex.

Mnemonic device: "If it smiles at you $\smile$, it's convex." For twice continuously differentiable functions, convexity is equivalent to a positive semidefinite second derivative (Hesse matrix), and strict convexity to a positive definite second derivative.

Definition. *A* convex optimization problem *is given by the task*

$$\begin{aligned} &\text{minimize}_x f_0(x) \\ &\quad\text{given } f_i(x) \leq 0, \quad i = 1..N \end{aligned}$$

with convex functions $f_k : \mathbb{R}^n \to \mathbb{R},\ k = 0..N$ mapping the n-dimensional real space to the reals. f_0 is the objective function *and $f_i,\ i = 1..N$ are the* constraint functions*. The region in $\mathbb{R}^n$ in which all constraints are fulfilled is termed the* feasible set*.*

Sometimes, the constraints of a convex optimization problem are reformulated to explicitly allow for affine equality constraints. This case is actually contained in the above formulation, since an equality constraint is equivalent to two inequality constraints:

$$f_l(x) = b \Leftrightarrow \begin{cases} f_l(x) - b \leq 0 \\ -(f_l(x) - b) \leq 0 \end{cases}$$

The two inequalities can only be the constraints of a convex optimization problem if f_l as well as $-f_l$ are convex, which is only fulfilled for affine expressions.

Lemma. *The feasible set of a convex optimization problem is convex, that is, for any two points in the feasible set, the straight line connecting them is contained in the feasible set.*

Proof. First, we show that for a convex function f_1, the restricted set $D_1 = \{x | f_1(x) \leq 0\}$ is convex. Let $x \neq y \in D_1$. Then, $\forall\, 0 \leq \vartheta \leq 1$,

$$f_1((1-\vartheta)x + \vartheta y) \leq (1-\vartheta) f_1(x) + \vartheta f_1(y) \leq 0,$$

and therefore the line connecting x and y is contained in D_1 as well. In this way, each constraint i defines a convex restricted set D_i of points fulfilling it. The feasible set is the intersection of the D_i, $i = 1..N$, and it is convex as an intersection of convex sets: For any two points in the intersection, they are all contained in each D_i. Because all D_is are convex, the connecting line is also contained in each D_i, and thus in the intersection. ☐

The convexity conditions can, in fact, be relaxed a little: The constraint functions have to be convex only where they define the boundary of the feasible set, and the objective function has to be convex only within the feasible set. Since the shape of the feasible set is in general not a priori known, this relaxation is usually not very helpful.

The reason that convex optimization problems are so popular is that their solutions are very well-behaved, such that simple numerical algorithms like steepest descend methods are guaranteed to converge to the correct solution.

Theorem. *Convex optimization problems have the following properties:*

1. *Any local minimum is a global minimum.*
2. *The set of minima is convex.*
3. *If f_0 is strictly convex, the minimum is unique.*

Proof.

1. To see that any local minimum is a global minimum, assume that x is a local minimum. This can be expressed as

$$f_0(x) = \min\{f(z) | z \text{ feasible}, \ \|x - z\| \leq R\}$$

for some suitable radius R. Now assume that x is *not* a global optimum, i.e. that

$$\exists y : f_0(y) < f_0(x)$$

Because of the choice of R, we have:

$$\|x - y\| > R.$$

Now consider the point

$$z = (1 - \vartheta)x + \vartheta y, \qquad \vartheta = \frac{R}{2\|x - y\|}$$

It is feasible because the feasible set is convex, and $0 < \vartheta < 1$. By construction,

$$\|x - z\| = \vartheta \|y - x\| = \frac{R}{2},$$

and hence we expect $f_0(z) \geq f_0(x)$. But, by convexity of f_0:

$$f_0(z) = f_0((1 - \vartheta)x + \vartheta y) \leq (1 - \vartheta)f_0(x) + \vartheta f_0(y) < (1 - \vartheta)f_0(x) + \vartheta f_0(x) = f_0(x),$$

contradicting our assumption that x is a local minimum. Therefore, every local minimum must be a global minimum.

2. Assume that x, y are two global minima of the problem, with $f_0(x) = f_0(y) = A$. We have to show that $z = (1 - \vartheta)x + \vartheta y$, $\forall\, 0 \leq \vartheta \leq 1$, is also a global minimum. By convexity of the objective function, we have

$$f_0(z) \leq (1 - \vartheta)f(x) + \vartheta f(y) = A$$

Since $f_0(z) < A$ is impossible as we have assumed that A is the global minimum, we have $f_0(z) = A$, i.e. z belongs to the set of global optima.

3. Assume that $x \neq y$ are two distinct global optima of the problem, $f_0(x) = f_0(y) = A$, and consider $z = (1-\vartheta)x + \vartheta y$ for some $0 < \vartheta < 1$. The strict convexity of f_0 then yields

   $$f_0(z) < (1-\vartheta)f(x) + \vartheta f(y) = A$$

   in contradiction to the minimality of A. There can thus be only one minimum.

□

The only thing missing from this list is the *existence* of a global minimum. This can often be borrowed from basic results of real analysis, such as the following:

Theorem. *The existence of a solution of a convex optimization problem is guaranteed if the objective function is continuous and the feasible set is compact.*

For convenience, we will now use a slightly different terminology, separating equality and inequality constraints explicitly. Our standard problem will be

$$\begin{aligned} &\text{minimize}_x f_0(x) \\ &\quad\text{given } f_i(x) \leq 0, \quad i = 1..N \\ &\quad\text{and } h_j(x) = 0, \quad j = 1..M\,. \end{aligned} \tag{A.1}$$

with convex $f_i,\ i = 0..N$ and affine $h_j,\ j = 1..M$.

Definition. *For each convex optimization problem, it is possible to define a* dual problem *in the following way: First, we define the* Lagrangian *of the convex problem (not to be confused with the physicist's Lagrangian!) by*

$$L(x, \lambda, \nu) = f_0(x) + \sum_{i=1}^{N} \lambda_i f_i(x) + \sum_{j=1}^{M} \nu_i h_i(x)$$

with Lagrangian multipliers $\lambda \in \mathbb{R}^N,\ \nu \in \mathbb{R}^M$. *From this, the* Lagrange dual function

$$g(\lambda, \nu) = \inf_x L(x, \lambda, \nu)$$

is constructed. The dual problem *is defined to be:*

$$\begin{aligned} &\text{maximize}_{\lambda,\nu} g(\lambda, \nu) \\ &\quad\text{given } \lambda \succeq 0 \end{aligned} \tag{A.2}$$

with $\lambda \succeq 0$ *meaning* $\lambda_i \geq 0,\ i = 1..N$.
To distinguish the original problem from its dual problem, the former is often called the primal problem.

The Lagrange dual function is always concave, since it is the pointwise infimum of a family of affine functions of λ and ν (one family member for each x in the domain of the problem). As maximizing a concave function is equivalent to minimizing its negative (which is convex), the dual problem is always convex, even if the primal problem is not.

An important application of the dual formulation is the so-called weak duality inequality:

Lemma. Weak duality*: The dual optimal value d^* is a lower bound on the primal optimal value p^*, even if the primal problem is non-convex.*

Proof. For each feasible point $\tilde{x}$ and $\lambda \succeq 0$,

$$\sum_{i=1}^{N} \lambda_i f_i(\tilde{x}) + \sum_{j=1}^{M} \nu_i h_i(\tilde{x}) \leq 0\,,$$

because every summand the first sum is non-positive, and every summand in the second sum is zero. Therefore,

$$\begin{aligned}
&L(\tilde{x},\lambda,\nu) = f_0(\tilde{x}) + \sum_{i=1}^{N} \lambda_i f_i(\tilde{x}) + \sum_{j=1}^{M} \nu_i h_i(\tilde{x}) \leq f_0(\tilde{x}) \\
&\Rightarrow g(\lambda,\nu) = \inf_x L(x,\lambda,\nu) \leq L(\tilde{x},\lambda,\nu) \leq f_0(\tilde{x}) \; \forall\, \tilde{x} \text{ feasible}, \forall\, \lambda \succeq 0, \forall \nu \\
&\Rightarrow g(\lambda,\nu) \leq p^* \; \forall\, \lambda \succeq 0, \forall \nu \\
\Rightarrow &\sup_{\lambda \succeq 0,\nu} g(\lambda,\nu) = d^* \leq p^* \,. \qquad \text{(A.3)}
\end{aligned}$$

□

For a broad class of convex problems, it can be established that the dual and primal optimal values coincide, and furthermore, that they can both be found at the same saddle point of the Lagrangian. We say that in this case, *strong duality* holds. It gives us a tool to determine the minimal value p^* as well as a minimizer x^* of the primal problem in an unconstrained formulation as the saddle point of the Lagrangian. Beyond that, the dual formulation provides us with an alternative approach to the primal problem, which may be easier to solve, analytically or numerically, and which leads to the same solution.

As a preparation for the proof of strong duality, we introduce two sets and describe a geometric way to construct $g(\lambda,\nu)$. The first set we consider is the set of common values of the primal problem, $\mathcal{G}$.

Definition. *The* set of common values *of a (not necessarily convex) optimization problem is given by the points in* $\mathbb{R}^N \times \mathbb{R}^M \times \mathbb{R}$ *that can be expressed as a vector formed by the values of the constraint and objective functions:*

$$\mathcal{G} = \{(u,v,t) | u = (f_1(x), \dots f_N(x)),\; v = (h_1(x), \dots h_M(x)),\; t = f_0(x),\; x \in \mathcal{D}\}$$

where $\mathcal{D}$ *is the common domain of objective and constraint functions.*

The set $\mathcal{G}$ is illustrated in Fig. A.1 for the simple case of a problem with one inequality constraint and no equality constraints. In terms of $\mathcal{G}$, the primal optimal value can be expressed as

$$p^* = \inf\{t | (u,v,t) \in \mathcal{G}, u \preceq 0, \nu = 0\} \,.$$

The dual function can be written as

$$g(\lambda,\nu) = \inf\{(\lambda,\nu,1)^T (u,v,t) | (u,v,t) \in \mathcal{G}\} \,.$$

This has a geometric interpretation: The equality

$$g(\lambda,\nu) = (\lambda,\nu,1)^T (u,v,t)$$

determines a hyperplane tangent to $\mathcal{G}$, a so-called *supporting hyperplane*, with normal $(\lambda,\nu,1)$. Its geometric construction for the case of only one inequality constraint can be pictured in Fig. A.1: $(\lambda,1)$ is the normal of the supporting hyperplane L (in this case, the plane is one-dimensional, i.e. a line). This means that L is a line of slope $-\lambda$. L is shifted up and down until it touches $\mathcal{G}$ from below in the point (u_0,t_0) (which may only be a boundary point of $\mathcal{G}$ and not contained in $\mathcal{G}$). $g(\lambda)$ is then read off as the intersection of L with the t-axis.

The second set is the *epigraph of common values.*

Definition. *The* epigraph of common values *is the set*

$$\mathcal{A} = \{(u,v,t) | u \succeq (f_1(x), \dots f_N(x)),\; v = (h_1(x), \dots h_M(x)),\; t \geq f_0(x),\; x \in \mathcal{D}\}$$

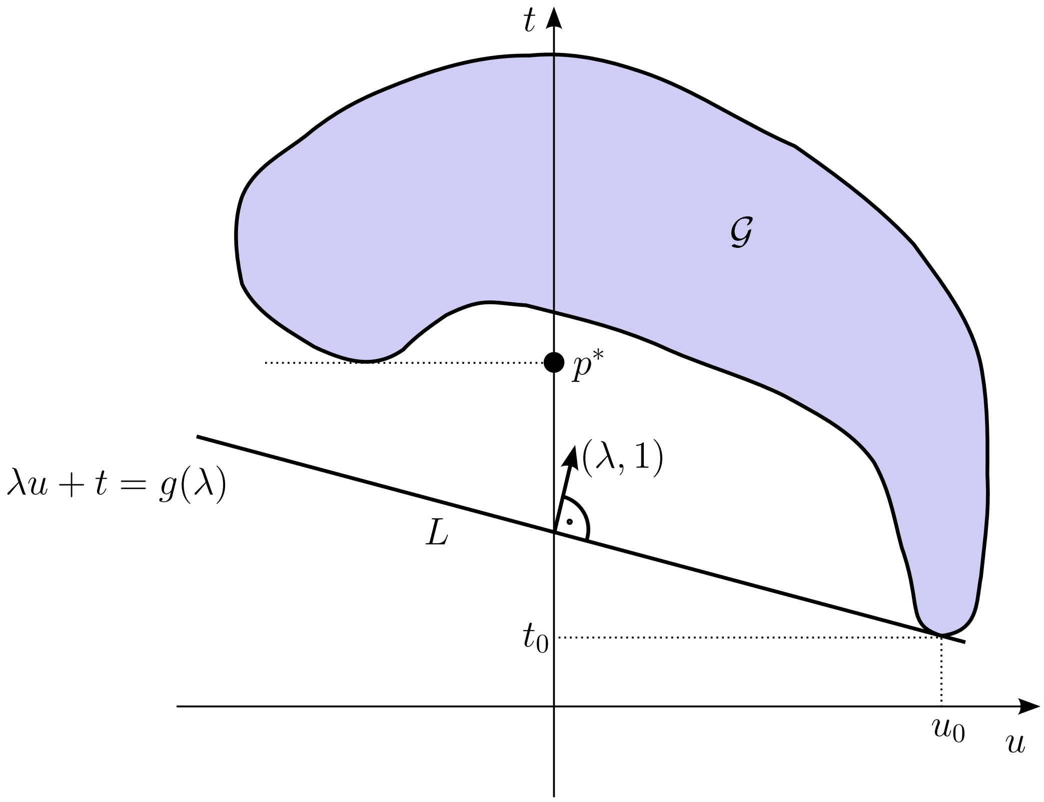

Figure A.1: The set $\mathcal{G}$, together with its supporting hyperplane L, which is determined as the line of slope $-\lambda$ that just touches $\mathcal{G}$ from below.

The term epigraph usually denotes the area above a graph, and similarly, the epigraph $\mathcal{A}$ contains the regions where the constraints are "more violated" or the objective function is larger. $\mathcal{A}$ is illustrated in Fig. A.2. The important thing about $\mathcal{A}$ is:

Lemma. *$\mathcal{A}$ is a convex set if the underlying problem is convex.*

Proof. We need to show that

$$(1-\vartheta)(u_1, v_1, t_1) + \vartheta(u_2, v_2, t_2) \in \mathcal{A} \ \forall \vartheta \in [0;1] \text{ if } (u_1, v_1, t_1), (u_2, v_2, t_2) \in \mathcal{A}\,.$$

Consider t. $t_1 \geq f_0(x_1)$ for some suitable x_1, and similarly for t_2. Therefore,

$$(1-\vartheta)t_1 + \vartheta t_2 \geq (1-\vartheta)f_0(x_1) + \vartheta f_0(x_2) \overset{(*)}{\geq} f_0((1-\vartheta)x_1 + \vartheta x_2)\,,$$

and thus $(1-\vartheta)t_1 + \vartheta t_2$ can be the t component of an element of $\mathcal{A}$. By construction of $\mathcal{A}$, the same pre-images x_1 and x_2 can be chosen for all components. The calculation for the components of u is then completely analogous. For v, all "$\geq$" can be replaced with "$=$", at the point $(*)$ because the equality constraint functions h_j are affine. ☐

p^* and $g(\lambda, \nu)$ can be expressed easily in terms of $\mathcal{A}$:

$$p^* = \inf\{t | (0,0,t) \in \mathcal{A}\}$$
$$g(\lambda, \nu) = \inf\{(\lambda, \nu, 1)^T (u, v, t) | (u, v, t) \in \mathcal{A}\}$$

As mentioned above, convexity alone does not guarantee strong duality. Different additional requirements, so-called constraint qualifications, have been found over time. We will use

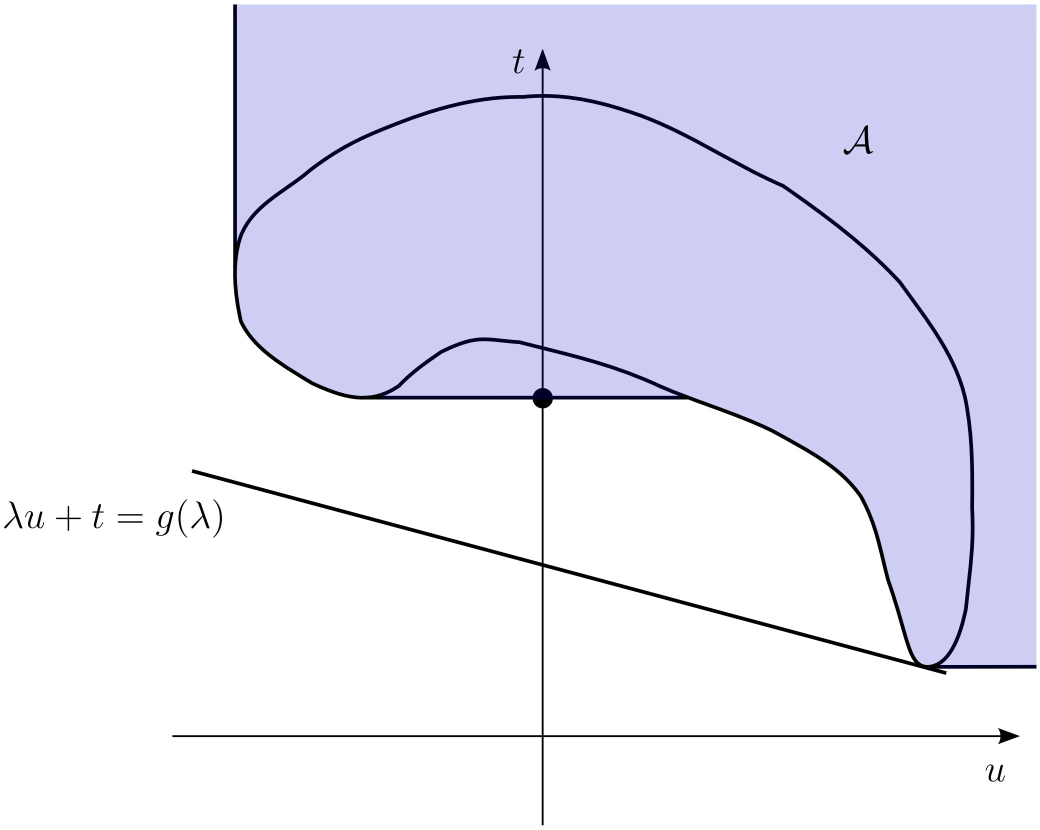

Figure A.2: The set $\mathcal{A}$, together with the line determined by its slope λ.

Definition. Slater's constraint qualification*: We say that a convex optimization problem fulfills Slater's constraint qualification if there exists a* strictly feasible point*, that is a feasible $\tilde{x}$ in the interior of the domain for which the inequality constraints are strictly true,*

$$f_i(\tilde{x}) < 0, \;\; i = 1..N\,.$$

Theorem. *For a convex optimization problem for which Slater's constraint qualification obtains, strong duality holds, that is, primal and dual optimal values are equal, $p^* = d^*$.*

Proof. We already know that $d^* \le p^*$. Now we show that under the given conditions, $d^* \ge p^*$. The proof is illustrated for the simple case of one inequality constraint in Fig. A.3.

We consider the convex set $\mathcal{A}$ and another convex set $\mathcal{B}$ as defined by

$$\mathcal{B} = \{(0,0,t) \in \mathbb{R}^N \times \mathbb{R}^M \times \mathbb{R} | t < p^*\}$$

$\mathcal{A}$ and $\mathcal{B}$ do not intersect, because a point in the intersection set would be feasible and have $f_0(x) < p^*$, which is a contradiction. For any non-intersecting two convex sets, it is possible to introduce a separating hyperplane between them. For a proof of this intuitively clear statement, see [94, Ch. 2.5]. We choose to describe this hyperplane by its normal, which we denote $(\lambda, \nu, \mu) \neq 0$. Since $\mathcal{A}$ and $\mathcal{B}$ are on different sides of this hyperplane, we have

$$\lambda^T u + \nu^T v + \mu t \ge \alpha \quad \forall\,(u,v,t) \in \mathcal{A} \tag{A.4}$$

$$\lambda^T u + \nu^T v + \mu t = \mu t \le \alpha \quad \forall\,(u,v,t) \in \mathcal{B} \tag{A.5}$$

for a suitable $\alpha \in \mathbb{R}$ and the appropriate sign of (λ, ν, μ). (If we had accidentally chosen (λ, ν, μ) such that "$\ge$" and "$\le$" were exchanged, we would just need to multiply the normal and α by (-1) to obtain the inequalities above.)

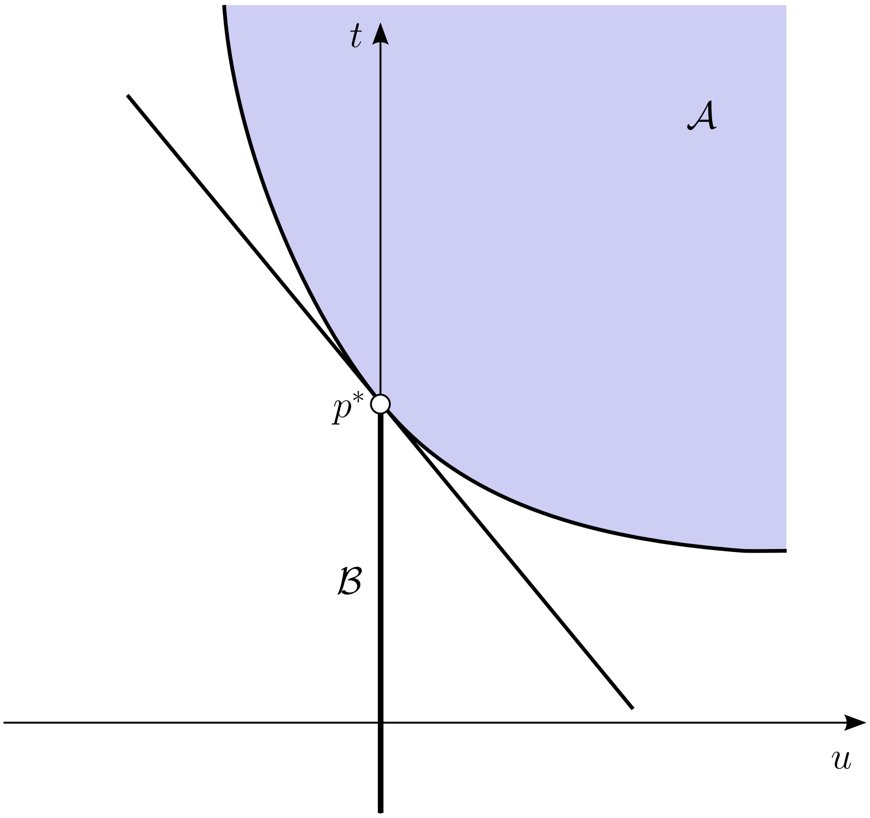

Figure A.3: The sets $\mathcal{A}$ and $\mathcal{B}$, together with their separating line, as used in the proof of strong duality, for the simple case of one inequality constraint.

From the shape of $\mathcal{A}$, which is unbounded from above in u and t, we can conclude that $\lambda \succeq 0$ and $\mu \geq 0$. In fact, if one or more components of them were negative, the scalar product in Eq. (A.4) would be unbounded from below and in particular not bounded from below by any fixed α.

We now distinguish two cases: $\mu = 0$ and $\mu > 0$. If $\mu > 0$, then we can divide by μ:

$$\sum_{i=1}^{N} \lambda_i f_i(x) + \sum_{j=1}^{M} \nu_j h_j(x) + \mu f_0(x) \geq \alpha \geq \mu p^* \quad \forall x \text{ (from Eq. (A.4) and (A.5))} \tag{A.6}$$

$$\Rightarrow \sum_{i=1}^{N} \lambda_i^* f_i(x) + \sum_{j=1}^{M} \nu_j^* h_j(x) + f_0(x) = L(x, \lambda^*, \nu^*) \geq p^* \quad \forall x,\ \lambda^* := \lambda/\mu,\ \nu^* := \nu/\mu$$

$$\Rightarrow g(\lambda^*, \nu^*) \geq p^* \,,$$

what was to be shown. This also shows that the pair (λ^*, ν^*) constructed in this way is a maximizer of $g(\lambda, \nu)$, and thus a solution to the dual problem.

The last step that needs to be completed is to rule out the case $\mu = 0$. This is where Slater's constraint qualification comes in. If $\mu = 0$, (A.6) reduces to

$$\sum_{i=1}^{N} \lambda_i f_i(x) + \sum_{j=1}^{M} \nu_j h_j(x) \geq 0 \,. \tag{A.7}$$

Inserting the Slater feasible point $\tilde{x}$, we get

$$\sum_{i=1}^{N} \lambda_i f_i(\tilde{x}) \geq 0 \,.$$

We know that all $f_i(\tilde{x}) < 0$ and all $\lambda_i \geq 0$. Fulfilling the above inequality is thus only possible if $\lambda = 0$. All that is left of (A.7) is now

$$\sum_{j=1}^{M} \nu_j h_j(x) \geq 0 \;\forall x. \tag{A.8}$$

We remember that the equality constraints of a convex problem must be affine, and thus we can rewrite (A.8) as

$$\nu^T(Ax - b) \geq 0 \;\forall x \tag{A.9}$$

for suitable A and b. Without loss of generality, we assume that A has rank M, that is, the M equality constraints are non-redundant (if they are, we can easily formulate an equivalent problem, just leaving out the redundant constraints). Since $\tilde{x}$ is contained in the interior of the problem's domain, the domain contains a ball of suitably small radius r around $\tilde{x}$, $B_r(\tilde{x})$. Since A has rank M, the image of $B_r(\tilde{x})$ is M-dimensional. There are M pre-image vectors $x_j \in B_r(\tilde{x}),\ j = 1..M$ such that the image of $B_r(\tilde{x})$ is spanned by $\{Ax_j\}_{j=1..M}$. We can choose them such that $\{Ax_j\}_{j=1..M}$ are orthogonal, and such that Ax_1 is parallel to ν, assuming $\nu \neq 0$. $\nu^T Ax_1$ is a linear function of x_1, while $\nu^T b$ is constant. In particular, $\nu^T(A\tilde{x} - b) = 0$, and hence $\nu^T(Ax - b) < 0$ for variations of x in one of the two x_1 directions, contradicting (A.9).

This leads to the conclusion $\nu = 0$ and thus $(\lambda, \nu, \mu) = 0$, contradicting the construction that (λ, ν, μ) is a normal vector of a plane. $\mu = 0$ is therefore not possible. □

Theorem. *When strong duality obtains for a convex optimization problem, the solutions of the primal and the dual problem can be determined as a saddle point of the Lagrangian. For differentiable objective and constraint functions, necessary and sufficient conditions for the saddle point are the* Karush-Kuhn-Tucker (KKT) conditions*:*

$$\nabla_x f_0(x^*) + \sum_{i=1}^{N} \lambda_i^* \nabla_x f_i(x^*) + \sum_{j=1}^{M} \nu_j^* \nabla_x h_j(x^*) = 0 \tag{A.10}$$

$$\lambda_i^* f_i(x^*) = 0 \tag{A.11}$$

$$f_i(x^*) \leq 0,\ i = 1..N \tag{A.12}$$

$$h_j(x^*) = 0,\ j = 1..M \tag{A.13}$$

$$\lambda_i^* \geq 0,\ i = 1..N \tag{A.14}$$

Proof. To see that the primal and dual optima form a saddle point of the Lagrangian, consider the following way of expressing the primal problem:

$$\begin{aligned}\sup_{\lambda \succeq 0, \nu} L(x, \lambda, \nu) &= \sup_{\lambda \succeq 0, \nu} f_0(x) + \sum_{i=1}^{N} \lambda_i f_i(x) + \sum_{j=1}^{M} \nu_j h_j(x) \\ &= \begin{cases} f_0(x) & \text{if } x \text{ feasible} \\ \infty & \text{else} \end{cases}\end{aligned}$$

Indeed, if $f_i(x) > 0$ or $h_j(x) \neq 0$, L is unbounded in λ or ν. The primal problem can thus be written as

$$\inf_x \sup_{\lambda \succeq 0, \nu} L(x, \lambda, \nu)\,.$$

By definition, the dual problem is given as

$$\sup_{\lambda \succeq 0, \nu} \inf_x L(x, \lambda, \nu)\,.$$

If strong duality obtains, the two limit processes can be interchanged, and thus, the primal and dual optimal points x^* and (λ^*, ν^*) form a saddle point (x^*, λ^*, ν^*) of the Lagrangian.

As for the KKT conditions, note that Eqs. (A.12) - (A.14) are simply the primal and dual feasibility, respectively. The only two new equations are Eqs. (A.10) and (A.11). Eq. (A.10) says that (x^*, λ^*, ν^*) is a critical point of the Lagrangian. Since $L(x, \lambda^*, \nu^*)$ is convex in x while $\lambda \succeq 0$ (Eq. A.14), x^* must be a minimizer of $L(x, \lambda^*, \nu^*)$. It follows that

$$\begin{aligned} g(\lambda^*, \nu^*) &= L(x^*, \lambda^*, \nu^*) \\ &= f_0(x^*) + \sum_{i=1}^{N} \lambda_i^* \nabla_x f_i(x^*) + \sum_{j=1}^{M} \nu_j^* \nabla_x h_j(x^*) \\ &\overset{(A.13),\,(A.11)}{=} f_0(x^*) \end{aligned}$$

Strong duality holds and x^* and (λ^*, ν^*) are primal and dual optima.

Conversely, if strong duality holds and x^* and (λ^*, ν^*) are primal and dual optima, then they must necessarily fulfill the constraints Eqs. (A.12) - (A.14). Furthermore, since x^* is supposed to minimize $L(x, \lambda^*, \nu^*)$, the gradient with respect to x must vanish, so we have Eq. (A.10). Finally, we have

$$\begin{aligned} f_0(x^*) &= g(\lambda^*, \nu^*) \\ &= \inf_x f_0(x) + \sum_{i=1}^{N} \lambda_i^* f_i(x) + \sum_{j=1}^{M} \nu_j^* h_j(x) \\ &\leq f_0(x^*) + \sum_{i=1}^{N} \lambda_i^* f_i(x^*) + \sum_{j=1}^{M} \nu_j^* h_j(x^*) \\ &\leq f_0(x^*) \end{aligned}$$

The last line shows that the inequalities must all, in fact, be equalities. Because of Eq. (A.13), we can conclude that

$$\sum_{i=1}^{N} \lambda_i^* f_i(x^*) = 0\,.$$

In particular, since all terms in the sum are non-positive, we can even conclude that all single terms must vanish individually, and thus have Eq. (A.11). □

Appendix B

Landuse to roughness table

Table B.1: Landuse to roughness table
Land use – surface roughness relations used for the conversion from the national land cover database (NLCD) atlas to surface roughness. Some classes not shown because they only apply to Alaska. Source: US geological survey (USGS), NLCD Land Cover Class Definitions [144].

USGS ID	Class	Roughness/m
11	Open Water – All areas of open water, generally with less than 25 % cover or vegetation or soil	0.0002
12	Perennial Ice/Snow – All areas characterized by a perennial cover of ice and/or snow,generally greater than 25 % of total cover.	0.005
21	Developed, Open Space – Includes areas with a mixture of some constructed materials, but mostly vegetation in the form of lawn grasses. Impervious surfaces account for less than 20 % of total cover. These areas most commonly include large-lot single-family housing units, parks, golf courses, and vegetation planted in developed settings for recreation, erosion control, or aesthetic purposes.	0.5
22	Developed, Low Intensity – Includes areas with a mixture of constructed materials and vegetation. Impervious surfaces account for 20-49 % of total cover. These areas most commonly include single-family housing units.	1
23	Developed, Medium Intensity – Includes areas with a mixture of constructed materials and vegetation. Impervious surfaces account for 50-79 % of the total cover. These areas most commonly include single-family housing units.	1
24	Developed, High Intensity – Includes highly developed areas where people reside or work in high numbers. Examples include apartment complexes, row houses and commercial/industrial. Impervious surfaces account for 80-100 % of the total cover.	2
31	Barren Land (Rock/Sand/Clay) – Barren areas of bedrock, desert pavement, scarps, talus, slides, volcanic material, glacial debris, sand dunes, strip mines, gravel pits and other accumulations of earthen material. Generally, vegetation accounts for less than 15 % of total cover.	0.03

USGS ID	Class	Roughness/m
41	Deciduous Forest – Areas dominated by trees generally greater than 5 meters tall, and greater than 20 % of total vegetation cover. More than 75 % of the tree species shed foliage simultaneously in response to seasonal change.	1
42	Evergreen Forest – Areas dominated by trees generally greater than 5 meters tall, and greater than 20 % of total vegetation cover. More than 75 % of the tree species maintain their leaves all year. Canopy is never without green foliage.	1
43	Mixed Forest – Areas dominated by trees generally greater than 5 meters tall, and greater than 20 % of total vegetation cover. Neither deciduous nor evergreen species are greater than 75 % of total tree cover.	0.5
52	Shrub/Scrub – Areas dominated by shrubs; less than 5 meters tall with shrub canopy typically greater than 20 % of total vegetation. This class includes true shrubs, young trees in an early successional stage or trees stunted from environmental conditions.	0.25
71	Grassland/Herbaceous – Areas dominated by grammanoid or herbaceous vegetation, generally greater than 80 % of total vegetation. These areas are not subject to intensive management such as tilling, but can be utilized for grazing.	0.1
81	Pasture/Hay – Areas of grasses, legumes, or grass-legume mixtures planted for livestock grazing or the production of seed or hay crops, typically on a perennial cycle. Pasture/hay vegetation accounts for greater than 20 % of total vegetation.	0.03
82	Cultivated Crops – Areas used for the production of annual crops, such as corn, soybeans, vegetables, tobacco, and cotton, and also perennial woody crops such as orchards and vineyards. Crop vegetation accounts for greater than 20 % of total vegetation. This class also includes all land being actively tilled.	0.1
90	Woody Wetlands – Areas where forest or shrub land vegetation accounts for greater than 20 % of vegetative cover and the soil or substrate is periodically saturated with or covered with water.	0.25
95	Emergent Herbaceous Wetlands – Areas where perennial herbaceous vegetation accounts for greater than 80 % of vegetative cover and the soil or substrate is periodically saturated with or covered with water.	0.03

Appendix C

Data tables for European logistic growth and subsequent new lines

Table C.1: End-point wind/solar mixes for three wind heavy, three solar heavy, and the single country optimal mix base scenario, expressed as the relative share α^{W} of wind in VRES. The wind resp. solar heavy scenarios lead to balancing needs increased by 1 %, 2 % and 5 % of the average load when transmission is not included. The second last row shows the load-weighted average of the mixes over all single countries, and the last row shows the corresponding mixes for an aggregated Europe, where load and generation are shared without transmission limits.

ISO code	**avg. load/ GW**	**wind fraction** α_{W}						
		solar heavy scenarios			**base**	**wind heavy scenarios**		
		+5 % bal.	+2 % bal.	+1 % bal.	opt. mix	+1 % bal.	+2 % bal.	+5 % bal.
AT	5.8	0.405	0.511	0.562	0.674	0.764	0.799	0.874
BA	3.1	0.413	0.523	0.574	0.683	0.765	0.797	0.872
BE	9.5	0.426	0.523	0.577	0.701	0.802	0.837	0.911
BG	5.1	0.368	0.484	0.540	0.659	0.753	0.789	0.869
CH	4.8	0.410	0.522	0.575	0.691	0.785	0.819	0.891
CZ	6.6	0.439	0.548	0.600	0.713	0.802	0.836	0.911
DE	54.2	0.454	0.551	0.601	0.716	0.810	0.849	0.934
DK	3.9	0.474	0.569	0.617	0.732	0.829	0.867	0.951
EE	1.5	0.570	0.671	0.717	0.813	0.895	0.931	1.000
ES	24.3	0.461	0.556	0.600	0.697	0.794	0.837	0.933
FI	9.0	0.531	0.638	0.689	0.796	0.878	0.912	0.991
FR	51.1	0.511	0.610	0.657	0.755	0.845	0.886	0.979
GB	38.5	0.547	0.641	0.687	0.787	0.873	0.911	0.996
GR	5.8	0.369	0.479	0.530	0.642	0.739	0.781	0.871
HR	1.6	0.351	0.464	0.520	0.640	0.734	0.768	0.840
HU	4.4	0.390	0.496	0.548	0.663	0.753	0.786	0.860
IE	3.2	0.514	0.606	0.651	0.754	0.843	0.880	0.962
IT	34.5	0.390	0.492	0.540	0.647	0.744	0.786	0.877
LT	1.5	0.538	0.640	0.688	0.789	0.874	0.912	0.997
LU	0.7	0.421	0.533	0.588	0.707	0.801	0.835	0.906
LV	0.7	0.575	0.672	0.717	0.811	0.894	0.932	1.000
NL	11.5	0.451	0.546	0.596	0.716	0.813	0.851	0.933
NO	13.7	0.614	0.710	0.755	0.849	0.926	0.961	1.000
PL	15.2	0.472	0.577	0.629	0.740	0.830	0.868	0.952
PT	4.8	0.412	0.511	0.559	0.661	0.756	0.797	0.887

ISO code	avg. load/ GW	wind fraction α_W						
		solar heavy scenarios			base	wind heavy scenarios		
		+5 % bal.	+2 % bal.	+1 % bal.	opt. mix	+1 % bal.	+2 % bal.	+5 % bal.
RO	5.4	0.423	0.532	0.583	0.689	0.777	0.816	0.904
RS	3.9	0.422	0.530	0.582	0.695	0.783	0.815	0.887
SE	16.6	0.572	0.672	0.719	0.818	0.901	0.937	1.000
SI	1.4	0.372	0.482	0.535	0.651	0.743	0.778	0.851
SK	3.1	0.438	0.546	0.597	0.707	0.792	0.825	0.901
agg.	345.3	0.611	0.698	0.738	0.822	0.907	0.945	1.000
avg.	345.3	0.475	0.575	0.623	0.730	0.821	0.859	0.942

Table C.2: Logistic growth of VRES installation, for the base scenario. Shown are the penetrations of wind and solar PV production in the total electricity production, for the reference years 2015-2050 in five-year steps, and the fit parameters, see Eq. (3.1). The last two rows contain the average development in Europe.

country	penetration in electricity production								fit parameters			
	2015	2020	2025	2030	2035	2040	2045	2050	a	b	m	y_0
AT (wind)	0.04	0.09	0.17	0.30	0.44	0.55	0.62	0.66	2.1e-05	0.69	0.16	1967
AT (PV)	0.00	0.00	0.04	0.12	0.21	0.29	0.32	0.33	1.1e-11	0.33	0.50	1980
BA (wind)	0.00	0.04	0.20	0.38	0.55	0.67	0.68	0.68	2.5e-09	0.68	0.56	1990
BA (PV)	0.00	0.02	0.08	0.15	0.23	0.30	0.31	0.32	4.7e-09	0.32	0.34	1975
BE (wind)	0.03	0.10	0.23	0.40	0.56	0.65	0.69	0.70	5.7e-07	0.70	0.22	1965
BE (PV)	0.00	0.01	0.04	0.12	0.19	0.26	0.29	0.30	3.8e-08	0.30	0.30	1978
BG (wind)	0.03	0.07	0.18	0.34	0.50	0.60	0.64	0.66	1.1e-05	0.66	0.22	1979
BG (PV)	0.00	0.01	0.08	0.16	0.25	0.32	0.34	0.34	1.1e-10	0.34	0.47	1980
CH (wind)	0.00	0.01	0.12	0.30	0.47	0.64	0.69	0.69	4.2e-13	0.69	0.61	1980
CH (PV)	0.00	0.01	0.06	0.13	0.21	0.28	0.31	0.31	6.3e-10	0.31	0.41	1979
CZ (wind)	0.00	0.02	0.10	0.27	0.45	0.63	0.70	0.71	1.3e-08	0.71	0.35	1979
CZ (PV)	0.01	0.02	0.06	0.13	0.20	0.26	0.28	0.29	1.7e-06	0.29	0.24	1979
DE (wind)	0.13	0.21	0.31	0.43	0.53	0.61	0.66	0.69	7.5e-05	0.73	0.13	1954
DE (PV)	0.03	0.07	0.14	0.21	0.25	0.27	0.28	0.28	3.5e-05	0.28	0.20	1979
DK (wind)	0.38	0.49	0.58	0.64	0.68	0.71	0.72	0.73	1.8e-02	0.74	0.12	1984
DK (PV)	0.00	0.00	0.01	0.06	0.13	0.20	0.26	0.27	4.0e-14	0.27	0.58	1980
EE (wind)	0.02	0.05	0.13	0.28	0.47	0.63	0.71	0.75	5.0e-06	0.77	0.21	1974
EE (PV)	0.00	0.00	0.01	0.06	0.12	0.18	0.23	0.24	4.7e-13	0.24	0.53	1980
ES (wind)	0.18	0.27	0.36	0.46	0.54	0.61	0.65	0.67	1.0e-03	0.71	0.11	1966
ES (PV)	0.04	0.08	0.15	0.22	0.27	0.29	0.30	0.30	2.0e-04	0.30	0.20	1988
FI (wind)	0.01	0.06	0.20	0.40	0.60	0.74	0.78	0.79	5.5e-06	0.80	0.29	1987
FI (PV)	0.00	0.00	0.01	0.05	0.10	0.15	0.20	0.20	2.2e-13	0.20	0.54	1980
FR (wind)	0.04	0.10	0.23	0.42	0.59	0.69	0.73	0.75	6.0e-05	0.76	0.21	1983
FR (PV)	0.00	0.01	0.05	0.11	0.18	0.23	0.24	0.24	1.9e-08	0.25	0.34	1980
GB (wind)	0.08	0.21	0.40	0.59	0.71	0.76	0.78	0.79	7.9e-05	0.79	0.22	1982
GB (PV)	0.00	0.01	0.05	0.10	0.15	0.20	0.21	0.21	8.6e-12	0.21	0.51	1980
GR (wind)	0.13	0.25	0.39	0.51	0.59	0.62	0.63	0.64	4.1e-05	0.64	0.19	1970
GR (PV)	0.01	0.05	0.14	0.23	0.32	0.35	0.36	0.36	4.9e-08	0.36	0.36	1980
HR (wind)	0.01	0.04	0.14	0.29	0.45	0.58	0.62	0.64	1.0e-05	0.64	0.27	1988
HR (PV)	0.00	0.02	0.10	0.19	0.28	0.35	0.36	0.36	1.3e-12	0.36	0.61	1981
HU (wind)	0.01	0.03	0.11	0.26	0.43	0.57	0.64	0.66	4.6e-07	0.67	0.26	1977
HU (PV)	0.00	0.00	0.05	0.14	0.22	0.30	0.34	0.34	9.1e-18	0.34	0.82	1980

country	**penetration in electricity production**								**fit parameters**			
	2015	2020	2025	2030	2035	2040	2045	2050	a	b	m	y_0
IE (wind)	0.14	0.24	0.35	0.48	0.58	0.66	0.71	0.74	1.6e-04	0.77	0.13	1960
IE (PV)	0.00	0.00	0.01	0.06	0.12	0.18	0.24	0.25	1.5e-14	0.25	0.60	1980
IT (wind)	0.03	0.07	0.15	0.28	0.43	0.55	0.61	0.64	1.6e-05	0.66	0.19	1975
IT (PV)	0.01	0.03	0.09	0.18	0.27	0.33	0.35	0.35	2.2e-06	0.35	0.26	1983
LT (wind)	0.04	0.09	0.21	0.39	0.57	0.68	0.73	0.75	6.8e-06	0.76	0.20	1972
LT (PV)	0.00	0.00	0.04	0.10	0.16	0.22	0.24	0.24	4.9e-18	0.24	0.83	1980
LU (wind)	0.01	0.04	0.12	0.28	0.46	0.61	0.68	0.70	1.5e-06	0.71	0.24	1977
LU (PV)	0.00	0.01	0.05	0.11	0.19	0.25	0.28	0.29	3.1e-07	0.29	0.26	1978
LV (wind)	0.04	0.11	0.25	0.44	0.62	0.71	0.74	0.75	6.9e-05	0.76	0.23	1987
LV (PV)	0.00	0.00	0.03	0.09	0.15	0.21	0.24	0.24	8.4e-19	0.24	0.85	1980
NL (wind)	0.11	0.24	0.40	0.55	0.64	0.69	0.71	0.71	8.3e-04	0.72	0.19	1988
NL (PV)	0.00	0.00	0.01	0.07	0.14	0.21	0.27	0.28	2.0e-13	0.28	0.55	1980
NO (wind)	0.05	0.19	0.40	0.61	0.78	0.83	0.85	0.85	2.1e-05	0.85	0.30	1988
NO (PV)	0.00	0.00	0.00	0.04	0.07	0.11	0.14	0.15	1.2e-13	0.15	0.54	1980
PL (wind)	0.03	0.09	0.23	0.42	0.59	0.69	0.72	0.74	6.2e-05	0.74	0.24	1988
PL (PV)	0.00	0.00	0.01	0.06	0.13	0.19	0.25	0.26	1.2e-11	0.26	0.46	1980
PT (wind)	0.17	0.27	0.38	0.48	0.56	0.61	0.64	0.65	1.4e-04	0.67	0.13	1959
PT (PV)	0.01	0.04	0.11	0.20	0.28	0.32	0.34	0.34	7.3e-07	0.34	0.28	1980
RO (wind)	0.02	0.11	0.29	0.46	0.62	0.68	0.69	0.69	9.5e-06	0.69	0.36	1993
RO (PV)	0.00	0.00	0.06	0.14	0.22	0.29	0.31	0.31	3.9e-15	0.31	0.70	1980
RS (wind)	0.00	0.04	0.21	0.38	0.56	0.68	0.69	0.69	1.7e-08	0.70	0.57	1994
RS (PV)	0.00	0.02	0.09	0.17	0.24	0.30	0.30	0.30	2.9e-11	0.31	0.52	1981
SE (wind)	0.04	0.09	0.20	0.38	0.58	0.71	0.78	0.81	2.3e-05	0.83	0.20	1977
SE (PV)	0.00	0.00	0.01	0.04	0.09	0.13	0.17	0.18	1.3e-13	0.18	0.55	1980
SI (wind)	0.00	0.01	0.14	0.30	0.47	0.62	0.65	0.65	5.4e-14	0.65	0.67	1980
SI (PV)	0.00	0.01	0.06	0.15	0.24	0.32	0.35	0.35	1.7e-10	0.35	0.45	1980
SK (wind)	0.00	0.02	0.13	0.31	0.49	0.66	0.70	0.71	1.6e-10	0.71	0.47	1980
SK (PV)	0.00	0.01	0.07	0.15	0.22	0.28	0.29	0.29	1.5e-13	0.29	0.63	1980
Avg. (wind)	0.07	0.15	0.27	0.43	0.57	0.66	0.70	0.72	-	-	-	-
Avg. (PV)	0.01	0.03	0.07	0.13	0.20	0.24	0.27	0.27	-	-	-	-

Table C.3: Line capacities for the reference year-dependent transmission capacity layouts 3, 4, and 5 (see Secs. 5.2.1–5.2.3) according to the base scenario in the years 2020, 2030, 2040, and 2050. Net transfer capacities are given in MW.

link	**today**	**70 % benefit**				**90 % benefit**				**unconstrained**			
		2020	2030	2040	2050	2020	2030	2040	2050	2020	2030	2040	2050
AT ⇄ CH	470	470	1210	1890	2030	470	2440	3460	3680	470	4900	12270	13720
	1200	1200	1350	1990	2100	1200	2430	3310	3510	1200	6250	10020	11050
AT ⇄ CZ	600	600	1580	2630	2850	600	3480	5000	5350	600	8660	15500	16100
	1000	1000	1500	2530	2740	1000	3280	4570	4850	1000	5650	10480	11720
AT ⇄ DE	2000	2000	2370	3940	4280	2000	5300	7830	8450	2000	11150	25300	28170
	2200	2200	2630	4180	4460	2200	5320	7260	7670	2200	10520	17420	17420
AT ⇄ HU	800	800	1450	2240	2410	800	2850	3900	4130	800	6930	8910	9590
	800	800	1310	2220	2380	800	2980	4690	5120	800	7340	19300	19860
AT ⇄ IT	220	220	2200	3390	3600	220	4250	5710	6050	220	7830	13840	15460
	285	290	2190	3560	3820	290	4590	6560	6990	290	10850	19050	21450
AT ⇄ SI	900	900	1240	2000	2160	900	2570	3410	3600	900	4360	7400	7830
	900	900	1180	1950	2140	900	2600	3910	4220	900	7000	14000	15500
BA ⇄ HR	600	600	600	950	1040	600	1300	2020	2210	600	3920	7100	7290
	600	600	620	930	990	600	1180	1590	1670	600	2580	3780	3850

link	**today**	**70 % benefit**				**90 % benefit**				**unconstrained**			
		2020	2030	2040	2050	2020	2030	2040	2050	2020	2030	2040	2050
BA ⇄ RS	350	350	420	730	790	350	980	1460	1580	350	2070	4170	4230
	450	450	450	640	680	450	810	1140	1210	450	2620	3850	4020
BG ⇄ GR	550	550	1040	1720	1840	550	2270	3410	3660	550	6080	15540	15780
	500	570	1180	1800	1900	1270	2240	3060	3270	2320	7290	10280	10560
BG ⇄ RO	600	600	600	940	1030	600	1300	1960	2110	600	4800	7220	7220
	600	600	710	1060	1130	600	1300	1740	1830	600	3050	4820	5260
BG ⇄ RS	450	450	790	1410	1540	450	1960	3010	3250	450	6330	10800	11230
	300	300	1080	1540	1620	300	1840	2340	2450	300	3420	5350	5790
CH ⇄ DE	3500	3500	3500	3810	4070	3500	4910	7100	7620	3500	9990	20700	22060
	1500	1500	2450	3860	4120	1500	4890	6760	7210	1500	9450	14730	16360
CH ⇄ IT	4165	4170	4170	4170	4170	4170	4890	6530	6860	4170	8660	13850	14950
	1810	1810	2310	3790	4100	1810	5000	7360	7890	1810	10380	23390	26300
CZ ⇄ DE	2300	2300	2300	2300	2340	2300	2840	4210	4580	2300	5620	14760	16820
	800	800	1580	2460	2620	800	3070	4180	4470	800	8370	10870	11810
CZ ⇄ SK	2200	2200	2200	2200	2200	2200	2200	2200	2340	2200	3530	5030	5360
	1200	1200	1200	1310	1420	1200	1710	2530	2740	1200	3710	8200	8790
DE ⇄ DK	1550	1550	1550	2250	2400	1550	2900	4050	4310	1550	9210	11590	12130
	2085	2090	2090	2430	2610	2090	3180	4500	4830	2090	5350	10470	12920
DE ⇄ LU	980	980	980	980	980	980	980	980	980	980	980	980	980
	NRL[1]	980	980	980	980	980	980	980	980	980	980	1360	1500
DE ⇄ SE	600	600	2310	3630	3860	600	4620	6370	6760	600	13830	16430	16580
	610	610	2240	3710	4030	610	4930	7090	7580	610	5020	16420	20370
EE ⇄ LV	750	750	750	750	750	750	750	980	1040	750	1730	2500	2580
	850	850	850	850	850	850	850	1060	1120	850	1120	2650	2910
FI ⇄ EE	350	350	490	800	860	350	1060	1560	1680	350	3000	4230	4350
	350	350	510	810	870	350	990	1520	1660	350	990	4230	5350
FI ⇄ SE	1650	1650	2650	4800	5240	1650	6570	9650	10390	1650	8280	22690	25290
	2050	2050	3100	4790	5100	2050	5990	7770	8170	2050	12130	15070	15420
FR ⇄ BE	3400	3400	3400	3400	3400	3400	3730	5310	5720	3400	11000	17130	18820
	2300	2300	2300	3010	3200	2300	3810	5360	5770	2300	6650	13060	13900
FR ⇄ CH	3200	3200	3200	3790	4090	3200	4800	6720	7120	3200	13990	21760	25250
	1100	1100	2330	3550	3810	1100	4470	6140	6550	1100	10280	22430	25370
FR ⇄ DE	2700	2700	3670	5810	6230	2700	7480	10590	11280	2700	20680	33290	35450
	3200	3200	3380	5400	5810	3200	7000	9850	10560	3200	14430	29190	29650
FR ⇄ ES	1300	1300	5210	8000	8530	1300	10120	14040	14950	1300	17440	37250	37860
	500	730	3490	6550	7280	3780	9310	15420	16880	15070	49600	65360	72750
FR ⇄ GB	2000	2000	3320	5450	5820	2000	6950	9650	10270	2000	20400	30070	31470
	2000	2000	4150	6520	6970	2000	8350	11280	11940	2000	16610	25930	27960
FR ⇄ IT	2575	2580	4180	6440	6860	2580	8070	10900	11530	2580	20930	31670	35380
	995	1000	3750	5990	6380	1000	7820	11570	12450	1000	16010	36580	39900
GB ⇄ IE	450	450	620	1040	1130	450	1340	1830	1930	450	3230	4510	4510
	80	80	700	1070	1120	80	1240	1680	1750	80	1240	3290	4230
GR ⇄ IT	500	630	1680	2900	3110	1810	3910	5930	6440	2320	14070	21510	21670
	500	500	2140	3100	3290	500	3780	4790	5010	500	8200	9880	11900
HR ⇄ HU	800	800	800	1160	1240	800	1520	2200	2370	800	4150	7200	7310
	1200	1200	1200	1200	1200	1200	1420	1910	2010	1200	2240	4260	4770
HR ⇄ RS	350	350	680	990	1050	350	1210	1560	1630	350	2480	3200	3230
	450	450	530	900	980	450	1210	1900	2040	450	3910	7780	7920
HR ⇄ SI	1000	1000	1000	1520	1620	1000	2010	3140	3370	1000	5260	12290	13030
	1000	1000	1000	1570	1690	1000	2030	2680	2830	1000	5170	6670	7100
HU ⇄ RS	600	600	1000	1600	1710	600	2090	2870	3050	600	3740	6330	6580
	700	700	930	1590	1700	700	2120	3320	3640	700	7110	12760	13280
HU ⇄ SK	600	600	1750	3100	3350	600	4150	6290	6840	600	12030	23040	24970
	1300	1300	1810	3080	3310	1300	4030	5550	5920	1300	6870	12890	14150

link	**today**	**70 % benefit**				**90 % benefit**				**unconstrained**			
		2020	2030	2040	2050	2020	2030	2040	2050	2020	2030	2040	2050
IT ⇄ SI	160	160	1250	1930	2060	160	2450	3400	3620	160	5550	11410	12280
	580	580	1220	1810	1910	580	2240	3110	3340	580	5030	12570	12890
LV ⇄ LT	1300	1300	1300	1300	1300	1300	1300	1300	1300	1300	1300	1680	1720
	1500	1500	1500	1500	1500	1500	1500	1500	1500	1500	1500	1840	2190
NL ⇄ BE	2400	2400	2400	2570	2720	2400	3280	4620	4920	2400	7210	12100	13080
	2400	2400	2400	2560	2750	2400	3390	4860	5210	2400	9970	14340	15980
NL ⇄ DE	3000	3000	3000	3270	3540	3000	4260	5860	6240	3000	10310	17240	19010
	3850	3850	3850	3850	3850	3850	3850	5170	5550	3850	10590	16370	19280
NL ⇄ GB	1000	1000	2340	4020	4350	1000	5270	7450	7930	1000	11700	24870	27920
	1000	1000	3120	5060	5400	1000	6450	8780	9270	1000	15420	24320	25300
NL ⇄ NO	700	700	2670	3950	4180	700	4870	6770	7190	700	14710	18290	19640
	700	700	2470	3930	4170	700	4940	6800	7210	700	9720	17990	20250
NO ⇄ DK	950	950	1350	2000	2110	950	2420	3090	3230	950	4310	7530	8120
	950	950	1190	1680	1770	950	2030	2600	2730	950	5630	6850	7510
NO ⇄ SE	3595	3600	3600	3600	3600	3600	3600	3810	4020	3600	9100	12180	12240
	3895	3900	3900	3900	3900	3900	3900	3900	3900	3900	5500	11950	13160
PL ⇄ CZ	1800	1800	1800	1990	2110	1800	2510	3450	3680	1800	3490	8010	8880
	800	800	1170	1880	2020	800	2410	3370	3580	800	5810	10610	11570
PL ⇄ DE	1100	1100	1510	2450	2630	1100	3170	4340	4630	1100	4040	11470	12780
	1200	1200	1630	2540	2730	1200	3250	4380	4640	1200	8500	11260	11960
PL ⇄ SE	1	0	1900	3000	3180	0	3760	5220	5580	0	8630	17090	18120
	600	600	1920	3140	3410	600	4080	5900	6270	600	7680	15850	16860
PL ⇄ SK	600	600	1730	2630	2790	600	3280	4520	4790	600	5550	10930	11430
	500	500	1530	2520	2730	500	3380	4940	5350	500	7990	16890	17940
PT ⇄ ES	1500	1500	1500	2040	2190	1500	2650	3840	4110	2250	7720	11780	12150
	1700	1700	1700	1900	2040	1700	2430	3240	3400	2540	5370	7850	7850
RO ⇄ HU	700	700	1240	2160	2350	700	2910	4470	4870	700	9250	15870	16330
	700	700	1400	2100	2240	700	2630	3490	3670	700	4640	7160	7570
RO ⇄ RS	700	700	700	910	1000	700	1250	1940	2120	700	3650	5480	5680
	500	500	660	900	950	500	1080	1390	1470	500	2750	3830	3830
SE ⇄ DK	1980	1980	1980	1980	1980	1980	2170	3060	3240	1980	2210	7040	8230
	2440	2440	2440	2440	2440	2440	2440	2900	3070	2440	6590	7340	7340

---

[1] no realistic limit

Appendix D

Side project: Master stability analysis for almost bipartite networks

D.1 Analytical treatment

We consider almost bipartite networks in the sense that in addition to the bipartite structure of links between two groups of nodes in a graph, there exist a few extra links within these two groups. We call the links between the two clusters "inter-cluster links" and the links within a cluster "intra-cluster links". We are interested in the collective dynamics, i.e. the synchronization behavior of such systems. It has been noted in numerical studies that the presence of additional intra-cluster links may lead to enhanced synchronization [145], an analytical treatment of the problem is, however, (to our knowledge) still missing.

Here, we will restrict ourselves to the case of coupled map networks, i.e. use time-discrete maps on a bounded interval instead of e.g. differential equations on an unbounded domain. Although this leads to some differences in the details, a large part of the calculation can be carried over without changes and our results are therefore of interest for both cases. For simplicity, only one dimensional maps will be employed. The generalization to higher dimensions is straightforward and can be pursued along the same lines as in e.g. Ref. [146].

Consider a graph consisting of two sets of nodes, $\{x_i\}_{i=1..N_x}$ and $\{y_i\}_{i=1..N_y}$. The idea is that the graph structure is almost bipartite with the x-nodes forming one part and the y-nodes forming the other, but more generally it can be any kind of division of the nodes into two sets. This is important since the splitting of a graph into two parts with an almost bipartite structure will generically not be unique and should follow the grouping of the observed dynamics. The dynamics are governed by the following equations:

$$\begin{aligned} x_i^{t+1} &= (1-\epsilon)F(x_i^t) + \epsilon\left[\sum_{j=1}^{N_y} A_{ij}^{xy} H(y_j^t) + \sum_{k=1}^{N_x} A_{ik}^{xx} H(x_k^t)\right] \\ y_i^{t+1} &= (1-\epsilon)F(y_i^t) + \epsilon\left[\sum_{j=1}^{N_x} A_{ij}^{yx} H(x_j^t) + \sum_{k=1}^{N_y} A_{ik}^{yy} H(y_k^t)\right] \end{aligned} \tag{D.1}$$

($0 \leq \epsilon \leq 1$). In this context, $F, H : [-1,1] \to [-1,1]$, and the entries of the blocks of the adjacency matrix $A^{xy/xx}$ and $A^{yx/yy}$ are normalized such that $\sum_{j=1}^{N_y} A_{ij}^{xy} + \sum_{k=1}^{N_x} A_{ik}^{xx} = 1$ (resp. for y) in order to ensure that $x_i^{t+1}, y_i^{t+1} \in [-1,1]$. Probably the simplest choice to achieve that is to set all entries of $A^{xy/xx}$ to $1/k_i$ where k_i is the number of incoming links at node i or, equivalently, the number of entries in the ith row of $A^{xy/xx}$. Note that the network may be directed or undirected, i.e. the complete adjacency matrix

$$A = \begin{pmatrix} A^{xx} & A^{xy} \\ A^{yx} & A^{yy} \end{pmatrix}$$

needs not be “symmetric” in any way (in the case mentioned above “symmetric” would mean symmetric up to the normalization factor $1/k_i$).

To simplify notation, the prefactors are from now on absorbed into the terms:

$$\begin{aligned} (1-\epsilon)F &\to F \\ \epsilon A &\to A \end{aligned}$$

We now investigate whether nearly synchronized behavior is stable, i.e. we assume that $x_i^t = \overline{x}^t + \delta x_i^t$ with small δx_i^t (resp. for y). We spell out the terms only for x_i^t; the y_i^t are completely analogous. The goal is to determine whether the δx_i^t shrink or grow. Linear expansion in δx_i^t and δy_i^t yields:

$$\begin{aligned} \delta x_i^{t+1} &= x_i^{t+1} - \overline{x}^{t+1} \\ &\approx F'(\overline{x}^t)\delta x_i^t \\ &\quad + \sum_{j=1}^{N_y} \left(A_{ij}^{xy} - \frac{1}{N_x} \sum_{k=1}^{N_x} A_{kj}^{xy} \right) \left(H(\overline{y}^t) + H'(\overline{y}^t)\delta y_j^t \right) \\ &\quad + \sum_{j=1}^{N_x} \left(A_{ij}^{xx} - \frac{1}{N_x} \sum_{k=1}^{N_x} A_{kj}^{xx} \right) \left(H(\overline{x}^t) + H'(\overline{x}^t)\delta x_j^t \right) \end{aligned}$$

Here, $\sum_i \delta x_i = 0$ by construction has been used. In order to arrange the terms more clearly, we make the following definitions:

$$\sum_{j=1}^{N_y} A_{ij}^{xy} = \epsilon_i^{xy}, \qquad \overline{\epsilon}^{xy} \text{ – average}, \qquad \delta\epsilon_i^{xy} = \epsilon_i^{xy} - \overline{\epsilon}^{xy},$$

$$d_j^{xy} = \frac{1}{N_x} \sum_{k=1}^{N_x} A_{kj}^{xy}, \qquad \tilde{A}_{ij}^{xy} = A_{ij}^{xy} - d_j^{xy}$$

and resp. for xx, yx and yy. This allows us to write the evolution of the mean value $\overline{x}$ as:

$$\overline{x}^{t+1} = F(\overline{x}^t) + \overline{\epsilon}^{xy} H(\overline{y}^t) + \overline{\epsilon}^{xx} H(\overline{x}^t) \tag{D.2a}$$

$$+ \sum_{j=1}^{N_y} d_j^{xy} \delta y_j^t H'(\overline{y}^t) + \sum_{j=1}^{N_x} d_j^{xx} \delta x_j^t H'(\overline{x}^t) \tag{D.2b}$$

If the synchronization was perfect, the second row would vanish. As this cannot be assumed here, we have to keep it. However, it has proved sufficient to take the first row of Eq. (D.2) as the evolution of the mean values in numerical studies, which is convenient because it is much simpler [146].

In vector notation, the evolution of the small deviations may be written as:

$$\begin{pmatrix} \delta X^{t+1} \\ \delta Y^{t+1} \end{pmatrix} = \left[\begin{pmatrix} F'(\overline{x}^t) & 0 \\ 0 & F'(\overline{y}^t) \end{pmatrix} + \begin{pmatrix} 0 & \tilde{A}^{xy} \\ \tilde{A}^{yx} & 0 \end{pmatrix} \begin{pmatrix} H'(\overline{x}^t) & 0 \\ 0 & H'(\overline{y}^t) \end{pmatrix} \right] \begin{pmatrix} \delta X^t \\ \delta Y^t \end{pmatrix} \tag{D.3a}$$

$$+ \begin{pmatrix} \tilde{A}^{xx} & 0 \\ 0 & \tilde{A}^{yy} \end{pmatrix} \begin{pmatrix} H'(\overline{x}^t) & 0 \\ 0 & H'(\overline{y}^t) \end{pmatrix} \begin{pmatrix} \delta X^t \\ \delta Y^t \end{pmatrix} \tag{D.3b}$$

$$+ \begin{pmatrix} H(\overline{x}^t) & 0 \\ 0 & H(\overline{y}^t) \end{pmatrix} \begin{pmatrix} \delta\epsilon^{xx} \\ \delta\epsilon^{yy} \end{pmatrix} + \begin{pmatrix} H(\overline{y}^t) & 0 \\ 0 & H(\overline{x}^t) \end{pmatrix} \begin{pmatrix} \delta\epsilon^{xy} \\ \delta\epsilon^{yx} \end{pmatrix} \tag{D.3c}$$

The expression in the first row is the normal bipartite evolution which is to be expected. The term in the second row occurs due to the additional intra-cluster links groups, and the terms in the third row are caused by the splitting of the adjacency matrix into blocks which are not "properly normalized" on their own. The latter could be avoided if one were to ensure that the row sums of the blocks $\tilde{A}^{xx}$ etc were all equal. In order to keep the argument general, such a normalization is not chosen at this point.

We now proceed as in the case of ideal bipartite synchronization and change to a basis in which the bipartite part of the adjacency matrix,

$$\begin{pmatrix} 0 & \tilde{A}^{xy} \\ \tilde{A}^{yx} & 0 \end{pmatrix},$$

is diagonal. It has to be emphasized at this point that in fact, it is not clear whether it is diagonalizable; this is an assumption we make.

As described in Ref. [147], the eigenvectors of the bipartite part have the following structure: Without loss of generality, we assume $N_x > N_y$. Then, there are at least $N_x - N_y$ eigenvectors of the form $(u_0, 0)$ with eigenvalue zero. This follows directly from the rank theorem applied to the block $\tilde{A}^{yx}$. The rest of the eigenvectors come in pairs: if (u_x, u_y) is an eigenvector with eigenvalue λ, then $(u_x, -u_y)$ is an eigenvector with eigenvalue $(-\lambda)$, as can be checked by direct computation. Since the matrix converting the standard basis to the basis of eigenvectors has the (w.o.l.g. normalized) eigenvectors as columns, it is of the following form:

$$S = \begin{pmatrix} S_x & S_0 & S_x \\ S_y & 0 & -S_y \end{pmatrix} \qquad S^{-1} = \frac{1}{2}\begin{pmatrix} S'_x & S'_y \\ 2S'_0 & 0 \\ S'_x & -S'_y \end{pmatrix} \tag{D.4}$$

It can be checked by straightforward computation that S^{-1} has a structure similar to S^T. It should be noted that since S_x and S_0 are not a square matrices, the primed blocks cannot be inverses. Rather, they must fulfil certain relations:

$$\begin{aligned} &S'_x S_x = S'_y S_y = \mathbb{I}_{N_y}, \qquad S'_x S_0 = 0, \qquad S'_0 S_x = 0 \qquad S'_0 S_0 = \mathbb{I}_{N_x - N_y}, \\ &S_y S'_y = \mathbb{I}_{N_y}, \qquad S_x S'_x = \begin{pmatrix} \mathbb{I}_{N_y} & 0 \\ 0 & 0_{N_x - N_y} \end{pmatrix} \qquad S_0 S'_0 = \begin{pmatrix} 0_{N_y} & 0 \\ 0 & \mathbb{I}_{N_x - N_y} \end{pmatrix} \end{aligned}$$

With this block structure, it is relatively easy to compute the transformation behavior of the block diagonal matrices in Eq. (D.3). It holds

$$S^{-1}\begin{pmatrix} a\mathbb{I}_{N_x} & 0 \\ 0 & b\mathbb{I}_{N_y} \end{pmatrix} S = \frac{1}{2}\begin{pmatrix} (a+b)\mathbb{I}_{N_y} & 0 & (a-b)\mathbb{I}_{N_x} \\ 0 & 2a\mathbb{I}_{N_x - N_y} & 0 \\ (a-b)\mathbb{I}_{N_x} & 0 & (a+b)\mathbb{I}_{N_y} \end{pmatrix}$$

for any numbers a, b. At this point, we already see that the first row of Eq. (D.3) can be decomposed in 2 × 2-blocks, consisting of the eigenvectors to $\pm\lambda$, and a set of one-dimensional equations corresponding to $\lambda = 0$. In fact, it can be further simplified by passing from the eigenvectors u_λ and $u_{-\lambda}$ to yet another basis, consisting of pairs

$$\begin{aligned} u_+ &= u_\lambda + u_{-\lambda} \\ u_- &= u_\lambda - u_{-\lambda} \end{aligned}$$

(The zero eigenvectors are simply kept.) This corresponds to a conjugation with the matrix

$$T = \begin{pmatrix} \mathbb{I}_{N_y} & 0 & \mathbb{I}_{N_y} \\ 0 & \mathbb{I}_{N_x - N_y} & 0 \\ \mathbb{I}_{N_y} & 0 & -\mathbb{I}_{N_y} \end{pmatrix}$$

which is its own inverse up to some factors of (1/2). This leads to two-dimensional "λ-blocks" in the first row of Eq. (D.3):

$$\begin{pmatrix} u_+ \\ u_- \end{pmatrix} = \left[\begin{pmatrix} F'(\overline{x}^t) & 0 \\ 0 & F'(\overline{y}^t) \end{pmatrix} + \lambda \begin{pmatrix} 0 & 1 \\ 1 & 0 \end{pmatrix} \begin{pmatrix} H'(\overline{x}^t) & 0 \\ 0 & H'(\overline{y}^t) \end{pmatrix} \right] \begin{pmatrix} u_+ \\ u_- \end{pmatrix}$$

This is very nice in the case of perfect bipartite networks since it reduces the stability analysis from an $(N_x + N_y)$-dimensional problem to a two-dimensional parametric equation. Also, the third line of Eq. (D.3) does not cause major problems – some definite linear combination of $H(\overline{x}^t)$ and $H(\overline{y}^t)$ is added in each direction. The question that remains is what happens to the non-bipartite part, the middle line of Eq. (D.3). It is useful to note that

$$ST = \begin{pmatrix} 2S_x & S_0 & 0 \\ 0 & 0 & 2S_y \end{pmatrix} \qquad (ST)^{-1} = \frac{1}{2} \begin{pmatrix} S'_x & 0 \\ 2S'_0 & 0 \\ 0 & S'_y \end{pmatrix}$$

with the primed blocks as in Eq. (D.4). It is now easy to calculate the transformed non-bipartite matrix:

$$T^{-1}S^{-1} \begin{pmatrix} \tilde{A}^{xx} & 0 \\ 0 & \tilde{A}^{yy} \end{pmatrix} ST = \begin{pmatrix} S'_x \tilde{A}^{xx} S_x & 1/2 S'_x \tilde{A}^{xx} S_0 & 0 \\ 2S'_0 \tilde{A}^{xx} S_x & S'_0 \tilde{A}^{xx} S_0 & 0 \\ 0 & 0 & S'_y \tilde{A}^{yy} S_y \end{pmatrix} =: \begin{pmatrix} B^{xx} & 0 \\ 0 & B^{yy} \end{pmatrix}$$

It is interesting to note that, while introducing a certain degree of mixture into the game, a block structure is retained. But this is easily understood when recalling that the basis vectors we now use have the form

$$\begin{aligned} u_+ &= u_\lambda + u_{-\lambda} = \begin{pmatrix} u_x \\ u_y \end{pmatrix} + \begin{pmatrix} u_x \\ -u_y \end{pmatrix} = \begin{pmatrix} 2u_x \\ 0 \end{pmatrix} \\ u_- &= u_\lambda - u_{-\lambda} = \begin{pmatrix} u_x \\ u_y \end{pmatrix} - \begin{pmatrix} u_x \\ -u_y \end{pmatrix} = \begin{pmatrix} 0 \\ 2u_y \end{pmatrix}. \end{aligned}$$

That is, our new basis consists of linear combinations of either x or y nodes. And the non-bipartite part of the adjacency matrix couples these two sets only among themselves.

Denoting the new basis vectors $\delta Q = (ST)^{-1}\delta X$ and $\delta R = (ST)^{-1}\delta Y$, Eq. (D.3) now reads:

$$\begin{pmatrix} \delta Q^{t+1} \\ \delta R^{t+1} \end{pmatrix} = \left[\begin{pmatrix} F'(\overline{x}^t) & 0 \\ 0 & F'(\overline{y}^t) \end{pmatrix} + \begin{pmatrix} 0 & 0 & \Lambda \\ 0 & 0 & 0 \\ \Lambda & 0 & 0 \end{pmatrix} \begin{pmatrix} H'(\overline{x}^t) & 0 \\ 0 & H'(\overline{y}^t) \end{pmatrix} \right] \begin{pmatrix} \delta Q^t \\ \delta R^t \end{pmatrix} \tag{D.5a}$$

$$+ \begin{pmatrix} B^{xx} & 0 \\ 0 & B^{yy} \end{pmatrix} \begin{pmatrix} H'(\overline{x}^t) & 0 \\ 0 & H'(\overline{y}^t) \end{pmatrix} \begin{pmatrix} \delta Q^t \\ \delta R^t \end{pmatrix} \tag{D.5b}$$

$$+ (ST)^{-1} \left[\begin{pmatrix} H(\overline{x}^t) & 0 \\ 0 & H(\overline{y}^t) \end{pmatrix} \begin{pmatrix} \delta\epsilon^{xx} \\ \delta\epsilon^{yy} \end{pmatrix} + \begin{pmatrix} H(\overline{y}^t) & 0 \\ 0 & H(\overline{x}^t) \end{pmatrix} \begin{pmatrix} \delta\epsilon^{xy} \\ \delta\epsilon^{yx} \end{pmatrix} \right] \tag{D.5c}$$

where Λ is a diagonal matrix with the positive eigenvalues on the diagonal.

D.1.1 Two simplifications

In order to explore the matter further, we can now follow two distinct routes to simplify the situation. Essentially, they consist of getting rid of either the second or the third row of Eq. (D.5). (D.5c) can be eliminated by choosing the row sums of A^{xx}, A^{xy} etc to be independent of the row, for example

$$\sum_{j=1}^{N_x} A_{ij}^{xx} = \epsilon(1-\delta) \text{ and } \sum_{j=1}^{N_y} A_{ij}^{xy} = \epsilon\delta,$$

$0 \leq \delta \leq 1$, and similarly for A^{yx} and A^{yy}. In this way, all the $\delta\epsilon_i$ s are zero, and (D.5c) is gone. In this setting, one can study the influence of the non-bipartite links without having to deal with the effects of the normalization. Furthermore, it allows for perfect synchronization of the form

$$\begin{aligned} s_x^{t+1} &= (1-\epsilon)F(s_x^t) + \epsilon(1-\delta)H(s_y^t) + \epsilon\delta H(S_x^t) \\ s_y^{t+1} &= (1-\epsilon)F(s_y^t) + \epsilon(1-\delta)H(s_x^t) + \epsilon\delta H(S_y^t). \end{aligned}$$

There is also a natural way of performing the “bipartite limit”, namely by letting $\delta \to 0$.

The other route is to ignore the non-bipartite links and focus on the effects of the different row-sums. Such a study (allowing for even more “parameter mismatches”) has been published in Ref. [146] for the case of complete synchronization and similar results are to be expected for the bipartite case, where the only modification is the passage from a parametric one-dimensional master stability function to a two-dimensional equation.

In an analogous setting, using differential equations instead of maps, analytical bounds on the δx_i, δy_i have been obtained in Ref. [148]. Retracing their steps for the case of discrete time maps, analogous bounds can be found. For the mathematical background, see e.g. Refs. [149–151]. They cover mainly the case of differential equations, but the latter also has some sections devoted to discrete time systems.

First, we rewrite Eq. (D.5) (without the non-bipartite part) as an N_x+N_y-dimensional equation.

$$Z^{t+1} = C^t Z^t + J^t$$

where we have absorbed both $F(\overline{x}^t)/F(\overline{y}^t)$ and $H(\overline{x}^t)/H(\overline{y}^t)$ into C^t and J^t. As in the case of differential equations, the time evolution of the solution from time t_0 to $t \geq t_0$ can be written as

$$Z^t = \Phi(t, t_0) Z^{t_0} + \sum_{s=t_0}^{t} \Phi(t, s) J^s$$

with the fundamental transition matrix $\Phi(t, t_0)$ which maps the state of the homogenous system at time t_0 to its state at time t. In the case of differential equations, it would be obtained by a kind of generalized exponentiation of the matrix C^t, in the case of maps, it is much easier, namely just the product

$$\Phi(t, t_0) = \prod_{s=t_0}^{t} C^s.$$

The general growth behavior of the solutions can be estimated in form of the Lyapunov exponents μ, i.e.

$$|Z(t)| \propto \mathrm{e}^{\mu(t-t_0)} \text{ for } t \gg t_0.$$

Since we are interested in the stability of the system only, it suffices to look at the largest Lyapunov exponent $\mu_{\max}$. If it is negative, the system is asymptotically stable. If we invoke ergodicity, it can be calculated as the limit

$$\mu_{\max} = \limsup_{t\to\infty} \sup_{\|Z^0\|=1} \frac{1}{t} \ln \left\| \Phi(t, t_0) Z^0 \right\| \tag{D.6}$$

independently of t_0. We now want to show that $\Phi(t,t_0)$ is bounded by

$$\|\Phi(t,t_0)\| < \gamma\,\mathrm{e}^{-\nu(t-t_0)} \tag{D.7}$$

for every $t \geq t_0$ and suitable constants γ and ν. It is clear that for every given t_0 and ϵ we can find a time t_1 such that

$$\sup_{\|Z^0\|=1} \frac{1}{t} \ln \left\|\Phi(t,t_0)Z^0\right\| < \mu_{\max} + \epsilon \quad \forall t > t_1;$$

this is just spelling out the definition of the limit Eq. (D.6). If we now set

$$\begin{aligned}\epsilon &= \frac{|\mu_{\max}|}{2},\ \nu = -(\lambda_{\max} + \epsilon),\ \text{and}\\ \gamma(t_0) &= \sup_{t\in[t_0,t_1]} \sup_{\|Z^0\|=1} \left\|\Phi(t,t_0)Z^0\right\|\end{aligned}$$

we arrive at the desired bound (D.7) for fixed t_0. In order to find a global γ, we have to assume ergodic behavior in the sense that the system behaves at least qualitatively in the same way for all possible start times t_0, as we already did when calculating the Lyapunov exponents. Doing so, we expect that $\gamma(t_0)$ will be roughly the same for all t_0 and is thus bounded by some maximum value which has to be inserted in Eq. (D.7).

With this global bound on $\Phi(t,t_0)$, it is now easy to estimate the overall growth behavior of Z^t in the case that all Lyapunov exponents are negative.

$$\begin{aligned}\left\|Z^t\right\| &\leq \left\|\Phi(t,t_0)Z^0\right\| + \left\|\sum_{s=t_0}^{t} \Phi(t,s)J^s\right\| \leq \gamma\,\mathrm{e}^{-\nu(t-t_0)}\left\|Z^0\right\| + \sum_{s=t_0}^{t} \gamma\,\mathrm{e}^{-\nu(t-s)}\left\|J^s\right\|\\ &\leq \gamma\,\mathrm{e}^{-\nu(t-t_0)}\left\|Z^0\right\| + \sum_{s=t_0}^{t} \gamma\,\mathrm{e}^{-\nu(t-s)} \sup_{s\in[t_0,t]}\left\|J^s\right\|\\ &= \gamma\,\mathrm{e}^{-\nu(t-t_0)}\left\|Z^0\right\| + \gamma\frac{1-\mathrm{e}^{-\nu(t-t_0+1)}}{1-\mathrm{e}^{-\nu}} \sup_{s\in[t_0,t]}\left\|J^s\right\|\\ &\overset{t\to\infty}{\longrightarrow} \frac{\gamma}{1-\mathrm{e}^{-\nu}} \sup_{s\geq t_0}\left\|J^s\right\| \end{aligned} \tag{D.8}$$

Where synchronization of the unperturbed system is stable, the amplitude of the deviations from the mean evolution in the perturbed system is bounded by the maximal applied perturbation.

D.2 Simulation

As an exercise to gain some experience in the programming of coupled map networks and also to observe examples of (almost) bipartite synchronization, the model described in Refs. [152, 153] was rebuilt and investigated. It consists of a coupled map network which is constructed using growth and preferential attachment with one link per new node [154]. The emerging network is by construction at the same time bipartite and can be cut into two pieces by severing a single link. The interaction is undirected, normalization is chosen to be $1/k_i$, and logistic maps are used. The term “synchronization” is taken here to mean phase synchronization, that is, the distance between two nodes i, j is measured as

$$d_{ij} = 1 - \frac{2n_{ij}}{n_i + n_j}, \tag{D.9}$$

where n_i is the number of minima occurring at node i and n_{ij} is the number of coincident minima at nodes i and j. This distance is calculated after the system has undergone a sufficient equilibrating phase.

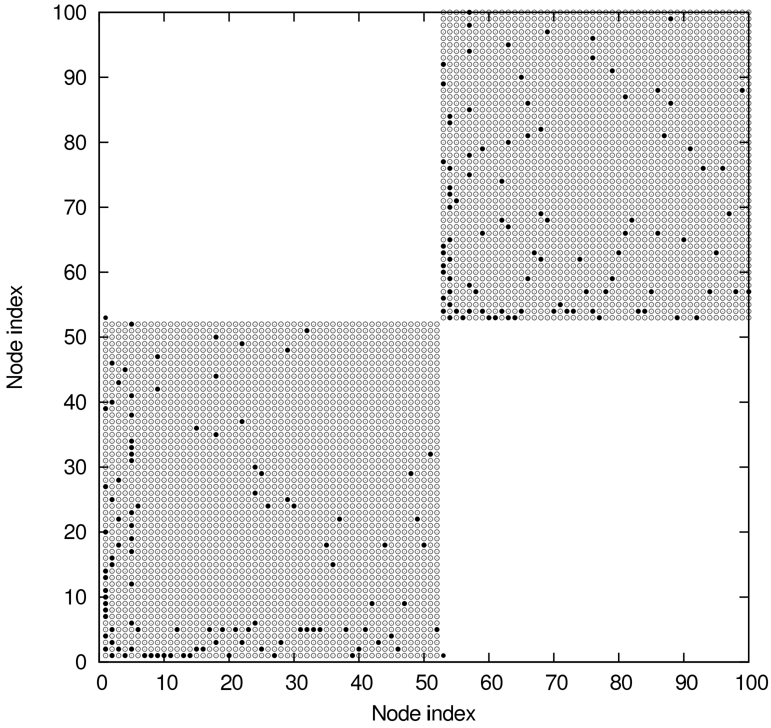

Figure D.1: Node-node plot of the synchronized clusters in the Amritkar-Jalan model. Open circles indicate synchronization, closed circles stand for links. The nodes have been reordered into clusters. Here, the coupling is $\epsilon = 0.16$, leading to intra-cluster coupling dominated synchronization.

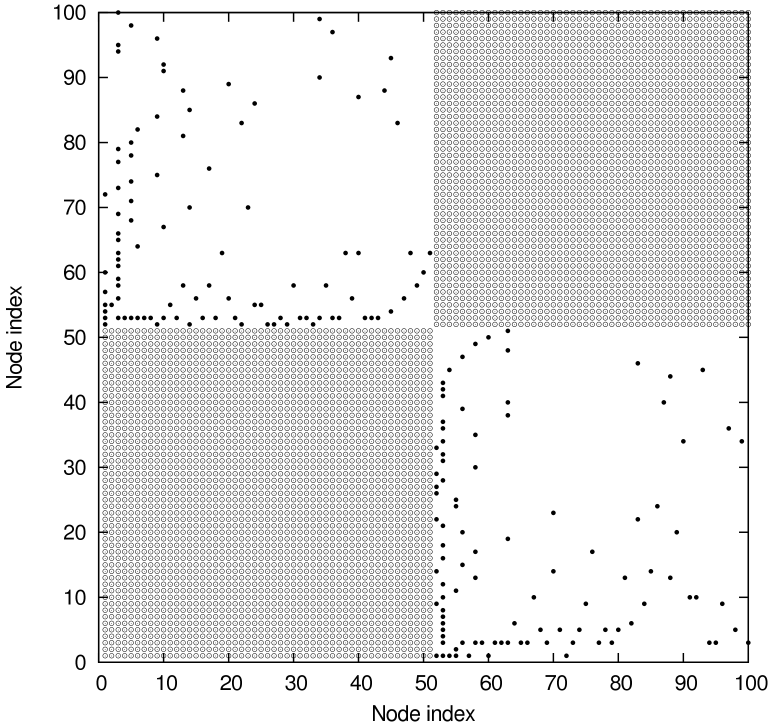

Figure D.2: Same as Fig. D.1, but with $\epsilon = 0.80$. In this case, the synchronization is caused by inter-cluster interaction.

In the context of synchronization, we order the nodes such that synchronized nodes get consecutive indices. In this way, the clusters are defined a posteriori. The nodes are regarded as belonging to the same cluster when their distance as in Eq. (D.9) is smaller than some threshold.

Using this model, the authors observe two kinds of synchronization: Roughly speaking, for small coupling parameter ($\epsilon \approx 0.16$), connected nodes synchronize, for large coupling ($\epsilon \approx 0.8$), unconnected nodes synchronize. The former can be thought of as a special case of the well-known complete synchronization in a network, only that now two networks appear which are typically connected by only one or two links. In this case, almost all the links are of intra-cluster type, i.e. the splitting into two clusters does not follow the underlying bipartite structure. For this kind of behavior, the authors use the term "self-organized synchronization". The latter is the case of bipartite synchronization, also termed "driven synchronization" in the paper, where we find almost exclusively inter-cluster links, i.e. the nodes split along the bipartite structure of the network. Apart from these dynamics, ϵ regions with no synchronization at all, splitting into more than two clusters etc can be seen.

With our simulation, we are able to reproduce their results, as can be seen in Figs. D.1 and D.2. We note that in addition to the "ideal" synchronization depicted here, we have quite frequently found some links "out of the pattern", i.e. single intra-cluster or inter-cluster links in a pattern otherwise dominated by the other link type. It was checked that these links are not due to a problem in the indexing of the nodes.

We now take a look at the threshold-dependence of the clusters. In the original publication, the threshold was taken to be zero. For our example coupling constants, we find that the phase distance is a very robust measure, leading to distances very close or equal to zero for nodes in one cluster and very close to or even equal to one for nodes belonging to different clusters. This leads to a very weak threshold dependence of the clusters, as can be seen in Fig. D.3 and even more clearly in Fig. D.4.

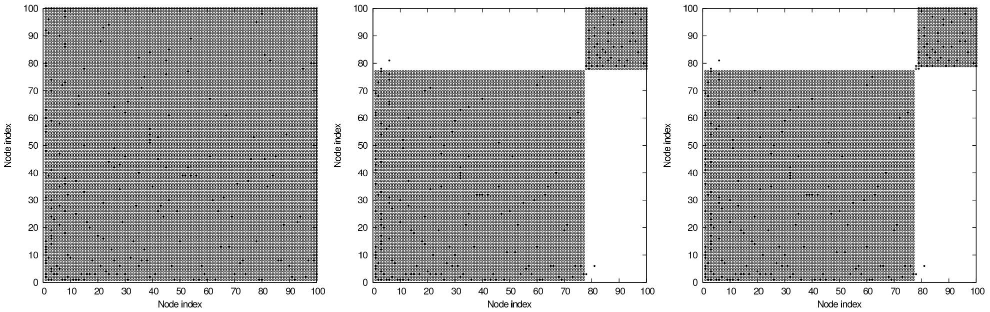

Figure D.3: Evolution of cluster size depending on the phase distance threshold. The thresholds in these figures are (from left to right) 1.0, 0.01, and 0.00001. The coupling constant is $\epsilon = 0.16$ where we have self-organized synchronization. Only for the largest possible distance of one, the two clusters merge into one, on the other hand, they fall apart only for a very small threshold below 0.01. Even in this case, there is only one node "falling off".

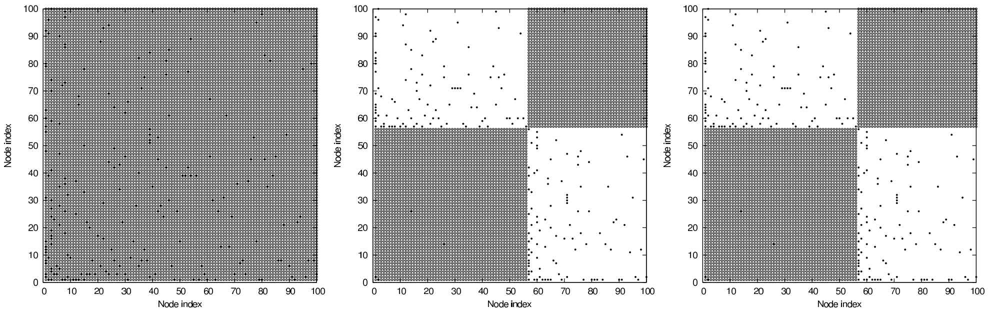

Figure D.4: Same as Fig. D.3, but with $\epsilon = 0.80$ where driven synchronization occurs. Here, only distances of either zero or one occur at all, so the two clusters don't ever (within numerical accuracy) fall apart, while they merge as in D.3 only for a threshold greater or equal to one.

For bipartite synchronization, phase distances of either one or zero have been observed exclusively, indicating that the two clusters are anti-phase synchronized; their minima never coincide. For the case of self-ordered synchronization, distances different from one and zero occur, which means that the nodes within one cluster are not perfectly in phase and those belonging to different clusters not perfectly anti-phase, but they are also very close to that state.

Of special interest to us is the presence of inter-cluster (non-bipartite) links in modes with high ϵ, where typically bipartite links dominate, see e.g. Fig. D.4. This raises our hopes to find an analytical explanation for cluster synchronization in almost bipartite networks.

In order to make contact with the calculation of the first section, we now replace the notion of distance from the original paper by the mean Euclidean distance

$$d_{ij} = \frac{1}{T} \sum_{t=1}^{T} |x_i^t - x_j^t|$$

which is closer to the idea of an average evolution of $\overline{x}$ within a cluster from which the deviations δx_i remain small.

We again investigate how the partition of the nodes into of clusters is affected by the threshold distance. We see that for the case of self-organized synchronization, all nodes merge into one cluster once the threshold distance rises up to approx. 0.5. For smaller thresholds, we first get two clusters, which remain until a threshold of approx. 0.1. For even smaller thresholds, the clusters disintegrate more and more.

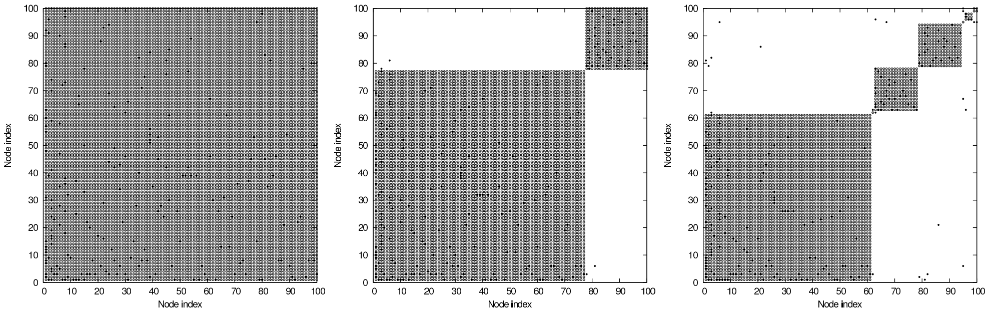

Figure D.5: Evolution of cluster size depending on the Euclidean distance threshold. The thresholds in these figures are (from left to right) 0.5, 0.1, and 0.05. The coupling constant is $\epsilon = 0.16$, so we are in the regime of synchronization of connected nodes.

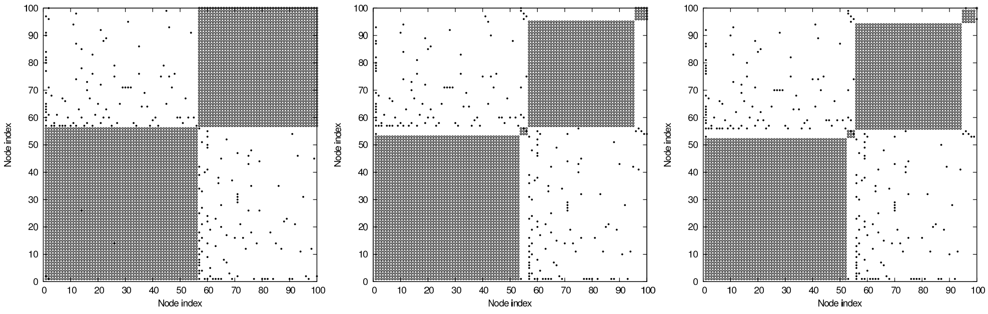

Figure D.6: Same as D.5, only this time we have $\epsilon = 0.80$ where bipartite synchronization occurs.

For the case of bipartite synchronization, two clusters can be observed in approximately the same region of the threshold parameter; they merge into one slightly above 0.5 and disintegrate slightly above 0.1.

It is clearly visible that the Euclidean distance is more sensitive to the threshold, i.e. it is a finer measure of synchronization.

D.3 Further ideas

- Simulation of exact network with no parameter mismatches (i.e. system as in Eq. (D.5) without the terms (D.5c)) vs simulation of bipartite network with noise – does noise approximation have a chance?
- Simulation of bipartite network with parameter mismatches (i.e. system as in Eq. (D.5) without the terms (D.5b)) – confirm numerically that the growth of the deviations is bounded as in the case of differential equations, see Eq. (D.8).
- Add weighted and/or directed links in perturbation matrix such that row sums equal zero as in Ref. [145] → get rid of terms (D.5c) in the perturbed master stability function (even no δ necessary)
- Treatment of non-bipartite part of the adjacency matrix as in quantum mechanical perturbation theory. This is always possible for finite dimensional matrices, see e.g. Ref. [155], but it destroys the block structure of the master stability function even if only the first order corrections to the eigenvectors are taken into account. Maybe eigenvalue corrections alone prove useful.

Academic CV

Education

Aug 2011 - Jul 2014	Physics PhD student at the Frankfurt Institute for Advanced Studies (FIAS), in close collaboration with Aarhus University, Denmark, under supervision of Prof. Dr. Stefan Schramm and Prof. Dr. Martin O.W. Greiner
Apr - Jun 2013	Scientific visit at Stanford University, collaboration with Prof. Dr. Mark Z. Jacobson and Bethany A. Frew
Oct 2004 - Feb 2011	Studies in physics and mathematics at the university of Göttingen
Feb 2011	Diploma in physics at the university of Göttingen, grade “Sehr gut” (very good)
	Diploma exam in theoretical physics, experimental physics (with focus on astrophysics), mathematics, and particle physics
	Diploma thesis: “Synthetic Spectra of Accretion Disks” (astrophysical computer simulation) under supervision of Prof. Dr. Stefan Dreizler, with support from Dr. Simon Hügelmeyer
Aug/Sep 2009	Attending a summer school on K-theory (mathematics) under supervision of Prof. Dr. Sebastian Goette and Prof. Dr. Annette Huber-Klawitter
Summer 2009	Specialisation course (full time) in theoretical particle physics/ mathematical physics under supervision of Prof. Dr. Detlev Buchholz
Jul - Sep 2008	Participating in the summer student programme of DESY (Deutsches Elektronen-Synchrotron), project work at the IceCube experiment (neutrino telescope) under supervision of Prof. Dr. Hermann Kolanoski and Dr. Fabian Kislat
Apr 2007	Intermediate exam (“Vordiplom”) in mathematics, grade “Sehr gut”
Oct 2006	Intermediate exam in physics, grade “Sehr gut”
Oct 2003 - Sep 2004	Studies in biology

1994 - 2003	Attendance at Friedrichs-Gymnasiums Herford, Germany
June 2003	Graduation: Allgemeine Hochschulreife (higher education entrance qualification), grade: 1.0 (very good)
Advanced courses:	Physics, mathematics

Teaching

2011 - 2014	Teaching assistant for online courses in physics for physicists, biologists, and pharmacists
2007 - 2010	Giving various tutorials for lectures in electrodynamics, quantum mechanics, thermodynamics as well as mathematics for physicists I and II
2010 and 2008	Giving a review lecture in thermodynamics (independent conception and conduct of the lecture, layout of exercises with solutions, answering the students' questions in a team of three or four fellow students, evaluated as good to very good)

Further activities

since Nov 2013	Student representative at FIAS
Jan - Mar 2011	Employment at the institute for astrophysics, Göttingen
2010	Student member of the institute board at the institute for astrophysics
Summer 2009	Student member of an appointments committee for a professorship in theoretical physics
2008	Student member of the institute board of the institute for theoretical physics

Awards

Jan 2008 - Sep 2009	Scholarship of the Studienstiftung des deutschen Volkes

List of publications

Andresen, G.B., Rasmussen, M.G., Rodríguez, R.A., Becker, S., and Greiner, M.: *Fundamental properties of and transition to a fully renewable pan-European power system*, in 2nd European Energy Conference, Maastricht 17-20 Apr 2012, EPJ Web of Conferences **33**, p. 04001 (2012). Online at http://dx.doi.org/10.1051/epjconf/20123304001.

Becker, S., Rodríguez, R.A., Andresen, G.B., Greiner, M.O.W., and Schramm, S.: *What can transmission do for a fully renewable Europe?*, in Proceedings of the 8th conference on Sustainable Development of Energy, Water, and Environment Systems (SDEWES), Dubrovnik 22-27 Sep 2013. Preprint available at http://arxiv.org/abs/1401.4298.

Andresen, G.B., Søndergaard, A.A., Rodríguez, R. A., Becker, S., and Greiner, M.: *Weather-Driven Modeling of Future Renewable Power Systems*, in Proceedings of the 8th conference on Sustainable Development of Energy, Water, and Environment Systems (SDEWES), Dubrovnik 22-27 Sep 2013.

Rodríguez, R.A., Becker, S., Andresen, G.B., Heide, D., and Greiner, M.: *Transmission needs across a fully renewable European power system*, Renewable Energy **63**, p. 467-476 (2014). Online at http://dx.doi.org/10.1016/j.renene.2013.10.005, preprint available at http://arxiv.org/abs/1306.1079.

Becker, S., Rodríguez, R.A., Andresen, G.B., Schramm, S., and Greiner, M.: *Transmission grid extensions during the build-up of a fully renewable pan-European electricity supply*, Energy **64**, p. 404-418 (2014). Online at http://dx.doi.org/10.1016/j.energy.2013.10.010; preprint available at http://arxiv.org/abs/1307.1723.

Becker, S., Frew, B.A., Andresen, G.B., Zeyer, T., Schramm, S., Greiner, M., and Jacobson, M.Z.: *Features of a fully renewable US electricity system: Optimal mixes of wind and solar PV and transmission grid extensions*, Energy **72**, p. 443–458 (2014). Online at http://dx.doi.org/10.1016/j.energy.2014.05.067; preprint available at http://arxiv.org/abs/1402.2833.

Becker, S., Frew, B.A., Andresen, G.B., Jacobson, M.Z., Schramm, S., and Greiner, M.: *Renewable electricity: Generation costs are not system costs*, Energy (2015). Online at http://dx.doi.org/10.1016/j.energy.2014.12.056; preprint available at http://arxiv.org/abs/1412.4934.

Andresen, G.B., Rodríguez, R.A., Becker, S., and Greiner, M.: *The potential for arbitrage of wind and solar surplus power in Denmark*, Energy **76**, p. 49-58 (2014). Online at http://dx.doi.org/10.1016/j.energy.2014.03.033.

Rodríguez, R.A., Becker, S., and Greiner, M.: *Cost-optimal design of a simplified, highly renewable pan-European electricity system*, submitted for review (2014).

Zusammenfassung

Die vorliegende Arbeit behandelt die Integration der variablen erneuerbaren Energien Wind- und Solarenergie in das europäische und US-amerikanische Stromnetz. Im Unterschied zu anderen Versorgungsnetzen wie etwa dem Gasnetz ist das Stromnetz praktisch nicht in der Lage, Energie zu speichern. Einspeisung und Verbrauch müssen sich daher immer die Waage halten. Bisher wurde die Lastkurve als starre Randbedingung angesehen, der das Gesamtsystem folgen muss. Grundgedanke des hier verfolgten Ansatzes ist, dass wetterabhängige Erzeugung eine Verschiebung der gesamten Ausrichtung der Elektrizitätsversorgung bedingt. Bei einem hohen Anteil von Wind- und Solarerzeugung fällt die Rolle der starren Randbedingung der Residuallast zu, also der verbleibenden Last nach Abzug der erneuerbaren Erzeugung. Ziel ist es also, die Wetterabhängigkeit genauso wie die Lastkurve in das Design einer zukünftigen Elektrizitätsversorgung miteinzubeziehen. In einigen Ansätzen wird darüber hinaus diskutiert, den Verbrauch zu flexibilisieren, also Laststeuerung (Demand-side management) zu betreiben. Solche Maßnahmen finden auf kurzen Zeitskalen z.T. schon seit einiger Zeit erfolgreiche Anwendung. Als Beispiel sei der Ausgleich von Windenergie mit Kühlhäusern erwähnt, deren Temperatur bei starkem Angebot von Windenergie stärker abgesenkt wird als notwendig, um bei schwächerem Windangebot für eine Weile abschalten zu können, ohne dass die gekühlten Waren Schaden nehmen [143]. Wir interessieren uns hier jedoch für längere Zeiträume von Stunden bis hin zu Jahren, und auf diesen Zeitskalen wird die Last als relativ unflexibel angesehen.

Die Arbeit beginnt mit einer Einleitung, die das weltweite Wachstum erneuerbarer Energien zeigt, einige Gründe dafür beleuchtet, und schließlich den allgemeinen Modellierungsansatz sowie den Aufbau dieser Arbeit beschreibt. Danach beschäftigen wir uns als Erstes mit der Berechnung langfristiger Erzeugungszeitreihen von Wind- und Solarenergie aus historischen Wetterdaten. Die dabei betrachteten Regionen sind Europa, gegliedert in die einzelnen Länder, und die USA, aufgeteilt in Regionen mit jeweils einem unabhängigen Systemoperator (vergleichbar mit einem Übertragungsnetzbetreiber in Europa), die sog. Federal Electricity Regulatory Council (FERC)-Regionen.

Die Quellen der Wetterdaten sind zum einen der US-amerikanische Wetterdienst NOAA [65] und zum anderen der kommerzielle Anbieter WEPROG. Sie besitzen eine Auflösung von 40-50 km und enthalten stündliche Mittelwerte. Mit Hilfe von einigen Annahmen werden aus den vorliegenden Daten die Bedingungen am Ort der Windturbinen und Solarmodule berechnet. Dazu ist es z.B. notwendig, die Windgeschwindigkeit auf der Höhe der Turbine aus Daten in 10 m Höhe oder die indirekte Sonneneinstrahlung aus dem Sonnenstand, der Luftfeuchtigkeit und der Bewölkung zu berechnen.

Es stellt sich heraus, dass der zeitliche Verlauf der Solarerzeugung auf der Skala von Ländern oder FERC-Regionen nur in geringem Maße von der räumlichen Verteilung der Photovoltaikanlagen abhängt.

Anders für die Winderzeugung: Schwankungen in der Windgeschwindigkeit werden durch die Leistungskurve einer Windturbine noch verstärkt. Die Leistungskurve gibt an, welche Leistung die Turbine bei welcher Windgeschwindigkeit liefert. In weiten Teilen ist sie proportional zur dritten Potenz der Windgeschwindigkeit, sodass kleine Schwankungen in der Windgeschwindigkeit in große Schwankungen in der abgegebenen Leistung übersetzt werden. Ein weiterer Effekt ist, dass bei Verwendung der mittleren Windgeschwindigkeit die Leistungsabgabe systematisch unterschätzt wird: Durch die dritte Potenz wirken sich Schwankungen der Windgeschwindigkeit nach oben überproportional auf die Leistungsabgabe aus, während Schwankungen nach unten weniger Einfluss haben. Weiterhin ergeben sich Komplikationen aus der Beschaffenheit, Bebauung und Vegetation des Geländes (Rauheit) und aus dem Höhenprofil der Landschaft (Orographie). Beide haben den Effekt, dass Schwankungen um eine mittlere Windgeschwindigkeit verstärkt werden, was dazu führt, dass die Winderzeugung sehr sensitiv auf die Position des Windrads ist. Diese Einflüsse sind in der Literatur dokumentiert und quantifiziert. Durch Einbeziehung der Effekte von Schwankungen auf Grund von Oberflächenrauheit und Orographie ist es in der vorliegenden Arbeit gelungen, realitätsnahe Winderzeugungszeitreihen zu berechnen.

Lastdaten werden von den Übertragungsnetzbetreibern zur Verfügung gestellt. Dies geschieht meist auf der Ebene von Ländern oder FERC-Regionen, bei einigen großen Ländern wie beispielsweise Deutschland oder Frankreich auch mit etwas höherer Auflösung. Sie zeigen, wie in Kap. 2 dargestellt, charakteristische Muster in der Zeit: Tagsüber ist der Verbrauch höher als nachts und am Wochenende niedriger als unter der Woche, sowohl in Europa als auch in den USA. Saisonale Schwankungen sind dagegen nicht in Phase: Während in Europa elektrische Heizungen und Beleuchtung die Nachfrage in den Wintermonaten gegenüber dem Sommer erhöht, ist sie in den USA durch Klimaanlagen im Sommer höher als im Winter.

Im folgenden Kap. 3 werden einige Begriffe und Modelle aus der Ökonomie eingeführt. Da wir uns für einen Leitungsausbau in Europa parallel zum Ausbau erneuerbarer Energien interessieren, führen wir das Konzept des logistischen Wachstums ein und wenden es auf die europäischen Länder an. Als Datenpunkte dienen dabei die historische Entwicklung, die 2020-Ziele und Entwicklungspläne der Europäischen Union, sowie das hypothetische Langfrist-Szenario eines vollständig erneuerbaren Europas im Jahr 2050. Der Mix von Wind- und Solarenergie wird im 2050-Szenario so gewählt, dass der Bedarf an Energie aus anderen Quellen minimiert wird.

Darüber hinaus werden einige Grundbegriffe aus der Betriebswirtschaft eingeführt, die in den folgenden Kapiteln Anwendung finden, nämlich die Annuität einer Investition und die Stromgestehungskosten.

Wir kehren nun wieder zu den einzelnen Knoten und der Diskrepanz zwischen Verbrauch und Wind- und Solarerzeugung zurück. Es gibt prinzipiell vier Möglichkeiten, um mit dem Ungleichgewicht zwischen Last und erneuerbarer Erzeugung umzugehen:

1. Überregionale Verteilung mit starken Leitungsnetzwerken: Hier werden Glättungseffekte ausgenutzt, die dadurch entstehen, dass das Wetter und damit die Wind- und Solarerzeugung an verschiedenen Orten nicht synchron sind. Durch langreichweitige Korrelationen (z.B. Tag-Nacht-Rhythmus oder Wetterfronten) sind diesem Ausgleich allerdings Grenzen gesetzt.
2. Ausgleich der Defizite mit zusätzlichen Kraftwerken, Verwerfen von Überproduktion: Wann immer die erneuerbare Erzeugung nicht ausreicht, um den Bedarf zu decken, werden regelbare Kraftwerke aktiviert. Wenn umgekehrt die Erzeugung den Verbrauch übersteigt, wird sie abgeregelt.
3. Mix von Wind- und Solarenergie: Sowohl Wind- als auch Solarerzeugung und Last zeigen charakteristische Schwankungen auf verschiedenen Zeitskalen. Durch geschickte Kombination von Wind- und Solarleistung lassen sich solche Schwankungen minimieren.
4. Speicher: Die erneuerbare Erzeugung wird zu Zeiten von Überproduktion in Speicher eingelagert, um sie bei Bedarf wieder abzurufen. Endliche Speicherkapazitäten, sowohl in Bezug auf die Ein- und Ausspeiseleistung als auch in Bezug auf die maximal speicherbare Energie sind hier die begrenzenden Faktoren.

Mit allen vier Teilen beschäftigt sich die vorliegenden Arbeit.

Zunächst wenden wir uns dem Leitungsnetz zu (Kap. 4). Einzelne Knoten in diesem Netzwerk sind die Länder bzw. FERC-Regionen. Diese wirken als Quellen oder Senken im Netzwerk, je nachdem, ob die Wind- und Solarerzeugung den Bedarf übersteigt oder aber nicht ausreicht. Um residuale Defizite zu decken, führen wir (abstrakte) regelbare Kraftwerke ein, die bei Bedarf eingeschaltet werden. Wir modellieren, wie die Leistung zwischen Ländern bzw. FERC-Regionen ausgetauscht wird (Lastflussberechnung), und bestimmen gleichzeitig, wo die zusätzlichen regelbaren Kraftwerke eingeschaltet werden sollten (dispatch). Ziel ist es, das Problem als konvexe Optimierung zu formulieren, weil solche Aufgaben mathematisch besonders „gutartig“ sind. Beispielsweise sind hier lokale Optima immer auch globale Optima. Darüber hinaus existieren dezidierte Algorithmen und teilweise auch fertige Implementationen für die numerische Lösung.

Nachdem einige Grundlagen aus der konvexen Optimierung eingeführt sind, zeigen wir die Äquivalenz zweier dieser Formulierungen für den Gleichstromfluss auf einem Netzwerk, einmal über elektrische Potentiale, und einmal über das Prinzip der minimalen Dissipation. Diese beiden Formulierungen sind für unsere Lastflussberechnungen nützlich, weil eine Vereinfachung der vollen Flussgleichungen für Wechselstrom mathematisch äquivalent zum Gleichstromfluss ist. Wir benutzen diese Formulierung, die im Voraus bekannte Quellen und Senken als gegeben annimmt, als Ausgangspunkt für eine Verallgemeinerung: Beim „klassischen“ Lastfluss wird vorausgesetzt, dass sich Quellen und Senken durch den Lastfluss genau ausgleichen. Das ist in unserer Anwendung nicht möglich, weil sich Quellen und Senken im generischen Fall nicht die Waage halten. Stattdessen verlangen wir, dass möglichst wenig regelbare Energie gebraucht wird, und minimieren anschließend die Dissipation beim Leitungsfluss, der proportional zum Quadrat des Flusses ist.

Dieser Algorithmus hat verschiedene Konsequenzen. Zunächst führt die Minimierung der Gesamt-Regelenergie dazu, dass ein möglichst großer Anteil der Last aus Wind- und Solarenergie gespeist wird. Begrenzt wird dieser Anteil nur dadurch, dass die Gesamt-Last zeitweise die Gesamt-Erzeugung übersteigt sowie durch endliche Leitungskapazitäten. Die Minimierung der Dissipation führt dazu, dass der Fluss soweit wie möglich reduziert wird. Das bedeutet, dass Regelenergie immer dort produziert wird, wo am Ende (nach dem Leistungsfluss) noch ein Defizit vorliegt, anstatt von einem Knoten produziert und am anderen verbraucht zu werden.

Letzteres bringt hohe Kapazitäten für Regelkraftwerke mit sich, die in der Realität sehr kostspielig sind, weil sie selten genutzt werden. Diese können reduziert werden, indem man mehr Kooperation zwischen den Netzwerkknoten erzwingt. Als ein möglicher Ansatz wird hier vorgestellt, die Regelkapazitäten auf einem bestimmten Stand zu kappen, sodass die Knoten sich in den meisten Fällen selbst versorgen wie oben beschrieben, bei extremen Defiziten aber kooperieren und Regelenergie für andere produzieren. Radikalere Ideen gehen dahin, die Regelkraftwerke in allen Knoten synchron zu betreiben, was allerdings ein hinreichend starkes Leitungsnetz und ein hohes Niveau an überregionaler Kooperationsbereitschaft voraussetzt.

Da Leitungsengpässe der Minimierung der Regelenergie entgegenstehen, ist der nächste logische Schritt, sich mit dem Netzwerkausbau zu beschäftigen. Dies geschieht in Kap. 5. Zunächst wird das Problem abstrakt formuliert: Wie kann eine gegebene Investition (verstanden als eine Summe von zusätzlicher Übertragungskapazität, oder aber auch als finanzielle Investition bei bekannten Leitungskosten) so auf die Leitungen verteilt werden, dass die benötigte Regelenergie (über einen Zeitraum von Jahren hinweg) am stärksten reduziert wird? Es stellt sich heraus, dass auch dieses Problem als konvexe Optimierung verstanden werden kann, was die Bearbeitung erheblich erleichtert.

Weil die Bestimmung der Regelenergie über Jahre hinweg mit stündlicher Auflösung für ein gegebenes Leitungsnetz einige Minuten in Anspruch nimmt, erscheint es trotz der theoretischen Möglichkeit einer konvexen Optimierung dieser Funktion wünschenswert, sich dem Problem mit heuristischen Methoden zu nähern. Eine solche Möglichkeit wird vorgestellt für den Netzausbau in Europa parallel zur Installation erneuerbarer Energien, wie oben angedeutet. Zur Vorbereitung sind einige Berechnungen notwendig: Zunächst wird das logistische Wachstum der erneuerbaren Installationen über die Jahre an die Daten angepasst. Danach wird für die Situation jedes einzelnen Jahres (also für die Anteile an Wind- und Solarenergie in jedem einzelnen Land, die für dieses Jahr berechnet wurden) über die gesamte vorhandene Zeitreihe an Wetter- und Lastdaten die Regelenergie mit verschiedenen Leitungsnetzen bestimmt. Als Fall mit der größtmöglichen Regelenergie wird ohne Leitungsnetz gerechnet. Der Fall mit minimaler Regelenergie ergibt sich, wenn man ein Leitungsnetz unbegrenzter Kapazität annimmt. Als interessante weitere Situation zwischen diesen beiden Extremen wird das Netzwerk untersucht, so wie es zur Zeit der Studie vorlag (2012).

Wenn man das Netzwerk mit a priori unendlicher Leitungskapazität betrachtet, kann man aus der Zeitreihe der sich ergebenden Flüsse endliche Leitungskapazitäten berechnen, einfach indem man das Maximum der auftretenden Flüsse als Kapazität setzt. Es stellt sich heraus, dass der Bau dieses Netzwerks eine Verzwölffachung der bestehenden Leitungskapazitäten bedeuten würde, mit einer Installationsgeschwindigkeit von einmal der Gesamtkapatität des heutigen Netzwerks pro Jahr in den Jahren 2020-2030. Da dies unrealistisch erscheint, suchen wir nach einem Kompromiss zwischen der Reduktion der Regelenergie einerseits und dem begrenzten Leitungszubau andererseits. Dazu sehen wir uns die maximale Regelenergie (ohne Leitungsnetz) und die minimale Regelenergie (unlimitieres Netz) an. Es stellt sich heraus, dass ein realistisch erscheinendes Netzwerk konstruiert werden kann, wenn für jedes Jahr 90 % der maximal möglichen Reduktion der Regelenergie gefordert wird. Dies entspricht einer Vervierfachung der Gesamtkapazität des Leitungsnetzes bis 2050.

Wie muss aber nun die zusätzliche Kapazität auf die Leitungen verteilt werden, um dieses Ziel zu erreichen? Es stellt sich heraus, dass es sinnvoll ist, mit Quantilen des unbeschränkten Flusses als Leitungskapazitäten zu arbeiten. Die Verteilung der unbeschränkten Flüsse weist ein Maximum bei oder in der Nähe von Null auf, und hat zu beiden Seiten stark konvex abfallende Flügel. Das bedeutet, dass der Fluss in den meisten Stunden weit unter den maximal auftretenden Werten bleibt. Deswegen ist für die meisten Stunden ein Bruchteil der Kapazität, die für unlimitierte Flüsse nötig wäre, völlig ausreichend.

In einer weiteren Studie wird danach untersucht, wie die Leitungskapazitätsverteilung optimiert aussieht und wie weit diese optimierte Verteilung von der heuristischen Quantilverteilung abweicht. Dazu wird ein Netzwerk für ein hypothetisches Szenario für die USA aufgebaut. Wind- und Solarerzeugung sind dabei so gewählt, dass sie im langjährigen Mittel soviel Energie erzeugen, wie verbraucht wird, durch Schwankungen in Last und Erzeugung aber noch eine Residuallast aus Regelkraftwerken zu decken bleibt. Wieder wird die dafür benötigte Regelenergie minimiert. Im Unterschied zu der Studie für Europa wird hier aber nicht der Aufbau von erneuerbaren Installationen und Leitungsnetz untersucht, sondern nur eine Momentaufnahme. Dafür wird das Leitungsnetz einer gründlichen Optimierung unterzogen, und zum Vergleich wird auch ein Quantil-Layout berechnet. Dabei stellt sich heraus, dass die Abweichungen zwischen beiden recht gering ausfallen. Bemerkenswert ist allerdings, dass, wenn Leitungskosten ins Spiel kommen, diese durch die Optimierung um etwa 10 % gegenüber dem Quantil-Leitungsnetz gesenkt werden können.

Im Rest des Kapitels werden andere Ansätze diskutiert, zum Teil eigene Näherungsideen, aber auch andere Alternativen aus der Literatur. Dort geht es allerdings zumeist um eine Kostenoptimierung des Gesamtsystems, sodass Resultate nicht direkt übertragbar sind.

Das nächste Kapitel, Kap. 6, beschäftigt sich mit dem Einfluss der Mischung von Wind- und Solarerzeugung auf den Bedarf an Regelenergie, auf Speicherkapazitäten und auch auf die Gesamtkosten der Erzeugung. Dazu werden zunächst einzelne Regionen als isolierte Netzwerkknoten betrachtet. Die Mischung aus Wind- und Solarenergie wird im Hinblick auf verschiedene Ziele optimiert:

1. Minimierung der Regelenergie: Die benötigte Regelenergie in einem hypothetischen Versorgungsmodell aus Windkraft, Solarenergie und Regelkraftwerken wird minimiert. Auf die Trägheit des regelbaren Kraftwerksparks wird dabei nicht eingegangen, sondern nur berechnet, wieviel Regelenergie benötigt wird. Es stellt sich heraus, dass der Regelenergiebedarf im Wesentlichen durch tägliche Anforderungen bestimmt ist. Da die Sonne nur tagsüber verfügbar ist, würde ein hoher Anteil an Solarenergie zu hohem Regelenergiebedarf führen. Der Solaranteil ist daher unterdrückt und macht typischerweise nur 20-30 % der Erzeugung beim optimalen Mix aus.

2. Minimierung der Speicherenergiekapazität: Hier wird ein anderes System betrachtet, in dem Wind- und Solarenergie mit einem idealisierten Speicher kombiniert werden, der alle Überschüsse speichert und alle Defizite deckt. Minimiert wird die Energiekapazität des Speichers. Endliche Leistungsaufnahme- oder -abgabekapazitäten des Speichers bleiben unberücksichtigt. Die Speicherkapazität hängt wesentlich von saisonalen Schwankungen ab, gegenüber denen

die täglichen Defizite oder Überschüsse nicht ins Gewicht fallen. Der optimale Mix liegt in etwa dort, wo sich saisonale Schwankungen von Wind- und Solarerzeugung ausgleichen bzw. wo sie den Schwankungen der Last folgen. Für Europa liegt dieser Mix bei etwa 60 % Windenergie, für die USA ist der Anteil an Solarenergie größer.

3. Minimierung der Stromgestehungskosten: Normalerweise werden Stromgestehungskosten pro erzeugter Energie berechnet, sodass sich je ein Wert für Wind- und Solarerzeugung ergibt, was auf eine triviale Minimierung führt. Wir entwickeln eine Methode, die es erlaubt, Verluste durch Überschussproduktion zu berücksichtigen, wobei angenommen wird, dass Überschüsse verworfen werden müssen (ohne Speicher). Damit steigen die Kosten, je höher der Anteil erneuerbarer Energien steigt, und zwar desto mehr, je mehr Überschüsse produziert werden.

Die Mischung aus Wind- und Solarenergie bezüglich dieser unterschiedlichen Ziele wird berechnet und die Werte von Regelenergie, Speicherkapazität und Stromgestehungskosten für optimale und nicht optimale Mischungen wird verglichen. Zusätzlich wird der optimale Aufbau von erneuerbaren Energien für die US-FERC-Regionen untersucht, einmal im Hinblick auf minimale Regelenergie und einmal im Hinblick auf minimale Gestehungskosten. Ergebnis der Untersuchung ist, dass sich die kostengünstigste Mischung mit steigendem Anteil Erneuerbarer der Mischung mit minimaler Regelenergie annähert.

Schließlich wird in diesem Kapitel auch beleuchtet, wie sich das Leitungsnetz auf den optimalen Mix von Wind- und Solarenergie auswirkt. Für das Beispiel Europa stellt sich heraus, dass ein starkes Leitungsnetz die Integration der Windenergie fördert (Ausgleichseffekte auf längeren räumlichen Skalen), während es einen geringeren Effekt auf die Solarenergie hat. Daher verschiebt sich der optimale Mix in Richtung Wind. Speicher haben übrigens einen gegenteiligen Effekt: Für Windenergie, die typischerweise auf Skalen von einigen Tagen schwankt, sind kleine Speicher wenig hilfreich. Für Solarenergie helfen sie dagegen, Produktion am Tag für den Abend zu speichern und sie so besser zu integrieren.

Das letzte Kapitel, Kap. 7, geht schließlich am Beispiel Europas genauer auf die Regelkraftwerke ein. In den vorangegangenen Teilen wurden sie immer als ideal flexibel betrachtet, d.h. es wurden keine Beschränkungen von Herauf- oder Herunterfahrraten angenommen. Auf Grund vielfältiger Randbedingungen ist diese Annahme allerdings nur bedingt zulässig: Zum einen gibt es technische Limits, die nicht überschritten werden dürfen, weil sonst z.B. zu hohe Temperaturgradienten im Innern des Kraftwerks auftreten würden. Darüber hinaus ist ein Teillastbetrieb in der Regel mit Einbußen im Wirkungsgrad verbunden. Nicht zu vergessen ist hier aber auch die ökonomische Komponente: Um wirtschaftlich produzieren zu können, benötigen die Kraftwerke eine bestimmte Anzahl an Volllaststunden.

Um all diese Randbedingungen nicht explizit beschreiben zu müssen, haben wir den Zugang über die Lastzeitreihen gewählt: Es ist bekannt, dass die vorhandene Lastzeitreihe nachgefahren werden kann. Mittels einer Fourier-artigen Zerlegung der Last in Komponenten auf unterschiedlichen Zeitskalen werden Mindestkapazitäten bestimmt, die in den verschiedenen Flexibilitätsklassen vorhanden sein müssen, um der Last folgen zu können. Wir teilen dabei die regelbaren Kraftwerke in drei Klassen ein: Die langsamen haben eine Zeitkonstante von etwa einer Woche, die mittleren von etwa einem Tag, und die schneller sind in der Lage, der Last auf der Zeitauflösung unserer Daten (eine Stunde) zu folgen. Mit unserem Ansatz finden wir, dass etwa die Hälfte der Kapazität auf langsame Kraftwerke entfallen kann, und je etwa ein Viertel auf die beiden schnelleren Klassen.

Betrachtet man nun die Kapazitäten aus den Lastzeitreihen als Startpunkte und skaliert schrittweise den Anteil erneuerbarer Energie aus Wind- und Solarkraft hoch, finden wir, dass die regelbare Kapazität reduziert werden kann, angefangen mit den langsamsten Kraftwerken, die sowieso schlecht geeignet sind, der Residuallast zu folgen. Um regelbare Kraftwerke komplett zu ersetzen, wäre allerdings eine erhebliche Überinstallation an Wind- und Solarkapazitäten notwendig, sodass die gesamte erneuerbare Erzeugung in der Größenordnung des dreifachen Verbrauchs zu erwarten wäre. Erste Reduktionen wären dagegen schon ab Beginn der erneuerbaren Erzeugung möglich.

Voraussetzung für diesen Abbau ist allerdings wiederum eine ausgedehnte Kooperation zwischen den europäischen Ländern, verbunden mit einem starken internationalen Stromnetz in ähnlicher Größenordnung wie in Abschnitt 5.2 anvisiert.

References

[1] International Energy Agency, Key World Energy Statistics, Paris, France, 2013, `http://www.iea.org/publications/freepublications/publication/name-31287-en.html`.

[2] Eurostat, `http://epp.eurostat.ec.europa.eu`, Tables nrg_105a and nrg_107a, 2014, Online, accessed Apr 2014.

[3] Lüthi, D. et al., Nature **453** (2008) 379, `http://dx.doi.org/10.1038/nature06949`.

[4] Bradley, R. S., *Paleoclimatology: Reconstructing Climates of the Quarternary*, Academic Press, San Diego, CA, USA, 2 edition, 1999.

[5] IPCC, Summary for Policy Makers, in *Climate Change 2013: The Physical Science Basis. Contribution of Working Group I to the Fifth Assessment Report of the Intergovernmental Panel on Climate Change*, edited by Stocker, T. et al., Cambridge University Press, Cambridge, United Kingdom and New York, NY, USA, 2013, `http://www.ipcc.ch/report/ar5/wg1/`.

[6] Tans, P. and Keeling, R., Atmospheric CO_2 at Mauna Loa, `http://www.esrl.noaa.gov/gmd/ccgg/trends/`, 2014, Online, accessed April 2014.

[7] Floudas, D. et al., Science **336** (2012) 1715, `http://dx.doi.org/10.1126/science.1221748`.

[8] Jacobson, M. Z., Energy Environ. Sci. **2** (2009) 148, `http://dx.doi.org/10.1039/B809990C`.

[9] Sovacool, B. K. and Watts, C., The Electricity Journal **22** (2009) 95 , `http://dx.doi.org/10.1016/j.tej.2009.03.011`.

[10] Scott, R., The History of the IEA, 1994, `https://www.iea.org/aboutus/history/`, accessed Jul 2014.

[11] Gagnon, L., Energy Policy **36** (2008) 3317 , `http://dx.doi.org/10.1016/j.enpol.2008.05.012`.

[12] World Health Organization (WHO), 7 million premature deaths annually linked to air pollution, `http://www.who.int/mediacentre/news/releases/2014/air-pollution/en/`, 2014, Online, accessed Jul 2014.

[13] Brauer, M. et al., Environmental Science & Technology **46** (2012) 652, `http://dx.doi.org/10.1021/es2025752`.

[14] Delucchi, M. A. and Jacobson, M. Z., Energy Policy **39** (2011) 1170, `http://dx.doi.org/10.1016/j.enpol.2010.11.045`.

[15] Wikipedia, Photovoltaik in Deutschland — Wikipedia, Die freie Enzyklopädie, 2014, `http://de.wikipedia.org/w/index.php?title=Photovoltaik_in_Deutschland&oldid=131783086`, accessed Jul 2014.

[16] Umweltbundesamt, Flächenverbrauch für Rohstoffabbau, 2013, `http://www.umweltbundesamt.de/daten/flaechennutzung/flaechenverbrauch-fuer-rohstoffabbau`, accessed Jul 2014.

[17] Jacobson, M. Z. and Delucchi, M. A., Energy Policy **39** (2011) 1154–1169, `http://dx.doi.org/10.1016/j.enpol.2010.11.040`.

[18] Edenhofer, O. et al., editors, *Special Report on Renewable Energy Sources and Climate Change Mitigation*, Cambridge University Press, United Kingdom and New York, NY, USA, 2011.

[19] International Energy Agency, Potential Contribution of Bioenergy to the World's Future Energy Demand, 2007, `http://www.ieabioenergy.com/publications/potential-contribution-of-bioenergy-to-the-worlds-future-energy-demand/`.

[20] EU member countries, National Renewable Energy Action Plans, `http://ec.europa.eu/energy/renewables/action_plan_en.htm`, 2010, Online, accessed Jan 2012.

[21] Beurskens, L. W. M., Hekkenberg, M., and Vethman, P., Renewable Energy Projections as Published in the National Renewable Energy Action Plans of the European Member States, Technical report, Energy research Centre of the Netherlands, `http://ecn.nl/nreap`, 2011, Online, accessed September 2012.

[22] Lorenz, H., Fischer, P., Schumacher, B., and Adler, P., Waste Management **33** (2013) 2434–2448, `http://dx.doi.org/10.1016/j.wasman.2013.06.018`.

[23] de Wit, M. and Faaij, A., Biomass and Bioenergy **34** (2010) 188, `http://dx.doi.org/10.1016/j.biombioe.2009.07.011`.

[24] Anbau nachwachsender Rohstoffe in Deutschland, `http://mediathek.fnr.de/grafiken/daten-und-fakten/anbauflache-fur-nachwachsende-rohstoffe-2013-grafik.html`, 2013, Online, accessed Apr 2014.

[25] Tonini, D. and Astrup, T., Applied Energy **99** (2012) 234–246, `http://dx.doi.org/10.1016/j.apenergy.2012.03.006`.

[26] Union of the Electricity Industry (EURELECTRIC) – Hydropower and other renewable energies study committee, Study on the importance of harnessing the hydropower resources of the world, Technical report, EURELECTRIC, Brussels, 1997.

[27] Lehner, B., Czisch, G., and Vassolo, S., Energy Policy **33** (2003) 839 , `http://dx.doi.org/10.1016/j.enpol.2003.10.018`.

[28] ITER Organization, `http://www.iter.org/proj/iterandbeyond`, 2012, Online, accessed May 2012.

[29] McKinsey & Company, KEMA, The Energy Futures Lab at Imperial College London, Oxford Economics, and ECF, Roadmap 2050 – A practical guide to a prosperous, low-carbon Europe, Technical report, European Climate Foundation, `http://www.roadmap2050.eu/downloads`, 2010, Online, accessed June 2012.

[30] Williams, J. H. et al., Science **335** (2012) 53, `http://dx.doi.org/10.1126/science.1208365`.

[31] UCTE Investigation Committee, System Disturbance on 4 November 2006 – final report, Technical report, Union for the Coordination of Transmission of Electricity (UCTE), Brussels, 2007, Online available at `https://www.entsoe.eu/news-events/former-associations/ucte/other-reports/Pages/default.aspx`.

[32] Acebrón, J. A., Bonilla, L. L., Pérez Vicente, C. J., Ritort, F., and Spigler, R., Rev. Mod. Phys. **77** (2005) 137, `http://dx.doi.org/10.1103/RevModPhys.77.137`.

[33] Filatrella, G., Nielsen, A. H., and Pedersen, N. F., Eur. Phys. J. B **61** (2008) 485, `http://dx.doi.org/10.1140/epjb/e2008-00098-8`.

[34] Witthaut, D. and Timme, M., New J. Phys. **14** (2012) 083036, `http://dx.doi.org/10.1088/1367-2630/14/8/083036`.

[35] Rohden, M., Sorge, A., Timme, M., and Witthaut, D., Phys. Rev. Lett. **109** (2012) 064101, `http://dx.doi.org/10.1103/PhysRevLett.109.064101`.

[36] Jensen, T. V. and Greiner, M., The European Physical Journal Special Topics (2014) 1, `http://dx.doi.org/10.1140/epjst/e2014-02216-9`.

[37] Søndergaard, A. A., Development of a Renewable Energy Atlas and Extreme Event Analysis in Renewable Energy Systems, M. Sc. thesis, Aarhus University, Denmark, 2013.

[38] von Bremen, L., Saleck, N., and Heinemann, D., Journal of Physics: Conference Series **75** (2007) 012040, `http://dx.doi.org/10.1088/1742-6596/75/1/012040`.

[39] Zeyer, T., Modeling of spatio-temporal flow patterns in a fully renewable pan-European power system, M. Sc. thesis, Aarhus University, Denmark, 2013.

[40] Jensen, T. V., Structure modeling and renormalized power flow statistics of fully renewable energy networks, M. Sc. thesis, Aarhus University, Denmark, 2013.

[41] Archer, C. L. and Jacobson, M. Z., Journal of Applied Meteorology and Climatology **46** (2007) 1701, `http://dx.doi.org/10.1175/2007JAMC1538.1`.

[42] Holttinen, H., Wind Energy **8** (2005) 197, `http://dx.doi.org/10.1002/we.143`.

[43] Sinden, G., Energy Policy **35** (2007) 112–127, `http://dx.doi.org/10.1016/j.enpol.2005.10.003`.

[44] Wiemken, E., Beyer, H., Heydenreich, W., and Kiefer, K., Solar Energy **70** (2001) 513–518, `http://dx.doi.org/10.1016/S0038-092X(00)00146-8`.

[45] Mills, A. D. and Wiser, R. H., Implications of geographic diversity for short-term variability and predictability of solar power, in *2011 IEEE Power and Energy Society General Meeting*, pages 1–9, IEEE, 2011, `http://dx.doi.org/10.1109/PES.2011.6039888`.

[46] Widén, J., IEEE Transactions on Sustainable Energy **2** (2011) 177, `http://dx.doi.org/10.1109/TSTE.2010.2101620`.

[47] Kempton, W., Pimenta, F. M., Veron, D. E., and Colle, B. A., Proceedings of the National Academy of Sciences **107** (2010) 7240, `http://dx.doi.org/10.1073/pnas.0909075107`.

[48] Østergaard, P. A., Energy **33** (2008) 1453 , `http://dx.doi.org/10.1016/j.energy.2008.04.016`.

[49] Heide, D. et al., Renewable Energy **35** (2010) 2483, `http://dx.doi.org/10.1016/j.renene.2010.03.012`.

[50] Heide, D., Greiner, M., von Bremen, L., and Hoffmann, C., Renewable Energy **36** (2011) 2515, `http://dx.doi.org/10.1016/j.renene.2011.02.009`.

[51] Heide, D., *Statistical Physics of Power Flows on Networks with a High Share of Fluctuating Renewable Generation*, PhD thesis, Frankfurt Institute for Advanced Studies, University of Frankfurt, 2010, `http://publikationen.ub.uni-frankfurt.de/frontdoor/index/index/docId/21455`.

[52] Rasmussen, M. G., Andresen, G. B., and Greiner, M., Energy Policy **51** (2012) 642, `http://dx.doi.org/10.1016/j.enpol.2012.09.009`.

[53] Rodríguez, R. A., Becker, S., Andresen, G. B., Heide, D., and Greiner, M., Renewable Energy **63** (2014) 467, `http://dx.doi.org/10.1016/j.renene.2013.10.005`, preprint available at `http://arxiv.org/abs/1306.1079`.

[54] Becker, S., Rodríguez, R. A., Andresen, G. B., Schramm, S., and Greiner, M., Energy **64** (2014) 404, `http://dx.doi.org/10.1016/j.energy.2013.10.010`; preprint available at `http://arxiv.org/abs/1307.1723`.

[55] Becker, S. et al., Energy **72** (2014) 443–458, Online at `http://dx.doi.org/10.1016/j.energy.2014.05.067`; preprint available at `http://arxiv.org/abs/1402.2833`.

[56] Schaber, K., Steinke, F., Hamacher, T., and Mühlich, P., Energy Policy **42** (2011) 498, `http://dx.doi.org/10.1016/j.enpol.2011.12.016`.

[57] Schaber, K., Steinke, F., and Hamacher, T., Energy Policy **43** (2012) 123, `http://dx.doi.org/10.1016/j.enpol.2011.12.040`.

[58] Fürsch, M. et al., Roadmap 2050 – a closer look, Technical report, energynautics and Institute for Energy Economy at the University of Cologne, `http://www.energynautics.com/news/`, 2011.

[59] Steinke, F., Wolfrum, P., and Hoffmann, C., Renewable Energy **50** (2013) 826 , `http://dx.doi.org/10.1016/j.renene.2012.07.044`.

[60] Rodríguez, R. A., Becker, S., and Greiner, M., submitted for review (2014).

[61] Becker, S. et al., Energy (2015) –, Online at `http://dx.doi.org/10.1016/j.energy.2014.12.056`; preprint available at `http://arxiv.org/abs/1412.4934`.

[62] Becker, S., Rodríguez, R. A., Andresen, G. B., Greiner, M. O., and Schramm, S., What can transmission do for a fully renewable Europe?, in *Proceedings of the 8th conference on Sustainable Development of Energy, Water, and Environment Systems (SDEWES)*, 2013, Preprint available at `http://arxiv.org/abs/1401.4298`.

[63] Bofinger, S. et al., Raum-zeitliche Erzeugungsmuster von Wind- und Solarenergie in der UCTE-Region und deren Einfluss auf elektrische Transportnetze: Abschlussbericht für Siemens Zentraler Forschungsbereich (Temporal and Spatial Generation Patterns of Wind and Solar Energy in the UCTE-Region. Impacts of these on the Electricity Transmission Grid), Technical report, Institut für Solare Energieversorgungstechnik, ISET e.V., Kassel, 2008.

[64] Corcoran, B. A., Jenkins, N., and Jacobson, M. Z., Energy Policy **46** (2012) 399, `http://dx.doi.org/10.1016/j.enpol.2012.03.079`.

[65] Saha et al, S., Bull. Amer. Meteor. Soc. **91** (2010) 1015, `http://dx.doi.org/10.1175/2010BAMS3001.1`.

[66] Andresen, G. B., Søndergaard, A. A., and Greiner, M., Submitted for review (2014).

[67] M. Brower, for NREL, under supervision of D. Corbus, Development of Eastern Regional Wind Resource and Wind Plant Output Datasets, Technical report, AWS Truewind LLC, Albany, New York, 2009, Final data sets available at `http://www.nrel.gov/electricity/transmission/eastern_wind_dataset.html`.

[68] C. Potter and B. Nijssen, for NREL, under supervision of D. Lew, Development of Regional Wind Resource and Wind Plant Output Datasets, Technical report, 3TIER, Seattle, Washington, 2009, Final data sets available at `http://www.nrel.gov/electricity/transmission/western_wind_dataset.html`.

[69] Solar panel data, `http://www.scheutensolar.de`, 2012, Online, accessed 2012.

[70] Wind and solar resource maps, `http://www.nrel.gov/gis/maps.html`, 2013, Online, accessed Nov 2013.

[71] Co-ordinator: European Wind Energy Association, Integrating Wind – Developing Europe's power market, Technical report, Project Partners: Sintef Energiforskning AS, Risø–DTU, 3E, Kema Nederland BV, Technical Research Centre of Finland (VTT), Garrad Hassan and Partners Ltd, Tractebel Engineering, Deutsche Energie-Agentur (dena), 2009, Available online at `http://www.trade-wind.eu/`, accessed June 2014.

[72] Archer, C. and Jacobson, M., J. Geophys. Res. **108** (2003) 4289, `http://dx.doi.org/10.1029/2002JD002076`.

[73] Turbine overview, `http://www.vestas.com/en/wind-power-plants/procurement/turbine-overview.aspx`, 2011, Online, accessed 2011.

[74] Badger, J., Kelly, M. C., and Jørgensen, H. E., Regional wind resource distributions: mesoscale results and importance of microscale modeling, 2010, Online publication of conference talk slides at `http://emf.stanford.edu/events/snowmass_2010/`, accessed May 2013.

[75] Badger, J. and Jørgensen, H. E., A high resolution global wind atlas - improving estimation of world wind resources, in *Risø International Energy Conference 2011*, pages 215–225, 2011, `http://orbit.dtu.dk/fedora/objects/orbit:63370/datastreams/file_5564461/content`.

[76] Fry, J. et al., Completion of the 2006 National Land Cover Database for the Conterminous United States, Technical report, Multi-resolution land characteristics consortium, `http://www.mrlc.gov/nlcd2006.php`, 2011, Online, accessed May 2013.

[77] Petersen, E. L., Mortensen, N. G., Landberg, L., Højstrup, J., and Frank, H. P., Risø National Laboratory, Roskilde, Denmark (1998), `http://dx.doi.org/10.1002/(SICI)1099-1824(199804)1:1+<25::AID-WE4>3.0.CO;2-D`.

[78] ESRI, North America Digital Elevation Model Raster Dataset, Technical report, Redlands, CA, 2005.

[79] ENTSO-E, Country-specific hourly load data, `https://www.entsoe.eu/resources/data-portal/consumption/`, 2011.

[80] International Energy Agency, Energy in the Western Balkans, 2008, `http://www.iea.org/publications/freepublications/publication/name-3776-en.html`.

[81] Energiaftalen 22. marts 2012, 2012, Available online at `http://www.ens.dk/politik/dansk-klima-energipolitik/politiske-aftaler-pa-energiomradet/energiaftalen-22-marts-2012`, accessed November 2012.

[82] Schweizerische Eidgenossenschaft – Der Bundesrat, Energieperspektiven 2050 – Analyse der Stromangebotsvarianten des Bundesrats, 2011, Online available at `www.bfe.admin.ch/php/modules/publikationen/stream.php?extlang=de&name=de_180902397.pdf`, accessed Mar 2012.

[83] Kirchner, A., Ess, F., and Piégsa, A., Energieszenarien für die Schweiz bis 2050: Erste Ergebnisse der angepassten Szenarien I und IV aus den Energieperspektiven 2007 – Elektrizitätsangebot, Technical report, prognos AG Basel, 2011, `www.bfe.admin.ch/php/modules/publikationen/stream.php?extlang=de&name=de_773003560.pdf`, accessed Mar 2012.

[84] Croatian Parliament, Energy Strategy of Croatia, Official Gazette of the Croatian Parliament, 2009, Online available at `http://www.mingo.hr/page/strategy-security-of-supply-and-energy-balances`, accessed Apr 2012.

[85] SINTEF (Norwegian foundation for scientific and industrial research), `http://www.sintef.no/wind`, 2012, Online, accessed Sep 2012.

[86] European Commission, A roadmap for moving to a competitive low carbon economy in 2050, Technical report, EC, 2011, `http://ec.europa.eu/clima/policies/roadmap/documentation_en.htm`, accessed Mar 2012.

[87] Grübler, A., *The Rise and Fall of Infrastructures*, Physica-Verlag, Heidelberg, 1990.

[88] Moore, S. and Simon, J. L., Policy Analysis **364** (1999).

[89] Grübler, A., Nakićenović, N., and Victor, D. G., Energy Policy **5** (1999) 247, `http://dx.doi.org/10.1016/S0301-4215(98)00067-6`.

[90] Wilson, C. and Grübler, A., Natural Resources Forum **35** (2011) 165, `http://dx.doi.org/10.1111/j.1477-8947.2011.01386.x`.

[91] Fouquet, R., Energy Policy **38** (2010) 6586 , Energy Efficiency Policies and Strategies with regular papers. `http://dx.doi.org/10.1016/j.enpol.2010.06.029`.

[92] (Energistyrelsen), T. D. E. A. and Energinet.dk, Technology Data for Energy Plants – Generation of Electricity and District Heating, Technical report, `http://www.ens.dk`, 2012, Online, accessed October 2012.

[93] Konstantin, P., *Praxisbuch Energiewirtschaft: Energieumwandlung, -transport und -beschaffung im liberalisierten Markt*, Springer-Verlag, Berlin Heidelberg, 2 edition, 2009.

[94] Boyd, S. and Vandenberghe, L., *Convex Optimization*, Cambridge University Press, Cambridge, New York, Melbourne, Madrid, Cape Town, Singapore, São Paolo, Delhi, 2004.

[95] Dresden, A., Bulletin of the American Mathematical Society **26** (1920) 385, Protocol including Moore's derivation of the Moore-Penrose pseudo-inverse, `http://projecteuclid.org/euclid.bams/1183425340`.

[96] Penrose, R., Mathematical Proceedings of the Cambridge Philosophical Society **51** (1955) 406, `http://dx.doi.org/10.1017/S0305004100030401`.

[97] Kelner, J. A., Orecchia, L., Sidford, A., and Zhu, Z. A., A simple, combinatorial algorithm for solving sdd systems in nearly-linear time, in *Proceedings of the Forty-fifth Annual ACM Symposium on Theory of Computing*, STOC '13, pages 911–920, New York, NY, USA, 2013, ACM, `http://dx.doi.org/10.1145/2488608.2488724`.

[98] Oswald, B. and Oeding, D., *Elektrische Kraftwerke und Netze.*, Springer-Verlag, Berlin Heidelberg New York, 6 edition, 2004.

[99] ENTSO-E, Indicative values for Net Transfer Capacities (NTC) in Continental Europe. European Transmission System Operators, 2011, `https://www.entsoe.eu/publications/market-reports/ntc-values/ntc-matrix/Pages/default.aspx`, accessed Jul 2014.

[100] Van De Putte, J. and Short, R., Battle of the grids, `http://www.greenpeace.org/international/en/publications/reports/Battle-of-the-grids/`, 2011, Online, accessed June 2014.

[101] Tröster, E., Kuwahata, R., and Ackermann, T., European grid study 2030/2050, Technical report, energynautics GmbH, `http://www.energynautics.com/news/`, 2011, Online, accessed November 2012.

[102] De Decker, J. et al., Offshore Electricity Grid Infrastructure in Europe, Technical report, 3E (coordinator), dena, EWEA, ForWind, IEO, NTUA, Senergy, SINTEF, 2011, `http://www.offshoregrid.eu/`, accessed June 2014.

[103] Hagspiel, S. et al., Energy **66** (2014) 654 , `http://dx.doi.org/10.1016/j.energy.2014.01.025`.

[104] Kunz, F., *Managing Congestion and Intermittent Renewable Generation in Liberalized Electricity Markets*, PhD thesis, Fakultät Wirtschaftswissenschaften der Technischen Universität Dresden, 2012, `http://www.qucosa.de/recherche/frontdoor/?tx_slubopus4frontend[id]=10879`.

[105] Garver, L. L., IEEE Transactions on Power Apparatus and Systems **PAS-89** (1970) 1688 , `http://dx.doi.org/10.1109/TPAS.1970.292825`.

[106] Villasana, R., Garver, L. L., and Salon, S., IEEE Transactions on Power Apparatus and Systems **PAS-104** (1985) 349 , `http://dx.doi.org/10.1109/TPAS.1985.319049`.

[107] Romero, R., Gallego, R., and Monticelli, A., IEEE Transactions on Power Systems **11** (1996) 364 , `http://dx.doi.org/10.1109/59.486119`.

[108] Gallego, R., Alves, A., Monticelli, A., and Romero, R., IEEE Transactions on Power Systems **12** (1997) 181 , `http://dx.doi.org/10.1109/59.574938`.

[109] Gallego, R., Monticelli, A., and Romero, R., IEEE Transactions on Power Systems **145** (1998) 329 , `http://dx.doi.org/10.1049/ip-gtd:19981895`.

[110] Alguacil, N. and Conejo, A., IEEE Transactions on Power Systems **15** (2000) 196 , `http://dx.doi.org/10.1109/59.852121`.

[111] Binato, S., Pereira, M., and Granville, S., IEEE Transactions on Power Systems **16** (2001) 235 , `http://dx.doi.org/10.1109/59.918292`.

[112] Alguacil, N., Motto, A., and Conejo, A., IEEE Transactions on Power Systems **18** (2003) 1070 , `http://dx.doi.org/10.1109/TPWRS.2003.814891`.

[113] de la Torre, S., Conejo, A., and Contreras, J., IEEE Transactions on Power Systems **23** (2008) 238 , `http://dx.doi.org/10.1109/TPWRS.2007.913717`.

[114] Al-Saba, T. and El-Amin, I., Electric Power Systems Research **62** (2002) 117 , `http://dx.doi.org/10.1016/S0378-7796(02)00037-8`.

[115] Sum-Im, T., Taylor, G. A., Irving, M. R., and Song, Y. H., A differential evolution algorithm for multistage transmission expansion planning, in *42nd International Universities Power Engineering Conference, 2007. UPEC 2007.*, pages 357 – 364, IEEE, 2007, `http://dx.doi.org/10.1109/UPEC.2007.4468974`.

[116] Wang, Y. et al., Electric Power Systems Research **78** (2008) 1619 , `http://dx.doi.org/10.1016/j.epsr.2008.02.004`.

[117] Barnacle, M., Robertson, E., Galloway, S., Barton, J., and Ault, G., Energy Policy **52** (2013) 60 , `http://dx.doi.org/10.1016/j.enpol.2012.04.031`.

[118] Dt. Übertragungsnetzbetreiber: 50Hertz Transmission GmbH, Amprion GmbH, TenneT TSO GmbH, TransnetBW GmbH, Netzentwicklungsplan Strom 2014, erster Entwurf, `http://www.netzentwicklungsplan.de` (accessed Jul 2014), 2014.

[119] ENTSO-E, Scenario Outlook & System Adequacy Forecast 2011-2025, Technical report, ENTSO-E, 2011, `https://www.entsoe.eu/about-entso-e/system-development/system-adequacy-and-market-modeling/Pages/default.aspx`, accessed Jul 2014.

[120] European Network of Transmission System Operators for Electricity, ENTSO-E Ten Year Network Development Plan, Technical report, ENTSO-E, Brussels, 2012, Online at `https://www.entsoe.eu/major-projects/ten-year-network-development-plan/tyndp-2012/Pages/default.aspx`, accessed July 2014.

[121] The Danish Energy Agency (Energistyrelsen) and Energinet.dk, Technology Data for Energy Plants – Individual Heating Plants and Energy Transport, Technical report, `http://www.ens.dk`, 2012, Online, accessed Jul 2014.

[122] BritNed Construction, `http://www.britned.com/BritNed/AboutUs/Construction`, 2013, Online, accessed July 2013.

[123] The 580 kilometer-long NorNed link is the longest subsea high-voltage cable in the world, 2014, `http://new.abb.com/systems/hvdc/references/norned`, accessed Jul 2014.

[124] SwePol Link HVDC interconnection project, `http://www.abb.com/industries/ap/db0003db004333/c84945b54aa6cfb8c125774a00486402.aspx`, 2013, Online, accessed July 2013.

[125] Månedlig elforsyningsstatistik, summary tab B58-B72, `http://www.ens.dk`, 2012, Online, accessed Nov 2012.

[126] Short, W. et al., Regional Energy Deployment System (ReEDS), Technical report, National Renewable Energy Laboratory (NREL), Golden, Colorado, 2011, Report available at `http://www.nrel.gov/analysis/reeds/documentation.html`.

[127] Kirkpatrick, S., Gelatt, C. D., and Vecchi, M. P., Science **220** (1983) 671, `http://dx.doi.org/10.1126/science.220.4598.671`.

[128] Černý, V., Journal of Optimization Theory and Applications **45** (1985) 41, `http://dx.doi.org/10.1007/BF00940812`.

[129] Wikipedia, Simulated annealing — wikipedia, the free encyclopedia, `http://en.wikipedia.org/w/index.php?title=Simulated_annealing&oldid=568123430`, 2013, Online, accessed Sep 2013.

[130] The Scipy community, scipy.optimize.anneal documentation, scipy version: 0.13.0, `http://docs.scipy.org/doc/scipy-0.13.0/reference/generated/scipy.optimize.anneal.html`, 2013, Online, accessed Jul 2014.

[131] Hand, M. et al., Renewable Electricity Futures Study, `http://www.nrel.gov/analysis/re_futures/`, 2012, eds. 4 vols. NREL/TP-6A20-52409.

[132] European Commission, Memo on the Renewable Energy and Climate Change Package, `http://europa.eu/rapid/press-release_MEMO-08-33_en.htm?locale=EN`, 2008, Memo/08/33.

[133] de Oliveira, E., da Silva, I.C., J., Pereira, J., and Carneiro, S., J., IEEE Transactions on Power Systems **20** (2005) 1616 , `http://dx.doi.org/10.1109/TPWRS.2005.852065`.

[134] US Army Corps of Engineers, Civil Works Construction Cost Index System , Technical report, US Army Corps of Engineers, `http://planning.usace.army.mil/toolbox/library/EMs/em1110.2.1304.pdf`, 2011, Online, accessed Aug 2013.

[135] Energy and Environmental Economics (E3), San Francisco, CA, Cost and Performance Review of Generation Technologies: Recommendations for WECC 10- and 20-Year Studies, Technical report, `http://www.nwcouncil.org/media/6867814/E3_GenCapCostReport_finaldraft.pdf`, 2012, Online, accessed Aug 2013.

[136] Hart, E. K. and Jacobson, M. Z., Renewable Energy **36** (2011) 2278 , `http://dx.doi.org/10.1016/j.renene.2011.01.015`.

[137] Budischak, C. et al., Journal of Power Sources **225** (2013) 60 , `http://dx.doi.org/10.1016/j.jpowsour.2012.09.054`.

[138] Nelson, J. et al., Energy Policy **43** (2012) 436 , `http://dx.doi.org/10.1016/j.enpol.2012.01.031`.

[139] Transparent Cost Database, `http://en.openei.org/apps/TCDB/`, 2013, Online, accessed Aug 2013.

[140] Andresen, G. B., Rasmussen, M. G., Rodríguez, R. A., Becker, S., and Greiner, M., Fundamental properties of and transition to a fully renewable pan-European power system, in *2nd European Energy Conference*, volume 33, page 04001, 2012, `http://dx.doi.org/10.1051/epjconf/20123304001`.

[141] Andresen, G. B., Heide, D., Rasmussen, M. G., and Greiner, M., Transition to a Fully Renewable Power System in Europe, in *Proceedings of the 10th International Workshop on Large-Scale Integration of Wind Power into Power Systems as well as on Transmission Networks for Offshore Wind Power Plants*, pages 322–325, 2011, `http://www.windintegrationworkshop.org/old_proceedings.php`.

[142] Huber, M., Dimkova, D., and Hamacher, T., Energy **69** (2014) 236 , `http://dx.doi.org/10.1016/j.energy.2014.02.109`.

[143] EWE AG, Kühlhaus gleicht Windschwankungen aus, 2009, Pressemitteilung, `http://www.ewe.com/de/presse/ewe-ag/pressemitteilungen-1047.php`.

[144] Cowardin, L., Carter, V., Golet, F., and LaRoe, E., Classification of Wetlands and Deepwater Habitat of the United States, 1979, Online available at `http://landcover.usgs.gov/classes.php`, accessed June 2013.

[145] Sorrentino, F. and Ott, E., Phys. Rev. E **76** (2007) 056114, `http://dx.doi.org/10.1103/PhysRevE.76.056114`, preprint available at `http://arxiv.org/abs/0711.3716`.

[146] Sorrentino, F. and Porfiri, M., Europhysics Letters **935** (2011) 50002, `http://dx.doi.org/10.1209/0295-5075/93/50002`, preprint available at `http://arxiv.org/abs/1102.1709`.

[147] Schäfer, M. and Greiner, M., Chaos, Solitons & Fractals **45** (2012) 825 , `http://dx.doi.org/10.1016/j.chaos.2012.02.017`.

[148] Sun, J., Bollt, E. M., and Nishikawa, T., Europhysics Letters **856** (2009) 60011, `http://dx.doi.org/10.1209/0295-5075/85/60011`, preprint available at `http://arxiv.org/abs/0811.0649`.

[149] Perko, L., *Differential equations and dynamical systems*, Springer-Verlag New York, Inc., New York, NY, USA, 1991.

[150] Hartman, P., *Ordinary differential equations*, Society for Industrial and Applied Mathematics, Philadelphia, corrected reprint of the 2nd edition, 2002.

[151] Rugh, W. J., *Linear system theory*, Prentice-Hall, Inc., Upper Saddle River, NJ, USA, 2 edition, 1996.

[152] Amritkar, R. E. and Jalan, S., Physica A Statistical Mechanics and its Applications **321** (2003) 220, `http://dx.doi.org/10.1016/S0378-4371(02)01750-8`.

[153] Jalan, S. and Amritkar, R. E., Phys. Rev. Lett. **90** (2003) 014101, `http://dx.doi.org/10.1103/PhysRevLett.90.014101`.

[154] Barabasi, A.-L., Albert, R., and Jeong, H., Physica A Statistical Mechanics and its Applications **281** (2000) 69, `http://dx.doi.org/10.1016/S0378-4371(00)00018-2`.

[155] Hislop, P. D. and Sigal, I. M., *Introduction to spectral theory*, Springer-Verlag New York, Inc., New York, NY, USA, 1996.